Downloaded from orbit.dtu.dk on: May 05, 2023

DTU Library

Zooplankton Hydrodynamics

An investigation into the physics of aquatic interactions

Wadhwa, Navish

Publication date:
2015

Document Version
Publisher's PDF, also known as Version of record

Link back to DTU Orbit

Citation (APA):
Wadhwa, N. (2015). *Zooplankton Hydrodynamics: An investigation into the physics of aquatic interactions*. Technical University of Denmark.

General rights
Copyright and moral rights for the publications made accessible in the public portal are retained by the authors and/or other copyright owners and it is a condition of accessing publications that users recognise and abide by the legal requirements associated with these rights.

- Users may download and print one copy of any publication from the public portal for the purpose of private study or research.
- You may not further distribute the material or use it for any profit-making activity or commercial gain
- You may freely distribute the URL identifying the publication in the public portal

If you believe that this document breaches copyright please contact us providing details, and we will remove access to the work immediately and investigate your claim.

DTU Physics
Department of Physics

Centre for Ocean Life
VKR Centre of Excellence

Zooplankton Hydrodynamics

An investigation into the physics of aquatic interactions

Navish Wadhwa

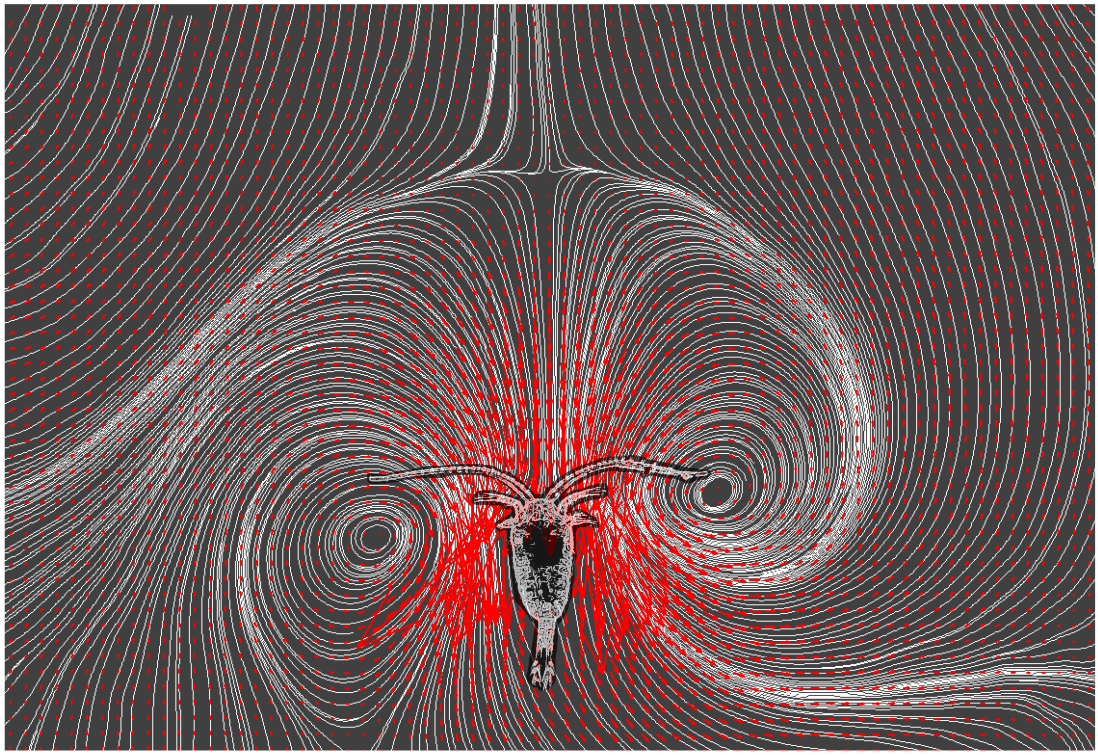

Ph.D. thesis

15 September 2015

Advised by Associate Professor Anders Andersen

Cover illustration: Streamlines and velocity vectors of the flow field due to the feeding current generated by the copepod *Temora longicornis*.

Zooplankton Hydrodynamics — An investigation into the physics of aquatic interactions

Copyright © 2015 Navish Wadhwa All Rights Reserved
Typeset using LaTeX.

http://www.fysik.dtu.dk/english/Research/FLUIDS
http://wadhwanavish.wix.com/home

To the memory of my father,
who never gave up

Abstract

Zooplankton are hugely abundant organisms found in all aquatic environments and form an important part of the marine ecosystems. Most zooplankton swim in order to find food and mates, and to avoid predators. In spite of its advantages, swimming comes with trade-offs, it costs energy and creates flow disturbances that may attract predators. The first part of this thesis attempts to quantify the trade-offs associated with the swimming behaviour of diverse zooplankton.

We measured the swimming kinematics and flow fields around the 'jumping' copepod *Acartia tonsa* at various stages of its life cycle, and found qualitative differences in flow structures, energy expenditure, and swimming efficiency, between the early and later stages. The spatial decay rate of flow disturbances was faster in the later stages, suggesting that those may be less vulnerable to predation. Broadening the scope, we then measured flows around a wide range of zooplankton which use a variety of swimming modes such as hovering, cruising, jumping, and breast stroke swimming. We found that the spatial decay rate of the flow velocity is dictated by the swimming mode. The modes used for swimming only, such as jumping and breast stroke swimming, had much faster spatial decay as compared to the other modes, resulting in 'quiet' swimming.

This motivated us to examine breast stroke swimming in more detail, for which flow velocity decayed spatially as one over distance cubed. We employed a simple model using three point forces to represent the forces acting on the swimmer. Our analysis showed a configuration-dependent spatial decay of flow velocity. Arranging the propulsive forces close to the equator resulted in changing the far field velocity decay from one over distance squared to one over distance cubed, comparing well with the experimental observations. To further investigate periodic swimming using breast stroke, we measured detailed swimming dynamics and induced flows for the cladoceran *Podon intermedius*. We estimated the propulsive forces acting on *P. intermedius*, which showed that the fast spatial decay in the induced flows was not explained by the three point force model. We speculate that this is due to inertial effects in the flow, which seem to play an important role in the swimming of

larger zooplankton. We also developed a simple model to mimic the dynamics of periodic swimming, which showed that non-linear drag terms are needed in the model to correctly capture the observed dynamics.

The second part of this thesis examines how size dictates transitions in life strategies, and thus acts as a structuring factor in marine life. To this end, we reviewed data on size-based scaling laws for resource acquisition, motility, sensing, and offspring size for all pelagic marine life, from bacteria to whales. We also reviewed and developed theoretical arguments for the observed scaling laws and for the characteristic sizes at which transitions from one strategy to another take place. Based on our findings, we divided life in the ocean into seven major realms based on trophic strategy, physiology, and life history strategy.

Finally, we delve deeper into size based structuring of sensory strategies in the ocean. Survival in the open ocean requires effective collection of information from the surroundings via the use of various sensory modes. We studied how sensing modes and their respective ranges depend on body size. We investigated the physiological constraints on sense organs, together with the physics of signal generation, transmission, and reception. Our analysis revealed a hierarchy of sensing modes - with increasing size, a larger battery of sensory modes becomes available and the sensing range increases. Our theoretical predictions of lower and upper size limits for various senses aligned well with the size ranges found in the literature. Although the scaling analyses and the size limits are only first order estimates, this work forms the first comprehensive analysis of the size based structuring of sensory modes used by marine life.

Resumé

Zooplankton er meget udbredte i havet og de ferske vande, og de udgør en vigtig del af det marine økosystem. De fleste zooplankton svømmer for at finde mad og mager, og for at undgå rovdyr, men der er omkostninger forbundet med svømning, da svømning koster energi og skaber strømningsforstyrrelser, som kan tiltrække rovdyr. Den første del af denne afhandling forsøger at kvantificere disse "trade-offs" for forskellige dyreplanktons svømning.

Vi målte svømmekinematik og strømningsfelter omkring den "hoppende" vandloppe *Acartia tonsa* i forskellige stadier af dens livscyklus, og vi fandt kvalitative forskelle i strømningsstrukturer, energiforbrug og svømmeeffektivitet mellem tidlige og sene stadier. Det rumlige henfald af strømningsforstyrrelsen var hurtigere i de sene stadier, hvilket tyder på, at de kan være mindre sårbare over for prædation. For at perspektivere resultaterne målte vi derefter strømninger omkring en bred vifte af dyreplankton, der anvender forskellige svømmeformer såsom hovering, cruising, hop og brystsvømning. Vi fandt, at den rumlige henfaldshastighed af strømningshastigheden er dikteret af svømmeformen. De former, der udelukkende anvendes til svømning, såsom hop og brystsvømning, havde meget hurtigere rumlige henfald i forhold til de andre svømmeformer, hvilket resulterer i "stille" svømning.

Disse observationer motiverede os til yderligere at undersøge brystsvømning, hvor strømningshastigheden henfaldt rumligt som en over afstanden i tredie. Vi anvendte en simpel model med tre punktkræfter til at repræsentere de kræfter, der virker på svømmeren. Vores analyse viste et positionsafhængigt henfald af strømningshastigheden. Placeres de fremaddrivende kræfter tæt på ækvator ændres henfaldet af fjernfeltet fra en over afstanden i anden til en over afstanden i tredie i god overensstemmelse med de eksperimentelle observationer. For yderligere at undersøge periodisk brystsvømning målte vi den detaljerede svømmedynamik og de inducerede strømninger for *Podon intermedius*. Vi estimerede de fremaddrivende kræfter, der virker på *P. intermedius*, og vi fandt, at det hurtige rumlige henfald i de inducerede strømningsforstyrrelser ikke blev forklaret af modellen baseret på tre punktkræfter. Vi formoder, at dette skyldes inertien i strømningen, som synes at spille en vigtig rolle for større dyreplanktons svømning. Endeligt udviklede vi en simpel model

til at beskrive dynamikken for periodisk svømning, som viste, at ikke-lineære termer er nødvendige for at modellere den observerede dynamik korrekt.

Den anden del af denne afhandling undersøger, hvordan størrelse bestemmer overgange i levestrategier, og dermed fungerer som en strukturerende faktor for det marine liv. Til dette formål har vi samlet og præsenteret data for størrelsesbaserede skaleringslove for ressourceoptag, motilitet, sansning, og størrelse af afkom for alle pelagiske livsformer, fra bakterier til hvaler. Vi har også revideret og udviklet teoretiske argumenter for de observerede skaleringslove og for de karakteristiske størrelser, hvor overgange fra en strategi til en anden finder sted. Baseret på vores resultater, har vi opdelt livet i havet i syv grupper baseret på trofisk strategi, fysiologi og livshistoriestrategi.

Endelig har vi dykket dybere ned i størrelsesbaseret strukturering af sensoriske strategier i havet. Overlevelse i det åbne hav kræver effektiv indsamling af oplysninger fra omgivelserne ved hjælp af forskellige sanser. Vi har undersøgt, hvordan sanserne og deres respektive virkeområder afhænger af kropsstørrelse. Vi undersøgte de fysiologiske begrænsninger for sanseorganerne, sammen med fysikken for signalproduktion, transmission og modtagelse. Vores analyse afslørede et hierarki af sansetilstande - med voksende størrelse, bliver flere sanser tilgængelige og detektionsafstanden øges. Vores teoretiske forudsigelser af nedre og øvre grænse for størrelsen af forskellige sansers funktionsområder stemte godt med størrelsesintervaller i litteraturen. Selve skaleringsanalysen og størrelsesgrænserne er kun første ordens skøn. Dette arbejde udgør den første omfattende analyse af størrelsesbaseret strukturering af de marine organismers brug af sanser.

Preface

This thesis is submitted as partial fulfilment of the requirements for obtaining the degree of Doctor of Philosophy (Ph.D.) at the Technical University of Denmark (DTU). The Ph.D. project was carried out at the Department of Physics at DTU, and as a member of the Complex Motion in Fluids Group, during a three year and two month period from August 2012 to September 2015. I gratefully acknowledge the funding support from the Villum Foundation through the Centre for Ocean Life, partial funding from DTU Physics, and two travel grants from the Otto Mønsteds Fond.

I must mention at the outset that the work presented in this thesis is not just mine, but a result of many fruitful collaborations that I was lucky to have during my time at DTU. I have had the great opportunity of being a part of the Centre for Ocean life, which truly fulfils its aim of bringing together people from various disciplines, and facilitating meaningful collaborations. It is only fitting that my Ph.D. thesis highlights the outcome of this teamwork.

I am pleased to take this opportunity to thank my main supervisor, Anders Andersen, for the enormous time and effort he has spent in training me. I thank him for pushing me to maintain high standards in my work, and for patiently guiding me through the tortuous journey that a Ph.D. is. Without his relentless support and vigilance, this Ph.D. would not have been possible. I also owe many thanks to my co-supervisor Thomas Kiørboe, who is the best example of a super-human that I know. With his unmatched insight into the fuzzy intersection of physics and biology, Thomas has been a tremendous source of inspiration and ideas. Thanks also to my co-supervisor Tomas Bohr, for being the way he is, for asking the tough questions, and for many wonderful discussions.

Next, I must thank Erik Martens, with whom I had the great pleasure of leading the 'size and senses' project. I enjoyed every bit of our collaboration, through many long workdays, numerous cups of coffee at Sankt Hans Torv, ever updating dropbox folders, and endless series of emails. Thanks also to Nis Sand Jacobsen, Christian Lindemann, Andy Visser, and Ken Haste Andersen, for making a great team for the project. Special

thanks to Ken for initiating and leading the 'size in the ocean' project, which formed an important part of my Ph.D. experience.

I have benefited greatly from the wonderful work atmosphere both at the FLUIDS section at DTU Physics, and at the Centre for Ocean Life. Insightful discussions with Julia Dölger helped to improve Chapter 8. I also acknowledge useful discussions with Hanna Rademaker, Lasse Tor Nielsen, Rodrigo Gonçalves, and Uffe H. Thygesen. I also had many interesting cross-border discussions with Blaise Delmotte, which we hope to turn into a real collaboration someday. I thank Anders, Thomas, Julia, and Monse, for carefully reading drafts of this thesis and making many valuable suggestions.

Finally, thanks to my family and friends, who make my life beautiful as it is, and make me look forward to every day for the experiences it has to offer.

Kongens Lyngby, 15 September, 2015

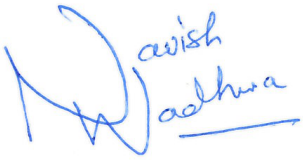

Navish Wadhwa

Table of Contents

List of Figures

List of Tables

List of symbols

Symbol	Description
$\frac{\partial \bullet}{\partial \circ}$	Partial derivative of $\bullet$ with respect to $\circ$
∇	Del operator
$\bullet \cdot \circ$	Dot product between $\bullet$ and $\circ$
$\hat{\bullet}$	Normalized version of $\bullet$
$\lvert \bullet \rvert$	Absolute value of $\bullet$
$\mathbf{v}$	Fluid velocity
$\mathbf{x}$	Position vector
t	Time
p	Pressure field
$\mathbf{f}$	Body force
S	Boundary of a domain
L	Characteristic length scale
T	Characteristic time scale
U	Characteristic velocity scale
β	Frequency parameter
Re	Reynolds number
ν	Kinematic viscosity
St	Strouhal number
r	Distance
$\mathbf{F}$	Force
p_{jk}	Dipole strength tensor
t_{jkl}	Quadrupole strength tensor
N	Total number
$\hat{\mathbf{r}}, \hat{\theta}$	Unit vectors in spherical polar coordinates
$P_n(x)$	Legendre polynomials
U^*	Threshold velocity
α	Aspect ratio

"I simply want to tell the story of my experiments with truth...as my life consists of nothing but those experiments."

Mohandas Karamchand Gandhi

Chapter 1

Introduction

1.1 Why study marine organisms?

Oceans cover 71% of Earth's surface and contain 97% of Earth's water. Life originated and continues to thrive in the oceans. The oceans are abundant with a remarkable variety of animals (Figure 1.1), on many of which human life is directly or indirectly dependent. For example, organisms like fish are heavily exploited for food throughout the world, and many coastal communities (which make 44% of the global population [124]) are directly dependent on them for their nutrition and livelihood. Then there are innumerable smaller organisms such as marine bacteria, phytoplankton, and zooplankton, which control the fate of global processes such as the biogeochemical cycles and climate, hence affect humans indirectly. A study of the diverse forms of oceanic life is thus of vital importance to us and may prove critical for future sustainable survival of our species.

1.2 Classification of life in the oceans

The various organisms in the oceans can be roughly classified based on their size and their role in the marine food chain (Figure 1.1), which is a rather simplistic representation of the complex food webs [97]. On one end of the scale are microscopic bacteria and viruses that play an important role in recycling organic material and form an important food source for many organisms. Next are the primary producers, phytoplankton, which capture the incoming energy from the sun using photosynthesis and make it available to the rest of marine life. Phytoplankton are thus the main engine that keeps the oceanic ecosystems running. They also control the balance of carbon dioxide in the atmosphere, directly affecting global climate. Massive blooms of phytoplankton are visible even from space in

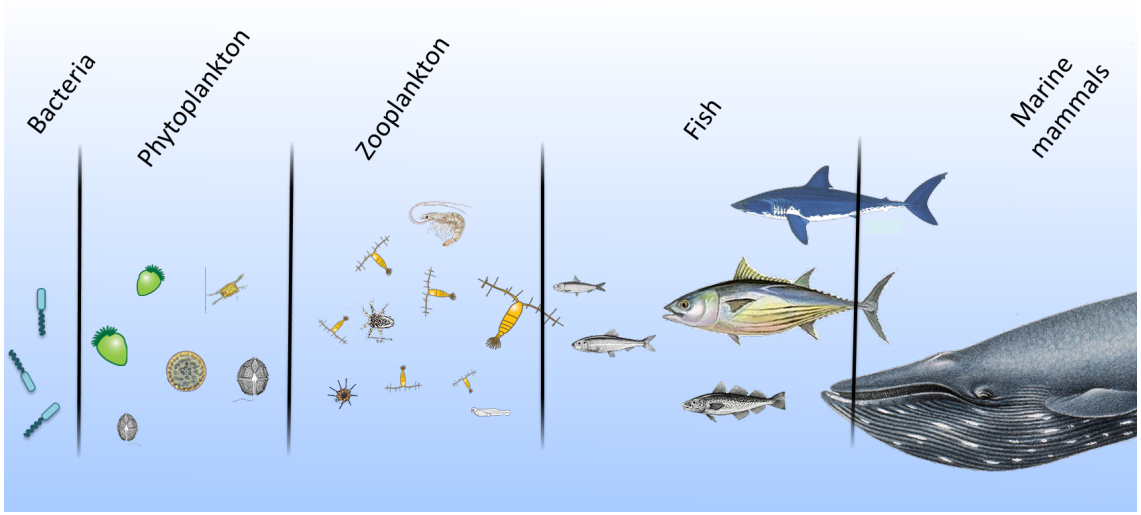

Figure 1.1: A schematic representation of life in the ocean, roughly organised by size. Modified with permission from Ken Haste Andersen.

the forms of beautiful patterns in the ocean (Figure 1.2).

Hugely abundant zooplankton come next, which inhabit the oceans in large diversity. Zooplankton live off phytoplankton and smaller zooplankton, and are the main food source for small planktivorous fish, including fish larvae. In this manner, zooplankton form the link between the primary producing phytoplankton and higher organisms such as fish. Phytoplankton blooms attract large aggregations of zooplankton [36], which in turn attract aggregations of larger predators [46]. Zooplankton fecal pallets are an important resource for the microbial community [121].

On the other end of this schematic are the top predators — large fish, sharks, and marine mammals. These are the organisms that humans interact and compete with, as top predators. Each level of this simplified picture of marine life is essential for its functioning. The interactions between trophic levels have implications for many important phenomena such as toxicity in marine food webs [122], ecosystem based fisheries management [95], and carbon cycling [76].

1.3 Focus of this thesis

This thesis investigates the physical basis of the interactions among marine organisms, especially zooplankton. The first part of the work is an attempt at quantifying the traits and trade-offs of swimming in zooplankton. Swimming allows organisms to search the vast

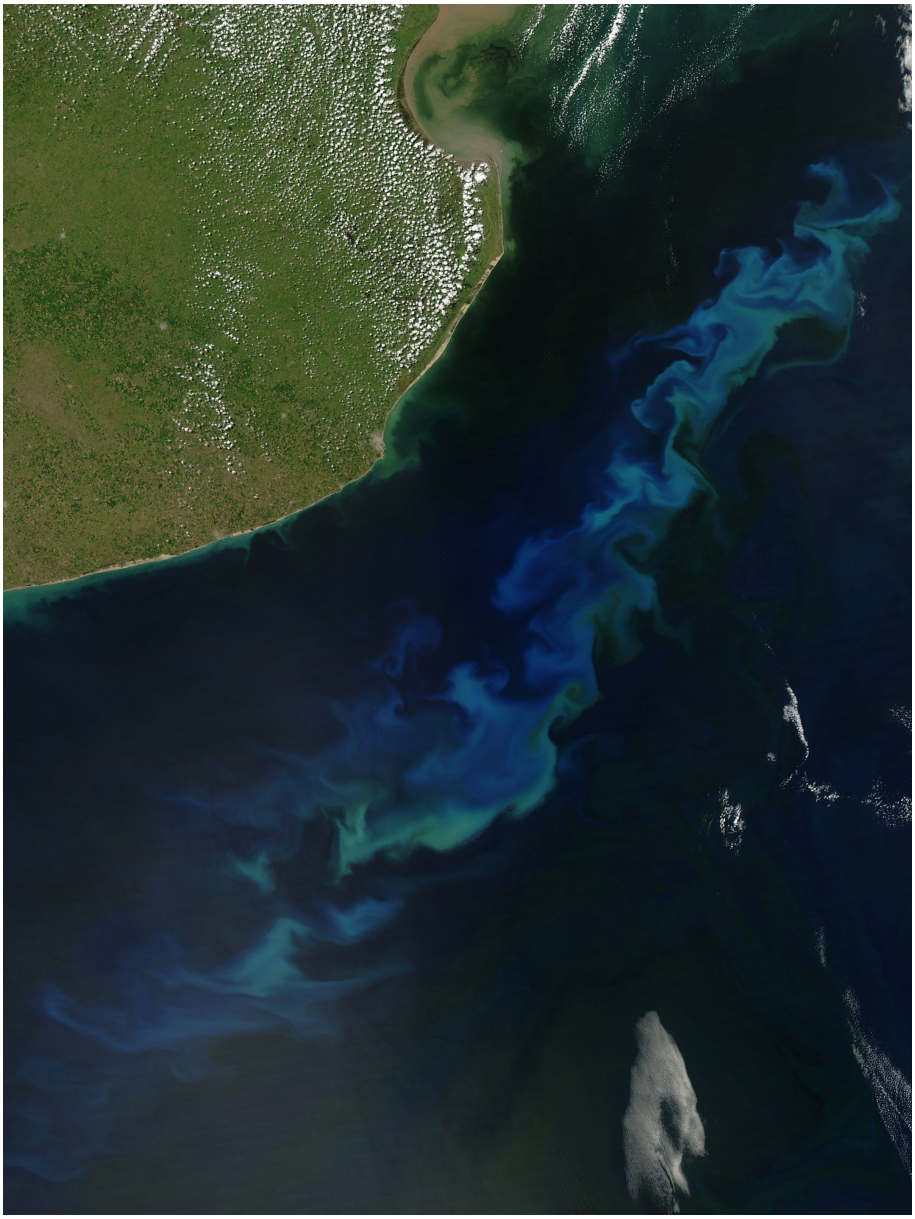

Figure 1.2: A phytoplankton bloom off the coast of Argentina. Chlorophyll and other phytoplankton pigments often give the water dark blue or green colours. Bright blue areas are often the result of the white, calcium carbonate (chalk) scales of organisms called coccolithophores. Image captured by the Moderate Resolution Imaging Spectroradiometer (MODIS) on NASA's Aqua satellite, on March 5, 2006. NASA image courtesy Jeff Schmaltz, MODIS Land Rapid Response Team at NASA GSFC.

oceans for food and mates. But it comes with trade-offs; there is a metabolic cost associated with swimming and it increases the chances of encounters with predators. Thus, the overall benefit of swimming for an organism's Darwinian fitness is a balance between the gains in the form of food and mates, and losses in the form of energy and survival. Naturally, fluid motion takes the central stage in this investigation. Processes such as feeding and swimming are intimately related to the physics of fluid motion. By understanding the interplay between the laws governing fluid motion and the behaviour of zooplankton, we hope to understand the overarching principles and constraints associated with those behaviours.

The second part of this thesis expands the scope to all marine organisms and asks how size of an organism enables and constrains the way the organism may gain information from the surroundings, using various sensory modes. Extending also the analysis from the laws of fluid motion to the laws governing the use of chemicals, sound, and light for sensing, we try to determine the limits imposed by physics and physiology on the usability of various sensory modes, depending on organism size. The analysis of sensory abilities forms a part of a larger study asking how size of an aquatic organism affects its life strategies in general, and how the size based transitions in strategies may structure life in the aquatic environments as we know it.

1.4 Context of the Ph.D. study

This Ph.D. study is one of the first Ph.D. projects at the Centre for Ocean Life at the Technical University of Denmark, a VKR center of excellence supported by the Villum foundation, which is a collaboration between three Danish universities (Technical University of Denmark, University of Copenhagen, and Roskilde University) and several departments within these universities. The centre aims at developing a novel trait based framework for marine ecology, moving away from the traditional species-based approaches and instead using organisms traits and their respective trade-offs to understand life in the ocean. A key element of this approach is identifying the key traits of marine organisms and developing a mechanistic understanding of the trade-offs associated with those traits.

The main Ph.D. project is an interdisciplinary effort to better understand the traits and trade-offs associated with the lives of aquatic organisms. Funding for the project was provided partly by the Centre for Ocean Life, and partly by the Department of Physics at the Technical University of Denmark. Our main focus has been on the swimming behaviour of planktonic organisms. Our approach has been to experimentally observe the swimming of plankton and the fluid flows around them, followed by a theoretical and analytical effort to

achieve a conceptual understanding. All experiments were carried out using the facilities at the National Institute of Aquatic Sciences at the Technical University of Denmark (DTU Aqua). The analysis of data and the theoretical investigations were carried out at the Department of Physics at the Technical University of Denmark (DTU Physics). Both the experiments and the analysis were done in close collaboration with Associate Prof. Anders Andersen and Prof. Thomas Kiørboe.

Another major activity which ran in parallel to the main Ph.D. project was the 'Size in the Ocean' project at the Centre for Ocean life, which involved 18 researchers including Ph.D. students, post-docs, research scientists, and professors. The project had an ambitious goal: to describe the differences in life strategies among all major life forms in the ocean, from bacteria to whales, based solely on the body size of the organisms. The work involved collecting large amounts of data from the literature, and establishing scaling relationships to understand size-based structuring of the various strategies involved in motility, sensing, offspring size, and resource acquisition by marine organisms. I, together with Erik Martens (Assistant Professor at the University of Copenhagen), led a smaller team of 6 members working on sensory strategies, analysing how an organism's body size plays a role in determining which sensory modes are employable. This project had more of literature review and theoretical analysis components, which were carried out at DTU Physics, DTU Aqua, and the University of Copenhagen.

Chapter 2

Physical background

2.1 Basic principles of hydrodynamics

To be able to propel themselves in water, organisms go through body deformations which move fluid backwards and in turn push the organism forward. The physics of these interactions is governed by the equations of fluid and solid motion. Here, let us consider only the fluid motions, which are governed by the Navier-Stokes and the continuity equations, written as

$$\rho\left(\frac{\partial \mathbf{v}}{\partial t} + (\mathbf{v}\cdot\nabla)\mathbf{v}\right) = -\nabla p + \mu\nabla^2\mathbf{v} + \mathbf{f}\,, \tag{2.1}$$

$$\nabla\cdot\mathbf{v} = 0\,, \tag{2.2}$$

where $\mathbf{v}$ is the velocity field, p is the pressure field, ρ is the fluid density, and μ is the dynamic viscosity. $\mathbf{f}$ is any externally applied body force, which in most cases is due to the gravitational field, but is absent if the organism is neutrally buoyant[1]. The equation 2.1 is the momentum equation which is the equivalent of Newton's second law for fluids, and 2.2 is the continuity equation which ensures mass conservation in an incompressible fluid. The state of the fluid medium, described by the velocity field $\mathbf{v}$ and the pressure field p everywhere in the space outside the boundary of the organism S, is determined by solving equations 2.1 and 2.2, with the condition that the fluid adheres the solid on the boundary S at all times (called the no-slip boundary condition).

[1] In many cases, marine organisms are close to neutrally buoyant, thus the external force term can often be ignored.

2.1.1 Dimensionless numbers

The governing equations can be written in dimensionless form by scaling all dimensional variables with characteristic scales,

$$\hat{\mathbf{x}} = \frac{\mathbf{x}}{L}\,, \quad \hat{t} = \frac{t}{T}\,, \quad \hat{\mathbf{v}} = \frac{\mathbf{v}}{U}\,, \quad \hat{p} = \frac{L\,p}{\mu\,U}\,, \tag{2.3}$$

where L is the characteristic length scale, T the characteristic time scale, and U the characteristic velocity scale. Using the dimensionless variables we can write the governing equations as

$$\beta\,\frac{\partial\hat{\mathbf{v}}}{\partial\hat{t}} + \mathrm{Re}\,(\hat{\mathbf{v}}\cdot\hat{\nabla})\hat{\mathbf{v}} = -\hat{\nabla}\hat{p} + \hat{\nabla}^2\hat{\mathbf{v}}\,, \tag{2.4}$$

$$\hat{\nabla}\cdot\hat{\mathbf{v}} = 0\,, \tag{2.5}$$

where we have introduced the two dimensionless parameters

$$\beta = \frac{L^2}{\nu\,T}\,, \tag{2.6}$$

$$\mathrm{Re} = \frac{L\,U}{\nu}\,. \tag{2.7}$$

Here ν is the kinematic viscosity defined as $\nu = \mu/\rho$. Re is the Reynolds number and the parameter β is referred to as the frequency parameter [100], which is often also written as the product of Re and the Strouhal number $\mathrm{St} = L/UT$. For an organism swimming in water, L can be the body size, U the swimming velocity, and T can be the time period of the swimming strokes. The Reynolds number Re measures the ratio of the inertial forces acting on the fluid to the forces due to viscosity. Thus at high Re, the flow is dominated by the inertial forces and the effect of fluid viscosity can be ignored. On the other hand, at low Re, which I discuss next, inertia can be neglected and viscous forces determine the dynamics. In this manner, the behaviour of fluids at any scale can be at least qualitatively characterized by these dimensionless parameters which can be readily estimated from the size, velocity, and time scales. Table 2.1 lists estimates of β and Re for the swimming of some organisms, to demonstrate the range. For small organisms like flagellates and ciliates, Re and β are both small, while for large organisms like fish and humans, they are both large. Re and β take intermediate values for many zooplankton such as copepods.

Table 2.1: Estimates of the various scales and the dimensionless parameters for the swimming of some organisms. Kinematic viscosity of water, $\nu = 10^{-6}$ m^2 s^{-1}. Dinoflagellates are represented by *Oxyrrhis marina*, ciliates by *Mesodinium rubrum*, copepods by *Acartia tonsa*, and fish by the American eel *Anguilla rostrata*.

	L (m)	U (m s^{-1})	T (s)	Re	β	Ref
Dinoflagellate	3×10^{-5}	2.5×10^{-4}	0.02	7×10^{-3}	0.045	[18, 92]
Ciliate	2.3×10^{-5}	10^{-2}	9×10^{-3}	0.2	0.06	[27]
Copepod	4.8×10^{-4}	8.3×10^{-2}	7.8×10^{-3}	39	30	[131]
Fish	0.2	0.27	0.32	5.4×10^{4}	1.25×10^{5}	[123]
Human	1.9	1.7	1	3.2×10^{6}	2.9×10^{6}	[20]

2.1.2 Hydrodynamics of small scale processes - the Stokesian regime

For small organisms like bacteria and flagellates, L and U are inherently small. As a simple example, let's take the case of a bacterium ($L \approx 10^{-6}$ μm) swimming in water ($U \approx 10^{-5}$ ms^{-1}), rotating the flagella with a typical frequency of ≈ 100 Hz ($T \approx 10^{-2}$ s). With these numbers, and with the known kinematic viscosity of water ($\nu = 10^{-6}$ m^{2}s^{-1}), we can approximate Re $\approx 10^{-5}$ and $\beta \approx 10^{-4}$ (also see other examples in Table 2.1). Thus, both Re and β tend to be small for small organisms, unless they swim at very high velocity or with very fast strokes. In such a situation, both the terms on the left hand side of equation 2.4 end up being small as compared to the other terms, hence the dynamics of the fluid medium surrounding the organisms are dominated by a balance between pressure gradients and viscous stresses. Dropping the terms on the left hand side of equations 2.4 and 2.1, we get the Stokes equations,

$$-\nabla p + \mu \nabla^2 \mathbf{v} = 0 \,, \tag{2.8}$$

$$\nabla \cdot \mathbf{v} = 0 \,. \tag{2.9}$$

The Stokes equations are much simplified from the full Navier-Stokes equations 2.1 and 2.2, in that they are linear in $\mathbf{v}$ and time-independent. The time independence implies that the flow is quasi-steady, i.e. the flow at any instant is fully prescribed only by the boundary conditions at that instant, and the momentum imparted to the fluid by the organism's boundary is diffused instantaneously throughout the fluid. The linearity of the equations 2.8 and 2.9 implies that if the forcing or the velocity of the boundary is multiplied by a constant, then the flow velocity everywhere gets multiplied by the same constant. It also allows superposition of different solutions, as long as the superposition is consistent with the boundary conditions.

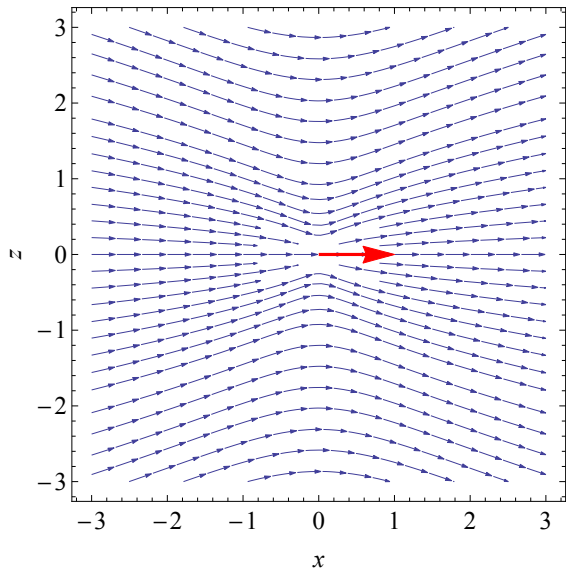

Figure 2.1: Velocity field due to a single point force (Stokeslet). The red arrow represents the applied force and the blue lines represent streamlines, with the blue arrows pointing in the direction of flow.

It is also easy to show that any organism swimming with time reversal symmetry cannot swim in the Stokesian regime. If an organism's swimming stroke is such that it looks the same with time going backwards as it does with time going forward, its net swimming velocity is constrained to be zero, even if it has instantaneous non-zero velocity. Thus an organism with motion involving only one degree of freedom, e.g. like the opening and closing of a scallop shell, is unable to swim in the Stokesian regime[2], leading to the now famous "scallop theorem", expressed as such by Purcell in a stimulating paper [102].

For many situations relevant to small organisms swimming in water, the solutions to the Stokes equations are readily available. The possibility of superposition allows for new solutions to complex situations to be found by superimposing known solutions to simpler situations.

2.1.3 Fundamental solution of Stokes equations

The most basic unit of all solutions for Stokes equations is the so called Stokeslet, which is the Green's function of the Stokes equations. Physically it represents the flow due to the single point force acting on the fluid. An exact formulation for the Stokeslet flow

[2]Ironically, the real scallop does in fact swim. It takes in fluid while opening the shell and ejects it from the hinge in the form of a jet. As this mechanism breaks time reversal symmetry, a scallop would swim even at zero Reynolds number.

is known [100], described as follows. The flow velocity $\mathbf{v} = (v_x, v_y, v_z)$ at the field point $\mathbf{x} = (x, y, z)$ due to a point force $\mathbf{F} = (F_x, F_y, F_z)$ acting at a source point $\mathbf{x}' = (x', y', z')$, is in index notation

$$v_i(\mathbf{x}) = \frac{1}{8\,\pi\,\mu}\left[\frac{F_i}{|\mathbf{x} - \mathbf{x}'|} + \frac{F_j\,(x_j - x_j')\,(x_i - x_i')}{|\mathbf{x} - \mathbf{x}'|^3}\right]. \tag{2.10}$$

This is the fundamental solution of the Stokes equations on which all other solutions are linearly dependent. The flow field of a Stokeslet is shown in Figure 2.1. The velocity due to a Stokeslet decays with distance $r = |\mathbf{x} - \mathbf{x}'|$ as $1/r$.

The concept of a point force may seem too artificial to have any direct relevance to the real world of plankton, but it turns out to be a useful idealization of two important small scale aquatic processes, a sinking particle or organism, and the feeding current of a small organism. In fact, the Stokeslet describes the flow far away from any body which exerts a non-zero force on an unbounded fluid [75]. This is directly a result of the far field behaviour of flow singularities in Stokes flows, discussed in the next subsection. Moreover, the usefulness of the Stokeslet lies in the fact that its higher order derivatives, which are all solutions of the Stokes equations and can be superimposed, form an excellent set of solutions to cherry pick from when faced with an unknown flow situation.

2.1.4 Higher order singularities and far field behaviour

Subsequent higher order singularities for Stokes flows can be found by sequentially differentiating the Stokeslet solution. The first derivative leads to the force dipole for which the flow velocity decays with distance r as $1/r^2$. Physically, the dipole represents two equal and opposite point forces acting at a short distance from each other. The dipole can be decomposed into its symmetric and anti-symmetric parts, the stresslet and the rotlet. The rotlet represents the flow due to a singular, point torque acting on the fluid. The remaining part of the dipole, the stresslet, exerts a zero net force or torque on the fluid, and causes a pure straining motion. Differentiating the dipole leads to what is known as a force quadrupole, for which the flow decays with distance r as $1/r^3$. Even higher order singularities can be found by further differentiation, although they are less and less important for describing real flows, due to their fast decaying flow fields.

A stresslet is an idealization of the flow due to a neutrally buoyant self-propelled organism, with the two point forces being an abstraction of the drag and the thrust acting on the organism (the total force and torque on a low Re swimmer must be zero). If the organism is not neutrally buoyant, then the resultant gravitational force acts as a Stokeslet and the net flow is then given by the sum of appropriate magnitudes of Stokeslet and stresslet

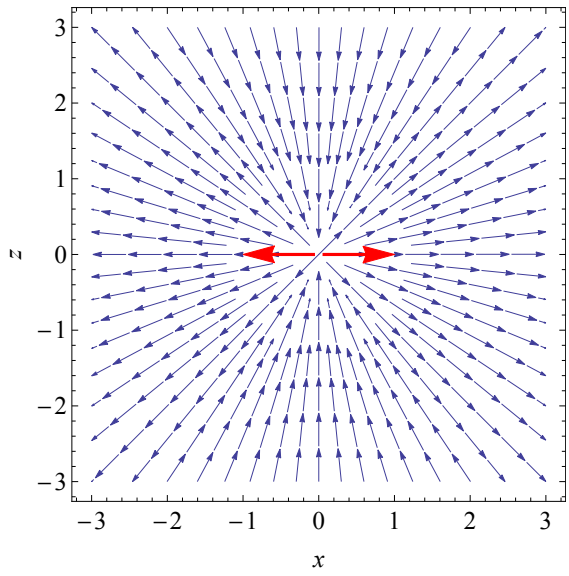

Figure 2.2: Velocity field due to a stresslet. The red arrows represent the two applied forces that form the stresslet, and the blue lines represent streamlines, with the blue arrows pointing in the direction of flow.

flows. In general, any Stokesian flow field can be constructed as a superposition of various fundamental singularities, in particular Stokeslets. Any irregularly shaped body moving in a fluid can be replaced by a distribution of Stokeslets over the surface of that body, and the flow resulting from the motion is found by solving for a distribution of Stokeslets that satisfies the boundary conditions. Such an approach can usually only be employed numerically, and forms the basis of various numerical methods such as the boundary-element and boundary-integral methods [75].

Since for each subsequent higher order singularity, velocity decays faster with distance, the flow far away from the origin is dominated by the lowest order singularity used in the description of the flow. Thus, for any negatively or positively buoyant organism (and in general for any body exerting a non-zero net force on an unbounded fluid), the flow sufficiently far away is dominated by a Stokeslet. For the same reason, the flow due to most neutrally buoyant swimmers is well represented by a stresslet in the far field, as such a swimmer is constrained to be force and torque free[3].

[3] Deviations from this idea are discussed in Chapter 7

2.1.5 The multipole expansion

Another approach to finding the flow due to a body in Stokes flows is to employ the multipole expansion for a Stokeslet. This allows a surface distribution of Stokeslets to be replaced with an internal distribution of point forces and their higher order derivatives. A multipole expansion is essentially the Taylor expansion of the Stokeslet flow given by equation 2.10 at the origin. This approach is analogous to the multipole expansion in electromagnetism, where it is used, for example, to find the electric potential due to an arbitrary distribution of point charges [56]. In fact, the terminology of "poles" used in the hydrodynamics literature has been borrowed from electromagnetism [130].

Far away, the distance of the origin from the field point $r = |\mathbf{x}|$ is much larger than that of the source point $r' = |\mathbf{x}'|$, thus by employing binomial series, one can find the multipole expansion

$$v_i(\mathbf{x}) = \frac{1}{8\,\pi\,\mu}\left[\left(\frac{\delta_{ij}}{r} + \frac{x_i\,x_j}{r^3}\right)F_j + \left(\frac{x_k\,\delta_{ij} - x_i\,\delta_{jk} - x_j\,\delta_{ik}}{r^3} + \frac{3\,x_i\,x_j\,x_k}{r^5}\right)F_j\,x'_k + \frac{1}{2}\left(\frac{2\,\delta_{ik}\,\delta_{jl} - \delta_{ij}\,\delta_{kl}}{r^3} - 3\,\frac{2\,\delta_{il}\,x_j\,x_k + 2\,\delta_{jl}\,x_i\,x_k + \delta_{kl}\,x_i\,x_j - \delta_{ij}\,x_k\,x_l}{r^5} + \frac{15\,x_i\,x_j\,x_k\,x_l}{r^7}\right)F_j\,x'_k\,x'_l + \cdots\right]. \quad (2.11)$$

The three terms in equation 2.11 represent the force monopole, the force dipole, and the force quadrupole, respectively. The expansion effectively separates the role of the source point and the field point in determining the velocity field - the expressions inside the parentheses for each term depend only on the field point, while the 'strengths' of each term given by the expressions outside the parenthesis depend only on the coordinates of the source point. The strength of the monopole is described by the vector F_j, of the dipole by the tensor $p_{jk} = F_j\,x'_k$ and that of the quadrupole by the tensor $t_{jkl} = (1/2)\,F_j\,x'_k\,x'_l$, and so on.

The above only describes the multipole expansion for a single Stokeslet, but as discussed, low Re flow around an arbitrarily shaped body can be approximated to a distribution of point forces on the surface. Each point force in the surface distribution can be represented as a multipole expansion at the origin, and superimposed with the expansions for the other point forces. Thus, to determine the total monopole, dipole, and quadrupole contributions in the far field flow due to a superposition of N point forces, we can add the individual contributions

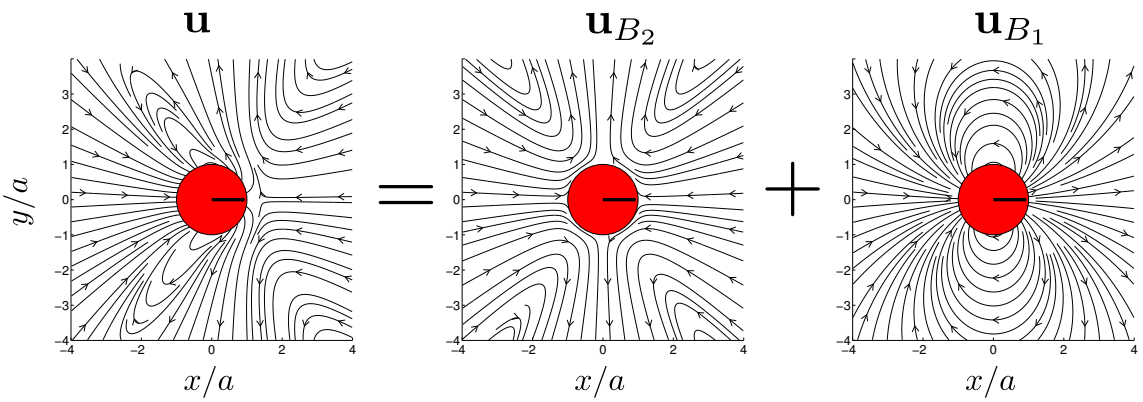

Figure 2.3: Decomposition of the velocity field due to a squirmer for ($\gamma = 1$) into the dipolar (B_2) and the quadrupolar (B_1) components. Reproduced with permission from [21].

$$F_j = \sum_{n=1}^{N} F_{n,j}, \quad p_{jk} = \sum_{n=1}^{N} p_{n,jk}, \quad t_{jkl} = \sum_{n=1}^{N} t_{n,jkl}. \tag{2.12}$$

These strengths depend only on the applied forces and their distribution in space. This is useful in determining the leading order of the flow field as it is dominated by the first non-zero pole in the multipole expansion, and the strengths of all poles are easily calculated by the expressions in 2.12.

Another interesting implication of the multipole expansion formulation is that the strengths of the dipole and higher order terms can be manipulated without changing the direction or magnitude of the point forces $F_{n,j}$, simply by reorganising the forces in space to modify the strength tensors. This is especially relevant for swimming organisms which make time-dependent shape changes as they go through a swimming stroke, resulting in time dependent strengths of the various poles [3, 71]. This can have important implications, as explored in more detail in Chapter 7.

2.1.6 The squirmer model

In addition to the singularity models, there is another model which deserves mention for its usefulness. In spite of their simplicity, the point force models and the multipole expansion suffer from the drawback of introducing singularities in the flow, and that for any real situation they are valid only in the mathematical limits of far field. There are very few situations in which an exact solution for Stokes flow around a swimmer is known. The squirmer model, originally due to Lighthill [78] and Blake [9] is one of the most widely used exact solutions for a Stokesian swimmer.

The squirmer model was originally developed to describe the swimming of small ciliates such as *Paramecium* or *Opalina* [9], with the motion of closely packed cilia approximated as axisymmetric deformations taking place at the surface of a spherical organism. If the deformation amplitude is small as compared to the size of the squirmer, then to leading order the boundary condition is represented by distributions of radial and tangential velocities on the surface of the squirmer [21, 55]. At the surface of a spherical squirmer with radius a swimming with a velocity U, the boundary condition thus becomes [9],

$$\mathbf{v}(r = a) = v_r \hat{\mathbf{r}} + v_\theta \hat{\theta} \tag{2.13}$$

where

$$v_r = U \cos\theta + \sum_{n=0}^{\infty} A_n(t)\, P_n(\cos\theta), \tag{2.14}$$

$$v_\theta = -U \sin\theta - \sum_{n=1}^{\infty} B_n(t)\, V_n(\cos\theta). \tag{2.15}$$

Here $P_n(x)$ are the Legendre polynomials, A_n and B_n are coefficients describing the surface deformations, θ is the angle measured from the swimming direction in spherical polar coordinates, and

$$V_n(\cos\theta) = \frac{2}{n\,(n+1)} \sin\theta\, P_n'(\cos\theta), \tag{2.16}$$

where $P_n'(x) = dP_n/dx$. This set-up allows sufficient generality to the problem, while still allowing for an exact solution to be found [9]. For the full solution to the flow field, we refer the reader to Blake [9] and Ishikawa et al. [55]. The requirement for the squirmer to have no net force acting on it provides a simple expression for the swimming velocity,

$$U = \frac{1}{3}\,(2B_1 - A_1)\,. \tag{2.17}$$

In most studies, a reduced squirmer model has been employed [21, 55, 88], in which it is assumed that $A_n = 0$ for all n and $B_n = 0$ for $n > 2$. This leads to great simplification without much loss of generality, as the first two modes alone are able to provide a good representation for many different swimming situations.

One sees that the B_1 term in the resulting velocity field represents the quadrupolar component of the field, while the B_2 term represents the dipolar (stresslet) component, as shown in Figure 2.3. The ratio of the two coefficients, $\gamma = B_2/B_1$, describes the relative

strength of the stresslet to the quadrupole, and it is the main parameter qualitatively describing the flow. For any non-zero γ, the flow in the far field of the squirmer is dominated by the slower decaying stresslet - for $\gamma > 0$, it acts like a 'puller', and for $\gamma < 0$, it acts like a 'pusher'. An example of the pusher stresslet is spermatozoa and bacterial, which push the fluid way in front of them and bring it in from the sides. An example of the puller stresslet is the time averaged flow around the green alga *Chlamydomonas*, for which the situation is reversed. Thus, a reduced squirmer is able to represent the flow fields for a variety of situations through the appropriate tuning of the two coefficients making it a powerful modelling tool. Indeed, the squirmer has been used for numerically and analytically investigating a variety of problems such as interaction between individual and a large number of micro-organisms [21, 25, 55, 88], chemical fields around micro-organisms [7], nutrient transport and uptake [81, 87], and inertial effects [132]. This model has recently been generalized for non-axisymmetric surface deformation [94].

2.1.7 Intermediate Reynolds numbers and unsteady effects

The conditions required to satisfy the assumptions for Stokes flows are not always met, even for small organisms. Some of the larger plankton, such as sub-millimetre sized copepods, can swim so fast that they reach Reynolds numbers of hundreds to thousands [16, 65, 126]. Even in their early life stages when they have smaller size, they are able to swim at Reynolds numbers of the order of 1 [131]. The intermediate Reynolds number regime with $\mathrm{Re} \in 1 - 100$ is notoriously difficult to treat analytically [6]. In this regime, small size or velocity changes, leading to a change in Re, can have a dramatic effect on the behaviour of a system, as has been illustrated in flows around simple shapes such as a sphere or a cylinder [6]. Plankton such as copepods go through precisely these changes as they increase size and swimming speeds during growth as a part of their life cycle, possibly leading to drastic hydrodynamic changes. The hydrodynamic changes experienced by these plankton are in turn expected to affect their Darwinian fitness by affecting quantities such as cost of propulsion, efficiency, and flow mediated interactions with predators. These aspects are explored in Chapter 5.

Even for very small organisms for which Stokes flow is a valid approximation near the body, the assumptions involved may break down when we go far away from the organism. This can be shown using a simple scaling analysis following Klindt and Friedrich [71], which in turn follows the elegant arguments of Landau and Lifshitz [72]. A neutrally-buoyant self-propelled swimmer at low Reynolds numbers acts as a dipole and the flow velocity decays with distance as $1/r^2$, as described earlier. Close to the organism, the assumptions made in subsection 2.1.2 are valid and thus Stokes equations are applicable to the fluid medium.

For a dipole flow with a characteristic velocity scale U, the unsteady acceleration term in equation 2.1, $\rho\,\partial\mathbf{v}/\partial t \sim \rho U\, r^{-2}$ decays slower than the viscous forces $\mu\nabla^2\mathbf{v} \sim \mu U\, r^{-4}$, which in turn decays slower than the convective acceleration term $\rho\,(\mathbf{v}\cdot\nabla)\mathbf{v} \sim \rho U^2\, r^{-5}$. Thus, with increasing distance away from the organism, the convective acceleration term remains small in comparison with the other terms, while the unsteady acceleration term becomes comparable to the viscous term at a distance $\delta \approx \sqrt{2\,\nu\, T}$, where ν is the kinematic viscosity and T is the time scale of the swimming stroke.

Therefore, at a distance $r \gg \delta$ Stokes approximation is invalid and the fluid behaviour is thus represented by the unsteady Stokes equations. The solution to the unsteady Stokes equations due to an oscillating forcing (such as that due to a small swimmer) is a potential flow decaying with distance as $1/r^3$. Klindt and Friedrich [71] call this phenomenon "inertial screening" which causes rapid attenuation of Stokes flows beyond a distance given by δ. We discuss this further in Chapter 8.

2.1.8 Concluding remarks on hydrodynamic theory

In this section, we summarized the main concepts from the hydrodynamics of small scale swimming, which are relevant to this Ph.D. study. The Navier-Stokes equations form the basis of all studies involving fluid motion, including this thesis, and is thus an important reference to always have in mind. The dimensionless numbers such as the Reynolds number (Re) and the frequency parameter (β) are used for discussion in several of the following chapters (e.g. Chapter 5, 6, and 8). The Stokes equations and the point force models, along with the multipole expansions form the basis of Chapter 7. The squirmer model is only briefly mentioned in Chapter 7, but it is a good reference for Chapter 7, as many of the concept discussed in that chapter using the three point force model are also applicable to the squirmer model. Finally, since many zooplankton - for instance copepods and cladocera - swim in an intermediate Reynolds number regime, inertial effects haunt the analysis of these organisms throughout this work.

2.2 Measurements of flows around small organisms

Flow visualisation and measurement is a vast and rich field, of which biological flow measurement is only a small sub-field [86]. Historically, the technological developments have come from physics and engineering, which have quickly been adapted by biologists for applications to swimming organisms. In this section, I will briefly cover a few flow measurement techniques and their application to flows around small aquatic organisms.

2.2.1 Qualitative flow visualization

Flow visualization by humans likely pre-dates even writing, going back to pre-historic humans looking at whirls in water made visible by dust and debris. Addition of a coloured dye to flow for visualization is the oldest experimental technique used by fluid scientists. Dye visualization was used by Osborne Reynolds to investigate the transition between laminar and turbulent flows [104]. Ludwig Prandtl used a water tunnel to study the structures in steady and unsteady flows, visualized by a suspension of mica particles in the surface of water [103]. Dye visualization (and its variant, smoke visualization) remains relevant today, used often for qualitative and inexpensive first characterization of flows both in biological and engineering applications [96, 99, 119]. Van Dyke's famous collection of photographs contains several very beautiful examples of flows in various situations visualized using dyes [128].

Flow can also be visualized without the addition of external material into the fluid, which may be desired in some situations. This can be done using optical techniques which rely on the fact that any change in the density of a fluid results in a change in the light refractive index of the fluid [86, 98]. There are three optical methods: shadowgraphy, interferometry, and schlieren imaging [98], all three of which are closely related to each other [85]. The physical basis of all three of these is Snell's Law of optics, which mathematically describes the refraction of light when interacting with matter of varying density. If fluid motion results in any gradients in density, then these can be visualised using the above mentioned techniques. Since the early pioneering use by Strickler [110], schlieren imaging methods have been used in studies for visualizing the flows created by plankton [19, 112, 115, 111, 139]. Schlieren pathways can be difficult to set up and maintain, but if done properly, they can be used to obtain remarkable images of flow around plankton (Figure 2.4). As the schlieren image obtained is a snapshot of the fluid density field, its relation to flow structures can sometimes be tricky, especially for very viscous flows. Moreover, schlieren often requires setting up a density gradient in the fluid to be visualized, which may potentially affect the natural behaviour of the organism and also the flows.

2.2.2 Quantitative methods

The main limitation of the dye visualisation and optical techniques discussed until now is that they are qualitative - they provide no quantitative information about the flow velocities. Accurate measurement of flow velocity is desired in many situations, for example to estimate the energy expenditure incurred by an organism while swimming [45]. There are many flow measurement techniques which give quantitative information about the various

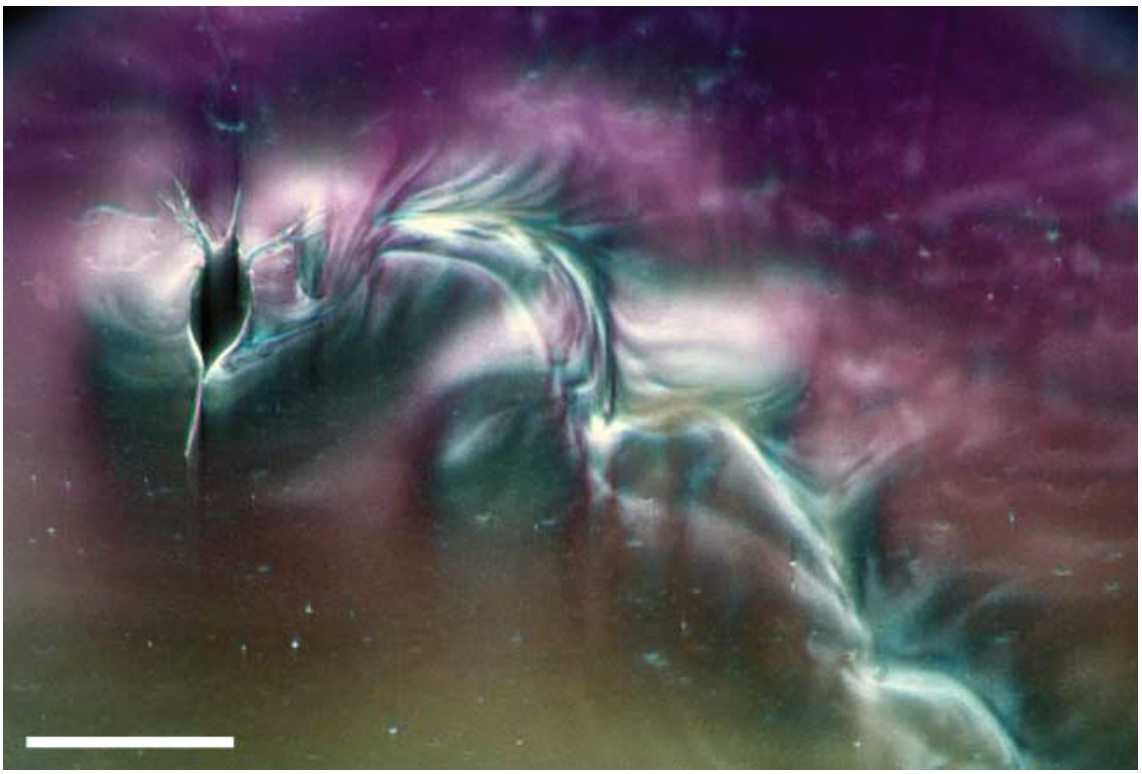

Figure 2.4: Schlieren visualisation of the flow created by a swimming *Daphnia lumholtzi*. Scale bar, 0.1 cm. Image reproduced from Strickler and Balázsi [115], with permission from J. Rudi Strickler.

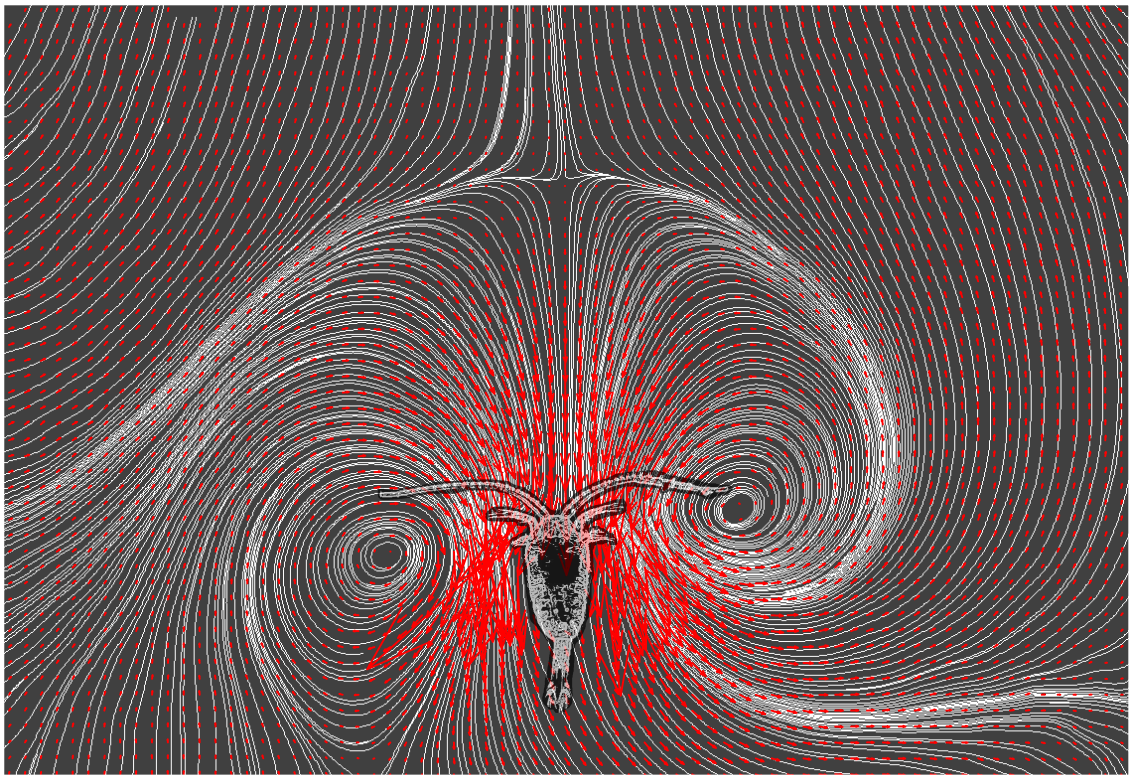

Figure 2.5: Streamlines and velocity vectors of the flow field due to the feeding current generated by the copepod *Temora longicornis*, measured using sum of correlation PIV.

flow variables such as velocity and pressure, and these can be divided into two categories - point measurement techniques and whole field techniques. Point measurements techniques allow velocity measurement only in a very small region of the flow (assumed to be a single point), and can typically do so with very high temporal resolutions. Examples of these techniques include hot-wire anemometry and laser Doppler anemometry, and pitot tube [35]. Since we are mainly interested in measurements of the velocity field around swimming organisms and not just at a point, these techniques are not discussed further.

2.2.3 Particle imaging techniques

There are very few whole field flow measurement techniques which are currently available, of which the most widely used are undoubtedly the particle-imaging techniques [1]. In these techniques, which evolved from laser speckle velocimetry, the flow to be measured is "seeded" with tiny reflective particles, whose motion can be measured to provide information about the flow that they are embedded in. There are several variations of these

techniques, but for the purpose of this research we are primarily interested in the particle tracking and particle image velocimetry techniques. Particle imaging techniques, together with many advanced post processing options available from several commercial suppliers, can be used for very good quality visualization and quantification of flow fields around zooplankton, for example, the feeding current flow around a *Temora longicornis* (Figure 2.5, which is also on the cover of this thesis).

In their classical form, both these techniques have only a thin plane illuminated within the fluid, the measured velocity field is thus a two dimensional field in that plane. When the seeding particle density is small, and individual particles can be tracked to measure their velocities, then the technique is called particle tracking velocimetry (PTV). If seeding density is high, then image correlation based methods are used to extract velocity and the technique is then called particle image velocimetry (PIV). The experimental set up in PTV and PIV is virtually the same, with the exception of particle density. For both techniques, the setup consists of an experimental section with optical access, laser source and sheet optics for illumination, camera and imaging optics for recording, and finally the flow seeded with tracer particles (Figure 2.6). Below I briefly discuss each of these components with a focus on the experimental setup used for PIV and PTV in our research.

Illumination

The quality of output from a PIV experiment depends greatly on the quality of images captured during the experiment. Ideally, all the light in the captured images should be that scattered from the tiny tracer particles, to obtain a high signal to noise ratio. This required the use of high power illumination sources. Typically laser sources are used because of their ability to produce high power monochromatic illumination. The laser beam can easily be transformed into a thin light sheet by using a combination of lenses.

For experiments with live organisms, additional challenges have to be met. High power lasers cannot be used because they can harm the animal, thus a compromise has to be made by using lower power lasers and highly sensitive cameras. Further, most organisms are sensitive to visible light, and therefore alter their behaviour in response to bright light. In the case of plankton and some other organisms, this issue can be resolved by using the infra-red range of the spectrum for illumination, to which many organisms are insensitive. In our experiments with copepods, for example, we used the infrared pulsed diode laser from Oxford Lasers, which produced light at 808 nm wavelength at an average power of 300 W.

The thickness of the light sheet should be small, to ensure that the measurement region is a good approximation to a two-dimensional plane. In practice, this is not feasible, as a

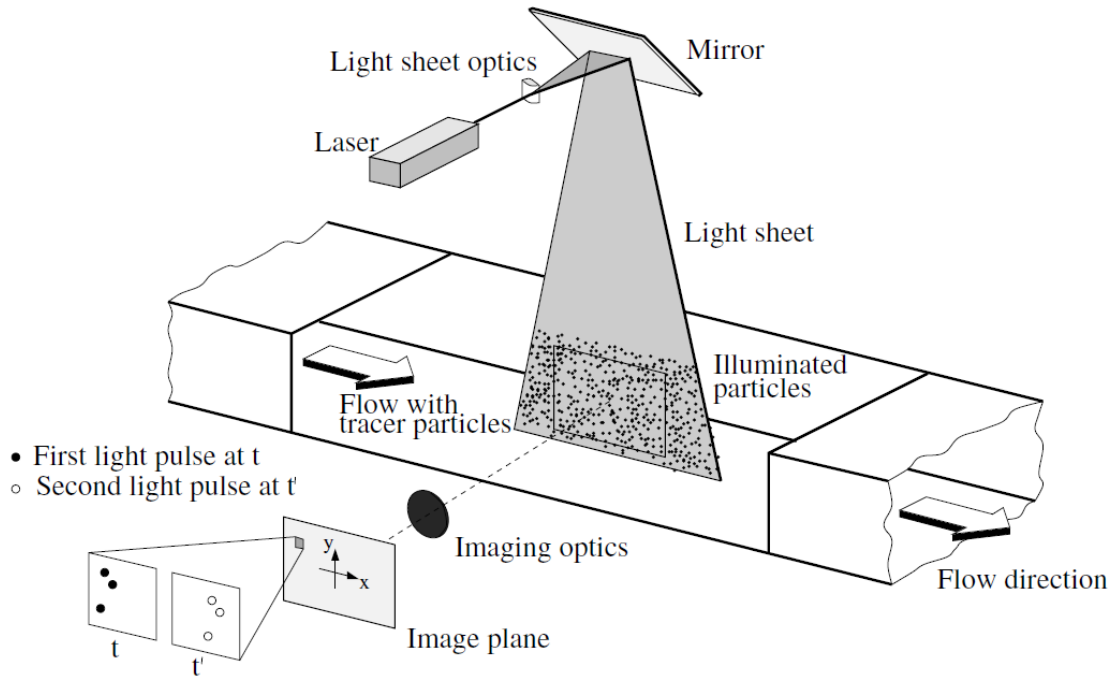

Figure 2.6: Experimental set up for particle image velocimetry. Figure reproduced from Raffel et al. [103].

thinner light sheet also reflects less light to the camera. Further, in case of flow measurement around live organisms, it is important that the sheet thickness is small compared to the size of the organism. The sheet forming optics we used formed a 150 μm thick light sheet. This was not an ideal situation in all experiments, because some of the smaller nauplii we worked with were barely 200 μm in size. A smaller sheet thickness, however, could not be achieved, so we had to work within the constraints of this limitation.

Tracer particles

Tracer particles are a key component of any particle-imaging set up. Both the fluid mechanical and the optical properties are important considerations while selecting tracer particles. Based on the density of seeding particles, the methods are characterized either as PIV or PTV. For PIV, tracer particles have to fulfil the following assumptions with regard to their mechanical properties:

- The particles are neutrally buoyant.
- The particles faithfully follow the flow.
- The particles are homogeneously distributed in the flow.
- The particles have a uniform displacement within an interrogation window.

Apart from these, the tracer particles are desired to be highly reflective and scatter the light well in the viewing direction. Often, the desired optical and the mechanical properties of tracer particles oppose each other. For example, for faithfully following the flow, smaller particles are more suitable than larger ones, but smaller particles scatter less light. For the experiments reported in Wadhwa et al. [131], we used titanium dioxide particles, which were processed to be smaller than 2 μm in size. Titanium dioxide is not neutrally buoyant and thus does not satisfy the first requirement listed above. However, a 2 μm diameter particle of TiO_2 has a terminal settling velocity of only about 7 $\mu m\,s^{-1}$, which is very small in comparison with the induced flow velocities of several millimetres per second. The exceptionally high reflective properties of TiO_2 particles resulted in very good quality images for the later PIV or PTV analysis.

Imaging optics and camera

Sharp and small images of particles are essential for good PIV or PTV analysis, therefore these experiments typically require very high quality imaging equipment. The lenses are required to be free of aberrations. In Wadhwa et al. [131], due to the small size of the

organisms (sometimes as small as 170 μm), high magnification was required. This had some trade-offs, namely that only a small amount of light reached the sensor and the plane of focus was very thin, resulting in a reduction in the particle density in images. To obtain the high magnification, we used an inverted 20 mm focal length lens together with magnifying bellows, resulting in field of view ranging from 2.19 mm $\times$ 1.37 mm to 5.73 mm $\times$ 3.58 mm.

Digital cameras provide fast image transfer to a computer monitor, and thus allow much needed rapid feedback while doing a PIV experiment. A sensor chip is the heart of any digital camera, which converts the optical information into an electronic form. The technical aspects of the sensor thus directly affect the PIV capabilities. The two most common types of sensors are charge coupled devices (CCD) or complementary metal-oxide-semiconductors (CMOS). CMOS sensor based cameras have become very common nowadays and offer the capability of achieving very high frame rates at reduced resolution. For PIV around live organisms using infrared light, the sensor needs to be sensitive in the infrared part of the spectrum. For almost all of the PIV data presented in the subsequent chapters, we used a Phantom v210 camera, procured from Vision Research. The frame rate used in the filming should be high enough for the fast, time dependent flow structures to be captured by PIV.

2.2.4 Particle image velocimetry processing

The main aspect in which the two particle imaging techniques differ is the processing of the images to obtain velocity data. At low particle densities when the individual particle images can be identified and tracked, PTV is used. In the case of medium particle density, the individual particles can still be identified in the images but they can no longer be uniquely tracked from one image to the next due to the higher density of particle images. In this situation, PIV is used to obtain the velocity field. In PIV, the image is divided into a grid of interrogation windows, typically 32 $\times$ 32 or 64 $\times$ 64 pixels squared. The number of interrogation windows in the image defines the resolution of vectors in PIV processing. The displacement of particles in each interrogation window is found by calculating a matrix of cross-correlation between the original image and the image in the next frame, displaced in x and y directions. The peak in this cross-correlation matrix represents a matching between original particle images and displaced particle images in the next frame, thus providing the displacement between frames. The displacement is converted into velocity by dividing by the time difference between frames, and the process is repeated for every interrogation window in the image, resulting in a full velocity field. The final velocity field is checked for outliers to remove erroneous vectors, and further post processed to obtain a

smoothed, accurate velocity field.

2.2.5 Particle tracking velocimetry processing

In particle image velocimetry, individual particles in the image are identified and tracked from one image to the next, providing the displacement and thus velocity data. In most modern processing routines, a hybrid PIV+PTV technique is used, in which a coarse resolution PIV is first carried out to obtain a 'first guess' of the velocity field. This is subsequently used to improve the tracking accuracy in particle tracking. The vectors thus obtained can be post processed using median filters and other outlier detection methods to remove erroneous vectors. PTV naturally results in a set of randomly located velocity vectors, which cannot be used for later processing such as calculation of gradient fields. To resolve this, the PTV velocity vectors are interpolated using standard techniques to fit on a rectangular grid. Further post processing can be done on this data, such as interpolation to fill holes due to outlier removal, smoothing, and de-noising.

2.2.6 Applications of particle imaging techniques

PTV and PIV have been used extensively in the literature for measuring flows created by numerous kinds of swimming and flying organisms, such as fish [74], insects [22], and birds [120]. In the zooplankton community, the velocity fields around organisms have been quantified in a number of studies, using PTV [13, 32, 113, 138, 139], PIV [17, 16, 15, 37, 60, 66, 109, 125, 126, 127], and more recently, using advanced techniques such as holographic PIV [61, 82] and tomographic PIV [90]. The use of regular PTV and PIV for measuring flows around unicellular organisms is difficult due to several challenges, such as stochastic noise, thin focal plane, and limits on particle density [41]. These challenges have been recently met by using micro-PIV [106] together with clever analysis approaches, providing velocity fields around unicellular organisms such as the green algae *Chlamydomonas reinhardtii* [24, 44] and the bacterium *Escherichia coli* [23].

In the following chapter, we move over from the physical side to the biological side, looking at what is currently understood about the interactions between planktonic organisms through the fluid surrounding them.

Chapter 3

Biological background

3.1 Study organisms

The two main groups of organisms studied during the Ph.D. work are copepods and caldocera. In the following, I briefly introduce them so that the uninitiated reader can develop some familiarity with the two. A full description of the biology of these organisms can fill many books, so in the interest of brevity, only a few selected aspects are mentioned. For more details about the various aspects of the biology of these organisms, the reader is referred to the literature cited in this section.

3.1.1 Copepods

Copepods are one of the main subjects of this research, due partly to their status as the most important and abundant zooplankton. Highly successful in the zooplankton community, these crustaceans are found in virtually all aquatic habitats on the planet, from deep sea vents [52] to high altitude Alpine lakes [59]. Copepods have even been found living in the canopy of redwood trees, hundreds of metres above ground level [101]. Although less diverse in terms of the number of species, copepods are estimated to outnumber insects and may even be the most abundant metazoans (multi-cellular organisms) on the planet [53, 64, 80].

The name copepod comes from the Greek words *kope*, an oar and *podos*, a foot. The name refers to the oar-like swimming legs of the copepod, which it uses for drag based propulsion. Most copepods are small and require the use of a microscope for studying them. The copepod *Oithona davisae*, for example, measures only around 300 μm in body length [105]. On the large end of the spectrum, some of the deep sea copepods can be as large as 20 mm [47]. The typical body plan of a copepod is divided into two main parts,

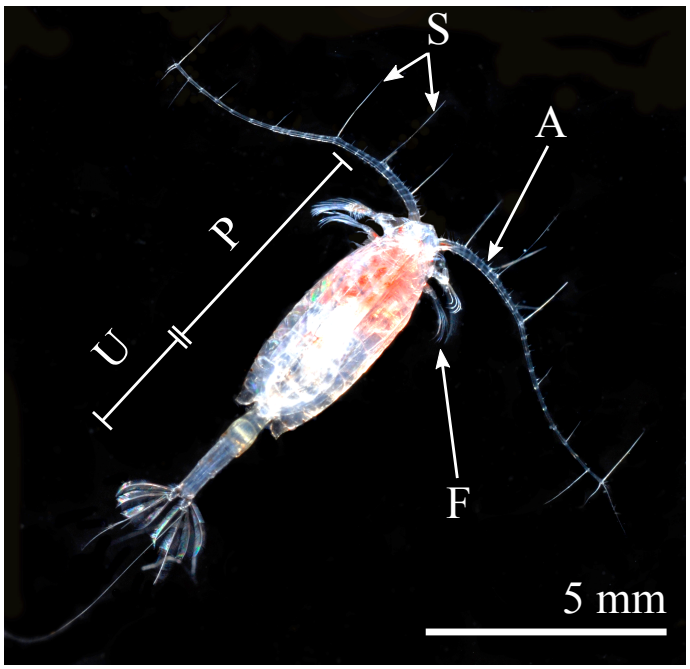

Figure 3.1: Dorsal view of the copepod *Paraeuchaeta norvegica* showing the prosome (P), urosome (U), antennules (A), feeding appendages (F), and setae (S). The swimming legs are not visible in this view. Image courtesy Erik Selander, University of Gothenburg.

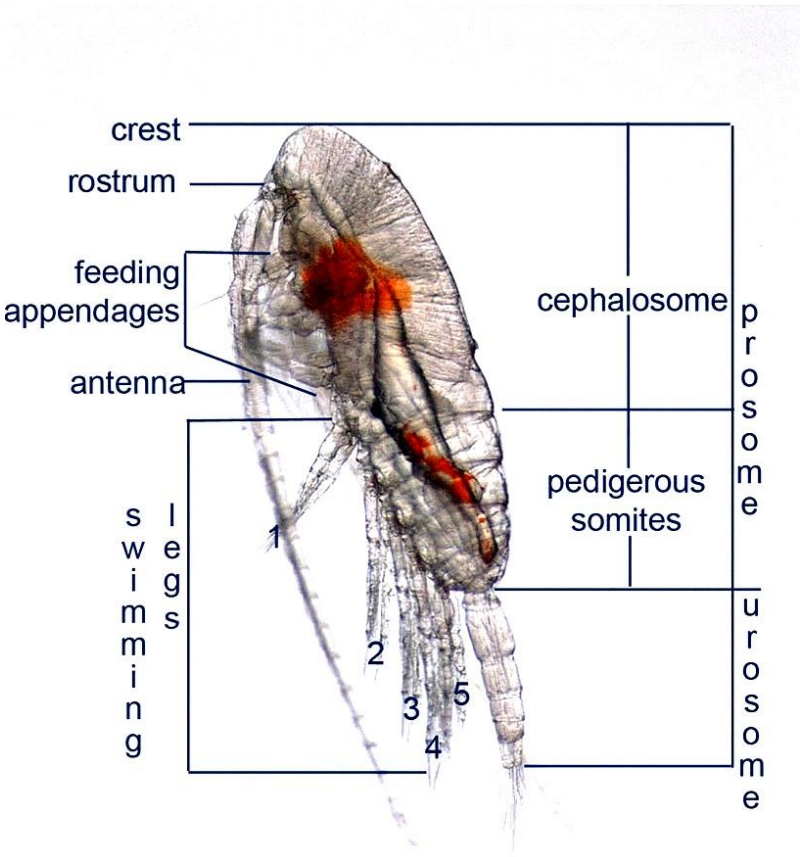

Figure 3.2: Lateral view of the calanoid copepod *Calanus australis* with the main body parts labelled. The total distance form the crest to the tip of the urosome is about 3.3 mm. Image courtesy Anita Slotwinski, CSIRO Marine and Atmospheric Research, University of Tasmania, Australia [117].

the prosome and the urosome (Figure 3.1). The segmented prosome is the pear shaped larger part of the body, further divided into cephalosome and the pedigerous somites (Figure 3.2). The size of a copepod is typically described in terms of the prosome length. The prosome contains the characteristically long antennules, which are used for chemosensing and mechanosensing and are covered with numerous setae, which are fine hairs used in mechanosensing. The prosome also contains a number of feeding appendages used for feeding and slow swimming, and swimming legs, which are used in impulsive 'jumps' through rapid metachronal strokes. The cephalosome bears the feeding appendages and the swimming legs are attached to the pedigerous somites, also called the metasome [47]. The thinner urosome, consists of the genital and anal segments, and is often used for direction control during swimming, like a rudder in a boat.

Copepods consist of ten orders, out of which three are free-swimming - the calanoids, cyclopoids, and harpacticoids. Of these, calanoids are the major herbivorous plankton dominant in many parts of the world's oceans [84], and therefore an important component of the food webs. Calanoids are distinguished from other orders by the joint between the fifth and sixth segments of the body, and a clear distinction between the prosome and the urosome (e.g. Figure 3.1). Long first antenna are also a key characteristic of calanoid copepods. Cyclopoids are rounder, with shorter antennules, and the females often carry two egg sacs [54]. Many cyclopoids are ambush predators, i.e. they remain motionless in water waiting for most of the time, and attack any motile prey that happens to swim by [116]. Harpacticoids are easily distinguished from the above two as they have an almost cylindrical body without a clear demarcation between the prosome and the urosome. Harpacticoids are primarily benthic or littoral [11], and most are marine.

Another interesting aspect of the life of a copepod is its ontogeny. Every copepod goes through a number of distinct developmental stages. Like all crustaceans, copepods moult by shedding their exoskeleton as they grow. Each moult marks the transition from one developmental stage to the next. A calanoid copepod, for example, goes through eleven developmental stages before reaching the twelfth and final stage as an adult (Figure 3.3). The first six developmental stages (NI-NVI) are nauplii, which have a smaller body size and a reduced number of segments and appendages (Figure 3.3). The later six stages are called copepodids (CI-CVI), the last of which is the adult form. Copepodids are essentially like smaller adults, which gradually develop adult characteristics during molts. Evidently, the most radical change takes place in going from the last naupliar stage (NVI) to the first copepodid stage (CI), when the shape and size of the copepods change dramatically. In many species of copepods (e.g. *Acartia tonsa*), the nauplius to copepodid transition is also associated with a radical change in swimming mode, as the nauplii of these species swim

with the bilaterally symmetric 'breast stroke', while the copepodids jump by throwing back the swimming legs which are all organised on one side of the body.

3.1.2 Cladocera

Cladocerans, commonly called 'water fleas', are another crustacean group which form a part of the metazoan zooplankton community in the oceans and in freshwater systems. Of the many hundred species of cladocera that have been described, most are freshwater species and fewer than ten are marine species belonging to the family Podonidae [2, 10]. While marine cladocerans form only a small fraction of the zooplankton in the open sea, they may seasonally outnumber the copepods in coastal and estuarine environments [10]. In freshwater habitats, on the other hand, cladocerans such as those of the genera *Daphnia* and *Bosmina* often dominate the herbivorous community and may be called the 'grazing cattle' of lakes and ponds [11]. The smaller cladocerans like *Daphnia* are usually filter feeders, while the larger ones like *Leptodora* are predatory, preying upon large prey such as rotifers and even copepods [11]. The marine cladoceran *Podon intermedius* has also been recorded to have preyed upon copepods (Thomas Kiørboe, unpublished data), though an attack has never been observed.

Adult cladocerans are typically about 1 mm long, with an ellipsoidal body, which is somewhat flattened along the left-right axis (Figure 3.4). A number of thoracic limbs are located on the ventral side which help with feeding. Cladocerans are able to do parthenogenetic reproduction, which means that the egg develops into an embryo without fertilization. The embryos are kept in the brood chamber which can be seen in Figure 3.5. The cladocerans are also unique in that their large head contains a relatively big compound eye (Figure 3.5), though the image forming capabilities of the eye are questionable [83].

Our study organism was the cladoceran *Podon intermedius* for the purpose of investigating the breast stroke swimming mode, which the organism uses for propelling itself. The *Podon* uses its large second antennae for swimming and beats them in a breast stroke like fashion. The second antennae are biramous with a variable number of setae for different species. The antennae and the setae act as flexible oars which are spread out during the down stroke for producing large thrust, and are folded together during the return stroke to reduce unwanted drag. This way of swimming is similar to other planktonic organisms such as copepod nauplii [5] and biflagellated green algae [41]. The swimming kinematics and the flow fields due to the cladoceran *Daphnia magna* have recently been analysed by Murphy [89], who concluded that a separate vortex ring was formed by each antennae during the beat cycle. He argued that the two vortex rings result from impulsively applied forces by the two antenna.

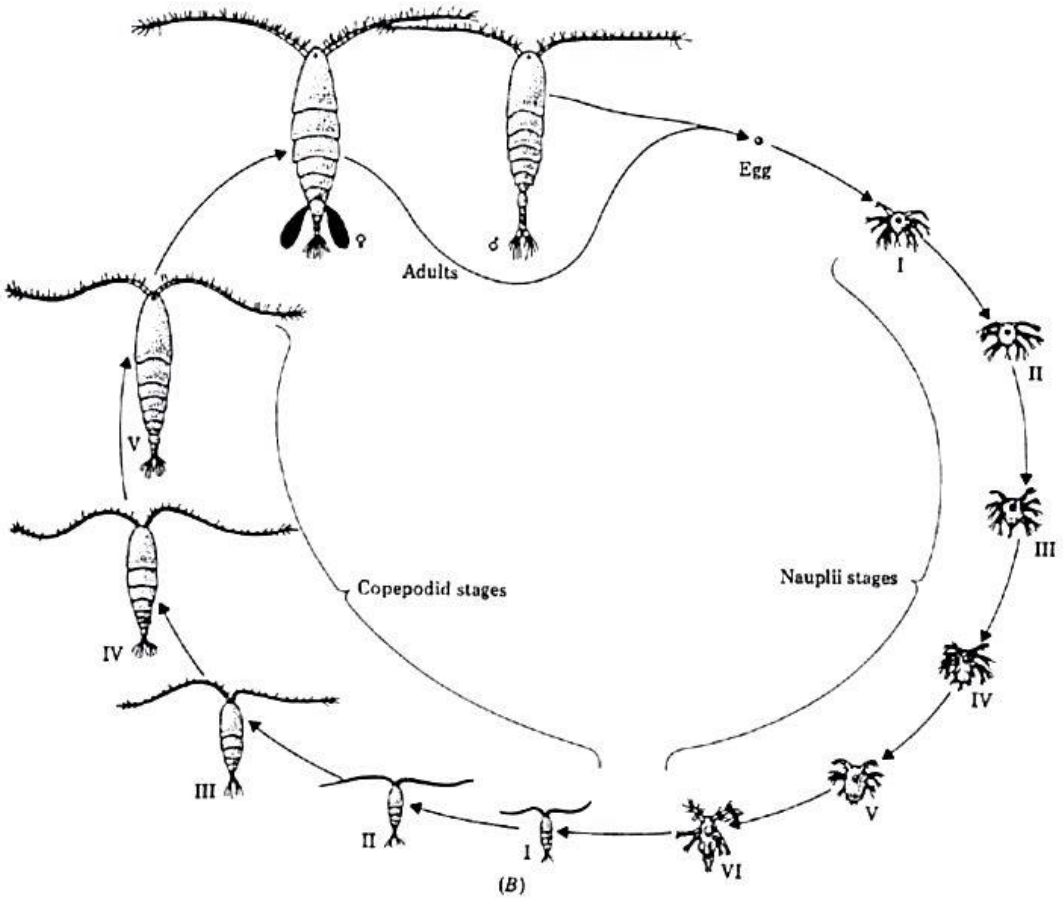

Figure 3.3: Schematic representation of the life cycle of a calanoid copepod. The first six developmental stages are called nauplii and the last six copepodids, with the final copepodid stage being the adult form. Figure adapted from [93]. The drawings are not to scale.

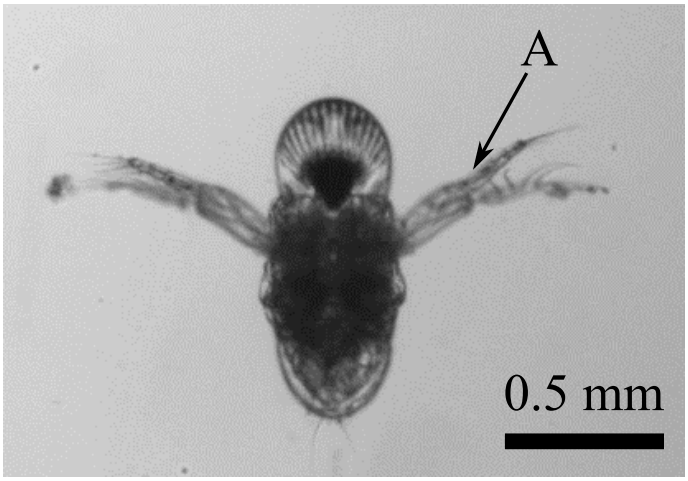

Figure 3.4: Frontal view of the cladoceran *Podon intermedius*. The biramous second antenna (A) is used for swimming and moves in a breast stroke like fashion.

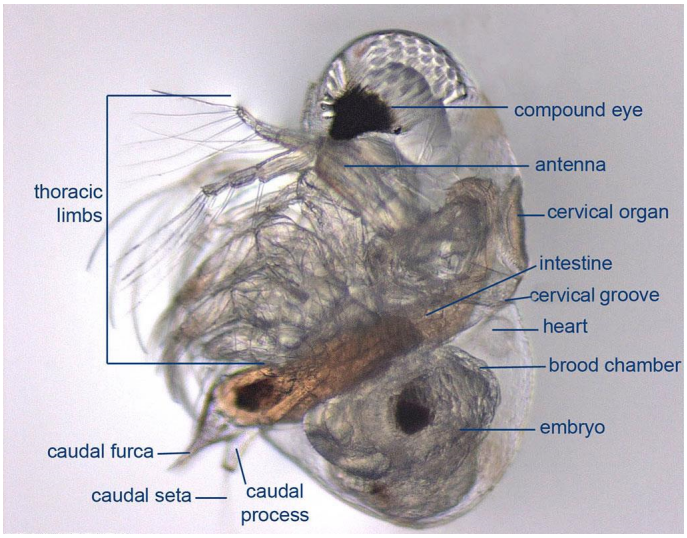

Figure 3.5: Lateral view of the cladoceran *Podon sp* with its anatomy labelled. Its body size is about 0.9 mm. Image courtesy Anita Slotwinski, CSIRO Marine and Atmospheric Research, University of Tasmania, Australia [117].

3.2 Mechanosensing in plankton

This section summarizes our knowledge of the biological aspects of flow mediated interactions between plankton. The purpose of this part is to give the readers coming from a physics background an overview of the biological research that has gone into the topic of flow mediated interactions between plankton.

3.2.1 Behavioural studies

Direct behavioural observations of the mechanosensing abilities of zooplankton started surfacing in the mid 20th century, starting with Grosser et al. [43], who had observed that *Daphnia magna* suspended in sucrose solution with density larger than itself had a reversed orientation of gravity, suggesting that external sensors were involved in sensing the direction of gravity, likely the setae. Schröder [107] found that the freshwater copepod *Mixodiaptomus laciniatus* was able to remotely detect transparent obstacles under water, speculating that the organism sensed the "noise" of their own swimming reflected from the obstacle. Singarajah [108], who systematically observed the response of plankton to suction flows generated by a siphon tube, noted that most plankton sensed the flow at some distance from the tube entrance and tried to swim away from it.

Many behavioural studies have since followed to investigate the mechanosensing capabilities of zooplankton. Szlauer [118] reported that *Daphnia pulex* avoided the approach of other plankton or inanimate objects. Chaetognatha make feeding attacks on a vibrating probe within a narrow range of frequency, amplitude, and distance, otherwise either made escape jumps or did not respond [26, 51]. Newbury [91] argued that the range of frequencies over which chaetognath responds are tuned to the beating frequency of their copepod prey.

There is also ample evidence of remote prey detection by copepods, resulting in directed ambush attacks from copepods towards self-propelling prey organisms [12, 62]. Copepods attack small fish larvae from a distance, specifically in response to the tail-beat by the larvae and ignore any motionless larvae [79]. Resting copepods are able to sense the approach of another organism and often respond with a directed escape away from the invader [110, 114]. Predation rates of copepods were found to decline sharply upon amputation of antenna, corroborating their role in prey detection [73]. Reduced response of *Temora longicornis* to water jets after antennal amputation leads to the same conclusion [40].

3.2.2 Physical modelling of mechanosensing

Legier-Visser et al. [77] first used modelling to study the mechanosensing of prey generated flows by copepods, concluding that pressure differences caused by sinking particles may be used by copepods for detection, though later investigations found flaws in their calculations and conclusions [42, 137]. Kiørboe and Visser [69] modelled mechanosensing in copepods using the example of theoretical flow fields around a sphere, and decomposed the fluid disturbance into translation, pure rotation (vorticity) and deformation rate. They argued that a prey perceiving a large predator detects the deformation component of the disturbance, while a predator perceiving a small prey detects the translation, i.e. velocity component of the disturbance. Their analysis successfully explained observations such as larval fish behaviour while capturing copepod prey, prey size effects on clearance rates, and feeding rates of copepod *Oithona similis* on motile plankton. Svensen and Kiørboe [116] successfully used the flow velocity as stimulus to explain the observed clearance rates of copepod *Oithona similis* preying upon motile flagellated prey. Visser [130] extended and refined the earlier models to various planktonic behaviours such as passive sinking, self-propulsion, feeding current flow, and copepod escape jumps.

3.2.3 Early experiments on quantification of the stimulus

Behavioural evidence does not give much information about the component of the fluid disturbance that is sensed by the plankton. Any fluid disturbance is fully described by a time dependent velocity field. The signal perceived by a plankton could be the velocity itself, or any of its spatial or temporal gradients. Which one of these is used by a plankton in its perception of its surroundings? This is where careful experimental and analytical studies gave further insight.

The first experiments in this direction were performed by Haury et al. [49], who elicited escape jumps of copepod *Calanus finmarchicus* in response to the flows created by a cylindrical obstacle in rotating flow. From their results, they identified the fluid deformation and deformation rate as the main contenders of the mechanosensory stimulus. Kirk [70] measured flow around *Daphnia pulex* with a hot wire anemometer and used observed attack distance on *D. pulex* by copepod *Chaoborus trivittatus* larvae together with the measured flow attenuation to estimate the attack threshold for the copepod.

A challenge in the proper understanding of the sensing of hydrodynamic signals was that the experimental evidence was restricted to behavioural and anatomical studies, and required reliable observations of the organism's response to a quantifiable fluid disturbance, which could be uniquely associated with one or another flow component. An influential

development in this topic was the calibration of the siphon tube set-up [33] previously used by Singarajah [108]. The siphon tube set-up with calibrated velocity fields was subsequently used in many studies to quantify the threshold sensitivities of various plankton to external flow disturbances [28, 30, 38, 58, 57, 68, 129, 136].

The most thorough experimental investigation of flow perception by copepods was carried out by Kiørboe et al. [68], who exposed *Acartia tonsa* to various quantifiable hydrodynamic environments, such as siphon flow, oscillating flow, and rotating flow. These simple flows could be easily decomposed into underlying hydrodynamic components. By combining the results from various experiments with earlier theoretical analysis [69], they concluded that fluid deformation rate was the component of flow that is responsible for escape response in copepods. Other studies have used different kind of stimuli such as a fine fluid jet [29, 31, 34, 40], a moving cylinder [14], tactile stimulation [39], a mechanical fish mimic [50], and a vibrating sphere [48]. Recent studies have found that the escape threshold for the copepods is modulated by orientation [28] as well as light conditions [30].

3.2.4 Physiological and anatomical studies

The idea that the setae of crustaceans have sensory function has been recognized at least since the mid 19th century [114]. Later studies using tactile stimulation and amputation have confirmed the role of antennae of copepods in sensing hydrodynamic or mechanical disturbances [39, 40]. Amputation of antennae also resulted in reduced predation rates among copepods, suggesting their role in the perception of prey [73]. Strickler and Bal [114] carried out an ultrastructural study of the antenna and the setae with electron microscopy and concluded that the setae on the antennules are likely mechanoreceptors.

The first electrophysiological studies of the antenna in several copepod species revealed the setae and antenna to be velocity sensors rather than displacement sensors, responding to velocities as small as 20 μm/s and the corresponding displacements as small as 10 nm [135]. Further, the setae are directionally sensitive, and the neural response can phase lock with an oscillating stimulus [135]. Yen et al. [135] hypothesised that the antenna may detect differences in velocity between the body and the distal end of the antenna, where the setae seemed to be particularly densely located and highly sensitive.

Fields et al. [29] carried out a more elaborate investigation of the signal transduction properties of individual setae at the distal end of the antenna of copepod *Gaussia princeps*. They quantified the physical and physiological response of the setae and also the flow velocity of the fine water jet that caused the bending of setae. By combining this information, they found that different setae were differently sensitive to the water flows. The longer distal hairs were physically less sensitive to water flow, but their neural response to angular

displacement was much stronger. Moreover, in spite of not having multiple innervation, the setae had differential sensitivity to directional stimulation, likely due to differences in their mechanical structure. Further, very high firing rates of the copepod antenna ($\sim$ 5 KHz) allow the copepod to be able to show fast behavioural responses within 1 – 5 ms [31].

Chapter 4

Summary of the results

4.1 Hydrodynamics and energetics of copepod nauplii and copepodids

Copepods go through a remarkable transformation from nauplii (early stages) to copepodids (later stages) as a part of their life cycle, during which they dramatically change their size, shape, and swimming mode (Figure 4.1). Throughout their life, most of the copepod species inhabit an intermediate Reynolds number regime, with the Reynolds number (Re) typically between ~ 1 and 100. In this regime, both viscosity and inertia have a strong contribution to the dynamics of the fluid around the organism, and neither can be neglected. Due to the life cycle related changes experienced by the copepods, their hydrodynamic environment also changes drastically. Even though copepods are acknowledged to be a planktonic group of primary importance, the ontogeny associated hydrodynamic changes are not previously characterized.

In this paper, we have made the first direct measurements of the flow fields around a copepod through its life cycle, focusing on the comparison between the nauplii and the copepodid stages. Our focus was on a) characterizing the qualitative hydrodynamic changes experienced by the copepod during growth, and b) quantifying the change in various costs associated with swimming - spatial and temporal decay of the flow disturbance, cost of locomotion, and energetic efficiency. We chose the copepod *Acartia tonsa* as a study organism, because all of its life stages swim with short lasting hops or jumps, resulting from impulsive strokes from their swimming appendages.

We found that there was a topological difference between the flow structure created by the nauplii and the copepodids. While the nauplii created a single vortical structure around them while jumping, the copepodid jump resulted in two counter rotating viscous

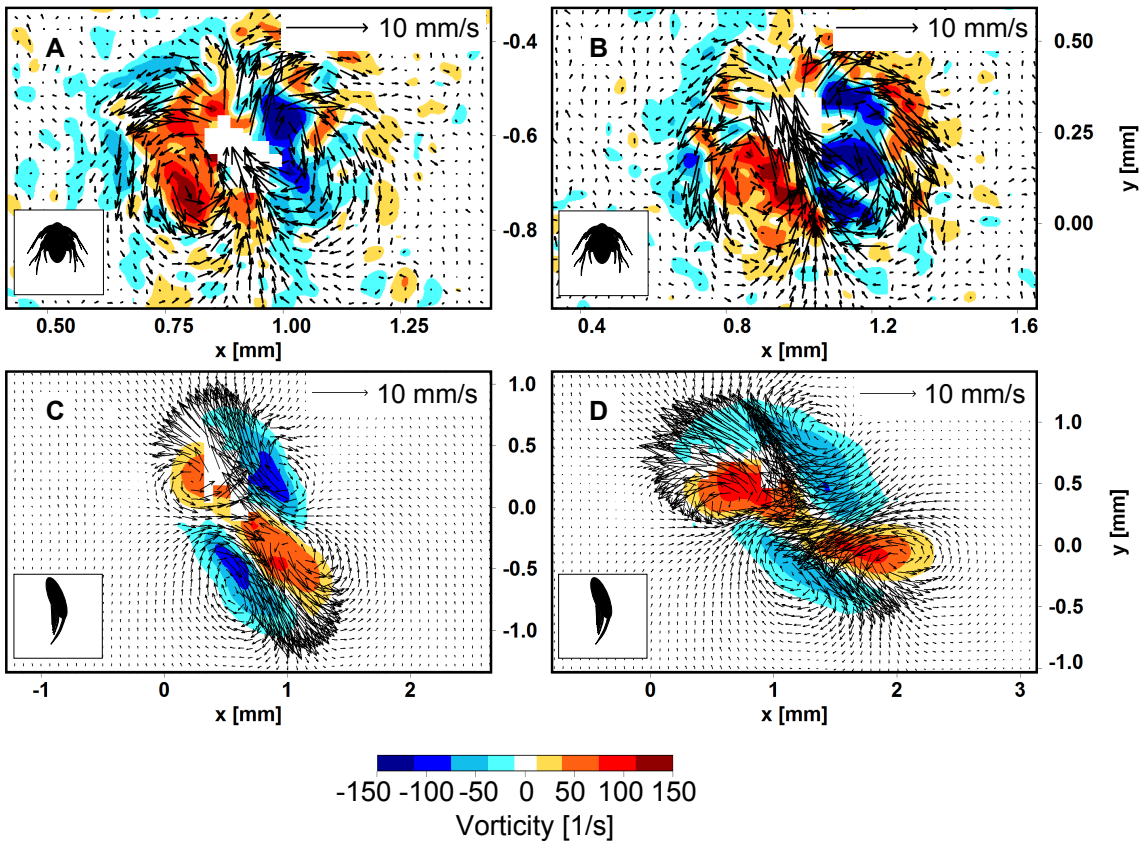

Figure 4.1: Snapshots of the flow fields around jumping nauplii and copepodids of different sizes at the end of their power strokes. (A) Small and (B) large nauplii and (C) small and (D) large copepodids. The flow structures caused by different sized nauplii are qualitatively similar, with a single toroidal vortex ring, and different from that caused by copepodids, which form two vortex rings. Adapted from [131].

vortex rings. A kinematic analysis of their swimming led us to plotting the Reynolds number, Re, against the frequency parameter, β, as these are the two main dimensionless numbers dictating the behaviour of the fluid through the Navier-Stokes equations. We found proportionality between Re and β for nauplii, and a higher slope of β-Re fit for copepodids showing a higher effectiveness of their jumps in covering distance.

An analysis of the temporal decay of the flow field showed that the time scales of velocity decay were dictated by the viscous time scale set by the size of the organism. The spatial decay of velocity was faster for copepodids than for nauplii suggesting that they the are hydrodynamically quieter of the two. From the time dependent energy dissipation in the measured flow fields, we could estimate the cost of locomotion and the energetic efficiency, in both of which copepodids fared better than the nauplii. Thus, our measurements suggest that as the nauplius grows into a copepodid, it enters a more favourable hydrodynamic regime, and becomes a more effective and efficient swimmer.

4.2 Flow disturbances generated by feeding and swimming zooplankton

This paper takes a step back and investigates the general patterns in the flow disturbance created during feeding and swimming by a wide range of plankton. To this effect, we measured and analysed the flow fields around a variety of plankton, using the technique of particle image velocimetry (PIV).

Plankton have diverse ways of feeding and propelling themselves, but on a coarse level the multitude of propulsion mechanisms can be divided into four categories. Many organisms remain stationary in water while creating a feeding current to filter for prey and nutrients, in a process termed hovering. Other plankton move in water with a steady speed while scanning the water for food and mates, and this propulsion mode is called cruising. Many other plankton use what is called breast stroke swimming, in which bilaterally organized swimming appendages or equatorial cilia move backwards simultaneously to push the organism forward, similar to human breast stroke swimming. In the last category called jumping, a number of appendages move backwards impulsively, thrusting the organism forward with high velocity and acceleration. Examples of various organisms using the above propulsion modes are shown in Figure 4.2.

Using PIV, we measured the velocity fields created by various free swimming plankton, with an aim to quantify the flow disturbance and to determine the effect of swimming mode on fluid disturbance [67]. From the velocity fields, we measured the size of the region around the organism where the flow velocity exceeded a certain threshold. By varying the

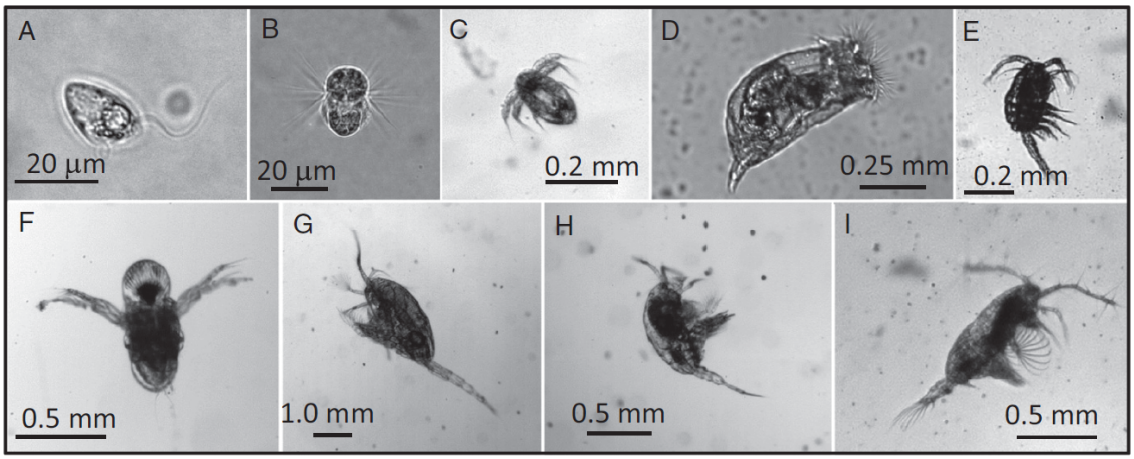

Figure 4.2: Examples of planktonic organisms which swim with different modes. The dinoflagellate *Oxyrrhis marina*, cruiser (A), the ciliate *Mesodinium rubrum*, breast stroke swimmer (B), *Acartia tonsa* nauplius (juvenile), breast stroke swimmer (C), the rotifer *Brachionus plicatilis*, cruiser (D), the copepod *Oithona davisae*, jumper (E), the cladoceran *Podon intermedius*, breast stroke swimmer (F), the copepod *Metridia longa*, cruiser (G), the copepod *Temora longicornis*, hoverer (H), and the copepod *A. tonsa*, jumper (I) [67].

threshold velocity and measuring the corresponding size of the region of influence, spatial decay of the swimming generated flow could be characterized and approximated in terms of power laws.

At the peak of the stroke when the disturbance is the largest (filled circles in Figure 4.3), the decay of the velocity (U^*) with distance (r) can be quantified in the form of power laws (Figure 4.3). The exponents of the power law describing the velocity decay for the different species fall into four groups. For hovering organisms, the velocity decays as r^{-1}, for cruisers, it decays as r^{-2}, for breast stroke swimmers, as r^{-3}, and for jumping plankton, velocity decays with distance as r^{-4}. Thus the spatial decay of velocity away from the organism was strongly affected by the swimming mode. Moreover, the modes used for swimming alone (breast stroke swimming and jumping) have a faster spatial decay of velocity, than the modes which are used for swimming and feeding at the same time (hovering and cruising). These modes can thus be called "hydrodynamically quieter", in the context of flow mediated ecological interactions.

The observed dependence of the spatial decay of velocity on the propulsion mode can be explained with the help of simple point force models (Figure 4.4). The case of a hovering organism can be approximated by a single point force acting on the fluid (Figure 4.4A). This idealized force configuration has been studied thoroughly, a well-known analytical solution known as the Stokeslet describes the flow created by such a configuration. The Stokeslet

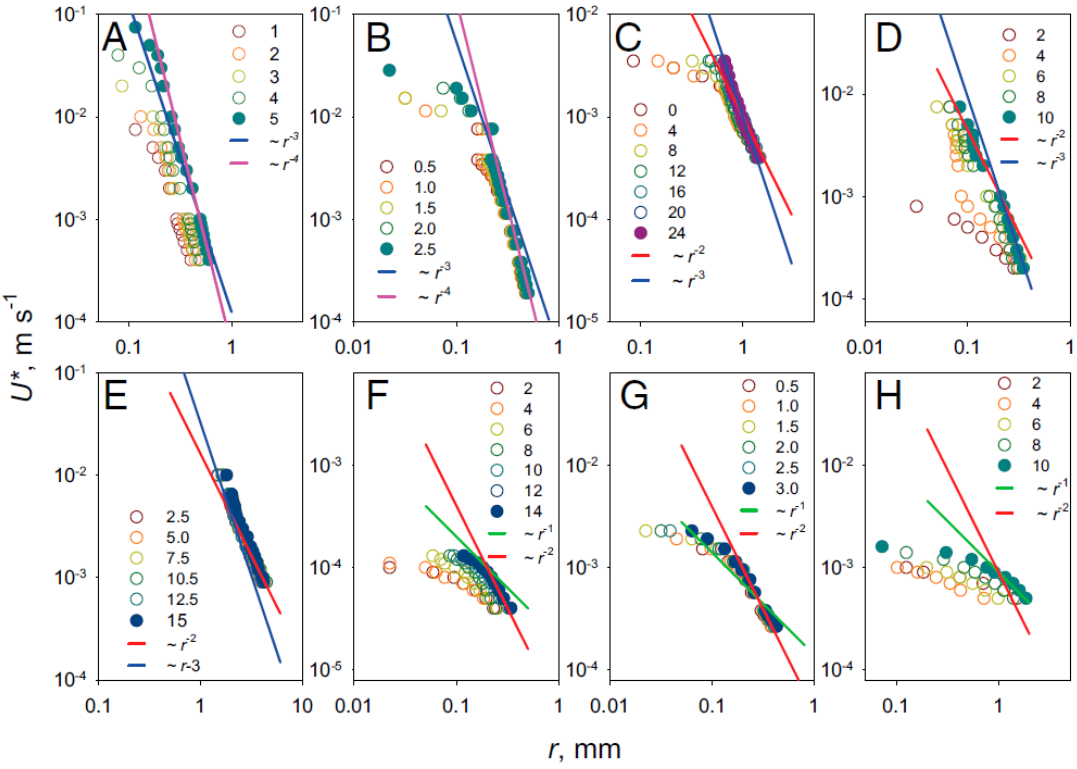

Figure 4.3: Measured spatial attenuation of flow velocities. *A. tonsa* copepodite jump (A), *O. davisae* jump (B), *P. intermedius* breast stroke (C), *A. tonsa* nauplius breast stroke (D), *M. longa* cruising (E), *O. marina* cruising (F), *T. longicornis* nauplius feeding(G), and *T. longicornis* hovering (H). The solid circles show the velocity at the peak of the power stroke and the open circles the velocity during the time leading up to the peak at times given in milliseconds. The solid lines show power laws with slopes between -1 and -4 and were adjusted to line up with the far field flow attenuation at the peak of the power stroke. Adapted from [67].

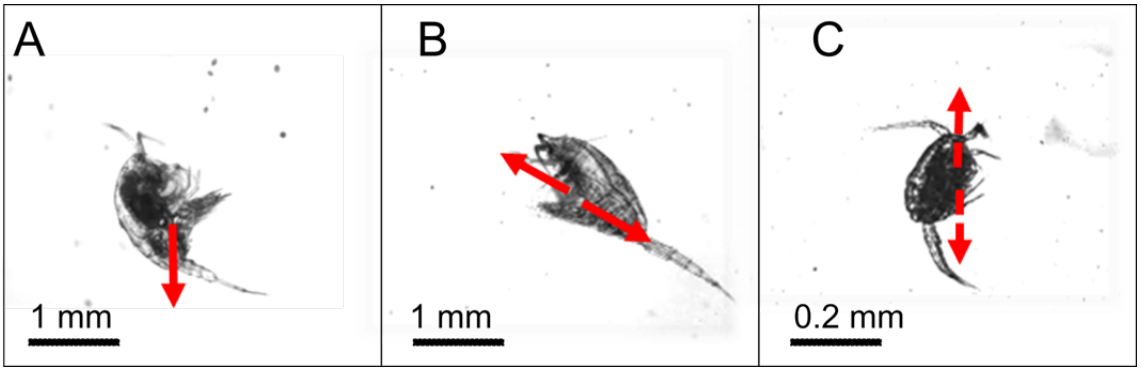

Figure 4.4: Schematic representation of the propulsive forces and the drag forces for a hovering *T. longicornis* (A), a cruising M. longa (B), and a jumping O. davisae (C). Only the red forces act on the water. The dashed vectors in (C) represent the impulsiveness of the point forces.

indeed gives a flow-field in which the velocity decays with the inverse of distance, similar to the measurement for hovering organisms. For the cruising organisms, the flow behaviour can be described by another singularity model known as the stresslet, in which the velocity decays as r^{-2}. A stresslet is composed of two equal and opposite point forces acting at points separated by a small distance, a configuration which approximates the thrust and drag forces applied on the water by a cruising organism (Figure 4.4B). If the forces act for only a very short amount of time, as is the case for jumping organisms (Figure 4.4C), then the solution is given by an impulsive stresslet, for which the velocity decays as r^{-4}.

4.3 Quiet swimming at low Reynolds number

Breast stroke swimming is a common mode of swimming among plankton, and there has been much work towards understanding the associated hydrodynamics. Most of the previous work has focused on the biflagellate green algae *Chlamydomonas reinhardtii*, particularly focusing on questions related to synchronization of flagella [41]. While there have been measurements of the velocity field created by *C. reinhardtii* [24, 44], the spatial decay of velocity has only been measured for the time averaged flow in [24]. Also, flow fields created by other planktonic breast stroke swimmers have received little attention in the literature. In this paper, we focussed on the breast stroke swimming mode and described a simple model that explains the observed decay of velocity for such swimmers [3]. Our work on breast stroke swimming also highlights the more general question of how far field flow disturbances can be modified by changes in the spatial organization of the propulsive forces.

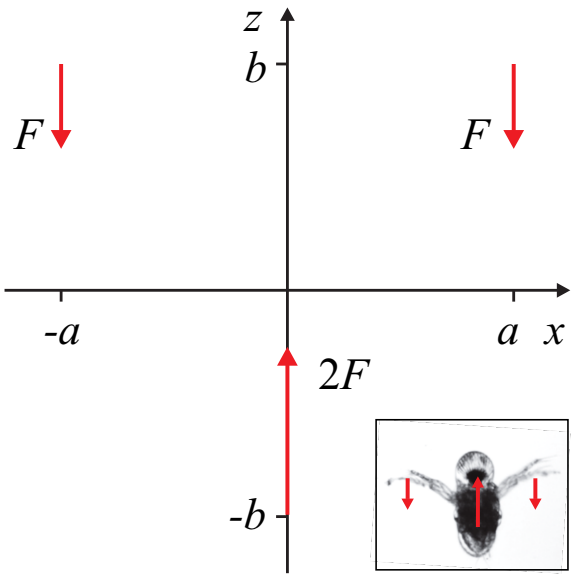

Figure 4.5: The three point force model for breast stroke swimmers. The forces act in xz plane and the sum of forces is zero. The inset shows a schematic representation of the three point forces produced by a swimming *Podon intermedius*.

The simple model we used to represent breast stroke swimming organisms consists of three point forces acting on the water, all acting in the xz plane (Figure 4.5). The thrust produced by the swimming appendages is represented by two point forces of magnitude F each, acting at (a, b) and $(-a, b)$ in the negative z direction. The drag force on the body is represented by a single force of magnitude $2F$ acting at $(0, -b)$ and pointing in the positive z direction. There is thus no net force acting on the water, a condition required for low Reynolds number propulsion by neutrally buoyant organisms. In our analysis, we keep the force magnitude constant and only vary the aspect ratio α of the configuration, given by $\alpha = a/b$.

The flow field due to a single point force acting at a point is given by the Stokeslet, for which the velocity field is given by equation 2.10. Since the Stokes equations are linear, flow due to a number of Stokeslets distributed in space, like the configuration shown in Figure 4.5, can be added together to find the net flow resulting from the action of all of the forces. We analyzed the net flow due to the three point force model, and studied the effect of the aspect ratio α on the flow structures and the spatial decay of velocity. It is worth noting again that the far field flow behaviour for arbitrary force configurations can be conveniently studied by applying a multipole expansion on them, as described in Section 2.1.5. In the following plots, we also show for reference the far field velocity predicted by the multipole expansion.

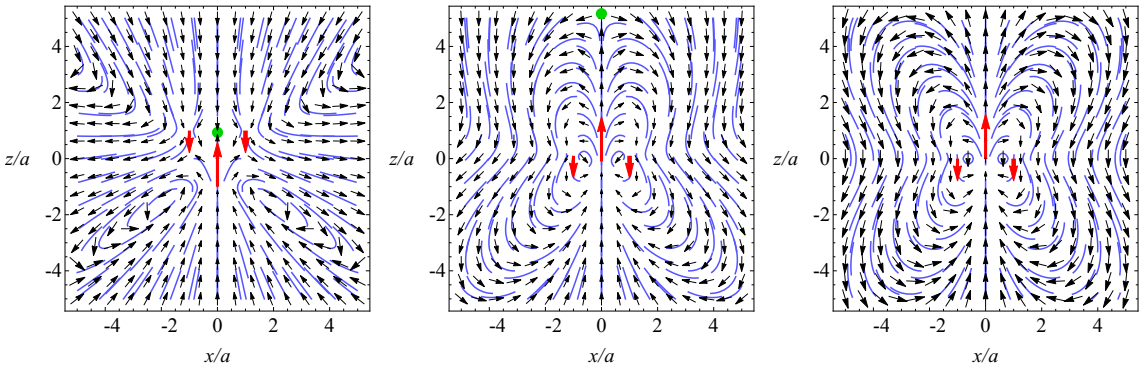

Figure 4.6: Velocity fields in the three point force model for $\alpha = 1$ (left), $\alpha = 0.1$(middle), and $\alpha = 0$ (right). The red arrows represent the point forces and the green dots the stagnation points on the z axis. The flow fields are shown as black vectors and blue streamline segments. Adapted from [3].

Figure 4.6 shows the flow fields due to the three point force model for three different values of α: 1, 0.1, and 0. It is evident that the flow structure changes quite significantly with changing values of α. When $\alpha = 1$, the flow structure resembles the flow fields for a puller stresslet, with downwards flow on the positive z axis and upwards on the negative z axis. The distinguishing feature is the two counter-rotating whirls on each side of the z axis, and a stagnation point on the positive z axis. As α is reduced, the stagnation point moves further up along the z axis and eventually when $\alpha = 0$, the stagnation point moves away to $+\infty$. In this situation, the flow mainly consists of two counter-rotating flow structures, qualitatively similar to what has been experimentally observed for breast stroke swimming plankton [131].

The velocity magnitude in the three point force model for the different values of α is shown in Figure 4.7. Only the velocity on the z axis is shown here, but the far field behaviour is qualitatively the same in all directions. The expressions for the far field velocity predicted from the multipole expansion are also shown for reference in red and green for $\alpha = 1$ and $\alpha = 0$, respectively. We find that just like the flow structure, the spatial decay of velocity is strongly affected by the value of α. For $\alpha = 1$, the far field flow velocity decays as one over distance squared (red curve), while for $\alpha = 0$, the far field decay is faster as the velocity decays as one over distance cubed (green curve). In general, the flow field of a three point force model is composed primarily of dipole and quadrupole components, which decay as r^{-2} and r^{-3} respectively. Thus, for large α, the flow is dominated by a dipole while for $\alpha = 0$, the dipole is eliminated and the flow is dominated by a quadrupole. For small values of α, e.g. 0.1, while the far field flow decays as a dipole (r^{-2}), closer to the organism the flow field is dominated by the quadrupole

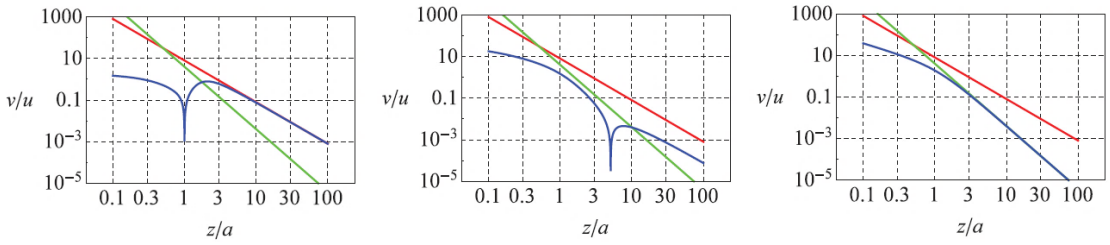

Figure 4.7: Magnitude of the velocity in the three point force model (blue) on the positive z axis with $\alpha = 1$ (left), $\alpha = 0.1$ (middle), and $\alpha = 0$ (right). Also shown are the far field approximations for $\alpha = 1$ (red) and $\alpha = 0$ (green), based on the multipole expansion. Adapted from [3].

component with r^{-3} decay. Moreover, not just the spatial decay is faster, the magnitude of the far-field flow velocity is smaller for $\alpha = 0$ as compared to the case with $\alpha = 1$.

Thus, our study shows that with small α, a three point force model captures the velocity decay observed for breast stroke swimmers. It further highlights the role of spatial organisation of propulsive forces on flow structures and velocity decay in low Reynolds number swimming, an aspect which has previously not been well recognized.

4.4 Inertial effects in the swimming hydrodynamics of zooplankton

This manuscript, which is currently under preparation, further investigates the periodic swimming of zooplankton, using the cladoceran *Podon intermedius* as a model organism. *P. intermedius* is a relatively large zooplankton with a typical body size of $L_s \approx 1$ mm (Chapter 3). It swims using the breast stroke swimming mode which we have discussed in the earlier sections. To what extent can low Reynolds number concepts and models, such as the three Stokeslet model, be applied to the swimming of a large zooplankton like *P. intermedius*?

The first step in answering that questions is to estimate the Reynolds number for the swimming. *P. intermedius* swims at a mean speed $V_m \approx 10$ mm/s, so we estimate a swimming Reynolds number of the order of $\mathrm{Re} = 10$. Thus, the swimming of *P. intermedius* falls into the regime of intermediate Reynolds numbers, hence inertial effects will be important to the hydrodynamics, but to what extent?

To answer these questions, we have measured the detailed swimming kinematics of *P. intermedius*, from which we are able to calculate time dependent drag and thrust forces acting on the organism. We find that the time dependent net force experienced by the

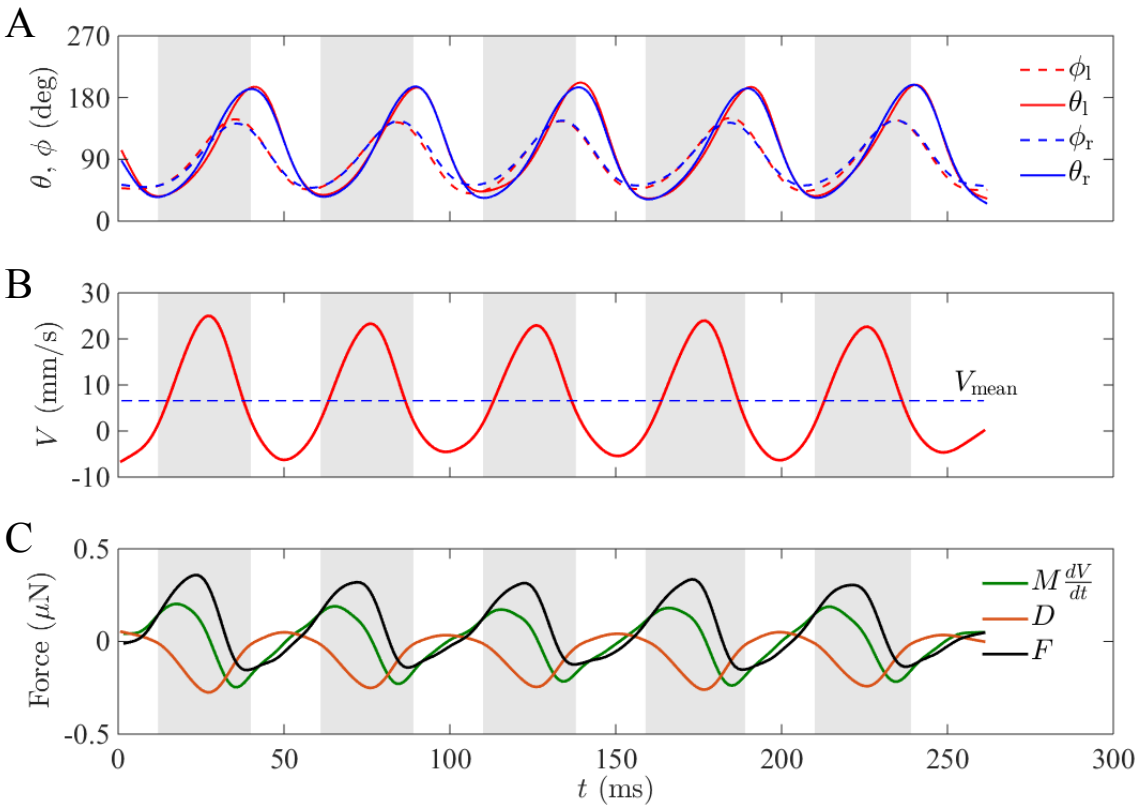

Figure 4.8: (A) Time series of the left arm and paddle angles (ϕ_l, θ_l), and right arm and paddle angles (ϕ_r, θ_r), for an instance of *P. intermedius* swimming horizontally. The paddle lags behind the arm by a small phase difference. The grey bars in the background represent the power stroke. (B) The measured swimming velocity (V) of the organism. (C) Time series of the drag force D (blue), the thrust F (black), and the total force MdV/dt (green) acting on the organism.

organisms is not negligible in comparison with the drag and thrust forces, showing that a low Reynolds number model in which thrust and drag balance may not apply. We also developed a simple model for a general periodic swimmer, by writing a force balance including inertial effects. Our simple model is able to capture many of the features of periodic swimming, such as the mean swimming velocity, propulsive forces, amplitude, and phase of the velocity fluctuations. Analysis of this simple model suggests that a low Reynolds number model with linear drag is a good approximation for the swimming behaviour for Reynolds numbers up to Re = 10. Interestingly, a more complete model including non-linear drag terms behaves like a low Reynolds number model at even higher values of the Reynolds number, where the linear model is not applicable. Thus, in general, a low Reynolds number model is a reasonable approximation for intermediate Reynolds number swimmers, at least up to Reynolds numbers around Re = 10.

We also measured the swimming-induced flow disturbances created by *P. intermedius*, and found that the velocity decays with distance away from the swimmer as $v \sim r^{-3}$. Moreover, due to the net force acting on the swimmer at most times during swimming, the three Stokeslet model does not capture the observed velocity decay, as such a model would be dominated by the resultant monopole contribution. We speculate that the fast spatial decay of velocity is due to inertial effects in the flow. The observed $v \sim r^{-3}$ decay in flow velocity may be due to potential flow in most of the region around the organism, except a small boundary layer like region immediately surrounding the swimming organism.

4.5 Characteristic sizes of life in the oceans

This paper is the main result from the 'Size in the ocean' project, a collaboration spanning institutes and disciplines under the umbrella of the Centre for Ocean Life. This study asks the question - how does the size of a marine organism affect its life? To answer this question, we examined how size dictates transitions in life strategies, and thus acts as a structuring factor in marine life. In this vast topic, we restricted ourselves to analysing some key aspects of marine life which are affected by size - resource encounter and trophic strategies, mobility, size limits and the sensing range of various sensory modes, and life history strategies of organisms. We collected large amounts of data for these different aspects, which allowed us to extract size based scaling laws applicable to them, and identify the transitions from one strategy to another. The scope of our analysis included all pelagic life forms found in the oceans, from bacteria to whales.

To take a concrete example from the different aspects covered in this paper, motility strategies of an organism depend strongly on their size. While the large organisms make use of inertia for locomotion, and are able to coast through water, the small organisms experience the water as highly viscous, and use drag based propulsion. The transition between the two regimes - inertial and viscous - is determined by the Reynolds number $\mathrm{Re} = \rho L V/\mu$, which approximates the ratio between inertial and viscous forces for an organism of size L swimming with velocity V in water with density $\rho \approx 10^3$ kg m^{-3} and dynamic viscosity $\mu = 10^{-3}$ Pa s. For $\mathrm{Re} \ll 1$, viscous forces dominate and for $\mathrm{Re} \gg 1$, inertial forces dominate the swimming hydrodynamics. The crossover between the two regimes takes place in $\mathrm{Re} \approx 1$ - 100. Data suggests that the scaling of swimming velocity with size is different in the two regimes, $V \sim L^{0.79}$ in the viscous regime while $V \sim L^{0.42-0.5}$ for the inertial regime [8, 63, 133, 134].

To complement the observed scaling laws and transitions in life strategies, we collated and developed simple arguments based on first principles, which could explain the observed

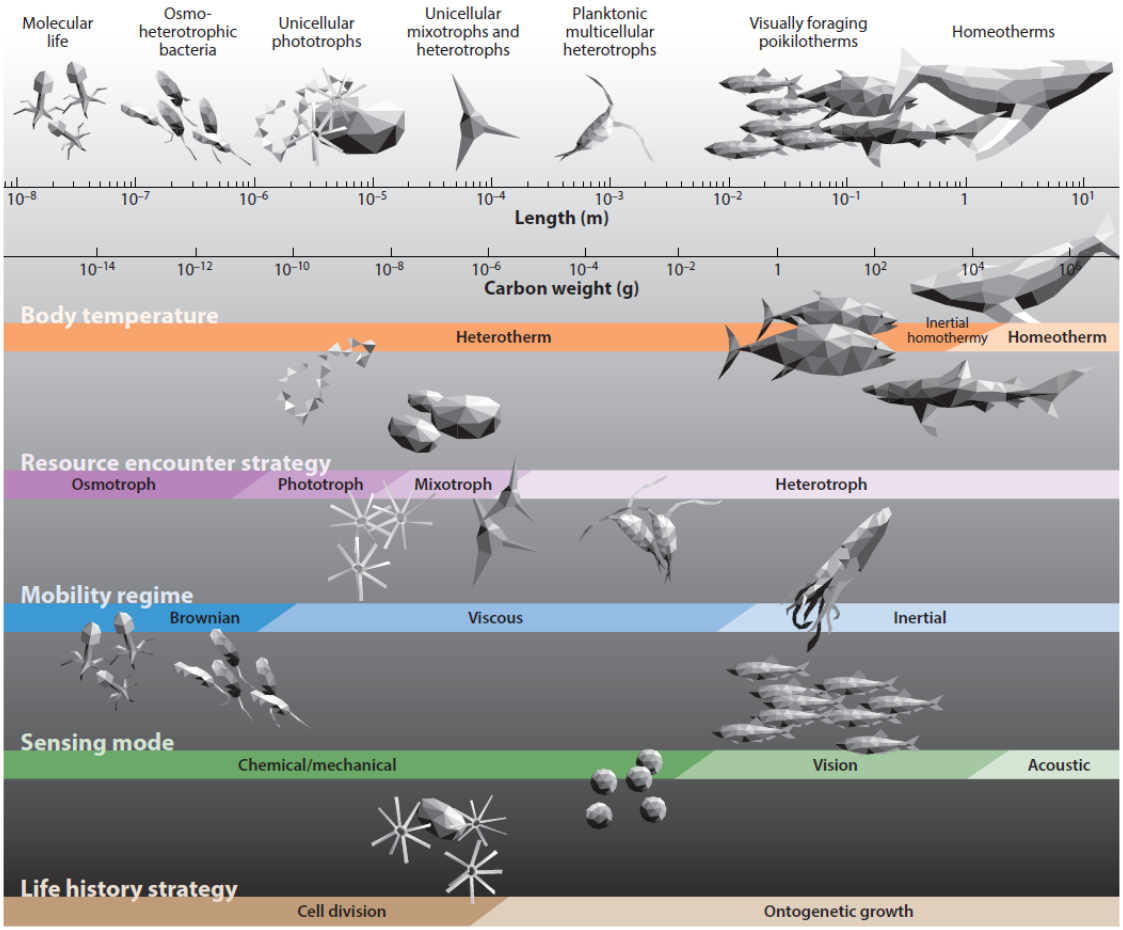

Figure 4.9: The five aspects of pelagic marine life examined in this paper: body temperature, resource encounter strategy, mobility regime, sensing mode, and life history strategy. Each aspect is illustrated in a horizontal bar, with the characteristic transitions indicated by changes in colour. The art at the top represents the seven realms of life as defined in this paper: molecular life (viruses), osmo-heterotrophic bacteria, unicellular phototrophs, unicellular mixotrophs and heterotrophs, planktonic multicellular heterotrophs (e.g., copepods), visually foraging poikilotherms (mainly teleosts, cephalopods, and cartilaginous fish), and homeotherms (cetaceans). Figure adapted from [4].

scaling laws and the corresponding transitions. Our study illustrates how size of an organism dictates the life strategies available to it, and thereby acts as an important factor in structuring the marine pelagic life in different realms (Figure 4.9).

4.6 Size structures sensory hierarchy in ocean life

Finally, we delve deeper into size based structuring of sensory strategies in the ocean. Survival in the open ocean requires effective collection of information from the surroundings via the use of various sensory modes. To fulfil their nutritional needs, organisms must scan a volume of water that is a million times their own body volumes per day [63]. While searching is a challenge in itself, there is also the continual risk of predation. Thus it is very beneficial for an organism to effectively gather information on the proximity of prey, mates and predators. We studied how this information collection using various sensing modes and the respective ranges depend on body size. There is at least some size-dependent hierarchy of sensory modes used in the pelagic ocean (open sea away from any boundaries). The smallest organisms such as free-swimming bacteria primarily use chemosensing, larger organisms such as copepods rely heavily on mechanosensing, and for even larger organisms such as fish and mammals, vision, hearing, and echolocation become prominent. How can we explain these trends based on the fundamental laws governing the working of these senses?

We investigated the working of five key senses - chemosensing, mechanosensing, vision, hearing, and echolocation. We identified the physiological constraints on sense organs, together with the physics of signal generation, transmission, and reception. From an analysis of these constraints, we found the minimum and maximum body sizes for the feasibility of these senses, as well as a size scaling of the corresponding sensing range for some of these senses. Our analysis revealed a hierarchy of sensing modes - with increasing size, a larger battery of sensory modes becomes available and the sensing range increases (Figure 4.10). Our theoretical predictions of lower and upper size limits for various senses aligned well with the size ranges found in the literature (Figure 4.10). Although the scaling analyses and the size limits are only first order estimates, this work forms the first comprehensive analysis of the size based structuring of sensory modes used by marine life.

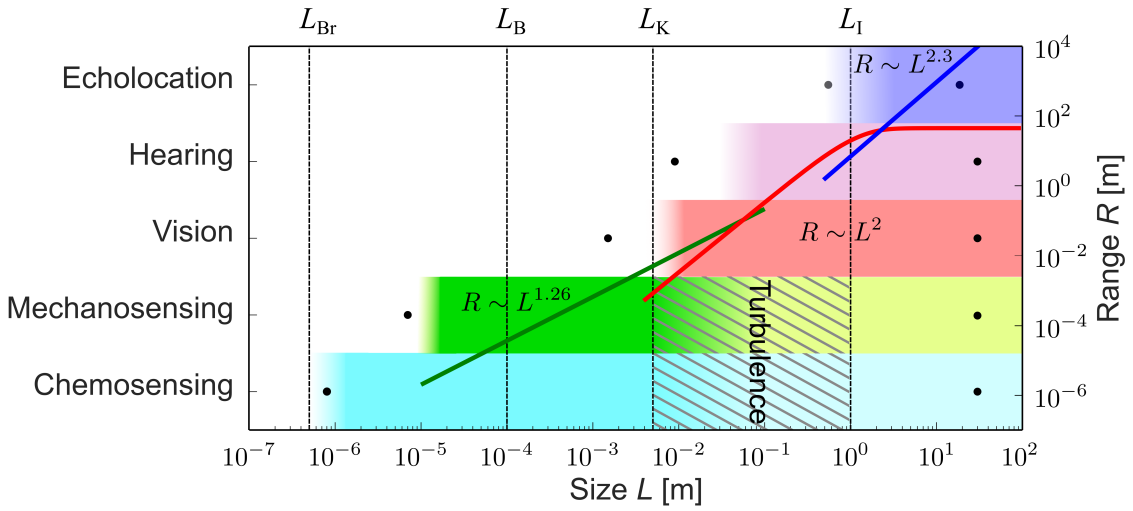

Figure 4.10: Upper and lower body size limits and ranges for different senses. Dots denote the largest and smallest organisms known to employ a given sense, and shaded rectangles show the theoretical estimates of the size range in which a sense is expected to work. The curves show the theoretical scaling of sensing range with size for mechanosensing (green), vision (red), and echolocation (blue), respectively.

Chapter 5

Hydrodynamics and energetics of jumping copepod nauplii and copepodids

Paper published in the Journal of Experimental Biology (2014)

© 2014. Published by The Company of Biologists Ltd | The Journal of Experimental Biology (2014) 217, 3085-3094 doi:10.1242/jeb.105676

RESEARCH ARTICLE

Hydrodynamics and energetics of jumping copepod nauplii and copepodids

Navish Wadhwa[1,*], Anders Andersen[1] and Thomas Kiørboe[2]

ABSTRACT

Within its life cycle, a copepod goes through drastic changes in size, shape and swimming mode. In particular, there is a stark difference between the early (nauplius) and later (copepodid) stages. Copepods inhabit an intermediate Reynolds number regime (between ~1 and 100) where both viscosity and inertia are potentially important, and the Reynolds number changes by an order of magnitude during growth. Thus we expect the life stage related changes experienced by a copepod to result in hydrodynamic and energetic differences, ultimately affecting the fitness. To quantify these differences, we measured the swimming kinematics and fluid flow around jumping *Acartia tonsa* at different stages of its life cycle, using particle image velocimetry and particle tracking velocimetry. We found that the flow structures around nauplii and copepodids are topologically different, with one and two vortex rings, respectively. Our measurements suggest that copepodids cover a larger distance compared to their body size in each jump and are also hydrodynamically quieter, as the flow disturbance they create attenuates faster with distance. Also, copepodids are energetically more efficient than nauplii, presumably due to the change in hydrodynamic regime accompanied with a well-adapted body form and swimming stroke.

KEY WORDS: Copepodids, Nauplii, Reynolds number, Swimming, Velocimetry, Energy dissipation

INTRODUCTION

Copepods are millimetre-sized crustaceans that are ubiquitous in both marine and freshwater aquatic systems. By some estimates, they are the most abundant metazoans in the oceans and form a vital part of the oceanic food web (Verity and Smetacek, 1996; Turner, 2004). Planktonic copepods are the dominant predator group for autotrophic and heterotrophic unicellular eukaryotes and a primary food source for higher trophic levels, such as planktivorous fish (Turner, 2004). As the biggest zooplankton group, copepods also provide an important link in the biogeochemical cycles. Thus, a good understanding of copepod ecology is essential for any attempt towards a holistic understanding of the aquatic ecosystems.

To feed, avoid predators and to find mates, a copepod must inevitably move through the water. However, there are costs associated with swimming, both in terms of energetic expenditures and in terms of predation risk, because fluid disturbances created by swimming copepods may signal their presence to rheotactic predators (Visser, 2001). Understanding and quantifying the trade-offs associated with fundamental activities, such as feeding and mate searching, allows predictions of optimal behaviours (Kiørboe and Jiang, 2013). Copepods inhabit an interesting intermediate Reynolds number range in between the low Reynolds number flows, which are dominated by viscous friction, characteristic of swimming microorganisms (Lauga and Powers, 2009), and the high Reynolds number flows, which are dominated by inertia, characteristic of larger organisms, such as swimming fish (Vogel, 1994). Previous studies involving intermediate Reynolds numbers have reported many interesting hydrodynamic phenomena, such as ciliary-to-flapping transition in molluscs (Childress and Dudley, 2004), change from viscous to inertial propulsion in ascidian larvae (McHenry et al., 2003) and rowing-to-flapping transition in a nymphal mayfly (Sensenig et al., 2009). Research on the hydrodynamics of swimming in adult copepods has revealed several important aspects of copepod locomotion, such as high swimming efficiency (Jiang and Kiørboe, 2011b), the formation of vortex rings (Yen and Strickler, 1996) and the resulting hydrodynamic camouflage (Jiang and Kiørboe, 2011a).

A little studied aspect of copepod swimming is the changes in hydrodynamic characteristics that take place during its development from egg to adult, a process associated with remarkable changes in size, morphology and swimming gait (Nybakken and Bertness, 2005). Copepods go through a number of intermediate developmental stages, each terminating with a moult. The first six stages are termed nauplius and the later six consist of five copepodid stages and the final adult form (Larink and Westheide, 2006). In many copepod species, both nauplii and adults swim in jumps, in which a quick power stroke is followed by a slow recovery stroke. In both nauplii and copepodids, swimming jumps involve a metachronal movement of the appendages and a simultaneous recovery (Andersen Borg et al., 2012; van Duren and Videler, 2003). The naupliar power stroke consists of the antennae moving backwards, followed by the antennules, both in a breaststroke-like fashion (Fig. 1A–F). In copepodids, the jumps are initiated by a downward movement of the first antennae, followed by a metachronal movement of the ventrally positioned swimming legs, which are all retracted together during the recovery stroke (Fig. 1G–L).

In this paper, we try to quantify the mechanistic changes experienced by a copepod during its life cycle, as it grows up from a nauplius to an adult. These changes are bound to affect the hydrodynamics of swimming and must have an effect on the Darwinian fitness of the organism. We consider the cost-side of swimming, i.e. the fluid disturbances generated and the energy expenditure. Specifically, we focus on the following questions: (i) how do the changes related to size and propulsion mode between the nauplii and copepodids affect the flow induced by the propulsion, (ii) how do the changes in flow structure affect the predation risk via the temporal and spatial attenuation of the induced disturbance and

[1]Department of Physics and Centre for Ocean Life, Technical University of Denmark, DK-2800 Kgs. Lyngby, Denmark. [2]National Institute for Aquatic Resources and Centre for Ocean Life, Technical University of Denmark, DK-2920 Charlottenlund, Denmark.

*Author for correspondence (nawa@fysik.dtu.dk)

Received 21 March 2014; Accepted 16 June 2014

The Journal of Experimental Biology

The Journal of Experimental Biology (2014) doi:10.1242/jeb.105676

List of symbols and abbreviations

b	scaling exponent for spacial decay of flow disturbance
C_d	drag coefficient
D	equivalent sphere diameter for an organism
F_d	drag force
L	body length
M	carbon mass of an organism
n	number of jumps
N	sample size
p	pressure
P	rate of viscous energy dissipation
PIV	particle image velocimetry
PTV	particle tracking velocimetry
r	distance from the organism
R	size of the disturbance
R_0	size of the disturbance at the end of the power stroke
Re	Reynolds number
Re_s	instantaneous Reynolds number
R_m	mass specific metabolic rate
S	area of influence
S_0	area of influence at the end of the power stroke
T	duration of the power stroke
T_{decay}	decay time scale
T_{end}	total duration of motion
T_{visc}	viscous time scale
U	maximum swimming velocity
U_t	flow velocity threshold
$\mathbf{v}$	flow velocity
v_f	flow velocity magnitude
V	instantaneous swimming velocity
W_{diss}	energy dissipation per jump
W_{drag}	useful work per jump
β	frequency parameter
ε_{ij}	rate of strain tensor
μ	dynamic viscosity
ν	kinematic viscosity
ρ	fluid density
ϕ	viscous dissipation function

(iii) how does it affect the cost of propulsion? To answer these questions, we make measurements of the velocity fields around the naupliar and copepodid stages of the copepod *Acartia tonsa* (Dana 1849), using particle tracking velocimetry (PTV) and particle image velocimetry (PIV). We show that the flow structures around nauplii and copepodids are fundamentally different and that copepodids are hydrodynamically quieter than nauplii. We also measure the viscous energy dissipation around the jumping copepods, and we show that the energetic efficiency of swimming is smaller for nauplii than for copepodids.

RESULTS

Flows created by jumping nauplii and copepodids

For a straight jump of a nauplius, the flow was approximately left–right symmetric with respect to the body axis at all times (Fig. 2). The insets in Fig. 2 correspond to the different stages of the jump shown in Fig. 1. Given the measurement noise, the dominant flow structure is hard to see at the beginning of the stroke (Fig. 2A,B), but in the later part of the power stroke, a strong circulation was seen on each side of the organism (Fig. 2C). The spatial extent of the structure was at its maximum at the end of the power stroke, when the antennules finished their beat (Fig. 2D). During the recovery stroke (Fig. 2E,F), the flow structure started dissipating and it had diminished considerably by the end of the recovery stroke, when the antennae and the antennules returned to their original positions. We observed qualitatively the same flow structure in all our observations, also when nauplii were swimming with the lateral side facing the camera. Thus, the observed flow structure, with its two regions of opposite circulation, is in fact a cross-section of a toroidal vortex ring. The axis of the ring was aligned with the swimming direction.

For copepodids, the observed flow structure was qualitatively different from that around nauplii. Instead of two, four regions of circulation were seen, two in the front and two in the wake of the organisms (Fig. 3). The same qualitative structure was observed in the dorsal and the lateral view, although we only included lateral view in our study because when viewed dorsally, copepods tended to jump out of the measurement plane. The copepodid jump thus resulted in two counter-rotating vortex rings (Fig. 3), one in the front and another in the wake of the organism. A strong backwards jet was observed towards the end of the power stroke (Fig. 3D).

The distinction between the flow structure around a jumping nauplius and a copepodid was consistent through the various development stages, as highlighted in Fig. 4, which shows the flow fields around differently sized nauplii and copepods at the end of the power stroke. The flow-fields around nauplii and copepodids were topologically different. While the nauplii had a single vortical structure around the body when they jumped, the copepodids had two of them.

Reynolds number versus frequency parameter

The flows due to swimming nauplii and copepodids are described by the Navier–Stokes equation and the continuity equation for a Newtonian and incompressible fluid:

$$\rho\left(\frac{\partial \mathbf{v}}{\partial t}+(\mathbf{v}\cdot\nabla)\mathbf{v}\right)=-\nabla p+\mu\nabla^2\mathbf{v}\,, \qquad (1)$$

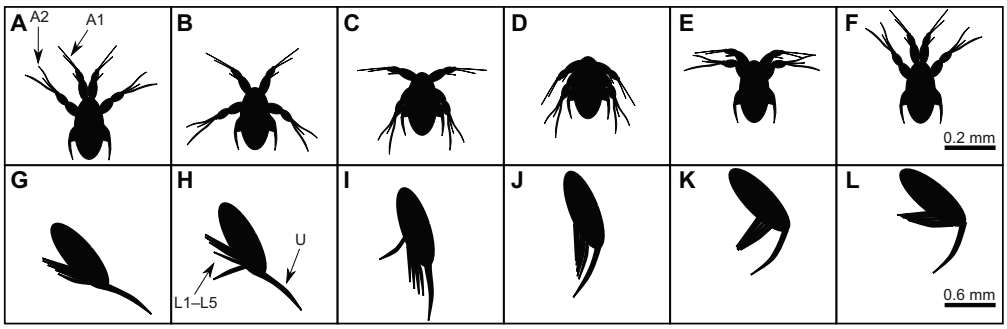

Fig. 1. Jumps of a nauplius and a copepodid. Series of snapshots showing the jump of a nauplius (A–F) and a copepodid (G–L). The first four panels in both rows show the power stroke, and the last two show the recovery stroke. The *Acartia tonsa* nauplius uses its antennules (A1) and antennae (A2) for propulsion (Andersen Borg et al., 2012). The copepodid uses its swimming legs (L1–L5) for propulsion and the urosome (U) for steering (Kiørboe et al., 2010). Copepodids have a variable number of pairs of swimming legs, and the final adult stage is shown here. The feeding appendages and the antennae are not shown for clarity.

The Journal of Experimental Biology

The Journal of Experimental Biology (2014) doi:10.1242/jeb.105676

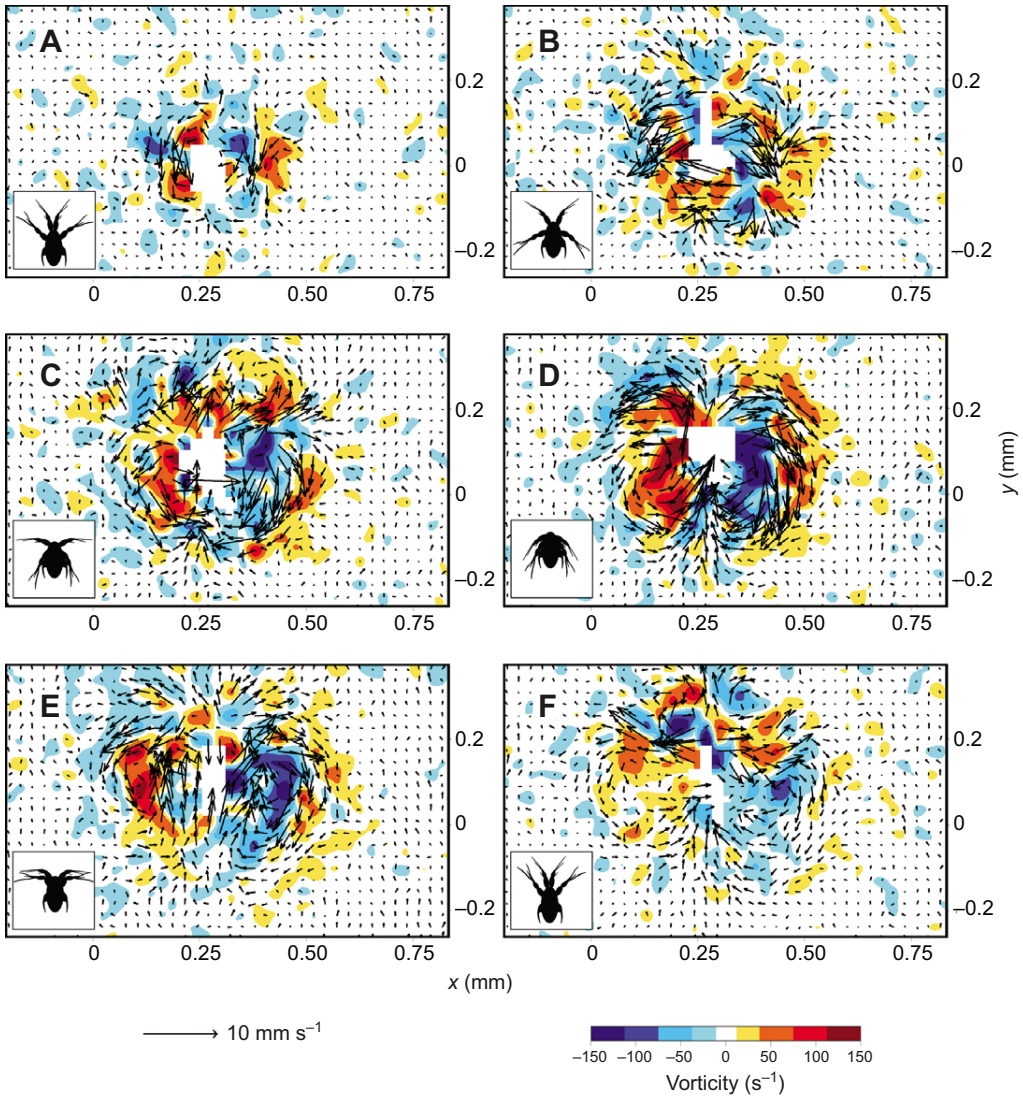

Fig. 2. Time series of the flow fields around a jumping nauplius. L=0.24 mm, T=7.5 ms, U=33.7 mm s^{-1}, β=7.4, Re=7.7. The position of the appendages is shown in the insets and correspond to the stages in Fig. 1. The arrows represent velocity vectors and the colours vorticity, with warm colours for counter-clockwise rotation and cool colours for clockwise rotation. (A–D) A toroidal vortex ring forms during the power stroke, and the maximum velocity is attained. (E,F) During the recovery stroke, the vortex ring is dissipated. Also see supplementary material Movie 1.

$$\nabla \cdot \mathbf{v} = 0\,, \tag{2}$$

where $\mathbf{v}$ is the velocity field, p is the pressure field, ρ is the fluid density and μ is the dynamic viscosity. The governing equations can be written in dimensionless form by introducing dimensionless variables:

$$\hat{\mathbf{x}}=\frac{\mathbf{x}}{L},\quad \hat{t}=\frac{t}{T},\quad \hat{\mathbf{v}}=\frac{\mathbf{v}}{U},\quad \hat{p}=\frac{Lp}{\mu U}\,, \tag{3}$$

where L is the characteristic length scale, T the characteristic time scale and U the characteristic velocity scale. Using the dimensionless variables, we can write the governing equations:

$$\beta\frac{\partial\hat{\mathbf{v}}}{\partial\hat{t}}+Re(\hat{\mathbf{v}}\cdot\hat{\nabla})\hat{\mathbf{v}}=-\hat{\nabla}\hat{p}+\hat{\nabla}^2\hat{\mathbf{v}}\,, \tag{4}$$

$$\hat{\nabla}\cdot\hat{\mathbf{v}}=0\,, \tag{5}$$

where we have defined the two dimensionless parameters:

$$\beta=\frac{L^2}{\nu T}\,, \tag{6}$$

$$Re=\frac{LU}{\nu}\,. \tag{7}$$

Here, ν is the kinematic viscosity defined as ν=μ/ρ. The parameter β is often referred to as the frequency parameter (Pozrikidis, 2011) and Re is the Reynolds number. To describe the swimming nauplii and copepodids, we used body length as the characteristic length scale L, the duration of the power stroke as the characteristic time scale T and the maximum swimming velocity during a jump as the characteristic velocity scale U. It is natural to regard the frequency parameter β as characterizing the motion of the swimming appendages during the power stroke, and to think of the Reynolds number Re as describing the resulting swimming motion (Childress and Dudley, 2004).

The Re and β data for nauplii and copepodids (Fig. 5; Table 1) segregated into two distinguishable groups – nauplii at lower values of both β and Re, and copepodids at higher values of β and Re. At low Reynolds numbers, swimming velocity is proportional to the swimming appendage speed, resulting in a direct proportionality between β and Re (Lauga and Powers, 2009). In the case of nauplii, there was indeed a strong one-to-one relationship between β and Re (Fig. 5, inset). A straight line fit of nauplii data forced through the origin (solid line) had a slope of 1.09±0.06 (95% confidence interval). A linear fit between β and Re for copepodids (dashed line) had a slope of 1.75±0.59, higher than that for nauplii data.

The Journal of Experimental Biology (2014) doi:10.1242/jeb.105676

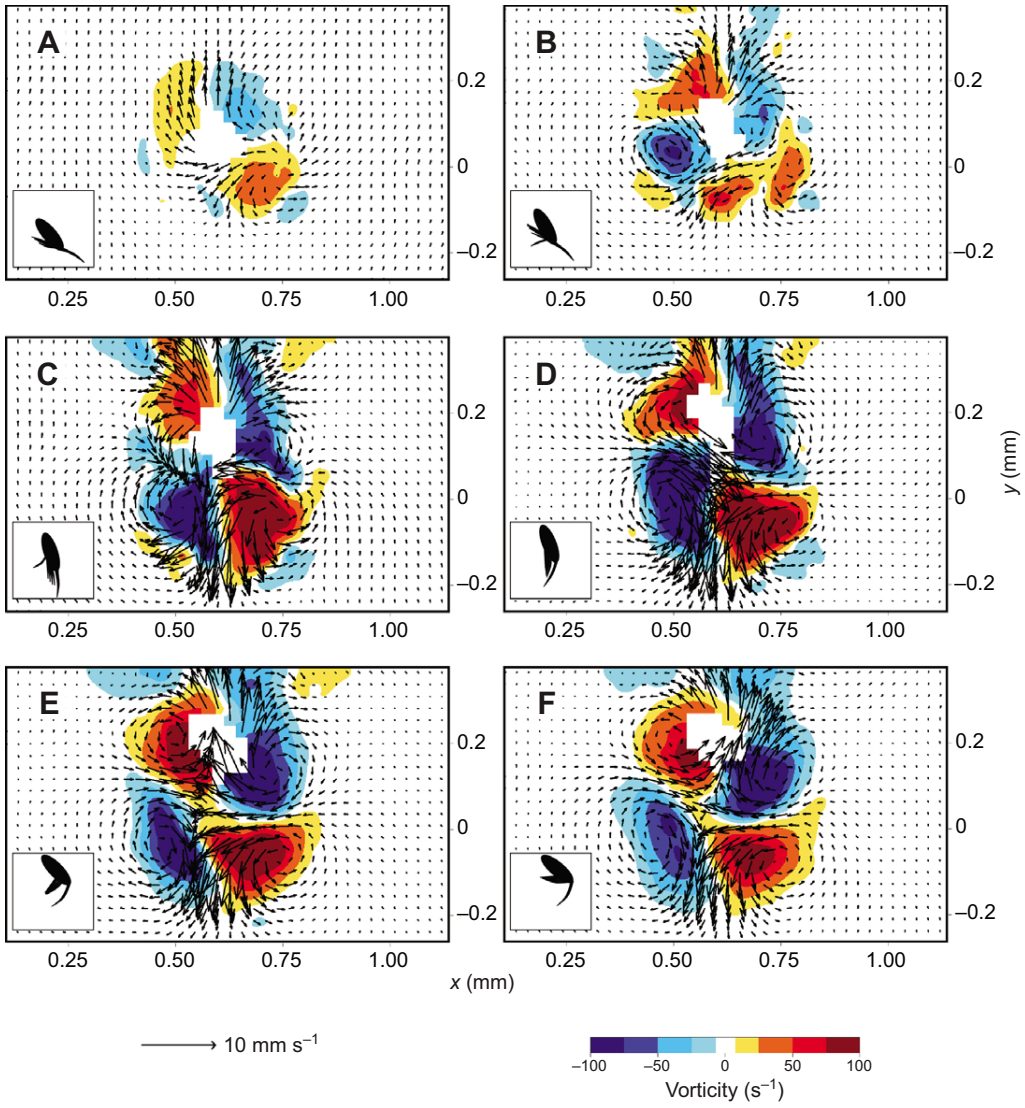

Fig. 3. Time series of the flow fields around a jumping copepodid. L=0.33 mm, T=5 ms, U=61.1 mm s^{-1}, β=18.6, Re=19.1. The position of appendages is shown in the insets and correspond to the stages in Fig. 1. The arrows represent velocity vectors and the colours vorticity, with warm colours for counter-clockwise rotation and cool colours for clockwise rotation. (A–D) Power stroke and (E,F) recovery stroke. Two vortex rings are formed during the jump. Also see supplementary material Movie 2.

Temporal evolution of the fluid disturbance

To characterize the extent of the disturbance created by the copepod, we measured the area of the region around the organism where the velocity exceeded a threshold U_t. We call this area the area of influence S and the characteristic size of the disturbance $R=\sqrt{S}$. In order to quantify how the fluid disturbance grew and decayed in time, we measured S as a function of time t (Fig. 6A). We chose U_t=1 mm s^{-1} so that we were able to measure large enough values of S that they were above the noise level. We then measured the time it takes for S at the end of the power stroke to decay to one-fifth of its value and called it the decay time scale T_{decay} (Fig. 6A). Any disturbance imparted to the fluid is diffused by the effect of viscosity, and the time scale over which this happens is the viscous time scale $T_{visc}=L^2/4\nu$, where L is the characteristic length, the body length in the present case. We compared the measured T_{decay} with T_{visc} and found a one to one correspondence between the two (Fig. 6B).

For nauplii, the disturbance was short lived (10–20 ms), whereas it lasted much longer for the copepodids (20–120 ms). In spite of the significant difference in size, the power stroke duration for nauplii and copepodids was comparable (Table 1). But the viscous decay of the flow was much slower in copepodids owing to their larger size. As a result, the copepodid vortex rings last much longer, even after the recovery stroke, in contrast to those formed by nauplii.

Spatial decay of the fluid disturbance

The spatial extent of the flow disturbance can be quantified by analysing how the size of disturbance R changes with the threshold velocity U_t. Power laws have often been used to describe the attenuation of flow fields generated by swimming organisms (Catton et al., 2007; Jiang and Kiørboe, 2011a; Murphy et al., 2012; Jiang and Kiørboe, 2011b; Visser, 2001; Guasto et al., 2012). To compare our observations with the existing models, we looked for a power law scaling of flow velocity with distance. If $R \sim U_t^{-b}$, then by rearranging the terms, we can find the change in the flow velocity magnitude v_f with distance r from the organism as $v_f \sim r^{-1/b}$.

We measured the size of the fluid disturbance R_0 at the end of the power stroke for different values of U_t ranging between 0.5 mm s^{-1} and 30 mm s^{-1}. Fig. 7A shows the plot of R_0 versus U_t for 50 jumps. At very high values of U_t, the plots plateaued, as the measured area of influence was just the area covered by the organism and the fluid velocity did not exceed U_t anywhere. At the lower end, the measurements were influenced by the background noise. For intermediate values of U_t, the curves can be approximated by a

The Journal of Experimental Biology (2014) doi:10.1242/jeb.105676

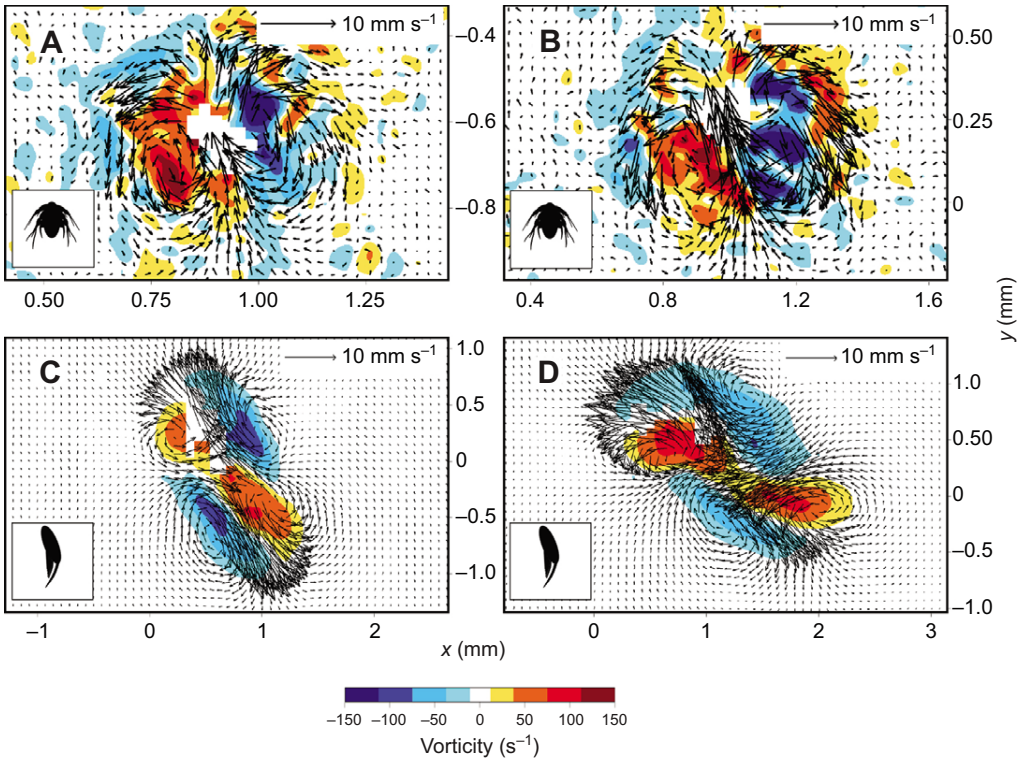

Fig. 4. Snapshots of the flow fields around jumping nauplii and copepodids of different sizes at the end of their power stroke. (A) Small and (B) large nauplii and (C) small and (D) large copepodids. (A) L=0.17 mm, T=7 ms, U=31.1 mm s^{-1}; (B) L=0.26 mm, T=6.5 ms, U=40.5 mm s^{-1}; (C) L=0.55 mm, T=11 ms, U=84.9 mm s^{-1} and (D) L=0.77 mm, T=18.5 ms, U=71.0 mm s^{-1}. The flow structures caused by different sized nauplii are qualitatively similar, with a single toroidal vortex ring, and different from that caused by copepodids, which form two vortex rings.

power law, although it should be kept in mind that the curves are not exactly straight lines on the log–log plot. We selected the range of U_t between 1 mm s^{-1} and 5 mm s^{-1} for calculation of the scaling exponent b, (Fig. 7A, shaded). Fig. 7B shows a scatter plot of b versus β for both nauplii and copepodids. b decreased with β, with a sharp contrast between nauplii and copepodids (Table 2), signifying a faster decay for copepodids than for nauplii.

Energy dissipation

We measured the rate of viscous energy dissipation P around the jumping nauplii and copepodids (Fig. 8A). P grew as the organism accelerated, peaked around the end of the power stroke, and then decayed back to the background level. By integrating the dissipation rate over time, we estimated the total energy dissipated in the fluid. Fig. 8B shows a plot of the energy dissipation per jump W_{diss} (Eqn 13, see Materials and methods) versus β for both nauplii and copepodids. W_{diss} for a nauplius was of the order of 10^{-11} J (Fig. 8B, inset), whereas W_{diss} for a copepodid depended strongly on β and was of the order of 10^{-10} J.

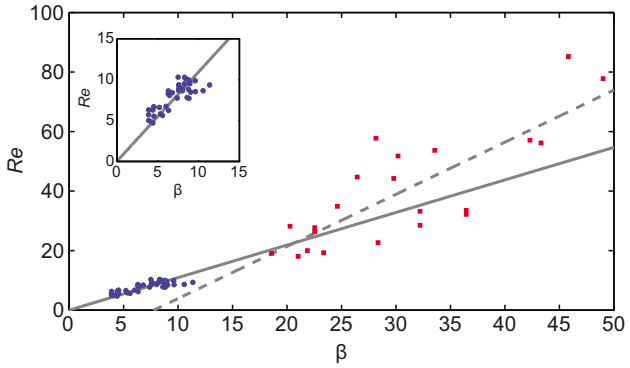

Fig. 5. *Re* versus β for nauplii jumps (blue circles) and copepodid jumps (red squares). The solid line is a straight line fit to the nauplii data (slope=1.09±0.06, R^2=0.38, forced through the origin). The inset shows a zoom on the nauplii data. The dashed line is the best fit for the copepodid data (slope=1.75±0.59, R^2=0.66, *Re*-intercept=–13.6±18.6). Nauplii and copepodid data form two groups, which clearly separate from each other on both the axes (Table 1).

DISCUSSION

Flow field structure

Flow velocimetry has previously been employed to measure the flows around adult copepods (Jiang and Kiørboe, 2011a; Murphy et al., 2012; van Duren et al., 2003). Here, for the first time, we have extended the use of these techniques to measure the flows caused by nauplii. The measured velocity fields showed that the flows induced in the vicinity of a jumping nauplius and a copepodid are qualitatively different from each other (Fig. 4). The induced flow around a nauplius consists of a single vortex ring, in contrast to the two counter-rotating vortex rings observed around copepodids, and this distinction is independent of the finer details of the flow or how well formed the respective flow structures are. The flow structure

Table 1. Quantities measured from kinematic analysis of videos

	Nauplius		Copepodid	
	Mean	Range	Mean	Range
N	41	n.a.	22	n.a.
L (mm)	0.22	0.17–0.26	0.48	0.33–0.77
T (ms)	6.8	5.5–8.5	7.8	3.5–18.5
U (mm s^{-1})	37.4	28.5–46.1	83.9	57.1–129.0
β	7.0	3.9–10.3	30.4	18.6–49.0
Re	7.9	4.7–10.3	39.6	18.0–85.2

L, T and U are the body length, power stroke duration and maximum swimming velocity, respectively. β is the frequency parameter and *Re* is the Reynolds number.

The Journal of Experimental Biology (2014) doi:10.1242/jeb.105676

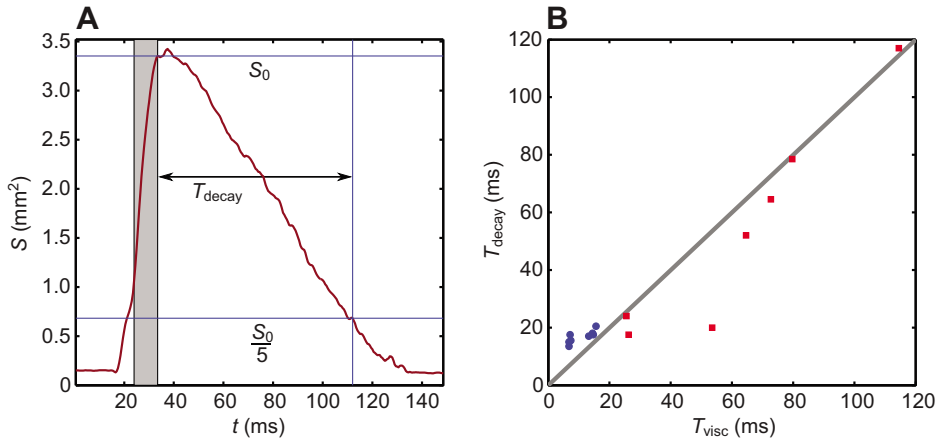

Fig. 6. Time scales associated with a jump. (A) Evolution of the area of influence S with time t for a copepodid (L=0.58 mm, T=9.5 ms, U=97.4 mm s^{-1}). The shaded area represents the power stroke starting with the movement of the swimming legs. The decay time T_{decay} is measured from the end of the power stroke to the instant when S has decreased to a fifth of its value S_0 at the end of the power stroke. (B) Decay time T_{decay} versus the viscous time scale T_{visc}. Blue circles are for nauplii data (N=8) and red squares are for copepodids (N=7). The straight line represents a one to one relationship.

around jumping copepodids is similar to the flow structure observed around adults in this and in other species (Jiang and Kiørboe, 2011a; Murphy et al., 2012; Yen and Strickler, 1996).

The difference between the nauplii and copepodids could either be due to the differences in morphology and propulsion mechanism, or due also to the hydrodynamical difference in the relative importance of viscosity and inertia. The nauplii flow pattern results from a combination of forces acting on the fluid in different directions – the appendages pushing the fluid backwards on each side of the body, and the drag acting on the body pushing the fluid forward. This force configuration is typical for breaststroke swimmers. In copepodids, by contrast, all propulsive forces are applied in one region by the swimming legs pushing the fluid backwards, while the drag on the body pushes the fluid forward. Owing to higher inertia in copepodids than in nauplii, viscosity does not diffuse the momentum away, and the fluid rolls up into vortices both in the front of the organism and in the wake, leading to the two vortex rings observed (Jiang and Kiørboe, 2011a).

The linear relationship between β and Re for nauplii (Fig. 5) suggests that the velocity and frequency scale for nauplii jumps are linearly related through the size of the organism. Even though the values of Re for nauplii are larger than unity, the proportionality expected from low Reynolds number swimming still holds to a large extent. A slope of ~1 indicates that a nauplius moving at peak velocity covers approximately one body length per power stroke, irrespective of the size and developmental stage. In the case of copepodids, the slope was 1.75, which shows that the copepodids cover more body lengths in each jump than the nauplii do. The slope of the Re–β plot is equal to UT/L, i.e. the inverse of the Strouhal number. The value for T was not significantly higher in copepodids than in nauplii (Table 1). Thus, the higher slope for copepodids, in spite of higher L, is mainly due to their higher swimming velocity U, showing that they are more effective swimmers than nauplii.

Decay of the flow disturbance

The fluid disturbance caused by the jump of a nauplius or a copepodid determines the predation risk associated with their

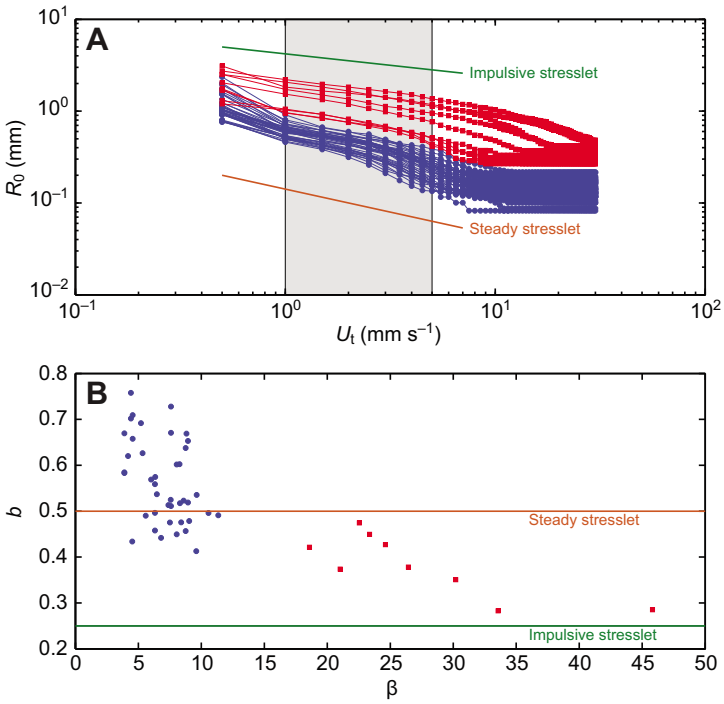

Fig. 7. Spatial decay of the fluid disturbance. (A) Size of the fluid disturbance R_0 measured at the end of the power stroke, versus U_t. Blue lines with circles are for nauplii data (N=41) and red lines with squares are for copepodids (N=9). The part of the plot used for power law fits is shaded in grey. The green and orange lines have scaling exponents equal to those of an impulsive stresslet (b=1/4) and a steady stresslet (b=1/2), respectively. (B) Scaling exponent b for the curves in A plotted against the frequency parameter β. Blue circles are for nauplii and red squares for copepodids.

The Journal of Experimental Biology (2014) doi:10.1242/jeb.105676

Table 2. Quantities measured from the flow fields

	Nauplius			Copepodid		
	N	Mean	Range	*N*	Mean	Range
T_{decay} (ms)	8	16.8	13.5–20.5	7	53.4	17.5–117
T_{visc} (ms)	8	10.8	6.8–15.6	7	62.4	25.6–114.5
Spatial decay exponent, *b*	41	0.56	0.41–0.75	9	0.38	0.28–0.47
W_{diss} (10^{-11} J)	12	3.77	2.56–5.35	7	20.6	1.2–66.9
W_{drag} (10^{-11} J)	12	0.95	0.53–1.42	7	19.3	2.2–70.2

T_{decay} and T_{visc} are the measured decay time scale of the flow disturbance and the viscous time scale, respectively. *b* is the exponent for spatial decay of the velocity field. W_{diss} is the energy dissipated in the fluid per jump, and W_{drag} is the useful work done against the drag force.

locomotion. Most rheotactic predators respond to disturbances exceeding only a certain threshold velocity (Kiørboe and Visser, 1999). The spatial and temporal decay rate is an important feature of the disturbance, which determines how far and for how long the organism stays vulnerable. We found that the temporal decay of the disturbance was controlled by the viscous time scale dictated by the size of the organism. At the small spatial scales involved, viscous diffusion acts as the main process responsible for the decay of fluid motion. The viscous time scale varies with the square of the length scale. As the nauplii have a body size much smaller than the copepodids, the disturbance created by them is dissipated much faster than that by the copepodids (Fig. 6; Table 2).

The spatial decay of the disturbance is characterized by the exponent of the power law used to describe the disturbance. The rate of decay and hence the exponent is different in the case of nauplii and copepodids (Fig. 7). The smaller magnitude of *b* for copepodids than for nauplii implies a faster decay of velocity with distance from the organism, as $v_f \sim r^{-1/b}$.

The exponent for the decay allows us to compare it with the idealized singularity models (Table 3), which are often used to model the flows generated by organisms swimming at low Reynolds numbers (Jiang and Kiørboe, 2011a; Jiang and Kiørboe, 2011b; Visser, 2001; Guasto et al., 2012; Murphy et al., 2012; Catton et al., 2007; Drescher et al., 2011). For example, a continuously moving free-swimming organism at low Reynolds number is often represented by a steady stresslet, which consists of two equal magnitude forces acting on the fluid in opposite directions, a small distance away from each other (Guasto et al., 2012; Visser, 2001). Also, unsteady jumps of adult copepods have been modelled using an impulsive stresslet model, in which the two forces act impulsively on the fluid (Jiang and Kiørboe, 2011a; Murphy et al., 2012). The range of *b* measured for the nauplii is comparable with the steady stresslet model, given the experimental variability and noise in the data. This suggests that the unsteadiness of the motion may be less important in case of nauplii and that the flow behaves in a more quasi-steady fashion, probably because of their small size and correspondingly small values of the frequency parameter β. In contrast, the values of *b* for copepodids approach the value expected for an impulsive stresslet, especially at higher values of β, emphasizing the unsteady nature of the jump.

The range of data available for curve fitting (Fig. 7A) was too small to draw strong conclusions about the exact model capturing the decay, but the relative difference between nauplii and copepodids is clear (Fig. 7B). We note that the comparison of nauplii swimming with a steady stresslet is limited to the far field spatial decay of the flow velocity, because the observed toroidal flow structure is incompatible with a steady stresslet. It is possible that the nauplius flow field is a combination of fundamental singularities

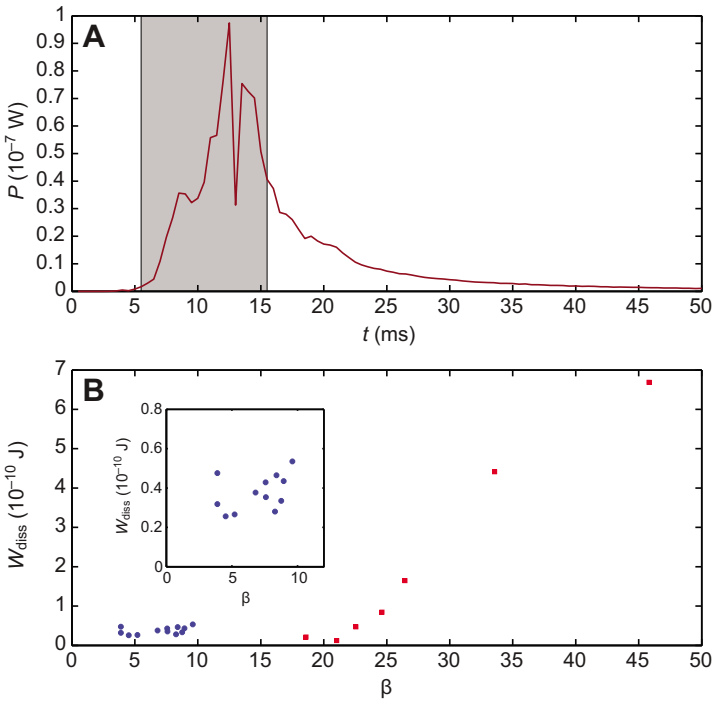

Fig. 8. Viscous energy dissipation during a copepod jump. (A) Energy dissipation rate *P* around a copepodid as a function of time *t* (*L*=0.69 mm, *T*=10 ms, *U*=129.0 mm s^{-1}). The shaded area represents the power stroke starting with the movement of the swimming legs. (B) Dissipation per jump W_{diss} versus β for nauplii (blue circles, *N*=12) and copepodids (red squares, *N*=7). The inset shows a zoom on the nauplii data.

The Journal of Experimental Biology (2014) doi:10.1242/jeb.105676

Table 3. The spatial decay exponent, *b*, measured for nauplii and copepodids, compared with idealized point force models

	Nauplii	Copepodids	Steady stresslet	Impulsive stresslet
b	0.56 (0.41–0.75)	0.38 (0.28–0.47)	1/2	1/4

and that the near field flow structure is dominated by other singularities, which decay faster with distance than a stresslet, resulting in the far field decay being described solely by a stresslet. Other factors, such as the complex shape of the organism and intermediate Reynolds numbers, might also make a pure stresslet model incompatible with the observations, motivating the development of new and more realistic models.

Energy budget

To compare the energy expenditure on swimming to the metabolic budget of the copepod, we used the metabolic rate scaling for calanoid copepods given in terms of the carbon mass as $R_m=3.46M^{-0.22}$, where R_m is the mass specific metabolic rate in $mlO_2\ mgC^{-1}\ h^{-1}$ and M is the mass of the organism in mgC (Kiørboe and Hirst, 2014). The carbon mass of nauplii varies between 30 and 250 ngC so we use a value of 100 ngC to get an order of magnitude estimate (Berggreen et al., 1988). Using an oxycalorific value of 13.8 J mgC^{-1}, we got a metabolic rate of 1.44×10^{-5} W for nauplii. With this metabolic rate, the energy budget of a nauplius over the duration of a typical jump (10 ms) is of the order of 10^{-7} J. Thus, the energy spent by a nauplius on swimming (~10^{-11} J) is approximately four orders of magnitude smaller than the metabolic budget. The same conclusion is applicable to copepodids, for which the swimming and metabolic budgets are of the order of 10^{-10} J and 10^{-6} J, respectively.

Many previous studies have made the same conclusion, for a range of swimming organisms, such as copepods (van Duren et al., 2003; Vlymen, 1970) and protists (Crawford, 1992). However, the above estimate does not take into account the losses involved at the different stages of energy conversion, which might have a significant effect on the net cost of propulsion. This could explain the observations made previously on copepods and larger crustaceans, which showed a significant increase in the metabolic rate of the organism during locomotion activity (Halcrow and Boyd, 1967; Torres and Childress, 1983; Svetlichny and Hubareva, 2005; Buskey, 1998). High propulsion costs would drive evolution towards optimizing swimming, something that has been proposed for other organisms (Spagnolie and Lauga, 2011; Tam and Hosoi, 2011).

Propulsion efficiency

Another interesting aspect of the energy expenditure of nauplii and copepodids is the efficiency of swimming. The conventional measure of efficiency is the so-called Froude efficiency $\eta_F=W_{drag}/W_{diss}$, which compares the total swimming work done by an organism W_{diss}, to the useful part of the work W_{drag}, which is done by the thrust forces against the drag on the organism. To estimate W_{drag}, we approximated the copepod with a sphere moving through water with the same kinematics as the real organism. An alternative approximation of a copepod body as a prolate spheroid results only in small quantitative differences, and for simplicity we chose the sphere approximation. We used the width of the copepod at the thickest part of the prosome as the diameter of the sphere, D, calculated from the body length L using the aspect ratios of 0.5 and 0.38 for nauplii and copepodids, respectively (Kiørboe et al., 2010; Andersen Borg et al., 2012). We thus modelled the drag (F_d) on the copepod using the quasi-steady expression,

$$F_d=\frac{1}{2}\pi\rho C_d\left(\frac{D}{2}\right)^2 V^2, \quad (8)$$

where V is the instantaneous swimming velocity. Following Lautrup (Lautrup, 2005), the drag coefficient (C_d) depends on the instantaneous Reynolds number for the sphere, $Re_s=DV/\nu$, as:

$$C_d=\frac{24}{Re_s}+\frac{5}{\sqrt{Re_s}}+0.4. \quad (9)$$

W_{drag} is calculated by integrating the drag power F_dV over the whole duration of motion, divided by the number of jumps. Fig. 9 compares W_{drag} to the energy dissipation per jump W_{diss}. The straight line in Fig. 9 represents a one to one proportionality and corresponds to 100% Froude efficiency described above. The data for copepodids were close to the 100% line (Fig. 9A), whereas those for nauplii were all much below the line (Fig. 9B). The value of the Froude efficiency for copepods was 1.19±0.40. Our measurements validate the predictions made from computational fluid dynamics calculations that the copepod jumps have a high Froude efficiency (Jiang and Kiørboe, 2011b). In comparison, the Froude efficiency for nauplii was 0.26±0.08. Thus, nauplii are energetically much less efficient in propulsion than the copepodids. Copepods swim at Reynolds numbers several orders of magnitude higher than that of most micro-organisms, and consequently, the swimming efficiency of both nauplii and copepodids was much higher than what has been predicted and measured for micro-organisms (Guasto et al., 2012). The dissipation is likely to have been underestimated due to the limited resolution of the PIV data, so the actual Froude efficiency is presumably less than that calculated here.

This way of calculating the efficiency requires one to be able to unambiguously separate the swimming forces into thrust and drag, which is often not possible for organisms swimming at intermediate or high Reynolds numbers. Even at low Reynolds numbers, where drag and thrust are unambiguously distinguishable, the above

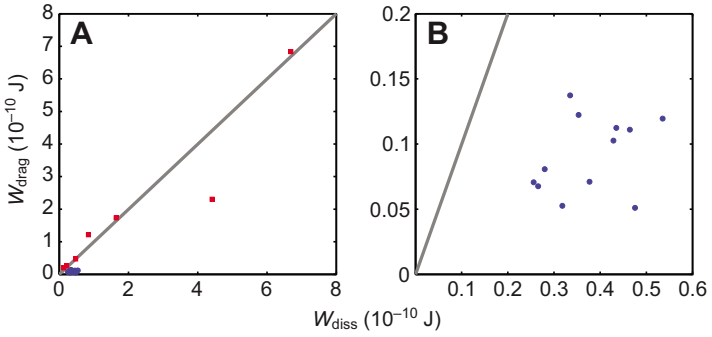

Fig. 9. Propulsion efficiency. (A) The useful work W_{drag} done in overcoming drag versus the dissipation per jump W_{diss} for nauplii (blue circles, N=12) and copepodids (red squares, N=7). The straight line represents W_{drag} = W_{diss}, corresponding to 100% Froude efficiency. (B) A zoom on the nauplii jump data.

The Journal of Experimental Biology (2014) doi:10.1242/jeb.105676

mentioned efficiency remains an ill-defined concept and can take arbitrarily large values (Childress, 2012; Leshansky et al., 2007). Thus, one needs to be careful when interpreting the Froude efficiency. Nevertheless, the above calculations demonstrate a significant difference between nauplii and copepodids.

It has been suggested that the nauplii have a body shape that is optimized for swimming at Reynolds number around unity (Andersen Borg et al., 2012). But this optimality in body shape changes with increase in size and a corresponding increase in the Reynolds numbers, and a more elongated body is preferred. It appears that the copepodid body plan and swimming stroke are also well suited for its physical environment and allow it to achieve a higher swimming efficiency. Thus, the hydrodynamic changes associated with changing size might explain the stark physical differences between nauplii and copepodids.

The breaststroke swimming gait used by copepod nauplii studied here is common among many aquatic organisms of diverse taxa and sizes, but its hydrodynamics are not well understood, and physically realistic models are needed. It is important that any such models capture the flow close to the organism, because the dominant flow structures and energy dissipation are observed here. We hope that the measurements presented here can be used for developing accurate intermediate Reynolds number models for flows around nauplii and copepodids.

MATERIALS AND METHODS

Experimental set-up

Copepods *Acartia tonsa* were cultured at 18°C. Before experiments, we transferred the copepods to the test aquarium that contained filtered sea water. We added only a few individuals to the aquarium in order to avoid any interaction between them. All experiments were conducted in a glass cuvette (1×1×4 cm) placed on a horizontal translation stage, at room temperature between 18°C and 20°C.

A vertical plane within the cuvette, orthogonal to the camera view, was illuminated by an infrared pulsed laser (808 nm wavelength) (Oxford Lasers Ltd, Oxon, UK) with a 150 µm thick light sheet. We used a Phantom v210 high-speed digital video camera (Vision Research, Inc., Wayne, New Jersey, USA), at a frame rate of 2000 frames s^{-1} and a resolution of 1280×800 pixels. The laser and the camera were synchronised. The camera was fitted with an inverted 20 mm focal length lens (Nikon Corporation, Tokyo, Japan) and a magnifying bellows tube to achieve a field of view ranging between 3.0 and 20.5 mm^2.

For PTV and PIV seeding, we prepared a suspension of TiO_2 particles by suspending a small amount of TiO_2 powder in ethanol and diluting it with filtered sea water, followed by treatment with ultrasound for 1 h, yielding particles smaller than 2 µm (Riisgård et al., 2011). We then added a small amount of the suspension to the aquarium to achieve an appropriate seeding density. The organisms were not affected by the presence of infrared light or seeding particles.

Kinematic analysis

Using the MATLAB-based image analysis software DLTdv5 (Hedrick, 2008), we digitized two ends of the prosome in order to measure the body size (L) and to establish the length axis. The mid-point of these two points was used for calculating the swimming velocity using a finite difference scheme. We smoothed the velocity data using a Savitzky–Golay smoothing filter (Savitzky and Golay, 1964). For each jump, we measured the duration of the power stroke (T). For nauplii, T was taken to be the time from the beginning of antennae movement to the end of the downward motion of the antennules. For copepodids and adults, acceleration started with movement of the antennae, but the main thrust was produced by the swimming legs. Thus, we measured T as the time taken for the backward motion of the swimming legs. A total of 63 jumps were analysed (Table 1), out of which 50 were used for further calculations based on flow fields. The rest were not used for flow field calculations due to misalignment between the plane of the laser sheet and the centreline of the copepod body.

Velocimetry

We used PTV for measuring the flows created by nauplii and PIV for the flows around copepodids (Raffel, 2007). For both, we used the software Davis (LaVision GmbH, Göttingen, Germany) for capturing and analysing the recordings. In PIV analyses, we used a multi-pass algorithm with decreasing size of the interrogation windows, with a final window size of 32×32 pixels with a 50% overlap. We used an algorithmic mask, consisting of a sliding averaging of the intensity values followed by thresholding to remove those pixels from the analysis that corresponded to the organism. The process of masking made it impossible for us to measure the flows right next to the organism, especially around the swimming appendages. We adjusted the masking parameters for each recording to minimize the loss of useful data. After every pass of the processing and during post-processing, we removed outlying velocity vectors using a median filter and de-noising.

We used a combined PIV+PTV method for the flow field measurements around jumping nauplii. A coarse grid (64×64 pixels) PIV calculation was used as the initial guess for the PTV. The velocity field obtained from PTV was passed through a median filter followed by de-noising. We then converted the resulting vector field to a grid with window size 16×16 pixels to achieve the same vector density as that in the PIV calculations described above.

Energy dissipation

For any swimming organism, all the energy supplied to the fluid eventually dissipates as heat, which is due to viscosity. For an incompressible Newtonian fluid, the rate of strain tensor, ε_{ij}, and the rate of viscous energy dissipation per unit volume, ϕ, called the viscous dissipation function, are given as (Batchelor, 1967):

$$\varepsilon_{ij} = \frac{1}{2}\left(\frac{\partial v_i}{\partial x_j} + \frac{\partial v_j}{\partial x_i}\right), \tag{10}$$

$$\phi = 2\mu\varepsilon_{ij}\varepsilon_{ij}. \tag{11}$$

The total energy dissipation rate P in a volume V is found by integrating ϕ over the volume,

$$P = \int_V \phi \mathrm{d}V. \tag{12}$$

In a series of n jumps, the energy supplied to the fluid by the copepod per jump (W_{diss}) is found by integrating P over the whole duration of motion (T_{end}) and dividing by the number of jumps,

$$W_{diss} = \frac{1}{n}\int_0^{T_{end}} P \mathrm{d}t. \tag{13}$$

We assume that the flow field is rotationally symmetric about the direction of jump and use a cylindrical polar coordinate system, such that the z-axis is aligned with the direction of swimming at peak velocity of the organism. The assumption of rotational symmetry is invalid in the close vicinity of the organism, as the body plan and swimming strokes are clearly not rotationally symmetric, but it allows us to integrate over the entire volume around the organism to include the observed vortex rings. For a rotationally symmetric flow, in the absence of swirl about the symmetry axis, the viscous dissipation function ϕ can be written in cylindrical polar coordinates as (Batchelor, 1967):

$$\phi = \mu\left[2\left\{\left(\frac{\partial v_r}{\partial r}\right)^2 + \left(\frac{v_r}{r}\right)^2 + \left(\frac{\partial v_z}{\partial z}\right)^2\right\} + \left(\frac{\partial v_r}{\partial z} + \frac{\partial v_z}{\partial r}\right)^2\right]. \tag{14}$$

We expect Eqn 14 to give a better estimate of the viscous energy dissipation around a jumping copepod, than the approximate expressions used in previous studies (van Duren et al., 2003; Catton et al., 2007). The volume integration in Eqn 12 was performed by integrating the planar measurements over the azimuthal angle, assuming rotational symmetry. To remove the background noise level of dissipation from the measurement, we

The Journal of Experimental Biology

removed those regions from the integration where the flow velocity was below a threshold of 0.5 mm s^{-1}.

Acknowledgements
We would like to thank Rodrigo Gonçalves, Jack Melbye, Lone Gram, Knud Erik Meyer, Pavlos Vlachos and Danny Grünbaum for their help and advice at different stages of this research.

Competing interests
The authors declare no competing financial interests.

Author contributions
N.W., A.A. and T.K. conceived the research and designed experiments; N.W. collected and analysed data; N.W., A.A. and T.K. interpreted results. N.W. and A.A. drafted the article and all authors revised it.

Funding
The Centre for Ocean Life is a Villum Kann Rasmussen Centre of Excellence supported by the Villum Foundation.

Supplementary material
Supplementary material available online at
http://jeb.biologists.org/lookup/suppl/doi:10.1242/jeb.105676/-/DC1

References

Andersen Borg, C. M., Bruno, E. and Kiørboe, T. (2012). The kinematics of swimming and relocation jumps in copepod nauplii. *PLoS ONE* **7**, e47486.
Batchelor, G. K. (1967). *An Introduction to Fluid Dynamics*. Cambridge, UK: Cambridge University Press.
Berggreen, U., Hansen, B. and Kiørboe, T. (1988). Food size spectra, ingestion and growth of the copepod *Acartia tonsa* during development: Implications for determination of copepod production. *Mar. Biol.* **99**, 341-352.
Buskey, E. J. (1998). Energetic costs of swarming behavior for the copepod *Dioithona oculata*. *Mar. Biol.* **130**, 425-431.
Catton, K. B., Webster, D. R., Brown, J. and Yen, J. (2007). Quantitative analysis of tethered and free-swimming copepodid flow fields. *J. Exp. Biol.* **210**, 299-310.
Childress, S. (2012). A thermodynamic efficiency for Stokesian swimming. *J. Fluid Mech.* **705**, 77-97.
Childress, S. and Dudley, R. (2004). Transition from ciliary to flapping mode in a swimming mollusc: flapping flight as a bifurcation in Re_{ω}. *J. Fluid Mech.* **498**, 257-288.
Crawford, D. W. (1992). Metabolic cost of motility in planktonic protists: Theoretical considerations on size scaling and swimming speed. *Microb. Ecol.* **24**, 1-10.
Drescher, K., Dunkel, J., Cisneros, L. H., Ganguly, S. and Goldstein, R. E. (2011). Fluid dynamics and noise in bacterial cell-cell and cell-surface scattering. *Proc. Natl. Acad. Sci. USA* **108**, 10940-10945.
Guasto, J. S., Rusconi, R. and Stocker, R. (2012). Fluid mechanics of planktonic microorganisms. *Annu. Rev. Fluid Mech.* **44**, 373-400.
Halcrow, K. and Boyd, C. M. (1967). The oxygen consumption and swimming activity of the amphipod *Gammarus oceanicus* at different temperatures. *Comp. Biochem. Physiol.* **23**, 233-242.
Hedrick, T. L. (2008). Software techniques for two- and three-dimensional kinematic measurements of biological and biomimetic systems. *Bioinspir. Biomim.* **3**, 034001.
Jiang, H. and Kiørboe, T. (2011a). The fluid dynamics of swimming by jumping in copepods. *J. R. Soc. Interface* **8**, 1090-1103.
Jiang, H. and Kiørboe, T. (2011b). Propulsion efficiency and imposed flow fields of a copepod jump. *J. Exp. Biol.* **214**, 476-486.
Kiørboe, T. and Hirst, A. G. (2014). Shifts in mass scaling of respiration, feeding, and growth rates across life-form transitions in marine pelagic organisms. *Am. Nat.* **183**, E118-E130.
Kiørboe, T. and Jiang, H. (2013). To eat and not be eaten: optimal foraging behaviour in suspension feeding copepods. *J. R. Soc. Interface* 10, 20120693.
Kiørboe, T. and Visser, A. (1999). Predator and prey perception in copepods due to hydromechanical signals. *Mar. Ecol. Prog. Ser.* **179**, 81-95.
Kiørboe, T., Andersen, A., Langlois, V. J. and Jakobsen, H. H. (2010). Unsteady motion: escape jumps in planktonic copepods, their kinematics and energetics. *J. R. Soc. Interface* **7**, 1591-1602.
Larink, O. and Westheide, W. (2006). *Coastal Plankton. Photo Guide for European Seas*. München, Germany: Pfeil.
Lauga, E. and Powers, T. R. (2009). The hydrodynamics of swimming microorganisms. *Rep. Prog. Phys.* **72**, 096601.
Lautrup, B. (2005). *Physics of Continuous Matter*. Bristol, UK: Institute of Physics Publishing.
Leshansky, A. M., Kenneth, O., Gat, O. and Avron, J. E. (2007). A frictionless microswimmer. *New J. Phys.* **9**, 145.
McHenry, M. J., Azizi, E. and Strother, J. A. (2003). The hydrodynamics of locomotion at intermediate Reynolds numbers: undulatory swimming in ascidian larvae (*Botrylloides sp.*). *J. Exp. Biol.* **206**, 327-343.
Murphy, D., Webster, D. and Yen, J. (2012). A high-speed tomographic PIV system for measuring zooplanktonic flow. *Limnol. Oceanogr. Methods* **10**, 1096-1112.
Nybakken, J. W. and Bertness, M. D. (2005). *Marine Biology: an Ecological Approach*, 6th edn. San Francisco, CA: Benjamin Cummings.
Pozrikidis, C. (2011). *Introduction to Theoretical and Computational Fluid Dynamics*, 2nd edn. Oxford, UK: Oxford University Press.
Raffel, M. (2007). *Particle Image Velocimetry: A Practical Guide*, 2nd edn. Heidelberg, Germany: Springer.
Riisgård, H. U., Jørgensen, B. H., Lundgreen, K., Storti, F., Walther, J. H., Meyer, K. E. and Larsen, P. S. (2011). The exhalant jet of mussels *Mytilus edulis*. *Mar. Ecol. Prog. Ser.* **437**, 147-164.
Savitzky, A. and Golay, M. J. E. (1964). Smoothing and differentiation of data by simplified least squares procedures. *Anal. Chem.* **36**, 1627-1639.
Sensenig, A. T., Kiger, K. T. and Shultz, J. W. (2009). The rowing-to-flapping transition: ontogenetic changes in gill-plate kinematics in the nymphal mayfly centroptilum triangulifer (Ephemeroptera, Baetidae). *Biol. J. Linn. Soc. Lond.* **98**, 540-555.
Spagnolie, S. E. and Lauga, E. (2011). Comparative hydrodynamics of bacterial polymorphism. *Phys. Rev. Lett.* **106**, 058103.
Svetlichny, L. S. and Hubareva, E. S. (2005). The energetics of *Calanus euxinus*: locomotion, filtration of food and specific dynamic action. *J. Plankton Res.* **27**, 671-682.
Tam, D. and Hosoi, A. E. (2011). Optimal feeding and swimming gaits of biflagellated organisms. *Proc. Natl. Acad. Sci. USA* **108**, 1001-1006.
Torres, J. and Childress, J. (1983). Relationship of oxygen consumption to swimming speed in *Euphausia pacifica*. *Mar. Biol.* **74**, 79-86.
Turner, J. T. (2004). The importance of small planktonic copepods and their roles in pelagic marine food webs. *Zool. Stud.* **43**, 255-266.
van Duren, L. A. and Videler, J. J. (2003). Escape from viscosity: the kinematics and hydrodynamics of copepod foraging and escape swimming. *J. Exp. Biol.* **206**, 269-279.
van Duren, L. A., Stamhuis, E. J. and Videler, J. J. (2003). Copepod feeding currents: flow patterns, filtration rates and energetics. *J. Exp. Biol.* **206**, 255-267.
Verity, P. and Smetacek, V. (1996). Organism life cycles, predation, and the structure of marine pelagic ecosystems. *Mar. Ecol. Prog. Ser.* **130**, 277-293.
Visser, A. (2001). Hydromechanical signals in the plankton. *Mar. Ecol. Prog. Ser.* **222**, 1-24.
Vlymen, W. J. (1970). Energy expenditure of swimming copepods. *Limnol. Oceanogr.* **15**, 348-356.
Vogel, S. (1994). *Life in Moving Fluids: The Physical Biology of Flow*. Princeton, NJ: Princeton University Press.
Yen, J. and Strickler, J. R. (1996). Advertisement and concealment in the plankton: What makes a copepod hydrodynamically conspicuous? *Invertebr. Biol.* **115**, 191-205.

Chapter 6

Flow disturbances generated by feeding and swimming zooplankton

Paper published in Proceedings of the National Academy of Sciences (2014)

Flow disturbances generated by feeding and swimming zooplankton

Thomas Kiørboe[a,1], Houshuo Jiang[b], Rodrigo Javier Gonçalves[a,c], Lasse Tor Nielsen[a], and Navish Wadhwa[d]

[a]Centre for Ocean Life, National Institute of Aquatic Resources, Technical University of Denmark, 2920 Charlottenlund, Denmark; [b]Department of Applied Ocean Physics and Engineering, Woods Hole Oceanographic Institution, Woods Hole, MA 02543; [c]Área de Ecología Animal, Estación de Fotobiología Playa Unión, 9103 Rawson, Chubut, Argentina; and [d]Centre for Ocean Life, Department of Physics, Technical University of Denmark, DK-2800 Kongens Lyngby, Denmark

Edited by William R. Young, University of California, San Diego, La Jolla, CA, and approved July 2, 2014 (received for review March 23, 2014)

Interactions between planktonic organisms, such as detection of prey, predators, and mates, are often mediated by fluid signals. Consequently, many plankton predators perceive their prey from the fluid disturbances that it generates when it feeds and swims. Zooplankton should therefore seek to minimize the fluid disturbance that they produce. By means of particle image velocimetry, we describe the fluid disturbances produced by feeding and swimming in zooplankton with diverse propulsion mechanisms and ranging from 10-μm flagellates to greater than millimeter-sized copepods. We show that zooplankton, in which feeding and swimming are separate processes, produce flow disturbances during swimming with a much faster spatial attenuation (velocity u varies with distance r as $u \propto r^{-3}$ to r^{-4}) than that produced by zooplankton for which feeding and propulsion are the same process ($u \propto r^{-1}$ to r^{-2}). As a result, the spatial extension of the fluid disturbance produced by swimmers is an order of magnitude smaller than that produced by feeders at similar Reynolds numbers. The "quiet" propulsion of swimmers is achieved either through swimming erratically by short-lasting power strokes, generating viscous vortex rings, or by "breast-stroke swimming." Both produce rapidly attenuating flows. The more "noisy" swimming of those that are constrained by a need to simultaneously feed is due to constantly beating flagella or appendages that are positioned either anteriorly or posteriorly on the (cell) body. These patterns transcend differences in size and taxonomy and have thus evolved multiple times, suggesting a strong selective pressure to minimize predation risk.

biological fluid dynamics | optimization

Zooplankters move to feed, find food, and find mates, so moving is critical to the efficient execution of essential functions. However, moving comes at a predation risk: Swimming increases the predator encounter velocity (encounter rate increases with prey velocity to a power ≤1), and feeding and swimming generate fluid disturbances that may be perceived by rheotactic predators, thus increasing the predator's detection distance (encounter rate increases with detection distance squared) (1–5). So, the advantages of moving and feeding must be traded off against the associated risks, and organisms should aim at moving and foraging in ways that reduce the predation risk and optimize the trade-off (6, 7). They may do so by moving in patterns that minimize encounter rates (8) and/or they may feed and propel themselves in ways that generate only small fluid disturbances (9). For example, theoretical models suggest that zooplankton that swim by a sequence of jumps may create a smaller fluid disturbance than similar-sized ones that swim smoothly (9), that a hovering zooplankter generates a larger fluid signal than one that cruises through the water (10, 11), and that a zooplankter moving at low Reynolds numbers will generate a relatively larger fluid signal than one moving at higher Reynolds numbers (11). Thus, motility patterns and propulsion modes may strongly influence predation risk and must be subject to strong selection pressure during evolution.

Zooplankton span a huge taxonomic diversity and a large size range (from microns to centimeters) and their propulsion mechanisms vary substantially (12). Unicellular plankton may use one or more flagella or cilia, and the flagella may be smooth or plumose, which has implications for whether the cell is pulled or pushed by the beating flagellum (13). Ciliates may have the cilia rather evenly distributed on the cell surface or concentrated on certain parts of the cell, typically either anteriorly or as an equatorial band. Small animals may have an anterior "corona" of cilia (e.g., rotifers and many pelagic invertebrate larvae) to generate feeding currents and propulsion, or they may have beating or vibrating appendages that can be positioned anteriorly, ventrally, or laterally. The implications and potential adaptive value of this diversity of propulsion modes for feeding and survival are largely unexplored.

Various idealized models, simplifying the swimming organisms to combinations of point forces acting on the water, have been used to describe the fluid disturbance generated by moving and feeding plankton. A self-propelled plankton is often described by a so-called stresslet (two oppositely directed point forces of equal magnitude), a hovering one by a stokeslet (a stationary point force), and a jumping animal by an impulsive stresslet (a stresslet working impulsively) (9, 11, 12). These highly idealized models yield very different predictions of the spatial attenuation of the fluid disturbance and, thus, of how far away the feeding and swimming animal can be detected. A few studies have compared observed flow patterns with those predicted from these simple models and in some cases found fair comparisons (4, 14–17). However, numerical simulations as well as observations of self-propelled microplankton have demonstrated that

Significance

Plankton compromise their survival when they swim and feed because the fluid disturbances that they generate may be perceived by predators. Because the abundance and population dynamics of zooplankton in the ocean are governed by their access to food and exposure to predators, an important question is to what extent and how zooplankton may minimize the fluid disturbances that they generate. We show that when swimming and feeding are integrated processes, zooplankton generate fluid disturbances that extend much farther in the water than is the case for zooplankton that swim only to relocate. Quiet swimming is achieved through "breast swimming" or by swimming by jumping, whereas other propulsion modes are much noisier. This pattern applies independent of organism size and species.

Author contributions: T.K. designed research; T.K., R.J.G., L.T.N., and N.W. performed research; H.J. contributed new reagents/analytic tools; T.K. and H.J. analyzed data; and T.K. and H.J. wrote the paper.

The authors declare no conflict of interest.

This article is a PNAS Direct Submission.

[1]To whom correspondence should be addressed. Email: tk@aqua.dtu.dk.

This article contains supporting information online at www.pnas.org/lookup/suppl/doi:10.1073/pnas.1405260111/-/DCSupplemental.

the distribution of propulsion forces, i.e., the position of flagella, cilia, or appendages on the (cell) body, may have a profound effect on the imposed fluid flow (18, 19). Also, most of the idealized models ignore the fact that swimming in most cases is unsteady, which leads to fluctuating flows at scales smaller than the Stokes length scale ($\sqrt{\nu/\omega}$, where ν is the kinematic viscosity and ω is the beat frequency) (e.g., ref. 19). The simple, idealized models hitherto applied may be insufficient to represent the diverse propulsion modes observed in real organisms and to understand the associated trade-offs.

Feeding and swimming are often part of the same process in zooplankton. Many zooplankton generate a feeding current that at the same time propels the animal through the water. In others, feeding and swimming are separate processes. For example, ambush feeding "sit-and-wait" zooplankters do not move as part of feeding but may swim to undertake vertical migration or to search for mates or patches of elevated food availability. Also, many of the plankton that generate a feeding current by vibrating appendages may in addition swim by using the same appendages in a different way (e.g., the nauplius larvae of most crustaceans) or by using other swimming appendages dedicated to propel themselves (most pelagic copepods and cladocerans).

Whereas feeding and swimming may both compromise the survival of the organism, the trade-offs may be different. To get sufficient food, zooplankters need to daily clear a volume of water for prey that corresponds to about 10^6 times their own body volume (20, 21) and hence, implicit in the feeding process is the need to examine or process large volumes of water. In contrast, dedicated swimming should translate the organism through the water as quietly as possible. Thus, we hypothesize that in microplankton, dedicated swimming produces flow fields that attenuate more readily and/or have a smaller spatial extension than the cases in which feeding and propulsion are intimately related.

In this study we use particle image velocimetry (PIV) to describe the flow fields generated by micron- to millimeter-sized feeding and swimming zooplankton that use a variety of propulsion modes. We show that—across taxa and sizes—dedicated swimming produces flow fields with a much smaller spatial extension and a faster spatial attenuation than those produced by the plankton for which feeding and swimming are integrated, and we characterize the propulsion modes that minimize susceptibility to rheotactic predators.

Results

The propulsion modes vary substantially between the organisms studied here, in terms of the nature of the propulsion machinery (flagella, cilia, or appendages), the location of the propelling structure on the organism (anteriorly, posteriorly, ventrally, or laterally), the frequency and duration of the power strokes, and the resulting speed and variability in speed (Figs. 1 and 2, Table S1, and Movie S1). These different ways of propelling the organism result in a fascinating diversity of flow fields (Fig. 3 and Movies S2–S4).

The dinoflagellates (20–50 μm) all swim by beating two flagella, a longitudinal, trailing flagellum that propels the cell through the water and a transverse flagellum that accounts for rotation and steering of the cell (22). The beating of the trailing flagellum creates a succession of short-lasting, counterrotating vorticity structures in the wake of the cell (Fig. 3*A*) and a highly fluctuating extension of the flow field (Fig. 2*A*). The rotifer *Brachionus plicatilis* (25–50 μm) generates a feeding current and is pulled through the water by cilia organized in frontal coronas that propel constantly (Movie S1); the resulting propulsion speed is near constant (Table S1) and the flow field is almost stationary in time and consists of two vortex rings, one around the translating body and another one of opposite direction around the feeding current (Movie S2). The nauplius (larval stage) of the copepod *Temora longicornis* (200–300 μm) creates very different flow fields, depending on whether it vibrates its three pairs of appendages to generate a feeding current, or it swims by powerful backward strokes of the appendages (Movie S3). The latter flow field is similar to that produced by the swimming nauplii of the copepod *Acartia tonsa* (140–240 μm) as well as by the ciliate *Mesodinium rubrum* (25 μm) and the much larger cladoceran, *Podon intermedius* (0.7–1.0 mm): The flow both anterior and posterior to the organism is in the swimming direction, whereas the flow lateral to the organism is directed backward (Fig. 3 and Movies S2 and S3). These organisms all "breast-stroke swim" by beating the laterally positioned appendages or cirri backward. The copepodites of the three calanoid copepods all swim and

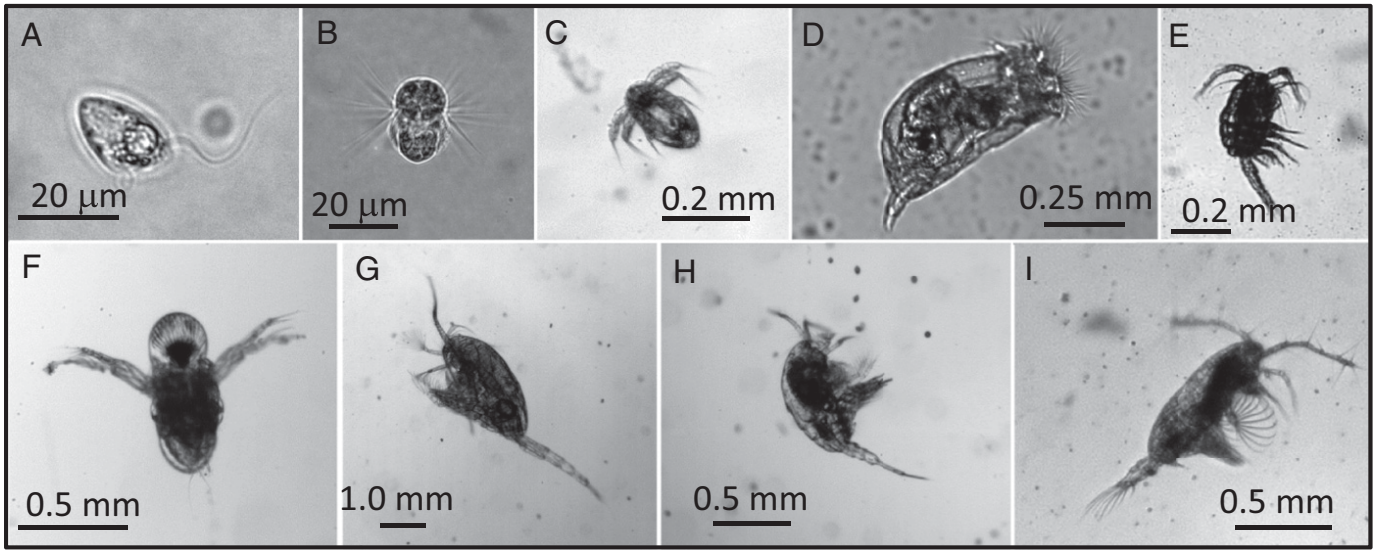

Fig. 1. The study organisms with their diverse propulsion equipment. (*A–I*) The dinoflagellate *Oxyrrhis marina* (the other dinoflagellates look similar) (*A*), the ciliate *Mesodinium rubrum* (*B*), nauplius of the copepod *Acartia tonsa* (the nauplius of *Temora longicornis* looks very similar) (*C*), the rotifer *Brachionus plicatilis* (*D*), the copepod *Oithona davisae* (*E*), the cladoceran *Podon intermedius* (*F*), the copepod *Metridia longa* (*G*), the copepod *T. longicornis* (*H*), and the copepod *A. tonsa* (*I*).

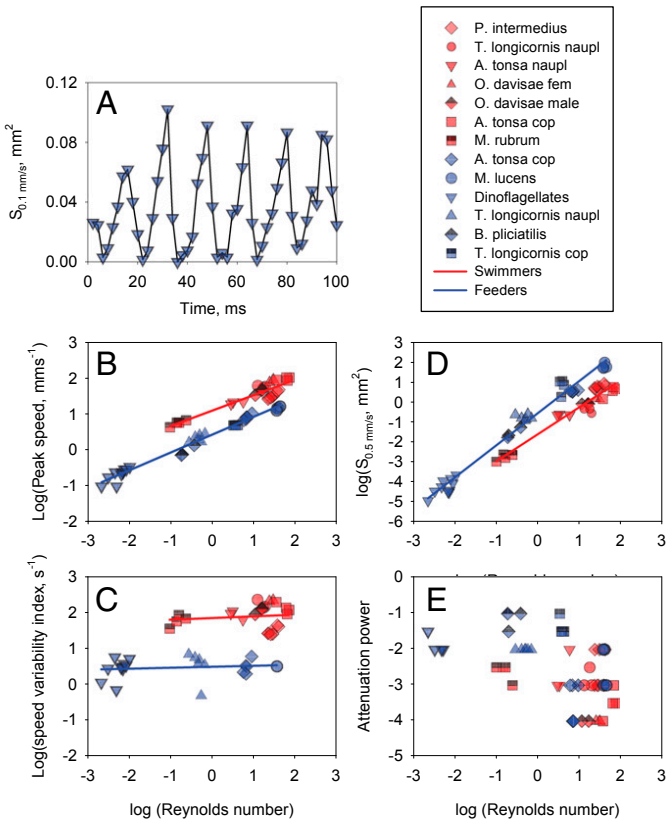

Fig. 2. (*A–E*) Temporal fluctuations in area of influence, $S_{0.1\ mm/s}$, for the dinoflagellate *O. marina* (*A*); peak propulsion speed (*B*); speed variability index (*C*); area of influence, $S_{0.5\ mm/s}$ during the peak of the power stroke (*D*); and power of spatial flow attenuation (*E*), all as a function of Reynolds number for swimmers (red symbols and lines) and feeders (blue symbols and lines). The regression lines in *D* are as follows: swimmers, Log(*S*, mm^2) = −1.54 + 1.36 Log (Re); feeders, Log(*S*, mm^2) = −0.48 + 1.61 Log(Re). Speed variability index is estimated as the difference between peak and average speed divided by the length of the organism. All data are reported in Table S1.

feed by vibrating the anterior-ventrally positioned five pairs of feeding appendages in a rhythmic but convoluted pattern, but the flow fields differ, depending on whether the animal is "hovering," i.e., generates a feeding current while itself remaining stationary and tethered by gravity (*T. longicornis*, 0.75 mm), or is cruising through the water (*Metridia longa*, 2.5 mm) (Fig. 3 *C* and *E*). The third calanoid copepod, *A. tonsa* (0.8 mm) is intermediate between the other two in that it simultaneously swims through the water and generates a feeding current (Movie S4), but it also differs in that it vibrates both its feeding appendages and its swimming legs when generating the current and propelling itself (Movie S1). Finally, all of the copepods can swim by sequentially kicking the four to five pairs of ventrally positioned swimming legs backward, either once or a few times (a repositioning jump: *A. tonsa*, *Oithona davisae* females), repeatedly at a high frequency (escape jump, none analyzed), or repeatedly at a lower frequency (swimming by jumping: *O. davisae* males). In all cases, and best illustrated by *A. tonsa* (Fig. 3*B* and Movie S4), two ephemeral vortex rings form, one in the wake of the animal and one around its forward-moving body. A simple categorization of the swimming and feeding behaviors described above is presented in Table 1.

Ignoring details in the flow structures and focusing on how bulk-induced flow velocity attenuates with distance to the organism, striking patterns emerge (Fig. 4, Table 1, and Table S1). For most species the imposed flow velocity is variable in time. The temporal variation in flow velocity is highest for small organisms and very near the body of the organisms, whereas at distances approaching or exceeding the Stokes length scale, the flow field is more constant in time. As a consequence, the spatial attenuation of the flow field is variable (Fig. 4). However, in the far field, and at the peak of the power stroke, the spatial attenuation tends toward a constant power relationship that is characteristic of each of the flow fields examined and robust to whether the organism is viewed from the dorsal, ventral, or lateral side (Fig. 4 and Table S1). For the zooplankton that swim independent of feeding, the spatial attenuation of the flow is fast and attenuates with distance to power near −4 for the ones that move by jumps (all of the copepods) and near −3 for those that have the swimming appendages organized laterally (the copepod nauplii, *P. intermedius* and *M. rubrum*). For those organisms and propulsion modes where swimming and feeding are intimately associated, the spatial attenuation is slower, with powers of between −2 and −1. The copepodite of *A. tonsa* deviates from this pattern in that its feeding current attenuates rapidly. The flow attenuation is related to, but not well predicted by, the Reynolds number of the moving organism (Fig. 2*E*) and organisms moving at the highest Reynolds numbers (Re > 10) show almost the full range of spatial attenuations. Thus, the propulsion mode is more relevant than the magnitude of Re for the imposed flow pattern.

As a consequence of the differences in spatial attenuation, the spatial extensions of the flow fields differ (Fig. 2*D*). Here, we define the spatial extension of the flow field, *S*, as the peak cross-sectional area within which the imposed fluid velocity exceeds a certain threshold velocity. We have chosen a critical velocity of 0.5 $mm{\cdot}s^{-1}$: This overlaps with or is close to the highest velocities produced by the smallest organisms examined and the lowest velocities measurable for the largest organisms. In the case of no overlap, we extrapolated from observations, using the estimated power of the spatial attenuation. The resulting area of course depends on the chosen threshold, but the pattern is robust to the choice of threshold: The area of the flow field increases with the Reynolds number of the organism and is nearly an order of magnitude larger for plankton that feed and swim simultaneously compared with those where feeding and swimming are separate processes. In organisms for which we have recordings of both feeding and pure swimming modes, e.g., nauplii of *T. longicornis* and copepodites of *A. tonsa*, one can see that they can increase their peak propulsion speed by more than one order of magnitude without (*A. tonsa*) or by only slightly (factor of 2.3, *T. longicornis*) increasing the spatial extension of the flow field, as defined above (Fig. 4 and Table S1).

Discussion

Our observations suggest that for plankton that swim to relocate, propulsion has been optimized to minimize the fluid disturbance that they generate, whereas for plankton in which swimming is constrained by a simultaneous need to feed, the fluid disturbance generated is manyfold higher with a consequently higher risk of being detected by a rheotactic predator. Because rheotactic predators respond to imposed fluid velocity magnitude rather than shear (23), the area of influence can be thought of as the encounter cross section toward a rheotactic predator and thus scales directly with predator encounter rate. The threshold velocity of 0.5 $mm{\cdot}s^{-1}$ was chosen for practical reasons (see above) and a threshold on the order of 0.1 $mm{\cdot}s^{-1}$ would be more in line with typical threshold flow velocities for prey detection in planktonic predators (21), and such a threshold yields an even larger difference between swimmers and feeders. The higher risk associated with feeding than with pure swimming, of course, may be warranted by the benefits of feeding, and thus plankton are no different from many other organisms that have to compromise their survival to acquire food (6).

What are the characteristics of "quiet" propulsion in contrast to "noisy" feeding and swimming and how do the swimmers reduce the spatial extension of their fluid disturbance? The

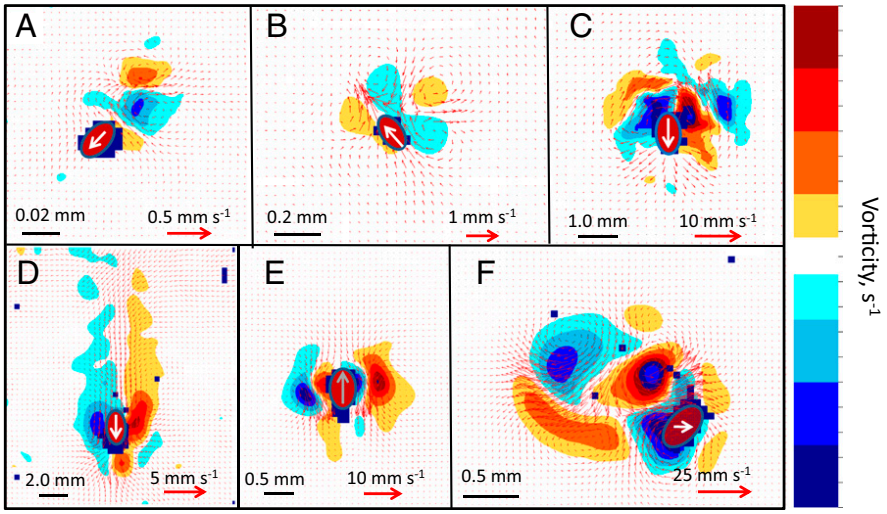

Fig. 3. Examples of snapshots of flow fields generated by swimming and feeding zooplankton. (*A–F*) Swimming *Oxyrrhis marina* (*A*), nauplius of *Temora longicornis* producing feeding current (*B*), swimming *Podon intermedius* (*C*), cruising *Metridia longa* (*D*), hovering *T. longicornis* (*E*), and repositioning jump of *Acartia tonsa* (*F*). The position of the organisms is indicated by red ellipses and the swimming direction by white arrows (gray arrow for the hovering *T. longicornis*). Flow field animations for all species examined are shown in Movies S2–S4.

propulsion speed in almost all of the organisms examined is unsteady due to the beating of appendages or flagella but the size-dependent beat frequencies do not differ significantly between the swimmers and feeders (Table S1). However, the power strokes are shorter in pure swimmers, their peak speeds as well as variability in speed are much larger than in similar-sized feeders, and their propulsion is consequently much more erratic (Fig. 2*C*, Table S1, and Movie S1). The higher Reynolds numbers of the swimmers than those of equal-sized feeders can only partly account for the limited extension of their flow fields. We have previously shown for swimming plankton that if the power stroke is short relative to the Stokes timescale, the flow structure formed may be characterized by two viscous vortex rings with a fast spatial and temporal attenuation (9). All of the jumping and swimming copepods in fact produce two such vortex rings (Fig. 3 and Movies S2–S4) consistent with previous observations in different species (4, 17, 24), and the observed far field spatial attenuation of the flow ($u \sim r^{-4}$) is consistent with that predicted from the idealized impulsive stresslet model (Table 1). Thus, the rapid power strokes may be considered an adaptation to minimize the production of fluid signals.

None of the other swimmers examined, the ciliate (*M. rubrum*), the copepod nauplii (*A. tonsa* and *T. longicornis*), and the cladoceran (*P. intermedius*), form similar vortex rings, but they are all "breast swimmers" with the propulsion apparatus positioned (bi)laterally symmetrically (Fig. 1 and Movie S1) and with quite similar flow fields (Movies S2–S4). The far field flow generated by them resembles that of a potential dipole (*SI Text*, Figs. S1–S4, and Tables S2–S5). A potential dipole can physically be thought of as a fluid point sink and a fluid point source, with strengths of equal magnitude m, to be placed at two points separated by a distance δ in such a way that $m \times \delta$ remains constant when the separation δ vanishes (25). A potential dipole is mathematically equivalent to a magnetic dipole. The striking swimming appendages follow rather well the streamlines of a potential dipole (equivalent to the magnetic field lines) (*SI Text* and Movie S5), which explains the similarities of the flows. Bulk properties of the flows are also similar in that the observed far field flow attenuation for these swimmers is close to that predicted by the potential dipole ($u \sim r^{-3}$) and the flow fields, streamlines, and velocity magnitudes are well predicted by the potential dipole model (*SI Text*). A previous computational fluid dynamics simulation study of the ciliate *M. rubrum* has similarly shown a dipole-like flow pattern and $\sim r^{-3}$ flow attenuation (26). Breast swimming can thus be considered an adaptation to minimize the fluid disturbances of swimming plankton. Its existence over a large size range and in diverse taxa suggests that this body plan and this propulsion mode have evolved multiple times in the course of evolution. Note that the nauplius is the characteristic pelagic larva not only of copepods but of many crustaceans, an abundant and widespread animal group in the ocean, and the nauplius has been characterized as one of the most successful larval forms in the pelagic environment (27).

The zooplankton that feed and swim simultaneously cruise through the water (*M. longa*, the dinoflagellates), hover in an almost stationary position while producing a feeding current (*T. longicornis* copepodite), or do something in between, i.e., translating through the water and simultaneously drawing water

Table 1. Plankton swimming behaviors, their purposes, and bulk properties of the induced flows

Behavior	Purpose	Species/groups	Idealized model	Spatial attenuation*
Hover	Feeding	*T. longicornis* copepodite	Stokeslet	r^{-1}
Cruise	Feeding and locomotion	*M. longa*, dinoflagellates	Stresslet	r^{-2}
Hover/cruise	Feeding and locomotion	*B. plicatilis*, *A. tonsa* copepodite feeding, *T. longicornis* nauplii feeding	Stokeslet+stresslet	r^{-1} to r^{-2}
Breast-stroke swim	Locomotion	*M. rubrum*, *P. intermedius*, nauplii swimming	Potential dipole	r^{-3}
Jumping	Locomotion	Copepods swimming by jumping	Impulsive stresslet	r^{-4}

*Describes how flow velocity scales with the distance, r, from the swimming plankton. The exponent is that predicted from the idealized models (*SI Text*) and approximated by the observations (*Table S1* and Fig. 4 of the main text).

ECOLOGY

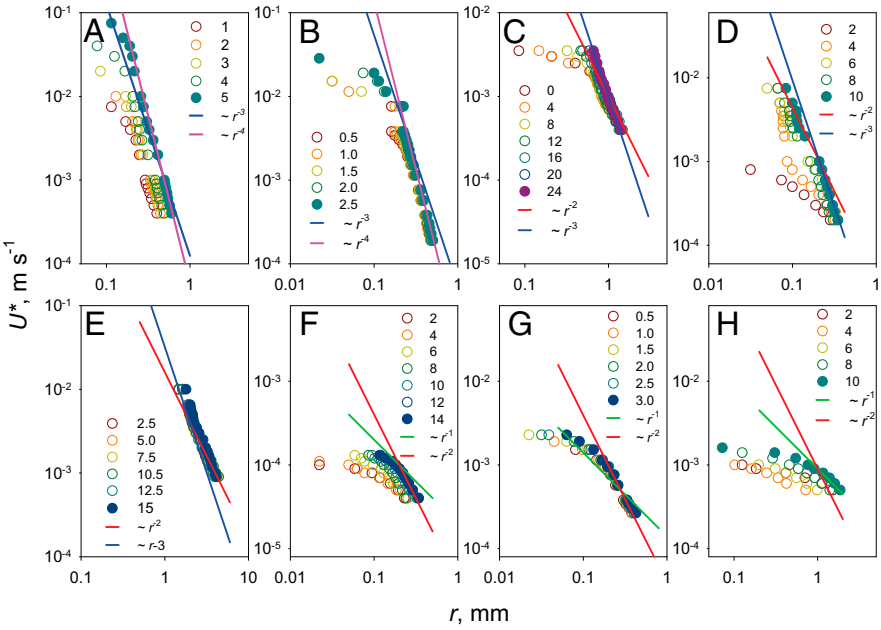

Fig. 4. Examples of the spatial attenuation of flow velocities. (*A–H*) *A. tonsa* copepodite repositioning jump (*A*), *O. davisae* female repositioning jump (*B*), *P. intermedius* swimming (*C*), *A. tonsa* nauplii swimming (*D*), *M. longa* cruise feeding (*E*), *O. marina* cruise feeding (*F*), *T. longicornis* nauplius feeding(*G*), and *T. longicornis* hovering (*H*). The solid circles show the attenuation at the peak of the power stroke and the open circles the attenuation during the time leading up to the peak at times given in milliseconds. The solid lines have slopes between −1 and −4 and were adjusted to line up with the far field flow attenuation at the peak of the power stroke. A characteristic far field flow attenuation was somewhat subjectively assigned to each experiment based on how well it compares with the observations; for observations that were between two integer values, we assigned an intermediate value.

toward themselves (all of the others). With the exception of *A. tonsa* copepodites, their observed far field spatial attenuation of the flow fields scales with the distance to powers between −1 and −2, comparable to that predicted by the idealized stokeslet (hovering, −1) and stresslet (cruising, −2) models (*SI Text*).

There is an additional consistent taxa-transcending difference between swimmers and feeders that allows the swimmers to further reduce their susceptibility to rheotactic predators: The swimmers swim intermittently, whereas the feeders feed and swim almost continuously—a difference that applies generally and not only to the study organisms. The frequency of reposition jumps in copepods and ciliates is between 1.0 s^{-1} and 0.01 s^{-1} (28, 29) (reviewed in ref. 4) with each jump lasting only a few milliseconds. The males of the copepod *Oithona* spp. swim for only about one-third of the time (30) and the actual swimming takes up only a fraction of that time. The cladocerans similarly have long breaks between swimming events. In contrast, flagellates, most ciliates, rotifers, nauplii, and copepods that generate a feeding current or cruise while feeding do so almost continuously (10, 28, 31). Because the swimmers propel faster than the feeders, the total distance they cover per unit time, and hence the average predator encounter velocity, may not be different between swimmers and feeders, but the swimmers produce only small ephemeral flow structures and are "invisible" to rheotactic predators for most of the time.

The copepod *A. tonsa* is different from the other feeding copepods, in that its flow field attenuates faster than predicted by the idealized models. It also differs in the way it produces the feeding current by vibrating both the feeding and the swimming appendages, as has been observed in other species of the genus (32), and it feeds only intermittently and for only 5–20% of the time (33). This suggests that its feeding current is very efficient and that its exposure to rheotactic predators is limited, which in turn may account for the evolutionary success of this particular family, as judged both from its numerical dominance in neritic plankton communities around the world and from its capacity to colonize new areas (34–37).

Propulsion strategy may be adapted to optimize a variety of functions. Hitherto propulsion and feeding in zooplankton have mainly been examined from the perspective of food acquisition and propulsion energetics (12), but optimization of feeding and propulsion should not only consider the energetics but also take inescapable predation risk into account (3). Our study suggests that predation is a strong selective agent in shaping the motility and propulsion strategy of zooplankton and that these organisms can substantially reduce their susceptibility to rheotactic predators as they swim when they are not constrained by a simultaneous need to gather food.

Methods

Most experimental organisms were taken from our laboratory cultures. Exceptions were the copepod *Metridia longiremis* that was collected in Disko Bay, Greenland, and the cladoceran *P. intermedius* that we collected in Gulmar Fjord, Sweden. We used PIV to visualize 2D transects of the fluid flow generated by swimming plankton. Briefly, swimming and/or feeding zooplankters were filmed with a high-resolution (1,280 × 800 pixels), high-speed (100–2,200 frames·s^{-1}) Phantom V210 video camera. The camera was equipped with lenses to produce appropriate fields of view (i.e., such that the entire extension of the flow field was covered), from 0.28 × 0.17 mm^2 for the smallest flagellates to 28 × 17 mm^2 for the largest copepods. Copepods (nauplii and copepodites) and cladocerans swam in small aquaria, varying in size from 1 × 1 × 4 cm^3 (nauplii and small copepodites) and 5 × 5 × 5 cm^3 (small copepods and cladocerans) to 8.5 × 10.2 × 3.2 cm^3 (large copepods).

Protists swam in ∼0.5-mm high, 10-mm radius chambers mounted on a microscopic slide. In all cases the fluids were seeded with tracer particles to visualize the flow, 0.5-μm polymer microspheres for the protists and 5- to 10-μm hollow glass spheres or ∼1-μm titanium oxide particles for the larger organisms. Illumination was provided by a pulsed infrared laser (808 nm) that was synchronized with the camera and passed through optics to produce a thin sheet (150–300 μm). The camera was oriented perpendicular to the laser sheet. The dinoflagellates, the rotifer, and the copepod nauplii were filmed in an inverted microscope. In this case the depth of the narrow focal plane rather than a laser sheet defined the thickness of the flow structure recorded. We selected short movie sequences (40–500 frames)

where the organisms moved in the focal plane or in the plane of the laser sheet. Because the imaging is in 2D and swimming is in 3D, this is a potential source of variation, but we minimized this variation by selecting sequences where the peak estimates of the spatial extension of the flow field (see below) were constant in time (i.e., not increasing or decreasing). These sequences were analyzed using DaVis PIV software to get quantitative descriptions of the temporal variation of the flow field generated by the swimming/feeding organism. We quantified the spatial extension of the flow by measuring the area, $S(U^*)$, within which the induced flow velocity exceeds a threshold value, U^*, for different values of U^*. Velocity estimates were made at a resolution of 16 pixels × 16 pixels, and $S(U^*)$ was estimated as the fraction of squares with velocity estimates exceeding U^* multiplied by the area of the field of view. We describe the spatial attenuation of the flow by plotting U^* as a function of the equivalent circular radius of that area. We did not mask the organisms before extracting the flow fields, and the motion of the organism itself thus appears as induced water motion. The reasons for not masking are twofold: (*i*) We focus on the far field flow and hence a correct description of the near field is of less importance, and (*ii*) by not masking we correctly estimate the area influenced by the organism. For presentation purposes, and to visualize the near field flow, we masked the animals (Fig. 3 and Movies S2–S5). We computed the body Reynolds number of the feeding and swimming organisms as Vl/ν, where V is the peak velocity of the animal relative to the fluid (i.e., its swimming velocity plus the oppositely directed component of feeding current velocity, both measured relative to the camera), l is the body length of the organism, and ν is the kinematic viscosity. The swimming speeds of the organisms were obtained by digitizing their position in subsequent frames. We also computed an index of the relative variability in swimming speed, as the peak minus the average speed divided by the length of the organism. To describe the propulsion modes of the different organisms we filmed them in the absence of PIV particles, using optimal illumination (Movie S1). We either shone infrared light through the swimming aquarium toward the camera or used the light provided by the microscope.

ACKNOWLEDGMENTS. The Centre for Ocean Life is a Villum Kahn Rasmussen Center of Excellence funded by the Villum Foundation. This work was further supported by a grant from the Danish Council for Independent Research, Natural Sciences (to T.K.). R.J.G. was supported by Consejo Nacional de Investigaciones Científicas y Técnicas de Argentina and Fondo para la Investigación Científica y Tecnológica (Argentina) [Proyecto de Investigación Científica y Tecnológica (Argentina) 2438]. H.J. was supported by National Science Foundation Grant OCE-1129496.

1. Evans GT (1989) The encounter speed of moving predator and prey. *J Plankton Res* 11:415–417.
2. Visser AW (2007) Motility of zooplankton: Fitness, foraging and predation. *J Plankton Res* 29:447–461.
3. Gerritsen J, Strickler JR (1977) Encounter probabilities and community structure in zooplankton. Mathematical model. *J Fish Res Bd Can* 34(1):73–82.
4. Kiørboe T, Jiang H, Colin SP (2010) Danger of zooplankton feeding: The fluid signal generated by ambush-feeding copepods. *Proc Biol Sci* 277(1698):3229–3237.
5. Tiselius P, Jonsson PR, Kaartvedt S, Olsen ME, Jarstad T (1997) Effects of copepod foraging behavior on predation risk: An experimental study of the predatory copepod *Pareuchaeta norvegica* feeding on *Acartia clausi* and *A. tonsa* (Copepoda). *Limnol Oceanogr* 42(1):164–170.
6. Houston AI, McNamara JM, Hutchinson JMC (1993) General results concerning the trade-off between gaining energy and avoiding predation. *Philos Trans R Soc Lond B Biol Sci* 341:375–397.
7. Lima S, Dill LM (1990) Behavioral decisions made under the risk of predation: A review and prospectus. *Can J Zool* 68:619–640.
8. Visser AW, Kiørboe T (2006) Plankton motility patterns and encounter rates. *Oecologia* 148(3):538–546.
9. Jiang H, Kiørboe T (2011) The fluid dynamics of swimming by jumping in copepods. *J R Soc Interface* 8(61):1090–1103.
10. Tiselius P, Jonsson P (1990) Foraging behavior of 6 calanoid copepods – observations and hydrodynamic analysis. *Mar Ecol Prog Ser* 66:23–33.
11. Visser AW (2001) Hydromechanical signals in the plankton. *Mar Ecol Prog Ser* 222: 1–24.
12. Guasto JS, Rusconi R, Stocker R (2012) Fluid mechanics of plankton microorganisms. *Annu Rev Fluid Mech* 44:373–400.
13. Christensen-Dalsgaard KK, Fenchel T (2004) Complex flagellar motions and swimming patterns of the flagellates *Paraphysomonas vestita* and *Pteridomonas danica*. *Protist* 155(1):79–87.
14. Catton KB, Webster DR, Brown J, Yen J (2007) Quantitative analysis of tethered and free-swimming copepodid flow fields. *J Exp Biol* 210(Pt 2):299–310.
15. Drescher K, Goldstein RE, Michel N, Polin M, Tuval I (2010) Direct measurement of the flow field around swimming microorganisms. *Phys Rev Lett* 105(16):168101.
16. Kiørboe T, Jiang H (2013) To eat and not be eaten: Optimal foraging behavior in suspension feeding copepods. *J R Soc Interface* 10(78):20120693.
17. Murphy DW, Webster DR, Yen J (2012) A high-speed tomographic PIV system for measuring zooplanktonic flow. *Limnol Oceanogr Methods* 10:1096–1112.
18. Jiang H, Paffenhöfer G-A (2008) Hydrodynamic signal perception by the copepod *Oithona plumifera*. *Mar Ecol Prog Ser* 373:37–52.
19. Guasto JS, Johnson KA, Gollub JP (2010) Oscillatory flows induced by microorganisms swimming in two dimensions. *Phys Rev Lett* 105(16):168102.
20. Hansen PJ, Bjørnsen PK, Hansen BW (1997) Zooplankton grazing and growth: Scaling within the 2-2,000-mu m body size range. *Limnol Oceanogr* 42:35687–35704.
21. Kiørboe T (2011) How zooplankton feed: Mechanisms, traits and trade-offs. *Biol Rev Camb Philos Soc* 86(2):311–339.
22. Fenchel T (2001) How dinoflagellates swim. *Protist* 152(4):329–338.
23. Kiørboe T, Visser AW (1999) Predator and prey perception in copepods due to hydromechanical signals. *Mar Ecol Prog Ser* 179:81–95.
24. Yen J, Strickler JR (1996) Advertisement and concealment in the plankton: What makes a copepod hydrodynamically conspicuous? *Inv Biol* 115(3):191–205.
25. Batchelor GK (1967) *An Introduction to Fluid Dynamics* (Cambridge Univ Press, Cambridge, UK).
26. Jiang H (2011) Why does the jumping ciliate *Mesodinium rubrum* possess an equatorially located propulsive ciliary belt? *J Plankton Res* 33:998–1011.
27. Martin JW, Olesen J, Høeg JT (2014) The nauplius. *Atlas of Crustacean Larvae*, eds Martin JW, Olesen J, Høeg JT (Johns Hopkins Univ Press, Baltimore), pp 8–16.
28. Buskey EJ, Coulter C, Strom S (1993) Locomotory patterns of microzooplankton: Potential effects on food selectivity of larval fish. *Bull Mar Sci* 53(1):29–43.
29. Fenchel T, Hansen PJ (2006) Motile behaviour of the bloom-forming ciliate *Mesodinium rubrum*. *Mar Biol Res* 2:33–40.
30. Kiørboe T (2008) Optimal swimming strategies in mate-searching pelagic copepods. *Oecologia* 155(1):179–192.
31. Titelman J, Kiørboe T (2003) Motility of copepod nauplii and implications for food encounter. *Mar Ecol Prog Ser* 247:123–135.
32. Rosenberg G (1980) Filmed observations of filter-feeding in the marine planktonic copepod *Acartia clausi*. *Limnol Oceanogr* 25:738–742.
33. Jonsson P, Tiselius P (1990) Feeding behaviour, prey detection and capture efficiency of the copepod *Acartia tonsa* feeding on planktonic ciliates. *Mar Ecol Prog Ser* 60: 35–44.
34. Durbin EG, Durbin AG, Smayda TJ, Verity PG (1983) Food limitation of production by adult Acartia tonsa in Narragansett Bay, Rhode Island. *Limnol Oceanogr* 28: 1199–1213.
35. Hoffmeyer M (2004) Decadal change in zooplankton seasonal succession in the Bahía Blanca estuary, Argentina, following introduction of two zooplankton species. *J Plankton Res* 26(2):181–189.
36. David V, Sautour B, Chardy P (2007) Successful colonization of the calanoid copepod *Acartia tonsa* in the oligo-mesohaline area of the Gironde estuary (SW France) – Natural or anthropogenic forcing? *Estuar Coast Shelf Sci* 71:429–442.
37. Aravena G, Villate F, Uriarte I, Iriarte A, Ibáñez B (2009) Response of *Acartia* populations to environmental variability and effects of invasive congenerics in the estuary of Bilbao, Bay of Biscay. *Estuar Coast Shelf Sci* 83:621–628.

Supporting Information

Kiørboe et al. 10.1073/pnas.1405260111

SI Text

Idealized Models of Flow Imposed by Feeding and Swimming Zooplankton, with Emphasis on the Potential Dipole Model

We here describe the idealized models used to characterize the flow generated by swimming and feeding plankton: the stokeslet model (a stationary point force), the stresslet model (two oppositely directed point forces of equal magnitude), the impulsive stresslet model (a stresslet working impulsively), and the potential dipole model. We and others have previously applied and described the first three models and we therefore refer to our earlier work for details and derivations (1, 2) and here only summarize the resulting equations (Table S2). Our main emphasis here is to describe the potential dipole and to demonstrate that it provides a good qualitative and quantitative description of the flow generated by "breast-swimming" plankton.

A potential dipole, also called a point-source dipole or a source doublet (e.g., refs. 3 and 4), is constructed by a limiting process: A point source and a point sink, with strengths of equal magnitude m, are placed at two points separated by a distance δ. As the separation δ approaches zero, the strength m approaches infinity, but the product of m and δ tends to a finite limit J (i.e., the dipole strength, with dimensions of volume times velocity). The resulting dipole flow equations can be written in a cylindrical polar coordinate system (x, r, ϕ) with the positive axial x direction coinciding with the direction from the source to the sink,

$$u = \frac{J}{4\pi}\frac{2x^2 - r^2}{(x^2 + r^2)^{5/2}} \quad \text{[S1a]}$$

$$v = \frac{J}{4\pi}\frac{3xr}{(x^2 + r^2)^{5/2}}, \quad \text{[S1b]}$$

where u is the fluid velocity in the axial direction and v is the fluid velocity in the radial direction. The stream function is

$$\psi_\phi = \frac{J}{4\pi}\frac{r^2}{(x^2 + r^2)^{3/2}}. \quad \text{[S2]}$$

From Eq. **S1**, the velocity magnitude is calculated as

$$U \equiv \sqrt{u^2 + v^2} = \frac{J}{4\pi}\frac{\sqrt{4x^2 + r^2}}{(x^2 + r^2)^2}. \quad \text{[S3]}$$

Thus, the velocity magnitude attenuates with distance to the power of 3.

The area of influence S is defined as the area in the meridian plane within which the flow velocity magnitude U is greater than a given velocity threshold U^*. To derive the formula for calculating S of the dipole flow field, two lengths are formed:

$$R_x^* = \left(\frac{1}{2\pi}\frac{J}{U^*}\right)^{1/3} \quad \text{[S4a]}$$

$$R_r^* = \left(\frac{1}{4\pi}\frac{J}{U^*}\right)^{1/3}. \quad \text{[S4b]}$$

It can be shown that the scaling for S is

$$\frac{S}{0.5\pi R_x^* R_r^*} \sim \text{constant} = 1.05. \quad \text{[S5]}$$

Combining Eqs. **S4** and **S5** yields

$$S = 0.3845\left(\frac{J}{U^*}\right)^{2/3}. \quad \text{[S6]}$$

To fit the particle image velocimetry (PIV) measured data of maximum area of influence imposed by real zooplankton swimming/jumping to the dipole model, Eq. **S6** is rewritten as

$$S_{\max} = 2 \times 0.3845\left(\frac{J}{U^*}\right)^{2/3} = 0.769\left(\frac{CU_{\max}V}{U^*}\right)^{2/3}. \quad \text{[S7]}$$

Here, the multiplier 2 is considered because the real zooplankton-imposed flow occupies the whole measurement plane that is twice the meridian plane. Also, the dipole strength J is rewritten as

$$J = CU_{\max}V, \quad \text{[S8]}$$

where $U_{\max}$ is the maximum swimming/jumping speed of the zooplankter, V is the zooplankter's body volume, and C is a fitting parameter. To represent the potential flow (relative to a stationary frame of reference) due to a sphere of radius a translating with a constant speed U in an infinite fluid space, one can put a potential dipole of strength $2\pi a^3 U$ at the instantaneous center of the sphere (ref. 4, p. 332). In this case, the parameter $C = 1.5$ (where the Reynolds number Re is infinity for potential flow). Similarly, we propose to put a potential dipole at the instantaneous center of a swimming/jumping zooplankter to represent the zooplankter-imposed instantaneous flow (relative to a stationary frame of reference) at the time instant when the flow reaches its maximum area of influence. We have fitted our PIV measured data of area of influence to Eq. **S7** and determined the fitting parameter C for the jumping ciliate *Mesodinium rubrum* (Fig. S1 and Table S3, mean $C = 6.4$), jumping copepod nauplii (Fig. S2 and Table S4, mean $C = 5.7$), and swimming marine cladoceran *Podon intermedius* (Fig. S3 and Table S5, mean $C = 3.2$). The results show that the estimates of C decrease as Re increases, as expected. Further, there is a good qualitative and quantitative correspondence between model predictions and the spatial attenuation of the flow (Figs. S1–S3), the magnitude of the imposed flow velocities, and the flow fields and streamlines created by the breast swimmers (Fig. S4 and Movie S5).

1. Jiang H, Kiørboe T (2011) The fluid dynamics of swimming by jumping in copepods. *J R Soc Interface* 8(61):1090–1103.
2. Kiørboe T, Jiang H (2013) To eat and not be eaten: Optimal foraging behavior in suspension feeding copepods. *J R Soc Interface* 10(78):20120693.
3. Batchelor GK (1967) *An Introduction to Fluid Dynamics* (Cambridge Univ Press, Cambridge, UK).
4. Pozrikidis C (1997) *Introduction to Theoretical and Computational Fluid Dynamics* (Oxford Univ Press, Oxford).

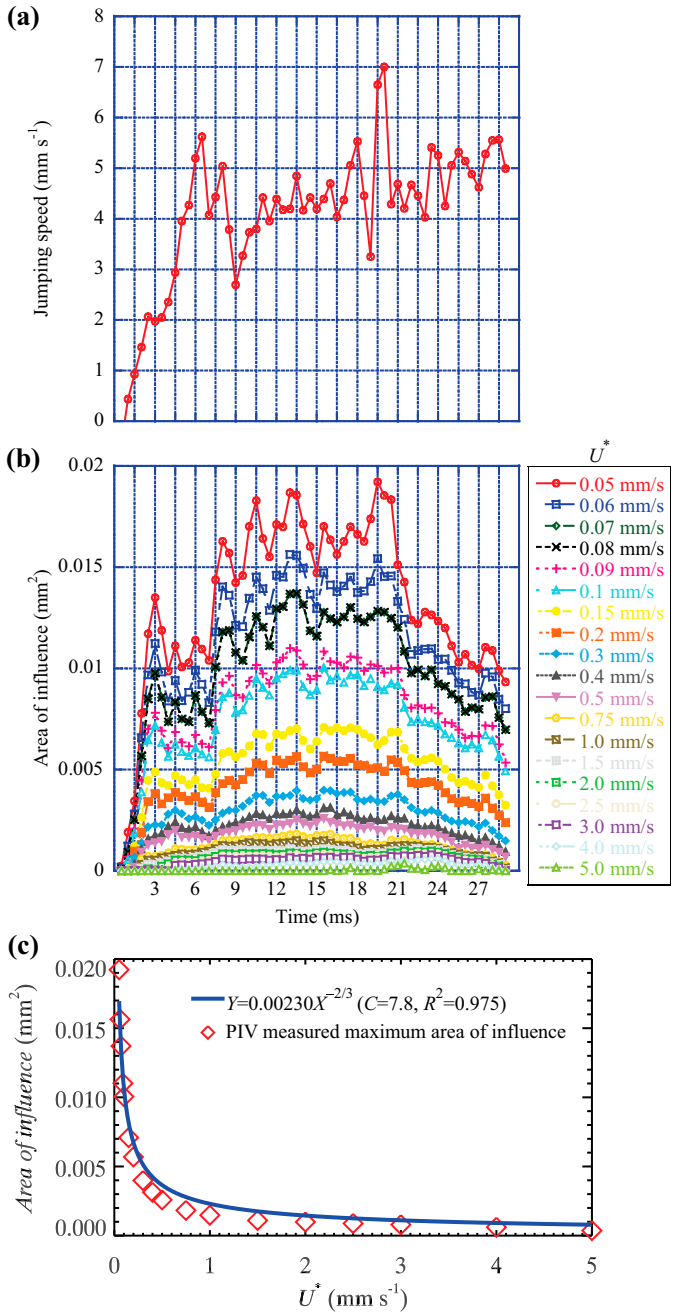

Fig. S1. Jumping ciliate *Mesodinium rubrum* (event 22 of Table S3). (*A*) Time evolution of the jumping speed. (*B*) Time evolutions of areas of influence of the jumping-imposed flow, corresponding to different velocity thresholds U^*. (*C*) Fitting of PIV measured data of maximum area of influence to the dipole model, Eq. **S7**.

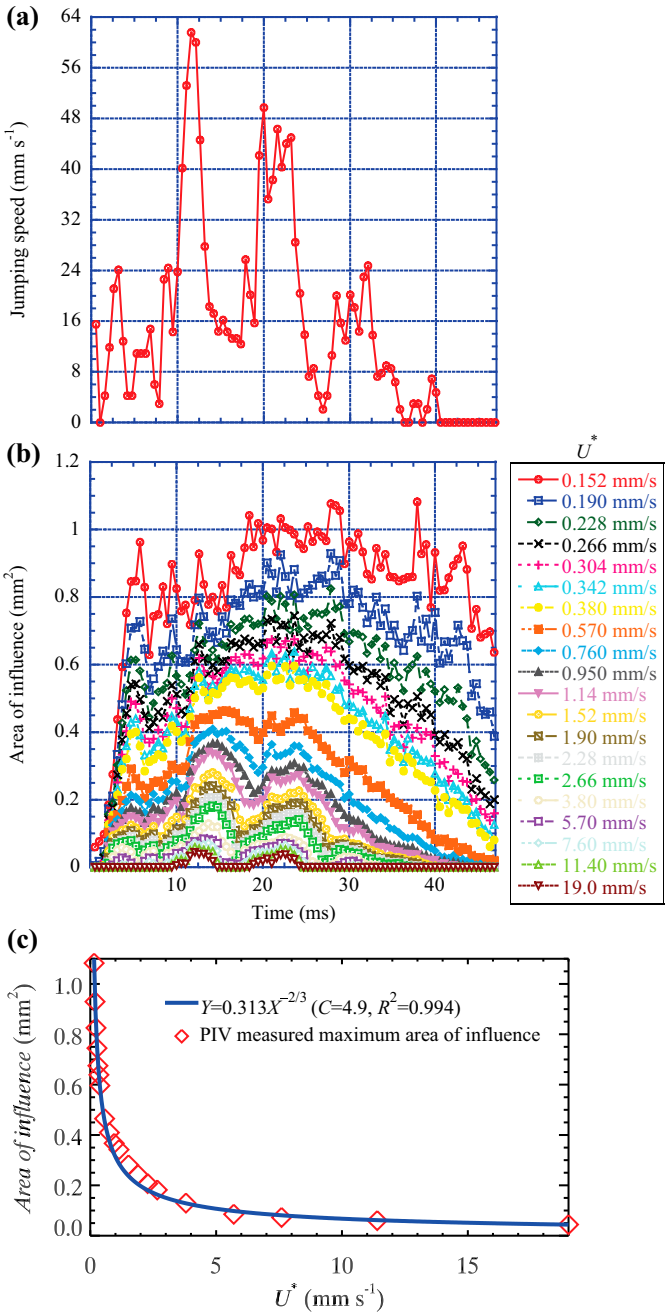

Fig. S2. Jumping *Temora longicornis* nauplius (event 06-05 of Table S4). (*A*) Time evolution of the jumping speed. (*B*) Time evolutions of areas of influence of the jumping-imposed flow, corresponding to different velocity thresholds U^*. (*C*) Fitting of PIV measured data of maximum area of influence to the dipole model, Eq. **S7**.

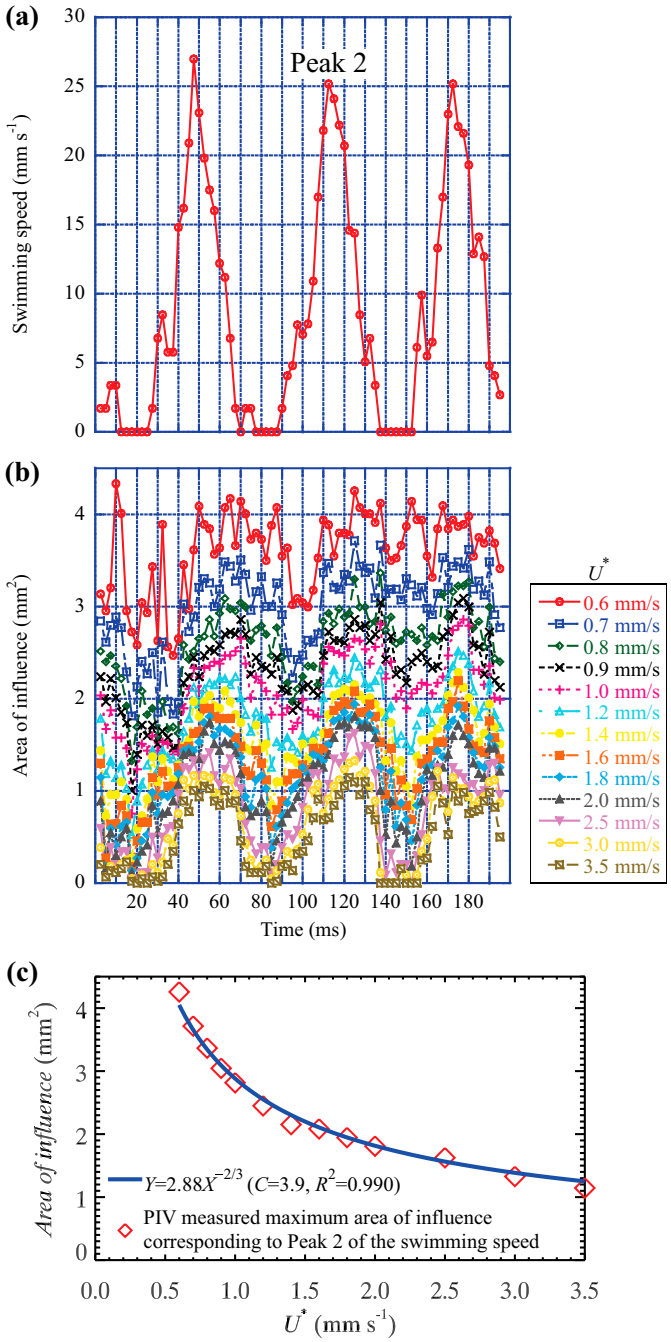

Fig. S3. Swimming marine cladoceran *Podon intermedius* (event 4 of Table S5). (*A*) Time evolution of the swimming speed. (*B*) Time evolutions of areas of influence of the swimming-imposed flow, corresponding to different velocity thresholds U^*. (*C*) Fitting of PIV measured data of maximum area of influence (corresponding to peak 2 of the swimming speed in *A*) to the dipole model, Eq. **S7**.

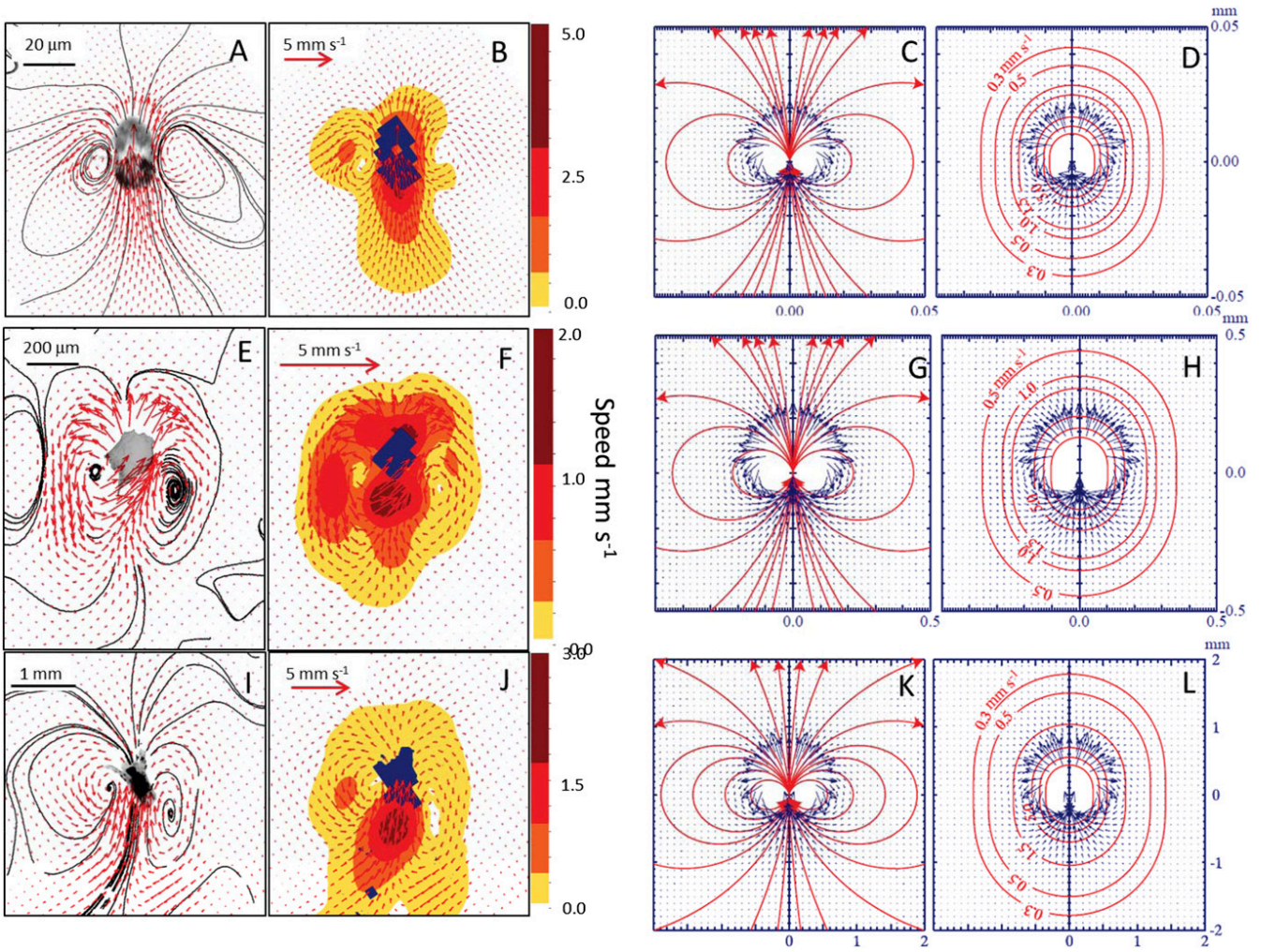

Fig. S4. Observed (*A*, *B*, *E*, *F*, *I*, and *J*) and calculated (*C*, *D*, *G*, *H*, *K*, and *L*) streamlines, flow fields, and velocity magnitudes for three species of breast-swimming zooplankton: *Mesodinium rubrum* (*A*–*D*), nauplius of *Temora longicornis* (*E*–*H*), and *Podon intermedius* (*I*–*L*).

Table S1. Summary information for each experiment

Species	Propulsion mechanism F/C/A; A/P/V/L/	Length, mm	Max speed, mm·s^{-1}	Speed variability index, s^{-1}	Reynolds no.	Beat frequency, Hz	Beat duration, ms	Power of spatial attenuation	$S_{0.5\ mm/s}$, mm^2	Orientation
Swimming										
Podon intermedius	-/-/A; -/-/-/L	0.75	30	28	22.5	15	36	−2	4.9	DV
P. intermedius	-/-/A; -/-/-/L	0.88	32.5	27	28.6	11	34	−2	6.3	LV→V
P. intermedius	-/-/A; -/-/-/L	0.78	35	33	27.3	13	29	−3	5.6	DV
P. intermedius	-/-/A; -/-/-/L	0.82	27	28	22.14	6	30	−3	5.6	D
P. intermedius	-/-/A; -/-/-/L	0.86	30	27	25.8	9	28	−3	6.8	VL
P. intermedius	-/-/A; -/-/-/L	0.8	50	44	40	20	28	−2	7.2	V
P. intermedius	-/-/A; -/-/-/L	0.83	45	48	37.35	18	28	−3	9.4	V
Temora longicornis, nauplius	-/-/A; -/-/-/L	0.31	60	156	18.6	111	5	−3	0.30	DL
T. longicornis, nauplius	-/-/A; -/-/-/L	0.30	56	144	16.8	125	4	−2.5	0.50	DL
T. longicornis, nauplius	-/-/A; -/-/-/L	0.19	65	246	12.4	38	6.3	−3	0.50	VL
Acartia tonsa, nauplius	-/-/A; -/-/-/L	0.24	23	68	5.5	67	12	−2	0.25	DL
A. tonsa, nauplius	-/-/A; -/-/-/L	0.14	22.5	118	3.2	67	9	−3	0.27	D
A. tonsa, nauplius	-/-/A; -/-/-/L	0.14	20	101	2.8	59	7	−3	0.24	D
Oithona davisae, female	-/-/A; -/-/V/-	0.30	80	224	24.0	57	11	−4	1.5	VL
O. davisae, female	-/-/A; -/-/V/-	0.31	95	239	29.5	57	11	−4	1.5	VL
O. davisae, male	-/-/A; -/-/V/-	0.32	48	137	15.4	11	12		0.92	L→V
O. davisae, male	-/-/A; -/-/V/-	0.31	35	95	10.9	17	17	−4	0.88	V→LV
O. davisae, male	-/-/A; -/-/V/-	0.32	50	139	16.0	14	12	−4	0.89	V
A. tonsa, copepodit	-/-/A; -/-/V/-	0.65	110	126	71.5		7	−3.5	5.0	L
A. tonsa, copepodit	-/-/A; -/-/V/-	0.37	95	211	35.2	67	6	−4	1.6	L
A. tonsa, copepodit	-/-/A; -/-/V/-	0.55	110	145	60.5		11	−3.5	4.0	L
A. tonsa, copepodit	-/-/A; -/-/V/-	0.7	91.5	98	64.1		—	−3	6.0	LV
Mesodinium rubrum	-/C/-; -/-/V/L	0.021	4.5	38	0.095	60	—	−2.5	0.0011	—
M. rubrum	-/C/-; -/-/V/L	0.023	6	61	0.138	60	—	−2.5	0.0025	—
M. rubrum	-/C/-; -/-/V/L	0.026	6	92	0.156	60	—	−2.5	0.0017	—
M. rubrum	-/C/-; -/-/V/L	0.033	7	73	0.231	60	—	−3	0.0024	—
Feeding and swimming										
A. tonsa, copepodit	-/-/A; A/-/V/-	0.81	8	6	8.9	67	—	−3	4.3	LV
A. tonsa, copepodit	-/-/A; A/-/V/-	0.86	6	3	6.5	60	—	−3	3.5	LV
A. tonsa, copepodit	-/-/A; A/-/V/-	0.77	5	2	6.5	76	—	−4	3.6	DL
A. tonsa, copepodit	-/-/A; A/-/V/-	0.8	5.5	3	6.8	68	—	−4	4.0	L
A. tonsa, copepodit	-/-/A; A/-/V/-	0.81	5	2	5.7	68	—	−3	4.0	LV
Metridia longa, copepodit	-/-/A; A/-/V/-	2.42	15	3	36.3	16	—	−3	55.6	L
M. longa, copepodit	-/-/A; A/-/V/-	2.48	15.5	0	38.4	20	—	−2	108.0	LV
M. longa, copepodit	-/-/A; A/-/V/-	2.51	17	0	42.7	19	—	−3	63.5	L
M. longa, copepodit	-/-/A; A/-/V/-	2.69	13.1	0	35.2	16	—	−2	60.0	L

Table S1. Cont.

Species	Propulsion mechanism F/C/A; A/P/V/L/	Length, mm	Max speed, $mm \cdot s^{-1}$	Speed variability index, s^{-1}	Reynolds no.	Beat frequency, Hz	Beat duration, ms	Power of spatial attenuation	$S_{0.5\ mm/s}$, mm^2	Orientation
T. longicornis, nauplius	-/-/A; A/-/V/-	0.18	1.5	5	0.49	50	—	−2	0.15	A
T. longicornis, nauplius	-/-/A; A/-/V/-	0.16	1.4	6	0.38	48	—	−2	0.17	A
T. longicornis, nauplius	-/-/A; A/-/V/-	0.23	1.2	4	0.46	33	—	−2	0.13	A
T. longicornis, nauplius	-/-/A; A/-/V/-	0.22	1	4	0.66	43	—	−2	0.17	L
T. longicornis, nauplius	-/-/A; A/-/V/-	0.31	0.25	1	0.54	39	—	−2	0.27	L
T. longicornis, nauplius	-/-/A; A/-/V/-	0.16	1.5	7	0.27	38	—	−2	0.25	
Brachionus plicatilis	-/C/-; A/-/-/-	0.26	0.99	0	0.36	10	—	−1	0.058	—
B. plicatilis	-/C/-; A/-/-/-	0.24	0.38	0	0.19	10	—	−1.5	0.023	—
B. plicatilis	-/C/-; A/-/-/-	0.24	0.34	0	0.18	10	—	−1	0.018	—
T. longicornis, copepodit	-/-/A; A/-/V/-	0.79	0.11	0	4.04	28	—	−1.5	8	D
T. longicornis, copepodit	-/-/A; A/-/V/-	0.63	0.06	0	3.19	26	—	−1	12	V
T. longicornis, copepodit	-/-/A; A/-/V/-	0.69	0.04	0	3.48	23	—	−1.5	2	D
T. longicornis, copepodit	-/-/A; A/-/V/-	0.73	0.06	0	3.69	26	—	−1.5	13	D
Akashiwo sanguinea	F/-/-; -/P/-/-	0.049	0.1	1	0.0049	50	—	−2	0.00012	—
Heterocapsa triquetra	F/-/-; -/P/-/-	0.021	0.1	1	0.0021	88	—	−1.5	1.2*E*-05	—
Karlodinium armiger	F/-/-; -/P/-/-	0.018	0.25	6	0.0045	85	—	−2	0.00006	—
K. armiger	F/-/-; -/P/-/-	0.017	0.18	3	0.0031	69	—	−2	0.000036	—
Oxyrrhis marina	F/-/-; -/P/-/-	0.028	0.25	3	0.0070	60	—	−2	0.00004	—
O. marina	F/-/-; -/P/-/-	0.027	0.25	3	0.0068	75	—	−1	0.000032	—
O. marina	F/-/-; -/P/-/-	0.025	0.3	4	0.0075	63	—	−2	0.000156	—
O. marina	F/-/-; -/P/-/-	0.029	0.22	3	0.0064	76	—	−1	0.000035	—
O. marina	F/-/-; -/P/-/-	0.028	0.3	4	0.0084	64	—	−1.5	9.3*E*-05	—
O. marina	F/-/-; -/P/-/-	0.029	0.35	6	0.0102	67	—	−2	0.00024	—

Propulsion mechanism refers to whether the organism uses flagella (F), cilia (C), or appendages (F/C/A) and where the propellers are positioned [anterior (A), posterior (P), ventrally (V), or laterally (L): A/P/V/L]. Length is the cell length for protozoans and the body length for animals. Speed variability index is computed as the difference between the maximum and average speed divided by the length of the organism. Reynolds number is the body Reynolds number computed from the velocity of the water past the organism. Beat frequency is the frequency of the beating of the flagella, cilia, or appendages. Beat duration is the duration of the power stroke for swimmers. Power of spatial attenuation was estimated from log–log plots of flow speed (U^*) vs. distance. $S_{0.5\ mm/s}$ is the area within which the induced flow velocity exceeds 0.5 $mm \cdot s^{-1}$. Orientation is the orientation of the organism relative to the camera: dorsal (D), lateral (L), ventral (V), or anterior (A) views or combinations of these (e.g., VL: ventrolateral). An arrow indicates that the organism turned during the sequence. In all cases the organisms were moving in the laser (or focal) plane. Orientation makes little sense for protists and is not recorded.

Table S2. Summary of the equations of the four idealized models used to describe flow generated by swimming and feeding zooplankton

Model	Velocity magnitude, U	Area of influence, S, for a given velocity threshold, U^*	Model parameter
Stokeslet	$U = \frac{F}{8\pi\mu}\frac{\sqrt{4x^2+r^2}}{x^2+r^2}$	$S = \frac{0.02}{\pi\mu^2}\left(\frac{F}{U^*}\right)^2$	F: point force magnitude, N
	$U \sim d^{-1}$	$S \sim (U^*)^{-2}$	
Stresslet	$U = \frac{Q}{8\pi\mu}\frac{\lvert 2x^2-r^2\rvert}{(x^2+r^2)^2}$	$S = \frac{0.2}{\pi\mu}\left(\frac{Q}{U^*}\right)$	Q: stresslet strength, N·m
	$U \sim d^{-2}$	$S \sim (U^*)^{-1}$	
Potential dipole	$U = \frac{J}{4\pi}\frac{\sqrt{4x^2+r^2}}{(x^2+r^2)^2}$	$S = 0.3845\left(\frac{J}{U^*}\right)^{2/3}$	J: dipole strength, $m^4 \cdot s^{-1}$
	$U \sim d^{-3}$	$S \sim (U^*)^{-2/3}$	
Impulsive stresslet, at $t = 0^+$	$U = \frac{3M}{4\pi}\frac{\sqrt{4x^4+r^4}}{(x^2+r^2)^3}$	$S = 0.868\left(\frac{M}{U^*}\right)^{1/2}$	M: impulsive stresslet strength, $m^5 \cdot s^{-1}$
	$U \sim d^{-4}$	$S \sim (U^*)^{-1/2}$	

The velocity magnitude scaling with distance, d, and the area of influence scaling with velocity, U^*, are emphasized. The solutions are written in the cylindrical polar coordinate system (x, r, ϕ), where x is the axial coordinate, r is the radial coordinate, and ϕ is the azimuthal coordinate. μ: dynamic viscosity ($kg \cdot m^{-1} \cdot s^{-1}$).

Table S3. Summary of dipole analysis of flow imposed by jumping *Mesodinium rubrum*

Event no.	Body length, mm	Maximum jumping speed, $mm \cdot s^{-1}$	Fitting parameter, C	R^2
22	0.024	7.0	7.8	0.975
25	0.021	4.6	6.5	0.906
26	0.026	5.2	6.5	0.926
29	0.033	5.6	4.6	0.924
Mean ± SD	0.026 ± 0.005	5.6 ± 1.0	6.4 ± 1.3	0.933 ± 0.030

Table S4. Summary of dipole analysis of flow imposed by jumping copepod nauplii

Event no.	Body length, mm	Maximum jumping speed, $mm \cdot s^{-1}$	Fitting parameter, C	R^2
Acartia tonsa nauplius 05-23	0.24	24.0	1.5	0.921
A. tonsa nauplius 05-26	0.14	21.9	13.5	0.972
A. tonsa nauplius 05-27	0.14	18.2	12.0	0.979
Temora longicornis nauplius 05-02	0.31	54.0	0.9	0.891
T. longicornis nauplius 05-03	0.30	56.3	1.5	0.910
T. longicornis nauplius 06-05	0.19	61.6	4.9	0.994
Mean ± SD	0.22 ± 0.08	39.3 ± 19.9	5.7 ± 5.6	0.945 ± 0.042

Table S5. Summary of dipole analysis of flow imposed by swimming *Podon intermedius*

Event no.	Peak	Body length, mm	Peak swimming speed, mm·s^{-1}	Fitting parameter, C	R^2
4	Peak 1	0.75	27.0	3.3	0.979
	Peak 2		25.2	3.9	0.990
	Peak 3		25.2	3.8	0.985
5	Peak 1	0.88	32.7	2.6	0.911
	Peak 2		28.0	2.8	0.952
	Peak 3		27.4	2.6	0.948
	Peak 4		27.4	2.3	0.985
6	Peak 1	0.78	32.3	2.5	0.970
	Peak 2		35.3	3.1	0.968
	Peak 3		37.6	2.9	0.952
	Peak 4		29.0	3.5	0.946
8	Peak 1	0.82	25.8	3.5	0.906
	Peak 2		24.3	3.9	0.976
	Peak 3		25.5	3.4	0.923
	Peak 4		24.2	3.7	0.956
19	Peak 1	0.86	29.2	2.6	0.873
	Peak 2		26.5	3.7	0.892
29	Peak 1	0.80	46.1	1.9	0.909
	Peak 2		43.5	2.7	0.886
31	Peak 1	0.83	46.1	4.0	0.939
	Peak 2		43.5	4.7	0.902
Mean ± SD		0.82 ± 0.04	31.5 ± 7.5	3.2 ± 0.7	0.940 ± 0.036

For each individual, two to four consecutive power strokes were analyzed.

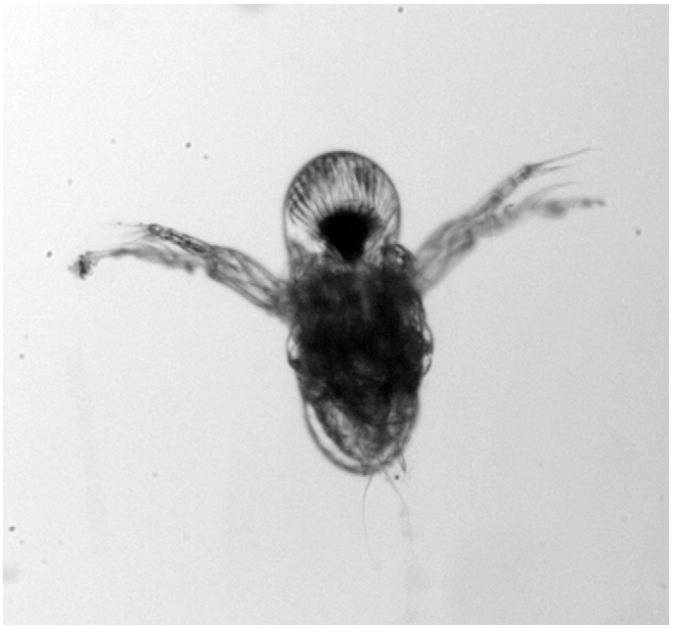

Movie S1. Swimming plankton. Short slow-motion video clips demonstrate the diversity of propulsion modes among the plankton organisms examined in this study. Each clip gives the name of the species, its size (for the scale), and by which factor the movie has been slowed down.

Movie S1

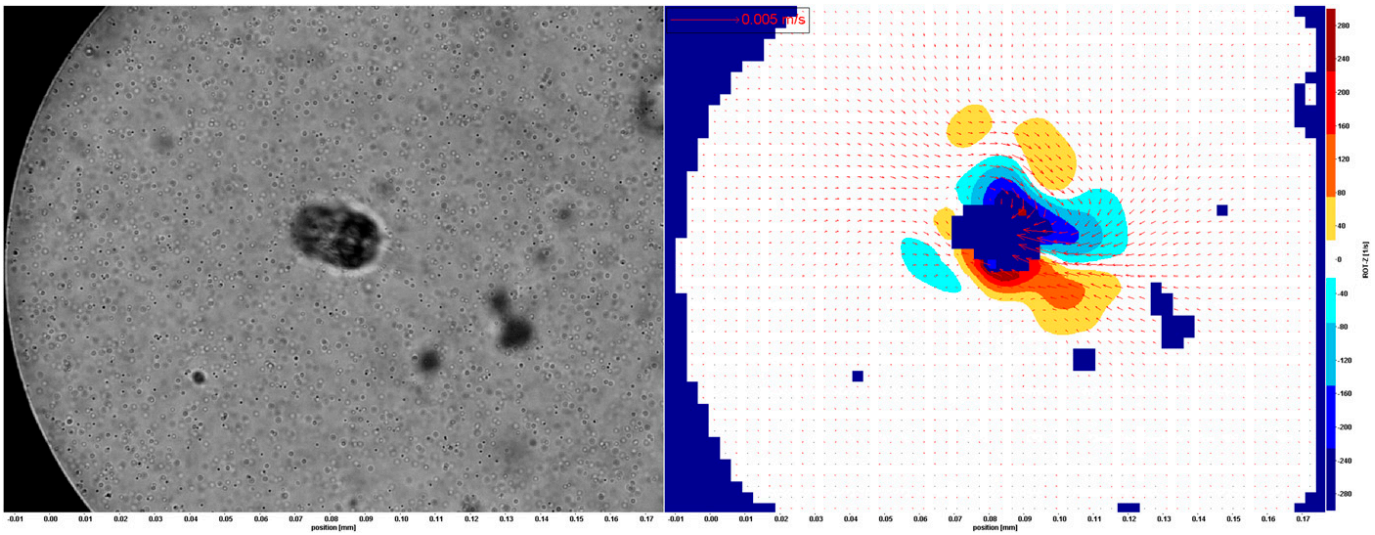

Movie S2. Animated flow and vorticity fields of swimming plankton: *Oxyrrhis marina* (dinoflagellate), *Brachionus plicatilis* (rotifer), and *Mesodinium rubrum* (ciliate).

Movie S2

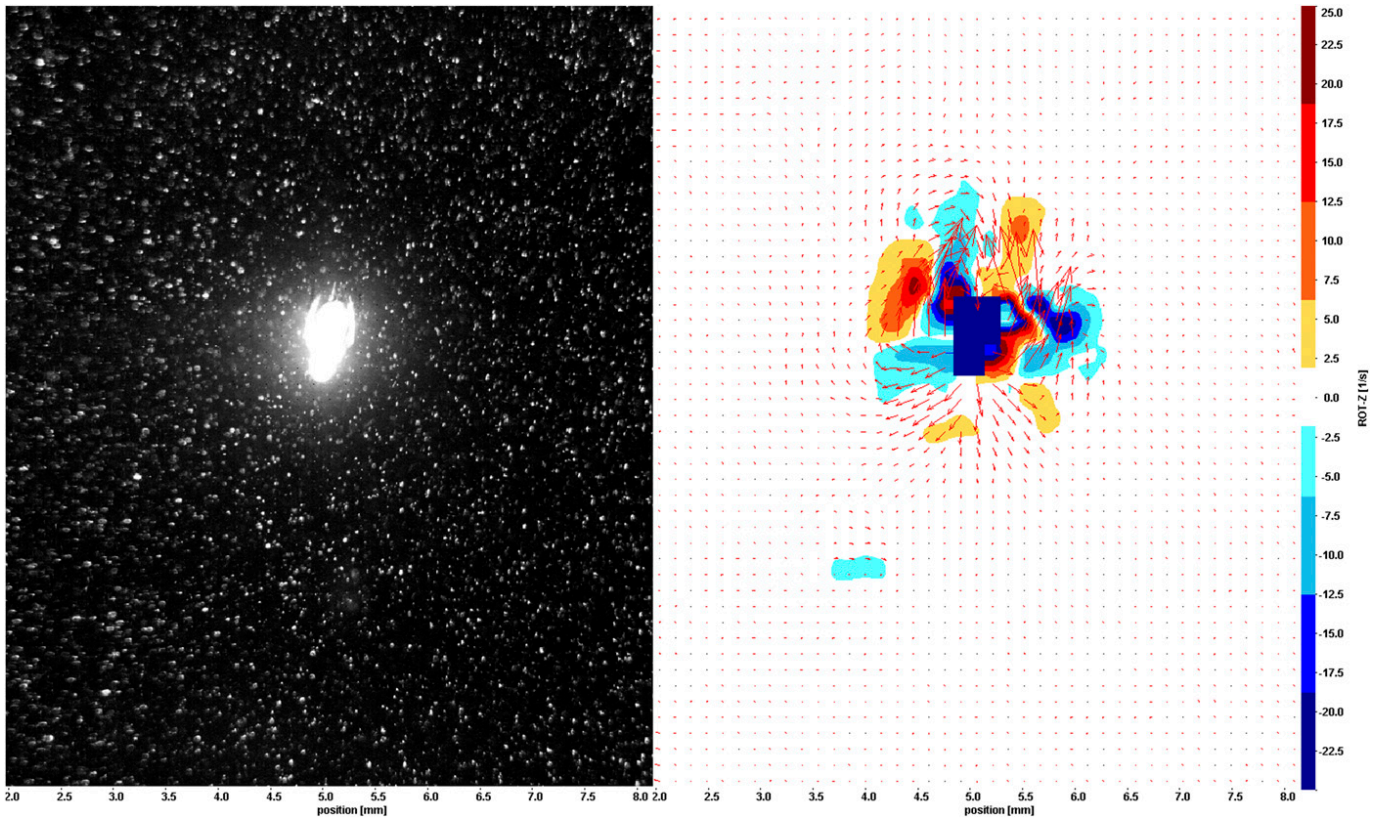

Movie S3. Animated flow and vorticity fields of swimming plankton: *Podon intermedius* (cladocera), feeding nauplius of *Temora longicornis* (copepod larva), and swimming nauplius of *T. longicornis* (copepod larva).

Movie S3

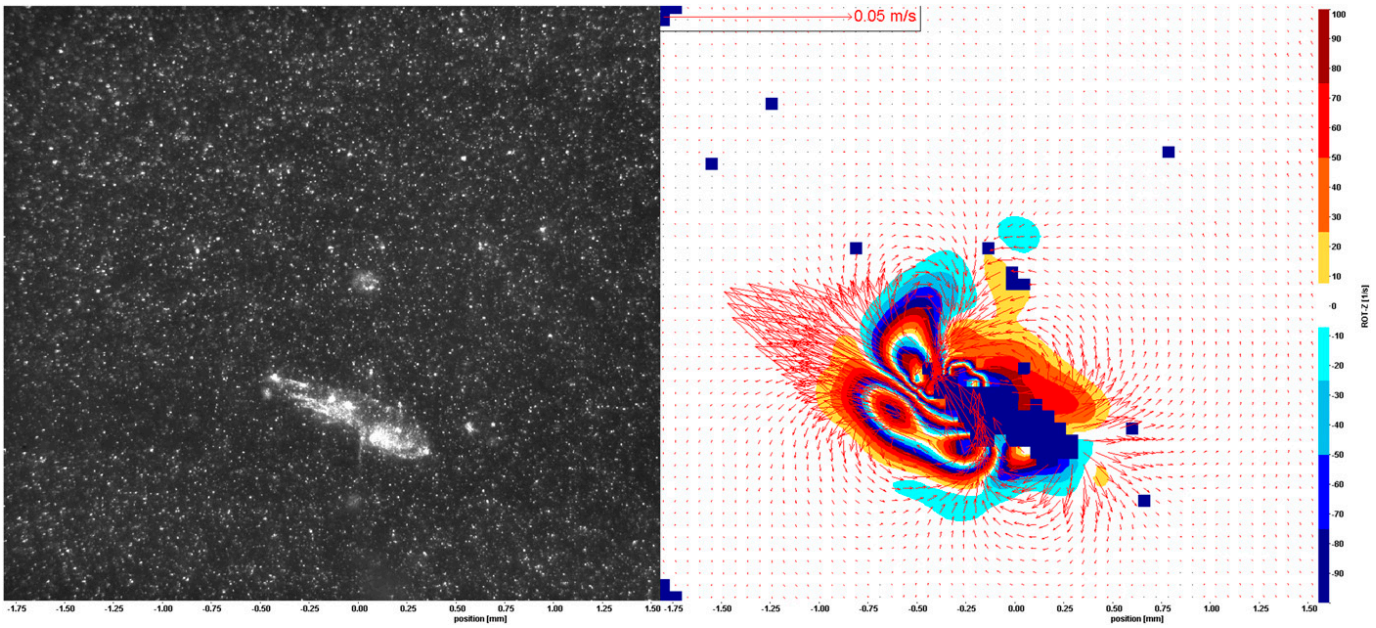

Movie S4. Animated flow and vorticity fields of swimming plankton: *Metridia longa* (copepod), feeding *Acartia tonsa* (copepod), and reposition jump of *A. tonsa*.

Movie S4

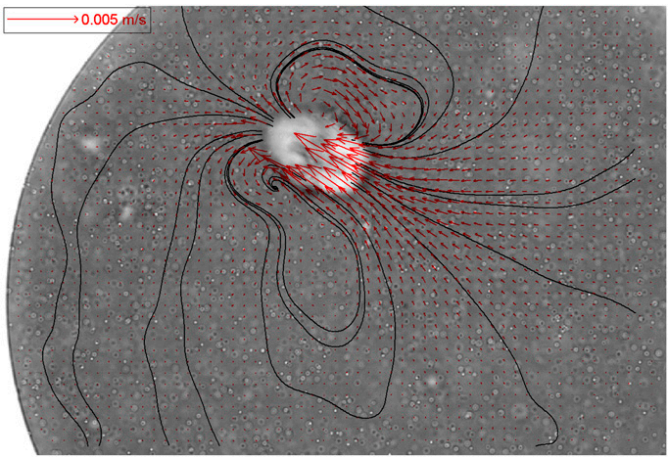

Movie S5. Animated flow fields and streamlines of swimming plankton (breast swimmers): *Mesodinium rubrum*, swimming nauplius of *Temora longicornis*, and *Podon intermedius*.

Movie S5

Chapter 7

Quiet swimming at low Reynolds number

Paper published in Physical Review E. (2015)

Quiet swimming at low Reynolds number

Anders Andersen,[1] Navish Wadhwa,[1] and Thomas Kiørboe[2]
[1]*Department of Physics and Centre for Ocean Life, Technical University of Denmark, DK-2800 Kgs. Lyngby, Denmark*
[2]*National Institute for Aquatic Resources and Centre for Ocean Life, Technical University of Denmark, DK-2920 Charlottenlund, Denmark*
(Received 18 July 2014; published 24 April 2015)

The stresslet provides a simple model of the flow created by a small, freely swimming and neutrally buoyant aquatic organism and shows that the far field fluid disturbance created by such an organism in general decays as one over distance squared. Here we discuss a quieter swimming mode that eliminates the stresslet component of the flow and leads to a faster spatial decay of the fluid disturbance described by a force quadrupole that decays as one over distance cubed. Motivated by recent experimental results on fluid disturbances due to small aquatic organisms, we demonstrate that a three-Stokeslet model of a swimming organism which uses breast stroke type kinematics is an example of such a quiet swimmer. We show that the fluid disturbance in both the near field and the far field is significantly reduced by appropriately arranging the propulsion apparatus, and we find that the far field power laws are valid surprisingly close to the organism. Finally, we discuss point force models as a general framework for hypothesis generation and experimental exploration of fluid mediated predator-prey interactions in the planktonic world.

DOI: 10.1103/PhysRevE.91.042712 PACS number(s): 47.63.Gd, 47.15.G−

Swimming is essential for feeding and reproduction of many aquatic organisms, as the encounter rates with prey and mates scale with swimming speed [1]. But there is a trade-off since the associated fluid disturbance may risk the survival of the swimmer by signaling its presence to rheotactic predators. Both the magnitude and the spatial decay of the fluid disturbance depend on the distribution of the propulsive forces and the drag forces on the organism [2–5]. The stresslet is the simplest possible model of the far field flow due to a single, freely swimming and neutrally buoyant low Reynolds number swimmer [6,7]. It describes the flow due to two oppositely directed point forces of equal magnitude that act at different points and represent the thrust due to the swimming appendages and the drag on the body of the organism, respectively. The stresslet gives rise to a fluid disturbance that decays as one over distance squared. Experimentally the stresslet has been found to capture the far field flow created by, e.g., the bacterium *Escherichia coli* [8].

For some low Reynolds number swimmers, the fluid forces due to the propulsion apparatus and the drag on the body of the organism cannot appropriately be described by two point forces only [6,7]. In a swimmer model with two point forces, the far field flow will be dominated by a force dipole. However, with three or more point forces, the force dipole term can be made to vanish and the far field flow will then be a force quadrupole that decays as one over distance cubed. Swimming spermatozoa provide such an example if only the middle portion of the flagellum produces thrust, whereas the two ends of the flagellum produce drag [3]. For such arrangements the force quadrupole can be the dominant term. Similarly the squirmer model can give rise to qualitatively different fluid disturbances depending on whether it represents a puller, a pusher, or a neutral swimmer for which the far field flow is a potential dipole [5,9–11]. The differences in the fluid interactions between pullers, pushers, and neutral swimmers have, e.g., been studied for dense suspensions of such squirmers [5].

In the present paper we focus on exploring the fluid disturbances due to low Reynolds number swimmers with breast stroke type kinematics. Breast stroke swimming is common among small aquatic organisms, and it has evolved independently in diverse taxonomic groups. Many unicellular organisms swim with breast stroke type kinematics [12–14], and the biflagellated green alga *Chlamydomonas reinhardtii* [Fig. 1(a)] has in particular been the subject of measurements and theoretical analysis [15–17]. The jumping ciliate *Mesodinium rubrum* [Fig. 1(b)] is also a breast stroke type swimmer since it propels itself with an equatorial ciliary belt [4]. The crustacean nauplii, e.g., *Acartia tonsa* [Fig. 1(c)], which is one of the most widespread and successful larval forms in nature [18], swim with a breast stroke [19,20], and the adults of the crustacean order Cladocera, e.g., *Podon intermedius* [Fig. 1(d)], are breast stroke swimmers. It has been suggested that the prevalence of breast stroke swimming in nature could be due to its reduced fluid disturbance. For breast stroke swimmers such as *M. rubrum*, *A. tonsa*, and *P. intermedius* the fluid disturbances have been measured using particle image velocimetry to decay as one over distance cubed [20]. This quiet swimming mode is advantageous for organisms that swim to locomote whereas organisms that swim to feed give rise to fluid disturbances with slower spatial decay [20]. Inspired by these observations and further motivated by the relevance of breast stroke swimming to many plankton, we investigate this propulsion method using a point force model in which two appendages, one on each side of the left-right symmetric organism, each generate half of the propulsive force. The model allows us to explore the possibility of modifying the fluid disturbance by repositioning the point forces that represent the propulsion apparatus.

The three-Stokeslet model is our main example (Fig. 2). The point forces 1 and 2, each of magnitude F, represent the forces due to the swimming appendages or flagella and the point force 3, of magnitude $2F$, represents the force due to the body of the organism. All three point forces are acting at points in the xz plane in the negative or in the positive z direction, respectively, and the organism is swimming in the positive z direction. The three-Stokeslet model has been used to successfully

 ©2015 American Physical Society

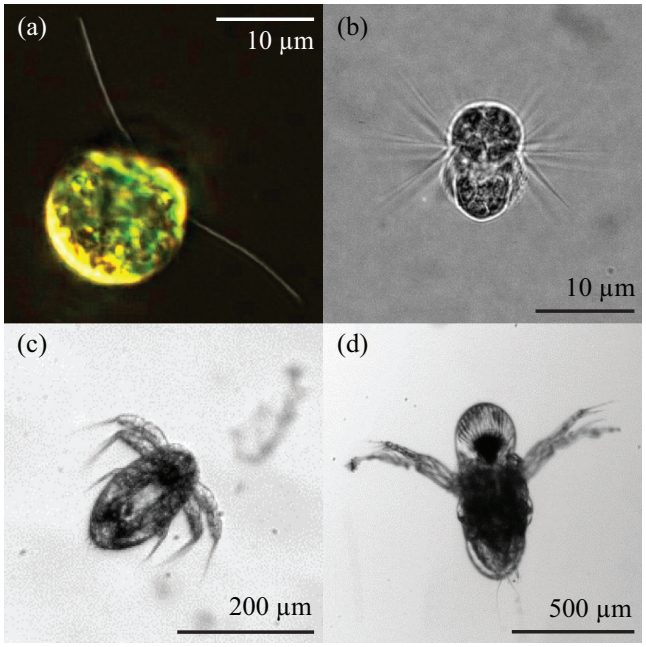

FIG. 1. (Color online) Planktonic breast stroke swimmers across taxonomic groups and sizes: (a) *Chlamydomonas reinhardtii*, a flagellate (image courtesy of Knut Drescher); (b) *Mesodinium rubrum*, a ciliate; (c) a nauplius (juvenile) of *Acartia tonsa*, a copepod; and (d) *Podon intermedius*, a cladoceran. The Reynolds numbers of the swimmers are approximately 10^{-3}, 0.1, 10, and 10, respectively.

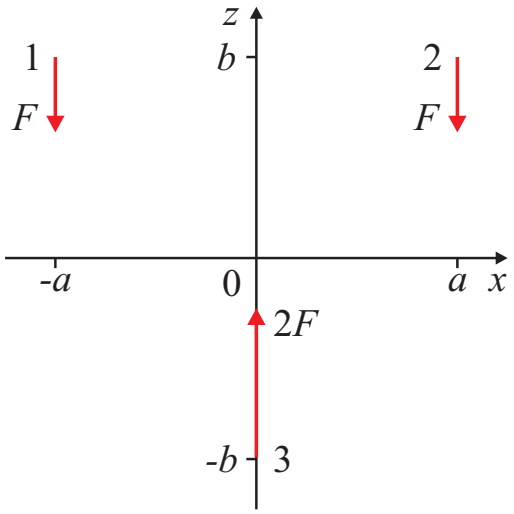

FIG. 2. (Color online) Three-Stokeslet model of a breast stroke swimming aquatic organism. The red vectors represent the point forces.

model the time-averaged flow field around freely swimming *C. reinhardtii* [15], and we believe that it is an appropriate model for both the near and the far field around other small breast stroke swimmers as well. Due to out of plane appendage motion some breast stroke swimmers rotate around their length axis while swimming. We only consider in-plane and left-right symmetric placement of propulsive forces, because the rotational frequency typically is an order of magnitude smaller than the appendage beat frequency and synchronous beating is the dominant mechanism in swimming [19,21].

The basic building block in point force models like the three-Stokeslet model is the low Reynolds number flow due to a point force $\boldsymbol{F} = (F_x, F_y, F_z)$ which is acting at a source point $\boldsymbol{x}' = (x', y', z')$. The resulting flow velocity $\boldsymbol{v} = (v_x, v_y, v_z)$ at the field point $\boldsymbol{x} = (x, y, z)$ is in index notation

$$v_i(\boldsymbol{x}) = \frac{1}{8\pi\mu}\left[\frac{F_i}{|\boldsymbol{x}-\boldsymbol{x}'|} + \frac{F_j(x_j - x_j')(x_i - x_i')}{|\boldsymbol{x}-\boldsymbol{x}'|^3}\right], \quad (1)$$

where μ is the dynamic viscosity of the fluid [22]. To describe the flow in the far field where the distance from the origin to the field point $r = (x_i\, x_i)^{1/2}$ is much larger than the distance from the origin to the source point $r' = (x_i'\, x_i')^{1/2}$, we make use of the binomial series and obtain the multipole expansion

$$v_i(\boldsymbol{x}) = \frac{1}{8\pi\mu}\left[\left(\frac{\delta_{ij}}{r} + \frac{x_i x_j}{r^3}\right)F_j + \left(\frac{x_k\delta_{ij} - x_i\delta_{jk} - x_j\delta_{ik}}{r^3} + \frac{3x_i x_j x_k}{r^5}\right)F_j x_k' + \frac{1}{2}\left(\frac{2\delta_{ik}\delta_{jl} - \delta_{ij}\delta_{kl}}{r^3} - 3\frac{2\delta_{il}x_j x_k + 2\delta_{jl}x_i x_k + \delta_{kl}x_i x_j - \delta_{ij}x_k x_l}{r^5} + \frac{15x_i x_j x_k x_l}{r^7}\right)F_j x_k' x_l' + \cdots\right], \quad (2)$$

where the three terms represent the force monopole, the force dipole, and the force quadrupole, respectively. The strength of the force monopole is described by the force vector F_j, the force dipole by the tensor $p_{jk} = F_j x_k'$, and the force quadrupole by the tensor $t_{jkl} = (1/2)F_j x_k' x_l'$. To determine the total monopole, dipole, and quadrupole terms in the far field flow due to a superposition of N point forces, we add the individual contributions

$$F_j = \sum_{n=1}^{N} F_{n,j}, \quad p_{jk} = \sum_{n=1}^{N} p_{n,jk}, \quad t_{jkl} = \sum_{n=1}^{N} t_{n,jkl}. \quad (3)$$

The strengths depend only on the applied forces and their distribution in space. For a given set of point forces, the dipole and higher order terms can be modified by rearranging the points of action of the forces. The force multipole solutions are usually used to approximate the far field solution for the flow due to an arbitrarily shaped body with a given surface stress distribution [23], analogous to the approach in electrostatics [24], or as a computational tool [22,25,26].

We now return to the three-Stokeslet model (Fig. 2). We note that the essential parameter in describing the geometry of the point force configuration is the aspect ratio $\alpha = b/a$. The exact velocity field in the model is the sum of the three point force contributions. In the following when plotting the velocity field we use the length scale a and the velocity scale $u = F/(8\pi\mu a)$. Figure 3 shows the velocity fields in the xz plane for $\alpha = 1$, $\alpha = 0.1$, and $\alpha = 0$, respectively. The flows

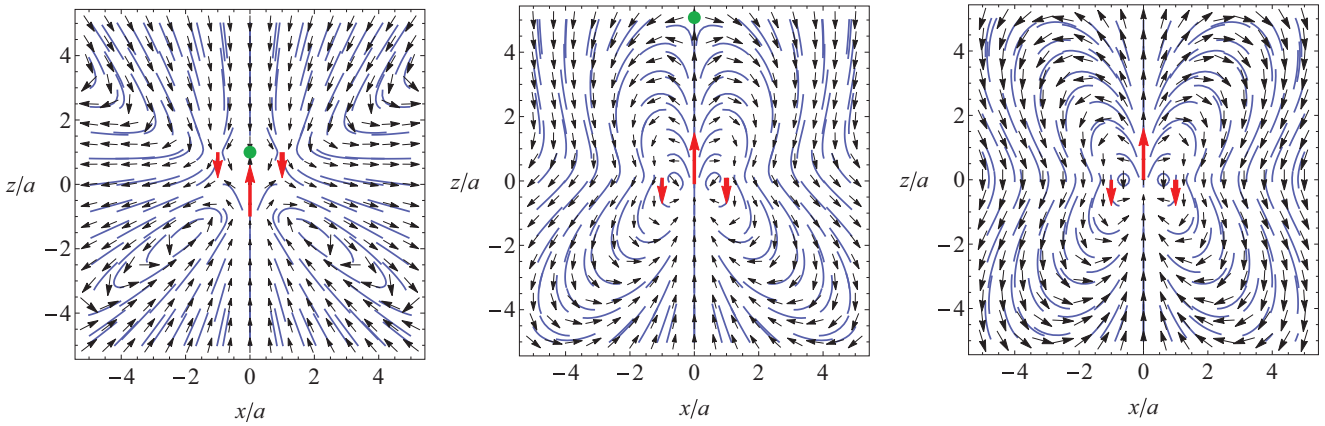

FIG. 3. (Color online) Velocity fields in the three-Stokeslet model: (left) $\alpha = 1$, (middle) $\alpha = 0.1$, and (right) $\alpha = 0$. The thick red arrows represent the point forces and the green dots the stagnation points on the z axis. The flow fields are shown as thin black vectors and blue streamline segments.

in the three cases are qualitatively different. When $\alpha = 1$ two large lateral whirls are present and the flow has a stagnation point on the positive z axis at $z/a = 1$. The stagnation point on the positive z axis is located approximately at $z/a \approx 1/(2\alpha)$ when $0 < \alpha \ll 1$. The stagnation point is therefore at $z/a \approx 5$ when $\alpha = 0.1$. When $\alpha = 0$ the flow on the entire z axis is in the positive z direction and the whirl centers are on the x axis at $x/a = \pm(\sqrt{5} - 1)/2 \approx \pm 0.6180$.

The predicted flow fields for low α values correspond qualitatively with the flow fields measured recently using particle image velocimetry for *A. tonsa* nauplii [27] and *P. intermedius* [20]. Also, the stagnation point on the positive z axis and the two large lateral whirls in the velocity field in the $\alpha = 1$ force configuration are found in the average velocity field observed around the breast stroke swimming *C. reinhardtii* [15]. Similarly, the flows due to our model swimmer with variable α agree qualitatively with the unsteady two-dimensional velocity field measured for *C. reinhardtii* in a thin liquid film [16]. This comparison suggests that unsteady flows around other breast stroke swimmers at low Reynolds number can be captured in quasisteady approximation by the three-Stokeslet model.

The forces in the three-Stokeslet model are pointing in the positive and in the negative z direction, respectively, and because of the left-right symmetry, p_{zz} is the only possible nonzero component of the tensor describing the strength of the force dipole. By adding the three contributions we obtain $p_{zz} = -4Fb$, which depends linearly on b and vanishes when $b = 0$. Similarly we find the only nonzero component of the tensor describing the force quadrupole $t_{zxx} = -Fa^2$. The multipole expansion of the three-Stokeslet velocity field becomes

$$v_x \approx \frac{F}{8\pi\mu}\left[\frac{4bx}{r^3}\left(1 - 3\left(\frac{z}{r}\right)^2\right) + \frac{3a^2xz}{r^5}\left(3 - 5\left(\frac{x}{r}\right)^2\right)\right], \tag{4}$$

$$v_y \approx \frac{F}{8\pi\mu}\left[\frac{4by}{r^3}\left(1 - 3\left(\frac{z}{r}\right)^2\right) + \frac{3a^2yz}{r^5}\left(1 - 5\left(\frac{x}{r}\right)^2\right)\right], \tag{5}$$

$$v_z \approx \frac{F}{8\pi\mu}\left[\frac{4bz}{r^3}\left(1 - 3\left(\frac{z}{r}\right)^2\right) + \frac{a^2}{r^3}\left(1 - 3\frac{x^2 - z^2}{r^2} - \frac{15x^2z^2}{r^4}\right)\right]. \tag{6}$$

For the magnitude of the velocity v on the x axis we find asymptotically

$$\frac{v}{u} = \begin{cases} \frac{4\alpha}{|x/a|^2}, & \text{if} \quad \alpha \neq 0, \\ \frac{2}{|x/a|^3}, & \text{if} \quad \alpha = 0, \end{cases} \tag{7}$$

and similarly on the z axis

$$\frac{v}{u} = \begin{cases} \frac{8\alpha}{|z/a|^2}, & \text{if} \quad \alpha \neq 0, \\ \frac{4}{|z/a|^3}, & \text{if} \quad \alpha = 0. \end{cases} \tag{8}$$

We find that the expressions provide good approximations of the flow for $r/a > 3$ when $\alpha = 1$ and $\alpha = 0$ (Fig. 4). The force dipole dominates for $r/a \gg 1/\alpha$ when $\alpha \neq 0$, and the magnitude of the flow velocity therefore decays as one over distance squared for $r/a > 3$ when $\alpha = 1$. In contrast the force dipole is eliminated when $\alpha = 0$ and the magnitude of the flow velocity is well described by the force quadrupole and decays as one over distance cubed. Asymptotically we find on both the x axis and the z axis that $v_{\alpha=1}/v_{\alpha=0} = 2(r/a)$, and as an example we therefore have $v_{\alpha=1}/v_{\alpha=0} \approx 10$ when $r/a = 5$. This shows that the fluid disturbance is reduced significantly by positioning the propulsion apparatus appropriately. When $\alpha = 0.1$ the far field flow for $r/a > 10$ is dominated by the force dipole, but comparison with the far field expressions (7) and (8) shows that the magnitude of the flow velocity in the intermediate range $3 < r/a < 10$ is dominated by the force quadrupole and the fluid disturbance is small and comparable to the situation when $\alpha = 0$.

Our study has demonstrated that by appropriately arranging its propulsion apparatus a breast stroke swimmer produces only a small fluid disturbance with a fast spatial decay as observed experimentally for breast stroke swimming plankton such as *M. rubrum*, *A. tonsa* nauplii, and *P. intermedius* [20]. Breast stroke swimming may thus be advantageous in the

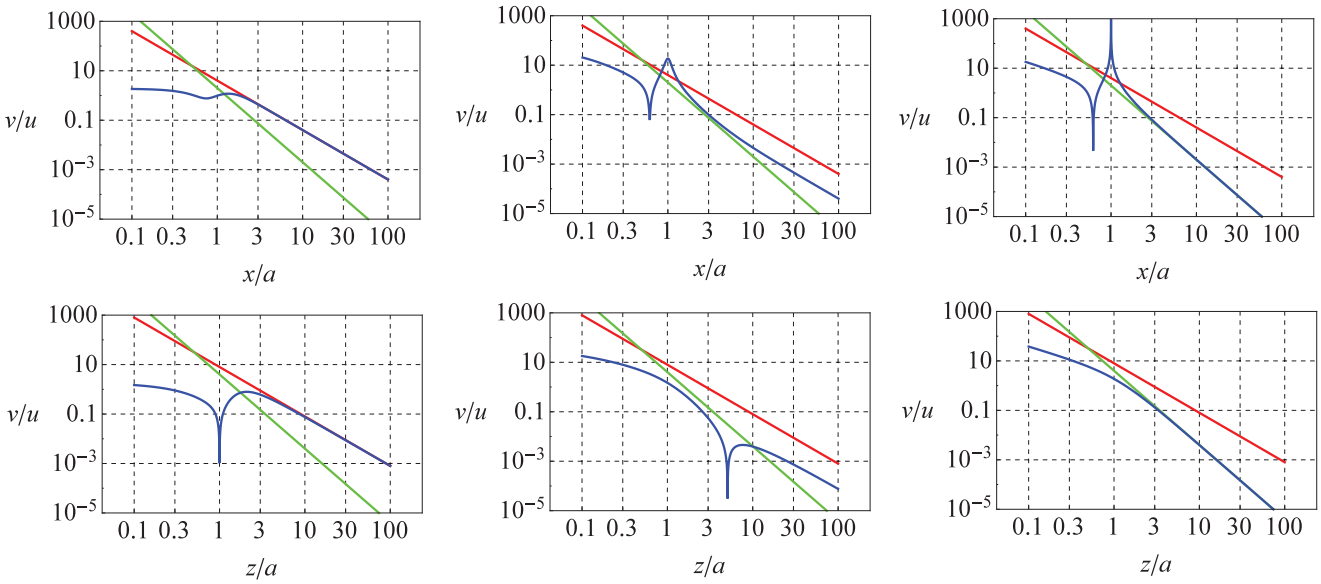

FIG. 4. (Color online) Magnitude of the velocity in the three-Stokeslet model (blue) on the positive x axis (top) and the positive z axis (bottom) with $\alpha = 1$ (left), $\alpha = 0.1$ (middle), and $\alpha = 0$ (right). Also shown are the far field approximations (7) and (8) for $\alpha = 1$ (red, r^{-2} decay) and $\alpha = 0$ (green, r^{-3} decay).

small-scale blind world of the plankton, where predator and prey perception is often mediated by fluid signals. We note, however, that our low Reynolds number model does not apply strictly to *A. tonsa* nauplii and *P. intermedius* since the Reynolds numbers of the swimmers are approximately 10 (Fig. 1). In the three-Stokeslet model with $\alpha \neq 0$, the force dipole term always dominates the far field region $r/a \gg 1/\alpha$, but the transition range, in which the force quadrupole term is dominant, extends farther and farther out as α is decreased to zero. In breast stroke swimming the propulsive forces are delivered during the entire beat of the swimming appendages, corresponding to different points of action of the forces. However, we presume that the highest propulsive forces are created in the middle of the power stroke when α is small and that our conclusions for breast stroke swimming are therefore robust.

Any small density mismatch of the organism will lead to a Stokeslet term that will dominate far away from the organism farther than some distance Λ. For an organism with a stresslet term one finds $\Lambda/a \sim F/F_g$, where F_g is the buoyancy corrected gravitational force on the swimmer [15], and for a quiet swimmer we estimate $\Lambda/a \sim (F/F_g)^{1/2}$. With a given density mismatch the Stokeslet term will be most significant for large organisms since the buoyancy corrected gravitational force is proportional to the volume of the organism, whereas the propulsive forces are roughly proportional to the length of the organism squared [28]. For a low Reynolds number swimmer to be quiet we must therefore have that both the density mismatch and the size of the organism are so small that the Stokeslet term only dominates far from the organism where the fluid disturbances are so small that they are irrelevant for any interaction with other organisms.

Reducing the flow disturbance generated by a swimming organism not only hides it from rheotactic predators, it also improves the chances of the organism capturing small prey. An organism moving towards a prey has to ensure that the prey is not warned and pushed away by the flow created by the organism. Millimeter sized planktonic organisms like copepods can do this by reducing the extent of the viscous boundary layer around them by moving quickly and achieving a Reynolds number sufficiently above unity [29]. Our analysis shows that it is also possible for low Reynolds number swimmers to reduce their induced flow disturbance, thereby allowing them to approach small prey quietly.

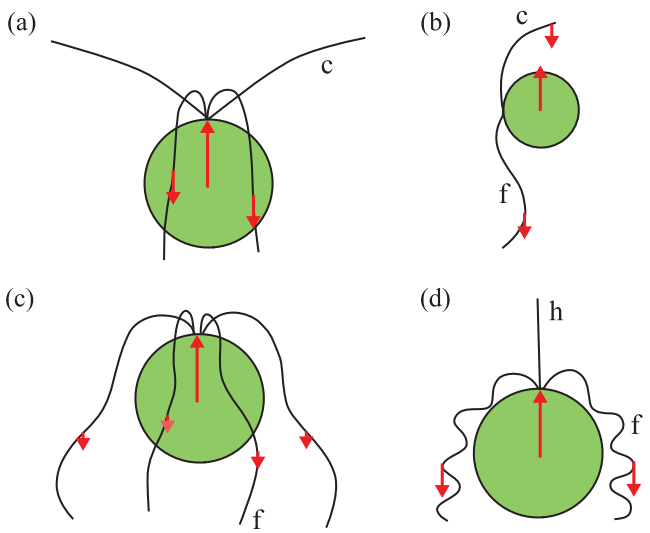

FIG. 5. (Color online) Micro-organisms with multiple flagella. In all cases the swimming direction is upwards, and the red vectors represent approximately the forces. The flagella function with either a flagellar beat, f, or a ciliary beat, c. Protists with (a) two pairs of flagella that beat out of phase, e.g., *Carteria*, (b) a leading and a trailing flagellum, e.g., *Nephroselmis*, and (c) all four flagella pushing steadily, e.g., *Cymbomonas* [13]. (d) A haptophyte with two flagella and a haptonema, h, in the front, e.g., *Chrysochromulina* [12].

Point force models should be used with care since they do not always capture the flow close to the swimmer [8], but for some swimmers they provide a powerful tool that can also capture the near field fluid disturbance surprisingly well [15]. In addition to the breast stroke swimmers there are many examples of aquatic organisms with multiple flagella for which the point force framework could form the basis for theoretical analysis. Figure 5 shows sketches of selected unicellular organisms reproduced after Refs. [12,13]. Organisms with flagella acting on the sides [Figs. 5(a) and 5(c)] may eliminate the force dipole term by locating the propulsive forces in the same transversal plane as the net drag force, and organisms with a leading and a trailing flagellum [Fig. 5(b)] may eliminate the force dipole term by suitably adjusting the two propulsive forces. We therefore speculate that all three arrangements of the propulsion apparatus might allow the organisms to swim quietly. Also the haptonema in the haptophyte [Fig. 5(d)], which is used to capture prey, might be so located that its tip reaches the region beyond the forward stagnation point, thus aiding it in encountering the prey entrained in the downwards flow. It would be interesting in future studies to experimentally explore the flows around such organisms.

Predator-prey interactions govern the structure and function of (pelagic) food webs. The idealized model framework can therefore be used for hypothesis generation and experimental exploration of concrete predator-prey interactions mediated by fluid signals among planktonic organisms with different arrangements of the propulsion apparatus and, thus, to more fully understand the functioning of pelagic food webs.

We thank Lasse Tor Nielsen for drawing our attention to Refs. [12,13]. The Centre for Ocean Life is a VKR center of excellence supported by the Villum Foundation.

[1] T. Kiørboe, *A Mechanistic Approach to Plankton Ecology* (Princeton University Press, Princeton, 2008).
[2] H. Jiang and G.-A. Paffenhöfer, Mar. Ecol.: Prog. Ser. **373**, 37 (2008).
[3] D. J. Smith and J. R. Blake, Math. Sci. **34**, 74 (2009).
[4] H. Jiang, J. Plankton Res. **33**, 998 (2011).
[5] J. J. Molina, Y. Nakayama, and R. Yamamoto, Soft Matter **9**, 4923 (2013).
[6] E. Lauga and T. R. Powers, Rep. Prog. Phys. **72**, 096601 (2009).
[7] J. S. Guasto, R. Rusconi, and R. Stocker, Annu. Rev. Fluid Mech. **44**, 373 (2012).
[8] K. Drescher, J. Dunkel, L. H. Cisneros, S. Ganguly, and R. E. Goldstein, Proc. Natl. Acad. Sci. USA **108**, 10940 (2011).
[9] M. Lighthill, Commun. Pure Appl. Math. **5**, 109 (1952).
[10] J. R. Blake, J. Fluid Mech. **46**, 199 (1971).
[11] T. Ishikawa, M. P. Simmonds, and T. J. Pedley, J. Fluid Mech. **568**, 119 (2006).
[12] M. A. Sleigh, BioSystems **14**, 423 (1981).
[13] I. Inouye and T. Hori, Protoplasma **164**, 54 (1991).
[14] D. Bray, *Cell Movements: From Molecules to Motility*, 2nd ed. (Garland Science, New York, 2001).
[15] K. Drescher, R. E. Goldstein, N. Michel, M. Polin, and I. Tuval, Phys. Rev. Lett. **105**, 168101 (2010).
[16] J. S. Guasto, K. A. Johnson, and J. P. Gollub, Phys. Rev. Lett. **105**, 168102 (2010).
[17] D. Tam and A. E. Hosoi, Proc. Natl. Acad. Sci. USA **108**, 1001 (2011).
[18] J. W. Martin, J. Olesen, and J. T. Høeg, *Atlas of Crustacean Larvae*, edited by J. W. Martin, J. Olesen, and J. T. Høeg (Johns Hopkins University Press, Baltimore, MD, 2014), pp. 8–16.
[19] C. M. Andersen Borg, E. Bruno, and T. Kiørboe, PLoS One **7**, e47486 (2012).
[20] T. Kiørboe, H. Jiang, R. J. Gonçalves, L. T. Nielsen, and N. Wadhwa, Proc. Natl. Acad. Sci. USA **111**, 11738 (2014).
[21] M. Polin, I. Tuval, K. Drescher, J. P. Gollub, and R. E. Goldstein, Science **325**, 487 (2009).
[22] C. Pozrikidis, *Boundary Integral and Singularity Methods for Linearized Viscous Flow* (Cambridge University Press, Cambridge, UK, 1992).
[23] S. Kim and S. J. Karrila, *Microhydrodynamics: Principles and Selected Applications* (Butterworth-Heinemann, Boston, 1991).
[24] J. D. Jackson, *Classical Electrodynamics*, 3rd ed. (Wiley, New York, 1999).
[25] C. Pozrikidis, *Introduction to Theoretical and Computational Fluid Dynamics*, 2nd ed. (Oxford University Press, Oxford, U.K., 2011).
[26] L. G. Leal, *Advanced Transport Phenomena* (Cambridge University Press, Cambridge, UK, 2007).
[27] N. Wadhwa, A. Andersen, and T. Kiørboe, J. Exp. Biol. **217**, 3085 (2014).
[28] T. Kiørboe, Biol. Rev. **86**, 311 (2011).
[29] T. Kiørboe, A. Andersen, V. J. Langlois, H. H. Jakobsen, and T. Bohr, Proc. Natl. Acad. Sci. USA **106**, 12394 (2009).

Chapter 8

Inertial effects in the swimming hydrodynamics of zooplankton

Manuscript under preparation

Inertial effects in the swimming hydrodynamics of zooplankton

Navish Wadhwa,[1,*] Thomas Kiørboe,[2,†] and Anders Andersen[1,‡]

[1]*Department of Physics and Centre for Ocean Life, Technical University of Denmark, DK-2800 Kgs. Lyngby, Denmark*
[2]*National Institute of Aquatic Resources and Centre for Ocean Life, Technical University of Denmark, DK-2920 Charlottenlund, Denmark*

(Dated: September 15, 2015)

Zooplankton, an ecologically important group of aquatic organisms, have traditionally been treated as low Reynolds number swimmers. In this paper, we investigate the extent up to which low Reynolds number models can be applied to the periodic swimming of larger zooplankton. We use the cladoceran *Podon intermedius* as a case study and investigate two aspects - the dynamics of swimming and the induced flow disturbances. Using a simple model that captures the swimming dynamics of periodic swimmers such as *P. intermedius*, we find that the inclusion of the high Re non-linear drag results in the swimming dynamics similar to the low Re approximation, even in a range where the low Re model is inapplicable. We further find that the flow disturbances induced by *P. intermedius* are not explained by low Re models, and that inertial effects may explain the observed flow behaviour. More specifically, the observed one over distance cubed decay in flow velocity may be due to small boundary layer like region around the swimming organism, leaving the majority of the flow to act as fast decaying potential flow.

PACS numbers:

Plankton are an important group of aquatic organisms, most of which are smaller than a few millimetres. Phytoplankton, the photosynthesis performing plankton, are responsible for about half of the primary production on the planet [1]. Zooplankton, the non-photosynthetic plankton, feed on smaller plankton, making energy available to the higher organisms such as fish. Thus, phytoplankton and zooplankton form integral components of mass and energy fluxes in the global biogeochemical cycles [2].

Many zooplankton swim to find nutrients and mates, but swimming has risks associated with it since swimming generates flow disturbances which can be sensed by predators [3]. Many zooplankton rely heavily on mechanosensing for detecting the presence of other organisms, and have highly sensitive apparatuses dedicated to it [4, 5]. Thus, it may be advantageous for zooplankton to reduce the induced flow disturbance.

The Reynolds number Re, usually defined for swimming organisms as $\mathrm{Re} = \rho L_\mathrm{s} V_\mathrm{m}/\mu$, where L_s, V_m, ρ and μ are body length, mean swimming velocity, water density, and dynamic viscosity, respectively, describes the relative importance of inertial versus viscous forces. Zooplankton are typically treated as low Re swimmers [6–8], but for some of the larger zooplankton, inertial effects are potentially important. For low Re swimmers, the flow velocity v induced by the swimmer decays with distance r as $v \sim r^{-1}$ or $v \sim r^{-2}$ [9]. This is true for small swimmers like bacteria [10], flagellated green algae [11], and hovering or cruising zooplankton [12]. But recent observations have shown that some zooplankton are hydrodynamically quieter swimmers, for which the flow velocity decays as $v \sim r^{-3}$ or $\sim r^{-4}$ [12].

In particular, we are here interested in periodic swimming, which consists of successive identical beat cycles, unlike steady or sporadic swimming. Periodic swimming is common among zooplankton [7], and forms the basis of our investigation. To what extent can we use the low Re approximations for these organisms?

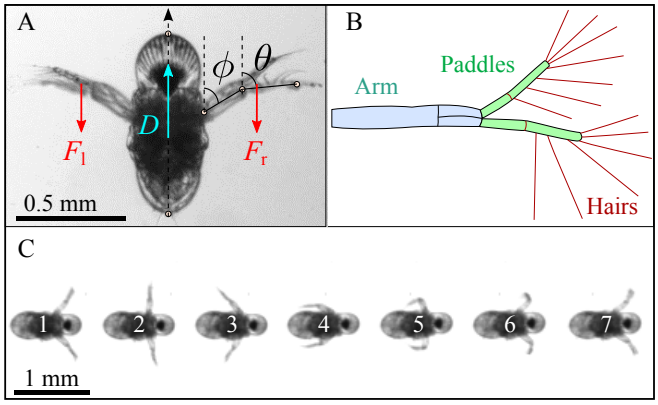

FIG. 1: (A) Dorsal view of the cladoceran *P. intermedius*, showing the body, the eye, and two second antenna. The angles ϕ and θ are formed by the arm and the paddle, respectively, with the body axis, as indicated. (B) A schematic of the second antenna, showing the 'arm' (blue), the two 'paddles' (green), and the 'hairs' (red). (C) A sequence of images showing one beat cycle of a *P. intermedius*, consisting of power stroke (1-4), and return stroke (5-7). Consecutive images are 7 ms apart.

We use the cladoceran *Podon intermedius* as a case study of our investigation (Figure 1). *P. intermedius* is one of the larger marine zooplankton. Millimetre sized cladocerans, which are a dominant herbivorous group in most freshwater ecosystems, also occasionally dominate

in the coastal waters [13]. *P. intermedius* has a slightly elongated body, and two large second antennae that it uses for swimming (Figure 1A). The biramous second antennae beat back and forth with a period $T \approx 50$ ms, resulting in thrust forces on the antennae while drag acts on the body (Figure 1A). The distal parts (paddles) of the antennae are covered with hairs (Figure 1B) to enhance thrust during the power stroke (Figure 1C, 1-4). During the return stroke (Figure 1C, 5-7), the antennae and the hairs fold inwards to minimize the production of backwards thrust.

We collected *P. intermedius* in Gulmar Fjord, Sweden, and filmed freely swimming organisms at 1000 frames per second with high magnification. Using the MATLAB based tool DLTdv5 [14], we digitized the body kinematics during swimming, from which we measured the instantaneous swimming velocity. We analysed films for six individuals for which the swimming kinematics were very similar. Figure 2 is a representative of the kinematics. From calibrated images, we measured the body length (L_s) of the organism as the distance between the distal and proximal ends. We approximated the body of *P. intermedius* with a prolate spheroid with polar diameter $a = L_\mathrm{s}$ and equatorial diameter $b = \gamma\, L_\mathrm{s}$, where $\gamma \approx 0.5$ is the aspect ratio. The mass M_s of the organism is calculated as $M_\mathrm{s} = \frac{1}{6}\pi\rho_\mathrm{s} a b^2$, where ρ_s is the density of the swimmer, assumed to be the same as the density of the water ρ.

The motion of the second antenna is described by two angles ϕ and θ, the angles formed by the body axis with the arm and the paddle, respectively (Figure 1A). The periodic motion of the appendages is approximately left-right symmetric and results in a periodic swimming velocity (Figure 2A,B). We define the power stroke intervals as the time intervals when the paddle angle θ is increasing, as the hair-bearing paddle is the main thrust producing part of the antenna. The organism accelerates until the middle of the power stroke, beyond which the velocity decreases and even becomes negative towards the middle of the return stroke. The Reynolds number based on the mean swimming velocity $V = 6.6$ mm/s and the body length is $\mathrm{Re} = 5.3$.

Can we understand the dynamics in Figure 2 using a simple model? We imagine a model swimmer with a spherical body of radius R, which propels itself with appendages of size L. The swimming is characterised by six dimensional quantities - the dynamic viscosity μ, the density ρ of the water, the density ρ_s of the swimmer, the radius R, the appendage size L, and the angular frequency ω of the propulsion force. From these, we can form three dimensionless numbers - the aspect ratio $\alpha = L/R$, the density ratio $\beta = \rho_\mathrm{s}/\rho$, and the frequency based Reynolds number $\mathrm{Re} = \rho L^2\omega/\mu$. We again assume that $\beta \approx 1$, i.e., $\rho_\mathrm{s} = \rho$.

The governing equation for the velocity V of a neutrally buoyant swimmer with mass M can be written

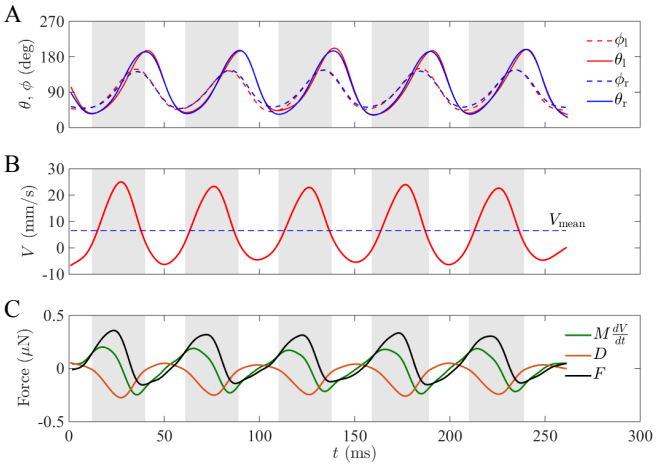

FIG. 2: (A) Time series of the left arm and paddle angles $(\phi_\mathrm{l}, \theta_\mathrm{l})$, and right arm and paddle angles $(\phi_\mathrm{r}, \theta_\mathrm{r})$, for an instance of *P. intermedius* swimming horizontally. The paddle lags behind the arm by a small phase difference. The grey bars in the background represent the power stroke. (B) The measured swimming velocity (V) of the organism. (C) Time series of the drag force D (blue), the thrust F (black), and the total force MdV/dt (green) acting on the organism.

$$M\,\frac{dV}{dt} = F - D\,, \tag{1}$$

where F is the thrust force produced by the propulsive apparatus of the organism, and D is the drag acting on the body. The mass M in equation (1) is the sum of the mass M_s and the added mass M_a. For a prolate spheroid with the same density as water, the added mass is $M_\mathrm{a} = c_\mathrm{m} M_\mathrm{s}$, where $c_\mathrm{m} \approx 0.2$ is the added mass coefficient for a prolate spheroid with $\gamma = 0.5$ [15]. For estimating the drag, we approximate the body of the organisms with a sphere with the same volume as the prolate spheroid, such that the equivalent radius R of the sphere is $R = \gamma^{\frac{2}{3}}(L_\mathrm{s}/2)$. We use the empirical relationship for the drag on a sphere over a range of Re,

$$D \;=\; 6\pi\mu R V + \frac{\pi\, C_1}{2^{3/2}}\sqrt{\rho\mu}R^{3/2}V|V|^{\frac{1}{2}} + \frac{\pi}{2}C_2\rho R^2 V|V| \tag{2}$$

where C_1 and C_2 are dimensionless empirical constants describing the strength of the two non-linear terms [16]. Using equations (1) and (2), we can calculate the thrust force F from the observed instantaneous swimming velocity V (Figure 2C). The thrust F is periodic but not a simple harmonic function, and it becomes negative during part of the return stroke. The mean thrust is $F_\mathrm{m} = 0.07\,\mu$N.

For a periodic swimmer, the thrust can be written as the sum of a constant part and a part which varies sinu-

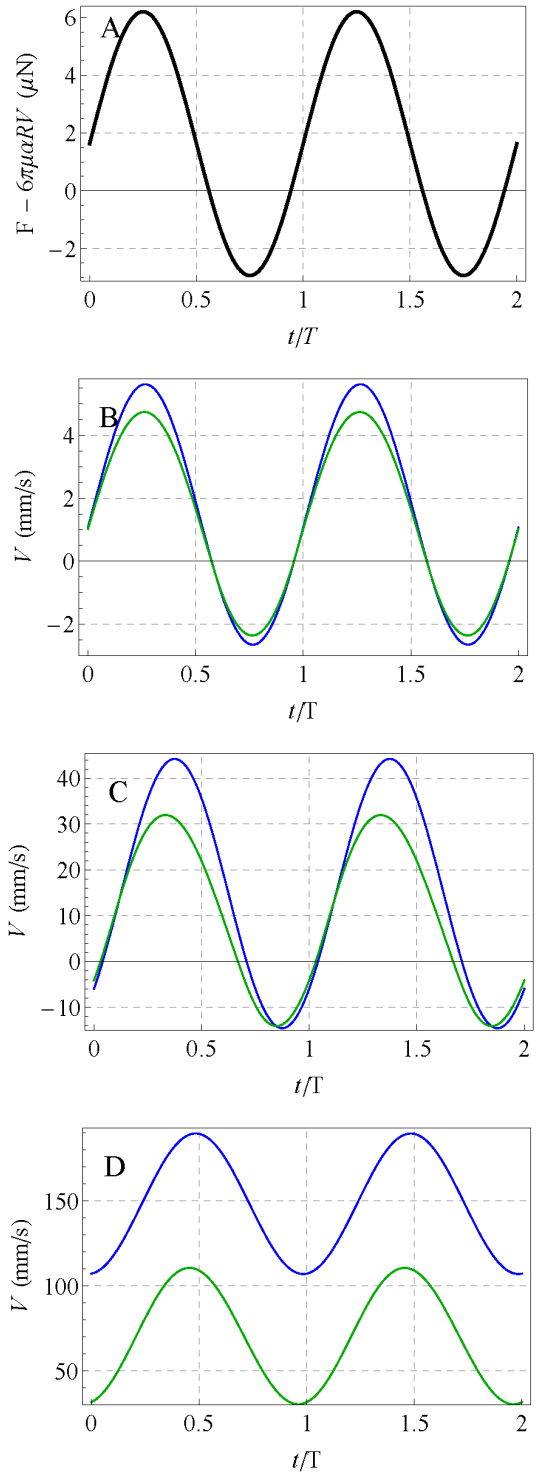

FIG. 3: The first term of equation (5) plotted against normalized time (A), and example solutions of the linear model (blue) and the non-linear model (green) for $\omega\tau = 0.1$ (B), 1 (C), and 10 (D). The various parameter values are $R = 0.27$ mm, $A_0 = 2.8$, $M = 10^{-7}$ kg, measured from the *P. intermedius* observations.

soidally in time

$$F = 6\pi\mu KL\,[\,U\,(1 + A_0\,\sin\omega t)\,-\,V\,], \qquad (3)$$

where U is the characteristic velocity of the swimming appendages, A_0 is the amplitude of the time varying part of the propulsion force, and K is a dimensionless constant which depends on the shape of the swimming appendage. The $-V$ term in equation (3) accounts for the reduction in appendage velocity relative to the quiescent ambient water when the organism is in motion. For simplicity, we set $K = 1$ and assume that $U =\sim L\omega$, leading to

$$F = 6\,\pi\,\mu\,\alpha^2\,R^2\omega\,(1 + A_0\,\sin\omega t) - 6\,\pi\,\mu\,\alpha RV. \qquad (4)$$

Combining equations (1), (2), and (4), gives the governing equation for our model

$$M\frac{dV}{dt} = 6\pi\mu\alpha^2R^2\omega(1 + A_0\sin\omega t) - 6\pi\mu(1+\alpha)RV \\ -\tfrac{\pi\,C_1}{2^{3/2}}\sqrt{\rho\mu}R^{3/2}V|V|^{\frac{1}{2}} - \tfrac{\pi}{2}C_2\rho R^2V|V|. \qquad (5)$$

Equation (5) does not offer an analytical solution, but we can solve it numerically (Figure 4). We compare the solution with the low Re approximation of the model with only the linear part of the drag ($C_1 = C_2 = 0$). The low Re model has an analytical solution for the swimming velocity,

$$V = V_{\rm m}\left[1 + \frac{A_0}{\sqrt{1+(\omega\,\tau)^2}}\sin(\omega\,t + \chi)\right], \qquad (6)$$

where the mean swimming velocity is given by $V_{\rm m} = \alpha^2R\omega/(1+\alpha)$. The amplitude $A = A_0/\sqrt{1+(\omega\,\tau)^2}$ and phase χ of the periodic part in V are determined by the normalized frequency $\omega\tau$, and χ satisfies $\tan\chi = -\omega\tau$, where $\tau = M/[6\pi\mu(1+\alpha)R]$ is the Stokes time-scale. We can write $\omega\tau$ in terms of the other dimensionless numbers as

$$\omega\tau = \frac{2}{9\alpha^2(1+\alpha)}{\rm Re}. \qquad (7)$$

α can be expected to be of the order 1, so we find that ${\rm Re} \approx 10\,\omega\tau$.

Using parameter values from the observations of *P. intermedius*, we find that the mean velocity $V'_{\rm m}$ for the non-linear drag case is in general smaller than for the one with linear drag (Figure 3). At low $\omega\tau$ (and thus low Re), swimming velocity is in phase with the applied force for both linear and non-linear models (Figure 3B), while at high $\omega\tau$, V lags behind by a quarter of a period (Figure 3D). When plotted over a range of $\omega\tau$, we find that the difference in $V'_{\rm m}$ and $V_{\rm m}$ becomes significant only for $\omega\tau > 1$ (Figure 4A). The solution to equation (5) is not a sinusoidal function, and to estimate A and χ, we normalize the solution V with the mean swimming velocity $V'_{\rm m}$, and locate the maxima and minima in velocity.

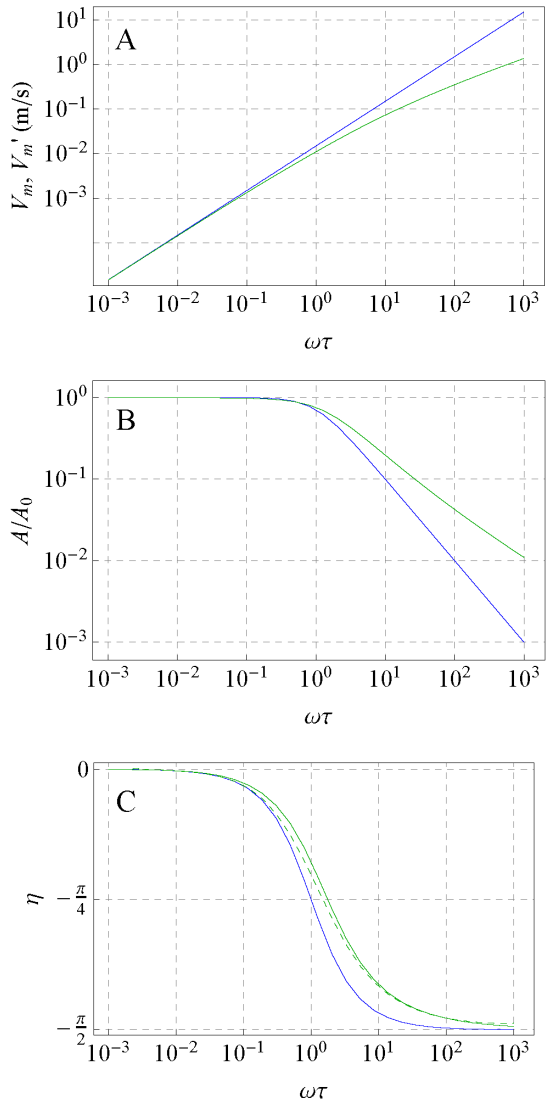

FIG. 4: The mean swimming velocity (A), the normalized amplitude (B), and the phase difference χ (C) for the model swimmer, in the case with linear drag (blue), and with non-linear drag (green), all as a function of $\omega\tau$. The solid and dashed curves in (C) are for the velocity maxima and minima, respectively.

The normalized amplitude (A/A_0) also deviates form the linear solution around $\omega\tau = 1$ (Figure 4B), and A/A_0 for the non-linear drag case is much more than the linear approximation. The phase difference χ can be measured in many ways; we here measure it for the maxima and the minima in velocity. For both of these, the phase difference in the non-linear case is smaller in magnitude than the linear case (Figure 4C). With $0.1 < \omega\tau < 10$ between 10^{-1}, the maxima and the minima have different phase shifts (Figure 4C), due to the asymmetry in drag.

Thus, various features of the non-linear model start to deviate strongly from the linear approximation at $\omega\tau \approx 1$ corresponding to Re ≈ 10. Interestingly, the non-linear model solutions for the $V_{\rm m}'$, A/A_0, and χ are such that it behaves like the lower $\omega\tau$ (thus lower Re) solutions of the linear model. The inclusion of non-linear terms results in low Re behaviour extending towards higher Re, suggesting that the low Re approximation gives correct solutions even at higher Re.

For *P. intermedius* with $L_{\rm s} \approx 0.9$ mm, and assuming $\alpha \approx 1$, we estimate that $\tau \approx 7$ ms, $\omega = 2\pi/T \approx 125$ rad/s, and $A_0 \approx 2.8$. Thus, for the sequence in Figure 2, $\omega\tau \approx 0.875$. With these numbers the linear model solution (6) predicts a mean swimming velocity $V_{\rm m} \approx 13$ mm/s, in contrast to the non-linear model prediction of $V_{\rm m}'$ 9.7 mm/s, which is closer to the observation. From the observations, we estimate that $A/A_0 = 0.84$, which is closer to the normalized amplitude predicted by model with the non-linear drag ($A/A_0 = 0.9$), than with only the linear drag ($A/A_0 = 0.75$). Moreover, the observed phase difference at the velocity maxima $\chi = 0.52$ is better predicted by the model with non-linear drag ($\chi = 0.47$) than with only linear drag ($\chi = 0.72$). The force scale from equation (4) is $6\pi\mu\alpha^2R^2\omega \approx 0.14\,\mu$N, the same order of magnitude as the mean thrust calculated from the observations. Thus, the overestimate of the mean thrust in the model is the likely cause of the overestimated mean swimming velocity in the non-linear model.

We now look at the flow disturbance induced in the water due to the swimming of *P. intermedius*. We measured the swimming generated flows by *P. intermedius* using time resolved particle image velocimetry (Appendix A). The near field flow structure resulting from the swimming of *P. intermedius* is similar to that of the other breast stroke swimmers, such as *Acartia tonsa* nauplii [17] and *Daphnia magna* [18]. The power stroke results in the vorticity generation in the fluid surrounding the organisms, which appears to be shed into the wake at the end of the power stroke (Figure 5A-D). The return stroke results in vorticity generation next to the body with reversed rotation compared to the power stroke (Figure 5E,F). At all times, vorticity is limited to a region of a size comparable to the body of the organism including appendages, and the area outside this region appears to be irrotational.

From the particle image velocimetry (PIV) data, we measured how the flow velocity induced by the swimming of *P. intermedius* decays with distance from the organism. We found power law decay of the flow velocity, close to $v \sim r^{-3}$ (Figure 6). The induced flow velocity and its spatial decay changes over the duration of the stroke, but at large distance from the organism and at the peak of the stroke it is close to $v \sim r^{-3}$. Thus the spatial decay of velocity in breast stroke swimming *P. intermedius* is faster than the $v \sim r^{-1}$ and $v \sim r^{-2}$ decay found in most low Re swimmers [19].

For a neutrally buoyant Stokesian swimmer, $M\,dV/dt$ is negligible in comparison with D and F, which are of equal magnitude [19]. Thus, in general a Stokesian breast

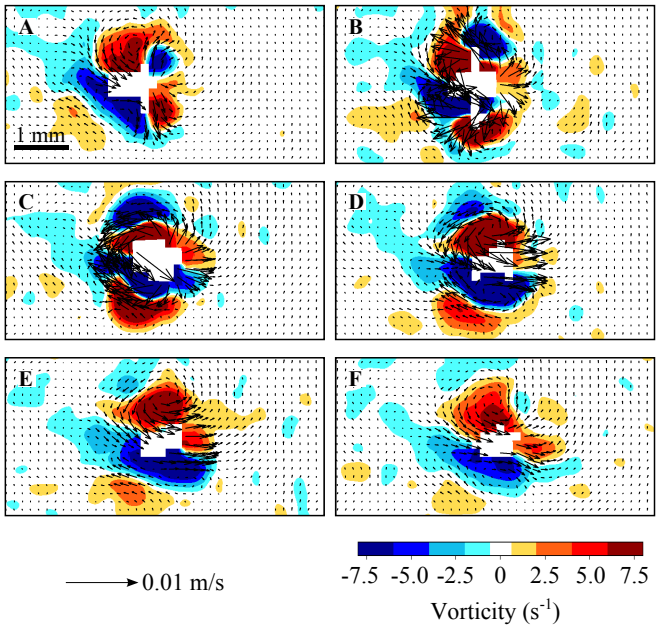

FIG. 5: Snapshots of the velocity field (black vectors) and the vorticity (coloured contours) at six instants during a beat cycle (A-F), corresponding to the first six images (1-6) in the kinetic image sequence (Figure 1C). Consecutive snapshots are 7 ms apart.

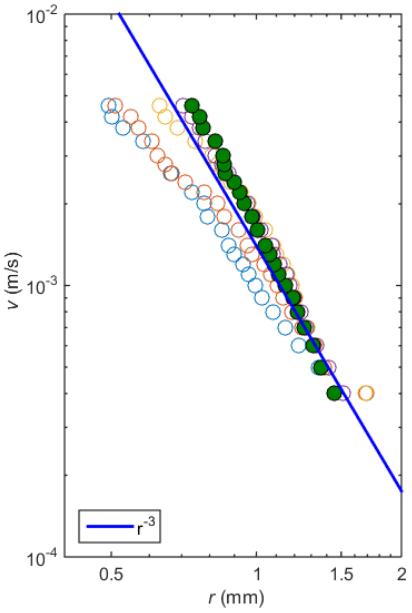

FIG. 6: Flow velocity (v) induced by one swimming event of *P. intermedius* as a function of distance (r). The open circles and the closed green circles represent the times leading up to the peak disturbance and the instant of the peak disturbance, respectively. The blue line is guide for the eye, representing the relationship $v \sim r^{-3}$.

stroke swimmer behaves as a force dipole with $v \sim r^{-2}$ velocity decay [19]. Recently, we have reported a simple model for a neutrally buoyant breast stroke swimming at low Re, consisting of three point forces (Stokeslets) [20], which demonstrated the possibility for a small breast stroke swimmer to generate a fast decaying flow disturbance. If the point of action of the two thrust forces and the drag force is collinear, then the dipole is eliminated and the swimmer behaves like a quadrupole with a faster $v \sim r^{-3}$ velocity decay [20]. The condition of zero net force is not satisfied for *P. intermedius*, which experiences a time dependent net force of the same order of magnitude as D and F (Figure 2C). Thus, at any instant, the organisms exerts a net force on the surrounding water, and a three Stokeslet model [20] or any similar low Re model for the swimmer would be dominated by a force monopole with a slow $v \sim r^{-1}$ velocity decay [21].

We speculate that the observed fast spatial decay of the induced flow velocity is due to inertial effects. The full Navier-Stokes equation for the flow velocity $\mathbf{v}$ is given by

$$\rho\left(\frac{\partial \mathbf{v}}{\partial t} + (\mathbf{v}\cdot\nabla)\mathbf{v}\right) = -\nabla p + \mu\nabla^2\mathbf{v}\ , \qquad (8)$$

$$\nabla\cdot\mathbf{v} = 0\ , \qquad (9)$$

where p is the pressure field. For an oscillating swimmer, the size and the frequency of the oscillations set the scales of the various terms in equation (8). Following Landau and Lifshitz [22], for the body of size scale R oscillating with a frequency ω, let a be the amplitude of oscillations. If $a \ll R$, then the non-linear term $(\mathbf{v}\cdot\nabla)\mathbf{v}$ scales as $a^2\omega^2/R$, and hence small as compared to the unsteady term $\partial\mathbf{v}/\partial t$ which scales as $a\omega^2$. In general, for a decaying flow velocity $v \sim r^{-k}$, the non-linear term $(\mathbf{v}\cdot\nabla)\mathbf{v} \sim r^{-2k-1}$ decays faster than both the unsteady term $\partial\mathbf{v}/\partial t \sim r^{-k}$ and the viscous term $\mu\nabla^2\mathbf{v} \sim r^{-k-2}$, for $k > 1$. Thus, for $a \ll R$ or $k > 1$, equation (8) is then reduced to the unsteady stokes equation,

$$\rho\frac{\partial \mathbf{v}}{\partial t} = -\nabla p + \mu\nabla^2\mathbf{v}\ . \qquad (10)$$

Taking a curl of equation (10) and because that curl of ∇p is zero, we get a diffusion equation for vorticity $\zeta = \nabla\times\mathbf{v}$ as

$$\frac{\partial \zeta}{\partial t} = \frac{\mu}{\rho}\nabla^2\zeta, \qquad (11)$$

which is analogous to the heat conduction equation. Thus vorticity decreases away from the body, and beyond a certain distance, the flow is irrotational. This is in agreement with our observations for *P. intermedius* described above. The distance at which that happens can be found from a comparison between the unsteady term and the viscous term, and is given by $\delta = \sqrt{2\nu/\omega}$, where

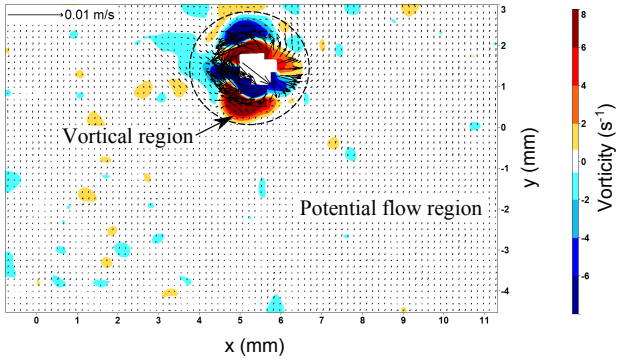

FIG. 7: Flow field created by the swimming of *P. intermedius* shown for the complete measurement region, showing that vorticity is contained in a small region (encircled), while most of the flow is irrotational (potential flow).

$\nu = \mu/\rho$ is the kinematic viscosity. Thus, for $r \gg \delta$, the flow is given by the incompressibility condition (equation 9) combined with $\zeta = \nabla \times \mathbf{v} = \mathbf{0}$. It follows from this that $\nabla^2 \mathbf{v} = \mathbf{0}$ and potential flow solutions apply to the velocity field, resulting in a fast $\sim r^{-3}$ velocity decay.

As a consequence of potential flow in the outer region, flow velocity in general decays as $v \sim r^{-3}$ in that region. For *P. intermedius*, $\omega \approx 125$ rad/s, so we get $\delta \approx 100$ μm. Thus, the vorticity containing region is very small as compared to the size of the organisms or the measurement window for PIV. Hence, almost all the region around the organism, barring a small area very close to the body (Figure 7), behaves as potential flow and exhibits a fast velocity decay as $v \sim r^{-3}$.

In conclusion, we confirm that inertial effects play a significant role in the periodically swimming larger zooplankton such as *P. intermedius*. The simple model we propose for periodic swimmers captures a lot of the dynamics, and shows, counter-intuitively, that inclusion of the non-linear drag terms in the model results in high Re dynamics becoming more similar to the low *Re* approximation. Finally, the fast decay of flow disturbance induced by the swimming of *P. intermedius* is not explained by low Re models and we speculate that it is due inertial effects. The vorticity generated at the body of swimming *P. intermedius* decays over a small distance, resulting in potential flow behaviour everywhere else, which exhibits fast $v \sim r^{-3}$ decay in flow velocity, matching the observations.

We wish to thank Julia Dölger for many useful discussions. The Centre for Ocean Life is a Villum Kann Rasmussen Centre of Excellence supported by the Villum Foundation.

APPENDIX

A. Particle image velocimetry

For PIV, we seeded the water with hollow glass spheres (10 μm diameter), and illuminated with a pulsed infrared laser of wavelength 808 nm (Firefly, Oxford lasers) that was synchronized with the camera to do time series PIV. The laser sheet thickness was 150 μm. We used the commercial software DaVis (LaVision GmbH, Göttingen) for capturing and analysing the images. For the processing, we used a multi-pass algorithm with decreasing size of the interrogation windows, and a final window size of 32 pixels × 32 pixels with 50 % overlap. Using an algorithmic mask, we removed the pixels corresponding to the animal from the PIV analysis.

* Electronic address: nawa@fysik.dtu.dk
† Electronic address: tk@aqua.dtu.dk
‡ Electronic address: aanders@fysik.dtu.dk

[1] P. G. Falkowski, R. T. Barber, and V. Smetacek, Science **281**, 200 (1998).
[2] C. Lalli and T. R. Parsons, *Biological Oceanography: An Introduction: An Introduction* (Butterworth-Heinemann, 1997).
[3] T. Kiørboe, H. Jiang, and S. P. Colin, Proc. R. Soc. B **277**, 3229 (2010).
[4] E. A. Martens, N. Wadhwa, N. S. Jacobsen, C. Lindemann, K. H. Andersen, and A. Visser, bioRxiv (2015).
[5] J. Yen and J. R. Strickler, Invertebr. Biol. **115**, 191 (1996).
[6] H. Jiang and T. R. Osborn, Surveys in Geophysics **25**, 339 (2004), ISSN 01693298.
[7] H. Jiang and T. Kiørboe, J. R. Soc. Interface **8**, 1090 (2011).
[8] D. Murphy, D. Webster, and J. Yen, Limnol. Oceanogr. Methods **10**, 1096 (2012).
[9] A. Visser, Mar. Ecol. Prog. Ser. **222**, 1 (2001).
[10] K. Drescher, J. Dunkel, L. H. Cisneros, S. Ganguly, and R. E. Goldstein, Proc. Natl. Acad. Sci. **108**, 10940 (2011).
[11] K. Drescher, R. E. Goldstein, N. Michel, M. Polin, and I. Tuval, Phys. Rev. Lett. **105**, 168101 (2010).
[12] T. Kiørboe, H. Jiang, R. J. Gonçalves, L. T. Nielsen, and N. Wadhwa, Proc. Natl. Acad. Sci. **111**, 11738 (2014).
[13] H. F. Bosch and W. R. Taylor, Marine Biology **19**, 161 (1973), ISSN 0025-3162.
[14] T. L. Hedrick, Bioinspir. Biomim. **3**, 034001 (2008).
[15] H. Chung and S. Chen, Tech. Rep., Argonne National Lab., IL (USA) (1984).
[16] B. Lautrup, *Physics of continuous matter* (Institute of Physics Publishing, Bristol, UK, 2005).
[17] N. Wadhwa, A. Andersen, and T. Kiørboe, The Journal of Experimental Biology (2014).
[18] D. Murphy, Ph.D. thesis (2012), URL http://smartech.gatech.edu/handle/1853/44860.
[19] E. Lauga and T. R. Powers, Rep. Prog. Phys. **72**, 096601 (2009).

[20] A. Andersen, N. Wadhwa, and T. Kiørboe, Phys. Rev. E **91**, 042712 (2015).
[21] C. Pozrikidis, *Introduction to theoretical and computational fluid dynamics* (Oxford University Press, Oxford, UK, 2011), 2nd ed.
[22] L. Landau and E. Lifshitz, Course of Theoretical Physics pp. 227–229 (1987).

Chapter 9

Characteristic sizes of life in the oceans, from bacteria to whales

Paper to appear in Annual Review of Marine Science (2016)

Review in Advance first posted online on July 8, 2015. (Changes may still occur before final publication online and in print.)

Annu. Rev. Marine. Sci. 2016.8. Downloaded from www.annualreviews.org
Access provided by Technical Information Center & Library of Denmark on 07/31/15. For personal use only.

Characteristic Sizes of Life in the Oceans, from Bacteria to Whales*

K.H. Andersen,[1,2] T. Berge,[1,3] R.J. Gonçalves,[1,2,4,5] M. Hartvig,[2,6,7] J. Heuschele,[1,2] S. Hylander [2,8] N.S. Jacobsen,[1,2] C. Lindemann,[2] E.A. Martens,[1,2,9] A.B. Neuheimer,[2,6,10] K. Olsson,[1,2] A. Palacz,[2] F. Prowe,[1,2,11] J. Sainmont,[1,2] S.J. Traving,[1,3] A.W. Visser,[1,2] N. Wadhwa,[1,12] and T. Kiørboe[1,2]

*Author affiliations can be found in the Acknowledgments section.

Annu. Rev. Mar. Sci. 2016. 8:3.1–3.25

The *Annual Review of Marine Science* is online at marine.annualreviews.org

This article's doi: 10.1146/annurev-marine-122414-034144

Copyright © 2016 by Annual Reviews. All rights reserved

Keywords

body size, metabolism, allometric scaling, plankton, mixotrophy, fish, whales

Abstracts

The size of an individual organism is a key trait to characterize its physiology and feeding ecology. Size-based scaling laws may have a limited size range of validity or undergo a transition from one scaling exponent to another at some characteristic size. We collate and review data on size-based scaling laws for resource acquisition, mobility, sensory range, and progeny size for all pelagic marine life, from bacteria to whales. Further, we review and develop simple theoretical arguments for observed scaling laws and the characteristic sizes of a change or breakdown of power laws. We divide life in the ocean into seven major realms based on trophic strategy, physiology, and life history strategy. Such a categorization represents a move away from a taxonomically oriented description toward a trait-based description of life in the oceans. Finally, we discuss life forms that transgress the simple size-based rules and identify unanswered questions.

Changes may still occur before final publication online and in print

Annu. Rev. Marine. Sci. 2016.8. Downloaded from www.annualreviews.org
Access provided by Technical Information Center & Library of Denmark on 07/31/15. For personal use only.

INTRODUCTION

Since Haldane's (1928) essay "On Being the Right Size," biologists have used organism size as a master trait to characterize the capabilities and limitations of individual organisms. There are good reasons for doing so. It is evident that the physiology and ecology of a copepod and a dolphin are vastly different, much more so than those of a copepod and a fish larva. Through power-law functions, organism size can be used to describe aspects of populations and organismal physiology across taxa (Peters 1983), including metabolism (leading to the celebrated 3/4 law for the scaling of resting metabolism with size) (Hemmingsen 1960, Kleiber 1932, West et al. 1997, Winberg 1960); population growth rates (Fenchel 1974, Gillooly et al. 2002); predator-prey relationships in terms of functional response (Hansen et al. 1997, Kiørboe 2011, Rall et al. 2012) and predator:prey size ratios (Barnes et al. 2008, Cohen et al. 1993, Hansen et al. 1994); fluid mechanical forces (Bejan & Marden 2006); swimming speed (Kiørboe 2011, Ware 1978); vision (Dunbrack & Ware 1987); diffusive uptake affinities (Aksnes & Egge 1991, Berg & Purcell 1977, Edwards et al. 2012, Litchman et al. 2007, Munk & Riley 1952, Tambi et al. 2009); and, for phytoplankton, affinities for light (Finkel 2001, Taguchi 1976) and maximum uptake rates (Edwards et al. 2012, Marañón et al. 2013). Size has also been used to describe macroecological patterns of size-dependent species diversity (Fenchel & Finlay 2004, May 1975, Reuman et al. 2014), and the biomass distribution of individuals as a function of size across major taxa (Boudreau & Dickie 1992, Sheldon & Prakash 1972) has been explained theoretically using the size relationships describing individual physiology (Andersen & Beyer 2006, Sheldon et al. 1977).

While developing these size-based relations, the focus has been on determining the exponent (the slope) and the constant (the intercept), with less attention paid to the sizes that limit the range of their validity. Close inspection shows that some power-law relationships change their scaling exponent and/or intercept around some particular size, or even break down altogether beyond a range of validity. For example, the fluid flow around a whale is turbulent, leading to a dominance of inertial forces and a drag force that scales with the length and velocity squared. By contrast, the flow around a unicellular organism is laminar and dominated by viscous forces, with a drag force that scales linearly with velocity and length. Consequently, the scaling of drag force changes at the organism size where there is a transition between viscous and turbulent flow. As an example of a breakdown, consider visual range: The larger an organism's eyes are, the farther it can see. However, there is an upper visual range determined by the sensitivity of the retina (Dunbrack & Ware 1987) as well as a lower limit of eye size determined by the sizes of the visual elements in the retina and the wavelength of light. The scaling law for visual range is therefore valid only within the upper and lower limits. Such changes or breakdowns in scaling laws have consequences for adaptations and strategies of marine organisms. For example, predators so large that they are in the inertial fluid regime develop a streamlined body shape for efficient swimming, and predators smaller than the lower size of an eye cannot rely on vision.

Haldane (1928) concluded that "for every type of animal there is a most convenient size, and a large change in size inevitably carries with it a change of form." Our aim is to determine the sizes where scaling relationships change or break down and to use those characteristic sizes to explain the fundamental differences in the form and function of marine organisms of different sizes. To this end, we build on the large existing literature of empirical size-based scaling relations and their theoretical explanations.

We categorize pelagic life in the ocean based on size in seven general realms: molecular life (viruses), osmo-heterotrophic bacteria, unicellular phototrophs, unicellular mixotrophs and heterotrophs, planktonic multicellular heterotrophs with ontogenetic growth (e.g., copepods), visually foraging poikilotherms (mainly teleosts, cephalopods, and cartilaginous fish), and homeotherms

Power law: $y = bx^a$ with factor b and exponent a; linear regression employs a logarithmic transformation $\log y = \log b + ax$, with $\log b$ being the intercept and a the slope

Phototroph: an organism that relies on photosynthesis as its carbon source and uses osmotrophic diffusive uptake of nutrients

Mixotroph: an organism that employs a mixed strategy to take up carbon and nutrients, typically combining photosynthesis with phagotrophy

Poikilotherm: an organism that maintains the same body temperature as its environment

Cephalopod: a squid, octopus, or cuttlefish, commonly referred to as inkfish

Cartilaginous fish: fish with skeletons made of cartilage rather than bone; this class (Chondrichthyes) comprises sharks, rays, and skates (Elasmobranchii) as well as ghost sharks (Holocephali)

Homeotherm: an organism that maintains a constant body temperature through internal heat sources

REVIEWS IN ADVANCE

Changes may still occur before final publication online and in print

Annu. Rev. Marine. Sci. 2016.8. Downloaded from www.annualreviews.org
Access provided by Technical Information Center & Library of Denmark on 07/31/15. For personal use only.

Table 1 Characteristic sizes of transitions between major realms of life in the ocean

Transition	Size	Notes
Lower size of a cell	0.15 μm ≈ 10^{-15} g_C	Limited by cell wall thickness and to a lesser extent genome size (Equation 8)
Osmo-heterotrophs to phototrophs	10^{-14} to 10^{-13} g_C	Transition from diffusion feeding on dissolved organic matter to photosynthesis (Equation 4)
Phototrophs to mixotrophs	10^{-8} g_C	Transition from acquiring inorganic nutrients by diffusion feeding to acquiring nutrients by active feeding (Equation 5)
Mixotrophs to heterotrophs	10^{-7} g_C (10^{-8} to 10^{-5} g_C)	Transition to acquiring carbon and nutrients solely by predation through active feeding (Equation 6)
Unicellular to multicellular organisms	10^{-6} g_C	Development of vascular networks
Copepods to fish	≈1 mg_{WW}	Smallest size for a functional camera eye
Fish to cetaceans	≈10 kg_{WW}	Smallest size for maintaining a homeothermic metabolism

(cetaceans, but not seals, penguins, or other animals that do not live their entire lives in the pelagic). This categorization of life is a deliberately crude representation of the roughly 200,000 eukaryotic species and the unknown number of archaea and bacteria in the ocean (May & Godfrey 1994), as it is explicitly designed to facilitate an understanding based on size. We describe the life forms in each realm according to their body size and determine characteristic sizes where there is a transition from one realm to another (see **Table 1**). In this manner, we emphasize body size as a fundamental driver of macroecological patterns in the oceans.

We examine five aspects of life where size is a dominant driver: (*a*) body temperature; (*b*) resource encounter through predation, diffusive uptake, or photosynthesis; (*c*) mobility; (*d*) sensing through chemical and hydromechanical signals, vision, and echolocation; and (*e*) life history strategy in terms of adult and progeny sizes (**Figure 1**). To this end, we draw on a wide range of theories: diffusion theory, fluid mechanics, optics, metabolic theory, and optimal life history theory. We review established theoretical and empirical scaling laws and establish characteristic sizes where the scaling laws change or break down. These characteristic sizes are used to formulate hypotheses about the dominant strategy for organisms of a given size within the five aspects—e.g., how an organism obtains carbon (through photosynthetic assimilation of inorganic carbon, from dissolved organic matter, or from particulate organic matter) or which senses it employs for prey encounter. We test the hypotheses by collecting data on strategies of individuals as a function of their size. Because our arguments are general in nature, they apply largely to all aquatic life, but our focus is pelagic marine life. The final synthesis is a description of the dominant forms and functions of life in the oceans. This is used to frame a discussion of strategies and life forms that transcend the general size-based patterns and to point toward unanswered questions.

WHAT IS SIZE?

The size of an organism can be characterized by its weight or by its length. The most common weight measures are wet weight, dry weight, and carbon weight; length is typically measured as the largest linear dimension or the equivalent spherical diameter. Depending on the question, one measure may be more appropriate than the other. For example, the flow around an organism is determined by its linear size and shape, not by its weight. Conversely, the bioenergetic budget

Cetacean: a whale, dolphin, or porpoise

REVIEWS IN ADVANCE

Changes may still occur before final publication online and in print

Annu. Rev. Marine. Sci. 2016.8. Downloaded from www.annualreviews.org
Access provided by Technical Information Center & Library of Denmark on 07/31/15. For personal use only.

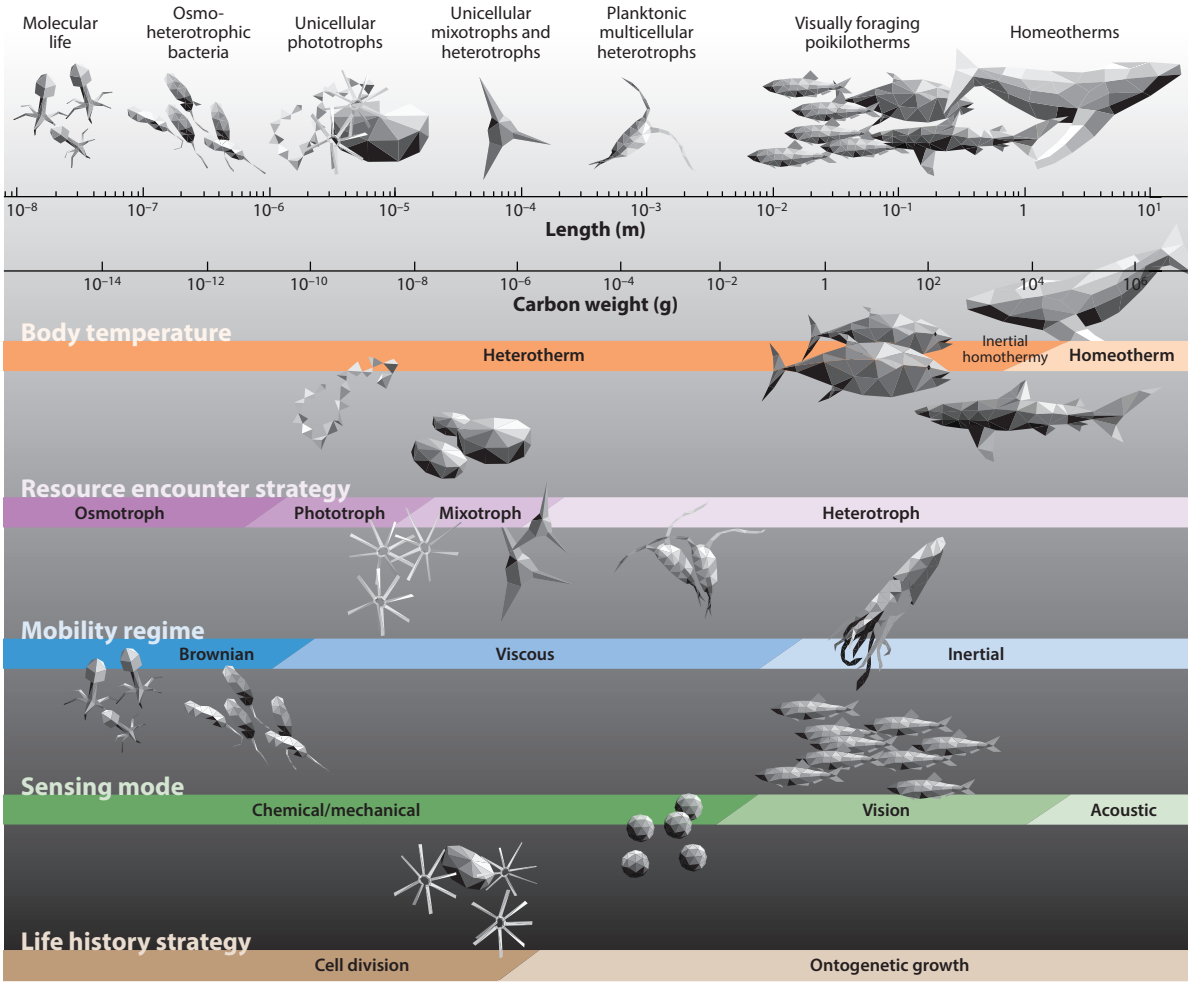

Figure 1

The five aspects of pelagic marine life examined in this review: body temperature, resource encounter strategy, mobility regime, sensing mode, and life history strategy. Each aspect is illustrated in a horizontal bar, with the characteristic transitions indicated by changes in color. The art at the top represents the seven realms of life as defined in this review: molecular life (viruses), osmo-heterotrophic bacteria, unicellular phototrophs, unicellular mixotrophs and heterotrophs, planktonic multicellular heterotrophs (e.g., copepods), visually foraging poikilotherms (mainly teleosts, cephalopods, and cartilaginous fish), and homeotherms (cetaceans).

of an organism is adequately described in terms of weight because the energetic budget should reflect a conservation of mass. For microbes, weight is often measured in carbon or in units of the limiting nutrients because water content and ratios between fundamental elements vary between organisms (Klausmeier et al. 2004). The elemental ratios and water content of vertebrates vary less than they do for invertebrates, so wet weight is often preferred as an intuitive measure of weight for vertebrates. Even though it would be possible to convert all sizes to a common measure, we do not find this useful, and consequently in this review we use the most convenient measure depending on the situation. We use the symbols w for weight, l for length, d for diameter, and r for radius, and we frequently make use of the conversion between length and weight as $w \propto l^3$. Units of weight are

REVIEWS IN ADVANCE

Changes may still occur before final publication online and in print

Annu. Rev. Marine. Sci. 2016.8. Downloaded from www.annualreviews.org
Access provided by Technical Information Center & Library of Denmark on 07/31/15. For personal use only.

indicated by subscripts, with g_{WW} and g_C referring to wet weight and carbon weight, respectively. Conversion relations are provided in **Supplemental Table 1** (follow the **Supplemental Material link** from the Annual Reviews home page at **http://www.annualreviews.org**).

Trophic strategy: the strategy used by an organism to gather nourishment; the suffix "-troph" derives from the ancient Greek *trophikós* (τροφικός), meaning "pertaining to food or nourishment"

RESOURCE ENCOUNTER AND TROPHIC STRATEGIES

Organisms acquire carbon and nutrients by feeding on encountered resources, which here refers broadly to dissolved inorganic nutrients, dissolved organic molecules, photons, or prey organisms. Resource encounters occur by three mechanisms: (*a*) active encounter through cruising, ambushing, or creation of a feeding current; (*b*) fixation of carbon through photosynthesis; or (*c*) passive encounter with food items that diffuse toward the feeding individual. The encounter rate (biomass per unit time) is described as

$$E = \beta C, \quad (1)$$

where β is the clearance rate (volume per unit time) and C is the resource concentration (biomass per unit volume). In terms of a type II functional response (Holling 1959), the clearance rate is the slope at the origin, i.e., the potential volume of water cleared for resources per unit time when uptake is not limited by handling time or physiological limits (digestion). These limitations are not considered here. The clearance rate is described as a power function of size $\beta = bl^a$. We employ the linear dimension l to characterize size because resource uptake is determined by the physical size of an organism, not by its weight.

In the following, we describe how the exponent a and the factor b depend on size for the three different resource acquisition mechanisms on the basis of physical processes and empirical cross-species relationships. This analysis allows us to characterize the dominant trophic strategy of particular organisms (e.g., phototrophs or heterotrophs) as a function of their size and the biotic and abiotic environment.

Active Predation

Large protozoans and metazoans have three fundamental modes of actively encountering prey: ambushing, generating a feeding current, and cruising through the water searching for prey (Kiørboe 2011). The clearance rate of each mode (β_A) can be estimated as a velocity multiplied by an encounter cross section. A planktonic filter feeder, for example, captures prey on its filter with a size scaling as the length of the organism squared (l^2), with a feeding-current velocity $u \approx l^{0.8}$ (Huntley & Zhou 2004), leading to a scaling exponent of the clearance rate of $a_A \approx 2 + 0.8 = 2.8$. Similar arguments for the other feeding modes all lead to exponents of approximately 2.8, i.e., slightly below 3, but multiplied by different factors (Kiørboe 2011). Because one feeding mode replaces the other depending on environmental conditions and the size of the prey and the predator, the average life-form-transcending scaling exponent becomes approximately 3 (**Figure 2*a***, **Supplemental Table 2**):

$$\beta_A = b_A l^3.$$

Weight-specific uptakes rates, $\propto \beta_A/w$, are therefore independent of size because $w \propto l^3$ (Kiørboe & Hirst 2014).

Photosynthesis

Fixation of dissolved CO_2 by photosynthesis requires encounter with photons (assuming that CO_2 is not limiting). Photosynthesis can in principle occur throughout the cell, but for larger cells it is

REVIEWS IN ADVANCE

Changes may still occur before final publication online and in print

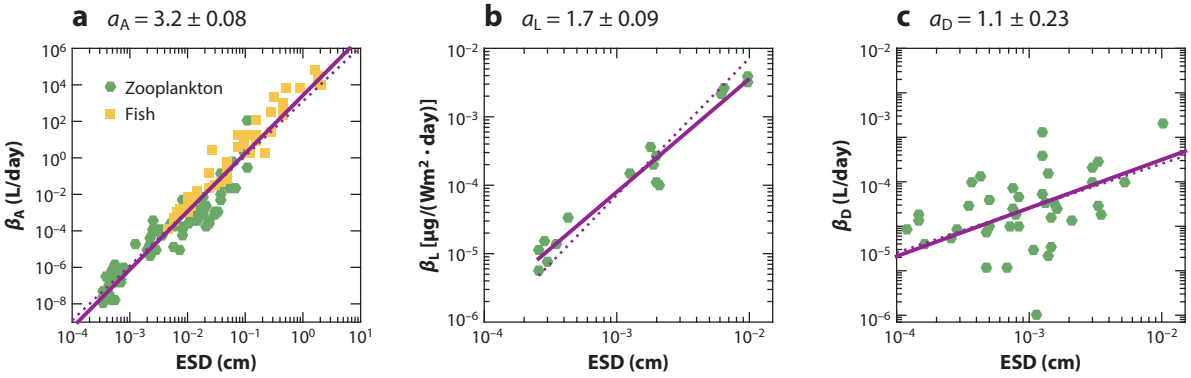

Figure 2

Clearance rate versus weight for organisms performing active predation, photosynthesis, and diffusion feeding on phosphorus. The solid lines are fits to data with the exponent a shown above each panel; the dotted lines are fits with theoretical exponents 3, 2, and 1 for panels *a*, *b*, and *c*, respectively (see **Supplemental Table 2**). (*a*) Clearance rate β_A for active predation by zooplankton (*green hexagons*) and fish (*yellow squares*), from Kiørboe (2011). (*b*) Clearance rate β_L (affinity) for carbon uptake from a series of experiments with diatoms under identical conditions (Taguchi 1976). Data compilations covering a wider range of sizes and phytoplankton groups give a similar exponent but a larger scatter (Schwaderer et al. 2011). (*c*) Clearance rate β_D (affinity) for diffusion feeding on dissolved phosphate, from Edwards et al. (2012) and Tambi et al. (2009). Abbreviation: ESD, equivalent spherical diameter.

limited by self-shading of photons (the so-called package effect) (Morel & Bricaud 1981). For the present arguments, it is sufficient to consider that the cross-sectional area of the cell $\propto l^2$ limits photosynthesis (**Figure 2*b***):

$$\beta_L = b_L l^2. \quad (2)$$

The clearance rate β_L is often termed light affinity or photosynthetic efficiency and is measured in dimensions of carbon fixed per photon multiplied by area. In terms of weight-specific scaling, the power 2 scaling of β_L results in a scaling of weight-specific rates of carbon fixation $\beta_L/w \propto w^{-1/3}$—i.e., smaller organisms have a higher specific rate of carbon fixation than larger ones. Organisms smaller than a certain size are therefore able to fix more carbon by photosynthesis than by active encounter because specific uptake by active encounter is independent of size.

Diffusion Feeding

Organisms that encounter resource items as they bump into the surface of the organism because of Brownian motion are termed diffusion feeders (Fenchel 1984). Diffusion feeding is used to assimilate dissolved organic molecules, inorganic carbon, and nutrients. The uptake rate is limited by the number of uptake sites on the surface of the cell, which can be expected to scale with l^2. However, the uptake also removes resources from the vicinity of the cell surface and creates a boundary layer of lower resource concentrations near the cell (Munk & Riley 1952). This effectively leads to the clearance rate β_D being limited by diffusion rather than by the surface, with a scaling proportional to the linear dimension of the cell (reviewed in Fiksen et al. 2013):

$$\beta_D = b_D l^1. \quad (3)$$

Weight-specific uptake rates are then $\propto w^{-2/3}$, i.e., high for small cells and declining with size. Small diffusion-feeding cells therefore have a higher encounter rate with dissolved nutrients or macromolecules than they could have obtained by active feeding. The theoretical scaling

Annu. Rev. Marine. Sci. 2016.8. Downloaded from www.annualreviews.org
Access provided by Technical Information Center & Library of Denmark on 07/31/15. For personal use only.

REVIEWS IN ADVANCE

Changes may still occur before final publication online and in print

prediction fits with data for phosphate affinity (**Figure 2*c***) (p value for a_D different from zero is 2.2×10^{-5}). Data for nitrogen affinity are less clear, with some being consistent with the theoretical scaling ($a_D = 1.2$) (Litchman et al. 2007) and others not ($a_D = 2.25$) (Edwards et al. 2012).

Protists: simple, typically unicellular, eukaryotic organisms that live in aquatic environments

Trophic Strategies

An organism's trophic strategy, i.e., which type of food it consumes, is to a large degree determined by its resource acquisition mechanism. It can be an osmo-heterotroph that diffusion feeds on dissolved organic matter (bacteria), a phototroph that captures light and diffusion feeds on dissolved inorganic nutrients (phytoplankton), a mixotroph that captures light and feeds on other organisms, or an actively feeding heterotroph (animals and many protists). If we use clearance rate as a proxy for competitive ability at low resource concentrations, we can assume that the dominant trophic strategy of organisms at a given size is determined by the resource acquisition mechanism yielding the highest encounter rate. Equation 1 gives the encounter rates for the four trophic strategies as a function of size, where the resource may be concentrations of dissolved organic molecules (C_{DOM}), nutrients (C_N), other prey organisms (C_P), or light flux (C_L). Phototrophs need special treatment because they assimilate inorganic carbon and nutrients by two different processes: Carbon is assimilated through photosynthesis and combined with diffusively encountered nutrients to achieve a C:N ratio c_{CN}. The limiting compound determines the encounter rate as described by Liebig's law of the minima:

$$E = \min\{c_{CN} \times \beta_D \times C_N, \beta_L \times C_L\}.$$

For a particular environment of light, nutrients, organic matter, and prey, an organism encounters different amounts of resources from the various encounter mechanisms (**Figure 3**). The smallest organisms get the highest encounter rate from diffusive encounter with dissolved organic matter. Diffusion-feeding heterotrophic bacteria (osmo-heterotrophs) therefore dominate among the smallest organisms. As size increases, the encounter rate with photons becomes sufficiently high that photosynthesis combined with diffusive uptake of inorganic nutrients becomes optimal—i.e., the dominant strategy becomes phototrophy. The transition size is when carbon fixation by photosynthesis ($\beta_L C_L = b_L l^2 C_L$) becomes equal to the diffusive encounter with dissolved organic matter ($\beta_D C_{DOM} = b_D l C_{DOM}$), which occurs at a size

$$l = \frac{C_{DOM} b_D}{C_L b_L}. \quad (4)$$

Cells larger than this size are expected to be light-limited phototrophs. When the cells reach a size

$$l = \frac{c_{CN} C_N b_D}{C_L b_L}, \quad (5)$$

the diffusive uptake of inorganic nutrients becomes limiting (Mei et al. 2009). Larger cells still benefit from acquisition of carbon through the aid of photosynthesis, but they are nutrient limited. At a size

$$l = \frac{c_{CN} C_N b_D}{C_F b_A}, \quad (6)$$

active encounter with prey organisms provides the highest encounter rates—i.e., the dominant strategy becomes heterotrophy. There is also a particular size range at which photosynthesis provides more carbon than active encounter (predation) but active encounter provides more nutrients than diffusive uptake of inorganic nutrients. In this range, a mixotrophic strategy is profitable, i.e., using photosynthesis (either from an ingested chloroplast or the organism's own chloroplast)

Annu. Rev. Marine. Sci. 2016.8. Downloaded from www.annualreviews.org
Access provided by Technical Information Center & Library of Denmark on 07/31/15. For personal use only.

REVIEWS IN ADVANCE

Changes may still occur before final publication online and in print

Annu. Rev. Marine. Sci. 2016.8. Downloaded from www.annualreviews.org
Access provided by Technical Information Center & Library of Denmark on 07/31/15. For personal use only.

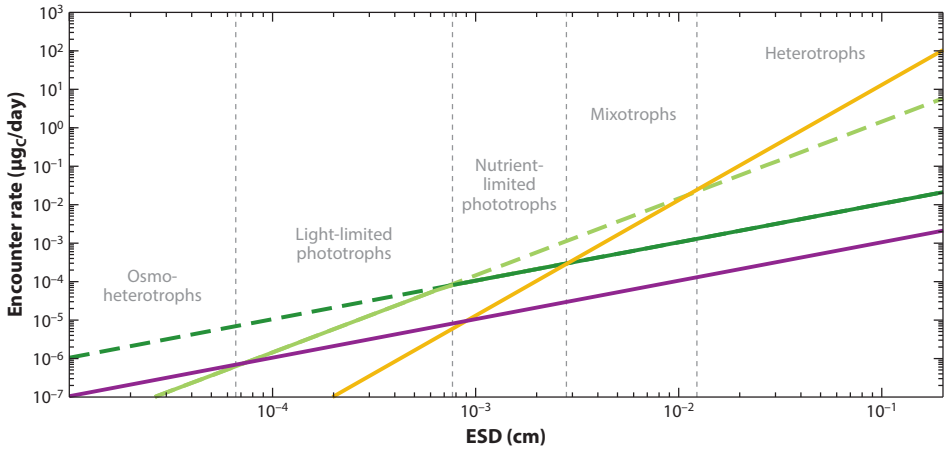

Figure 3

Encounter rates as a function of size for four different resource acquisition mechanisms and resource types: diffusive uptake of dissolved organic matter, scaling as l^1 (*solid purple line*); uptake of carbon through photosynthesis, scaling as l^2 (*dashed light green line*); diffusive uptake of dissolved inorganic nutrients (*dashed dark green line*); and active encounter of prey organisms, scaling as l^3 (*solid yellow line*). The combined uptake of carbon and nutrients by phototrophs is limited by Liebig's law and shown with solid green lines; light green is used for light-limited conditions, and dark green is used for nutrient-limited conditions. The concentration of dissolved organic matter is $C_{DOM} = 5$ μg$_C$/L, the concentration of inorganic nutrients is $C_N = 4$ μmol$_N$/L (corresponding to 50 μg$_C$/L), the light intensity at depth is $C_L = 2$ W/m^2, and the concentration of suitable prey organisms is $C_P = 10$ μg$_C$/L. Abbreviation: ESD, equivalent spherical diameter.

predominantly to provide carbon for metabolism, and using active feeding to assimilate nutrients and carbon for biomass synthesis (mixotrophs of types II and III; Stoecker 1998).

The size range in which a certain trophic strategy gives the highest yield depends on the concentration of available resources. If, for example, the concentration of prey organisms increases, the lower size limit where active feeding gives the highest yield decreases. The transition size between the dominant feeding strategies is therefore different under oligotrophic conditions (high light and low nutrient concentrations, such as summer surface conditions in seasonal environments or oceanic regions) than under eutrophic conditions (low light and high nutrient concentrations, such as spring surface conditions in seasonal environments or conditions at depth) (**Figure 4*a*,*b***). The general pattern of small diffusion feeders, medium phototrophs, and large active feeders is identical between oligotrophic and eutrophic environments, but the sizes at which the transitions occur vary: Oligotrophic conditions give rise to smaller phototrophs and a large size range of mixotrophs, whereas eutrophic conditions lead to larger osmo-heterotrophic bacteria, phototrophs, and mixotrophs. The general pattern fits well with the classical interpretation of the seasonal succession of cell size in temperate systems (Kiørboe 1993): Large cells (diatoms) dominate during nutrient-rich spring conditions but are overtaken by smaller cells (dinoflagellates and cryptophytes), often with a mixotrophic strategy, during the nutrient-depleted summer conditions (Barton et al. 2013).

A compilation of the dominant trophic strategies according to size largely confirms the theoretical predictions while also highlighting the large overlap in the size range between phototrophs, mixotrophs, and small heterotrophs (**Figure 4*c***). The overlap reflects that the compilation is based on observations from various environmental conditions, which, as demonstrated above, create a

REVIEWS IN ADVANCE
Changes may still occur before final publication online and in print

Annu. Rev. Marine. Sci. 2016.8. Downloaded from www.annualreviews.org
Access provided by Technical Information Center & Library of Denmark on 07/31/15. For personal use only.

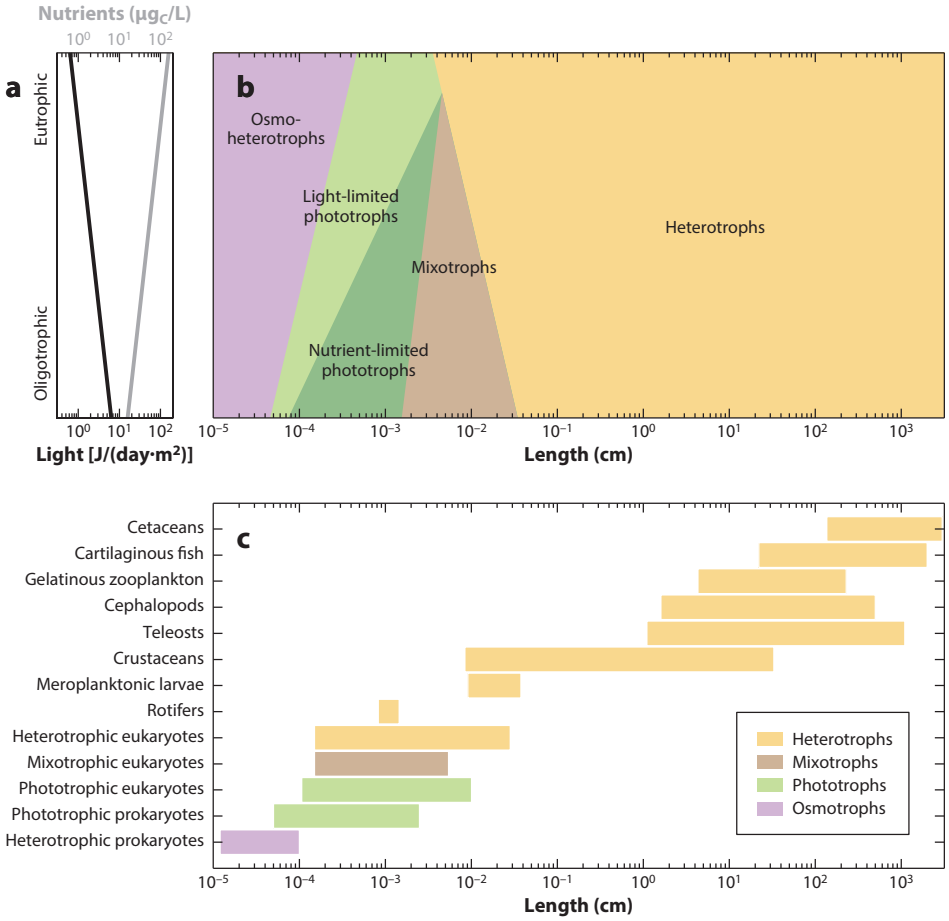

Figure 4

Trophic strategy as a function of size. (*a*) Resource conditions [nutrients (*gray line*) and light (*black line*)] used to create environments moving from oligotrophic conditions (high light, low nutrients; *bottom*) to eutrophic conditions (low light, high nutrients; *top*). (*b*) Strategies that yield the highest resource encounter rates as a function of size (*x* axis) and resource conditions (*y* axis). (*c*) Trophic strategies of 3,020 marine organisms as a function of length. Ciliates and flagellates have been categorized as phototrophs, mixotrophs, or heterotrophs depending on the trophic strategy for the specific species (see **Supplemental Table 3**). The groupings comprise cetaceans (whales, dolphins, and porpoises), cartilaginous fish (Elasmobranchii and Holocephali), gelatinous zooplankton (Cnidaria and Ctenophora), cephalopods (Cephalopoda), teleosts (Osteichthyes), meroplanktonic larvae (planktonic larvae whose adult stages are benthic), rotifers (Rotifera), crustaceans (including copepods), and unicellular eukaryotes or prokaryotes.

significant variation in the transition sizes where one trophic strategy gives a higher yield than another strategy.

MOBILITY

Movement is powered by muscles or flagella and is constrained by friction from the water. From an organism's perspective, the nature of water changes dramatically with size: Large organisms use

REVIEWS IN ADVANCE

Changes may still occur before final publication online and in print

Annu. Rev. Marine. Sci. 2016.8. Downloaded from www.annualreviews.org
Access provided by Technical Information Center & Library of Denmark on 07/31/15. For personal use only.

their inertia to coast through water, whereas smaller organisms experience water as thick and sticky. Very small organisms have to cope with the random forces of molecules that induce Brownian motion (Dusenbery 2009). The hydromechanics of movement can therefore be divided into three regimes: an inertial regime, a viscous regime, and a Brownian regime. Here, we are concerned mainly with the differences between the inertial and viscous regimes. The hydrodynamic regime determines the forces on the body, which in turn influences the optimal shape. In the viscous regime, the dominating force is surface friction, which scales with the linear dimensions of the body. In this regime, it is therefore optimal to reduce the surface area, i.e., to be spherical (although actually the optimal shape deviates slightly from spherical; Dusenbery 2009). In the inertial regime, the drag force is proportional to the projected frontal area of the organisms, making it optimal to reduce this area by streamlining.

Whether an organism is in the inertial or viscous regime depends on the Reynolds number, $Re = ul/\nu$, which describes the ratio between inertial and viscous forces operating on a body of size l moving at velocity u through water with a kinematic viscosity $\nu \approx 10^{-2}$ cm^2/s. The crossover between the two regimes is at $Re \approx 20$–30 (Webb 1988). The scaling of swimming velocity with size differs in the two regimes: In the viscous regime, the velocity was found empirically to scale as $l^{0.79}$ (Kiørboe 2011), whereas in the inertial regime, theoretical arguments predict it to scale as $l^{0.42}$ (Ware 1978) or $l^{0.5}$ (Bejan & Marden 2006); observation suggests a scaling $u \propto l^{0.45}$ (**Figure 5*a***). The empirical data indicate a crossover size between the viscous and inertial regimes at a body length of approximately 7 cm, corresponding to a Reynolds number on the order of 1,000. The relevance of size for body shape is evident (**Figure 5*b***): Small organisms do not appear to be constrained in their body shape, whereas fish and mammals are streamlined, with an average aspect ratio of approximately 0.25. Copepods are in between and have a significantly larger aspect ratio than fish. During jumps, however, the Reynolds number becomes large, thus giving them the advantage of a relatively slender body plan (Kiørboe et al. 2010).

SIZE AND SENSING

Actively feeding organisms perceive their prey by chemical or hydromechanical cues, vision, or echolocation. The range of sensing is determined by the size of the predator and the prey; a blue whale with an eye diameter of 15 cm sees much farther than a fish larva with an eye diameter of 1 mm. The sense with the furthest range for organisms of a given size can be expected to dominate among organisms of that size. Organisms using more than one sense complicate the analysis of senses. For example, sharks use smell to follow the trail of a prey at great distances; when closing in on the prey, vision becomes important (Hueter et al. 2004); and at distances below 1 m, they use electro-sensing to precisely locate the prey (Collin & Whitehead 2004). Copepods are generally considered mechanosensing organisms, yet they can sense and follow the chemical trail of a settling marine snow particle (Kiørboe 2001) and the pheromone trail of a potential mate (Bagøien & Kiørboe 2005). Leaving such complications aside, we review estimates of the sensory ranges of four senses where the range depends on the size of the predator: chemical sensing, sensing of hydromechanical signals, vision, and echolocation.

Chemosensing

In that all organisms depend on chemistry in one way or another, it may be safely assumed that they have machinery for chemical sensing. The question is how chemosensing together with behavior can bring organisms into contact with remote resources. The way organisms experience the coherence of chemical gradients and trails is determined by individual size in relation to

REVIEWS IN ADVANCE

Changes may still occur before final publication online and in print

Annu. Rev. Marine. Sci. 2016.8. Downloaded from www.annualreviews.org
Access provided by Technical Information Center & Library of Denmark on 07/31/15. For personal use only.

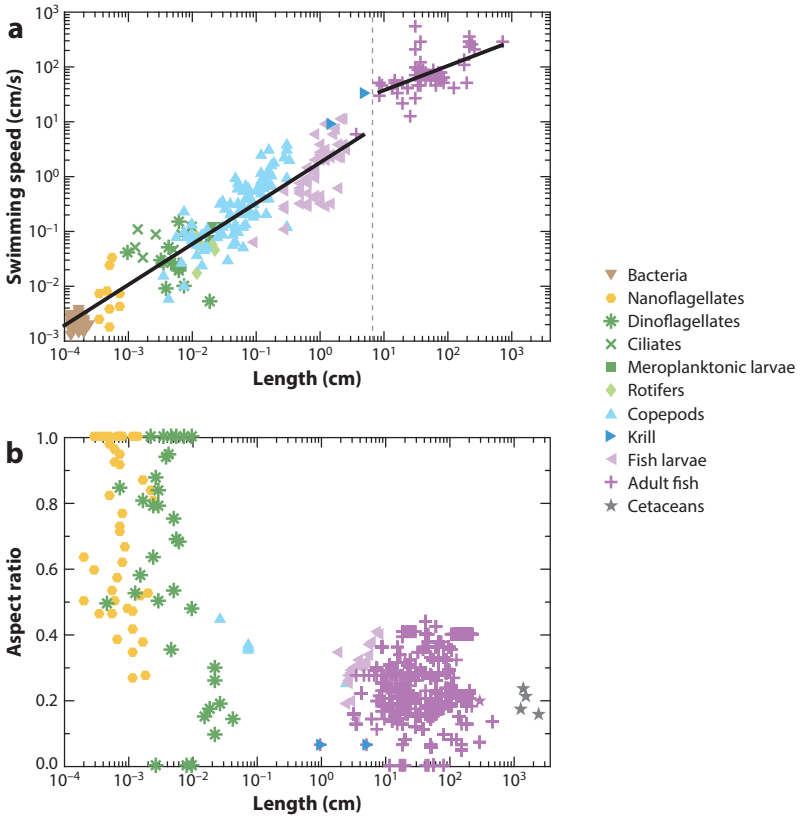

Figure 5

Swimming speeds and body aspect ratio versus body length. Length is measured as equivalent spherical diameter for planktonic organisms and as longest length for krill (*dark blue*), fish larvae (*light purple*), adult fish (*dark purple*), and cetaceans (*gray*). (*a*) Swimming speed as a function of length. Data for zooplankton (including fish larvae) are from Kiørboe (2011); data for fish (cruising speed) are from Sambilay (1990). The lines are power-law fits (see **Table 1**). The split between the two data sets was determined as the size that gave the lowest total residual of the fits. The crossover size at 6.6 cm corresponds to a Reynolds number of approximately 1,000. (*b*) Aspect ratio as a function of length for mobile marine organisms. Data for nanoflagellates and dinoflagellates are from Throndsen et al. (2003) and Tomas (1997); data for copepods are from Kiørboe et al. (2010); data for krill are from Watkins & Brierley (2002); data for fish larvae are from Ara et al. (2013), Morioka et al. (2013), Moser et al. (1986), and Oka & Higashiji (2012); and data for adult fish are from Froese & Pauly (2013).

turbulent eddies. Turbulence is characterized by three length scales (Tennekes & Lumley 1972): the Batchelor scale (≈10 μm in the upper ocean, where turbulence starts to erode the regularity of a gradient), the Kolmogorov scale (≈1,000 μm, where turbulence starts to impede the organism's ability to maintain direction), and the integral scale, (≈1–10 m, where turbulent energy is injected by large-scale motions).

We distinguish between two modes of chemosensing: gradient climbing (e.g., bacterial run-tumble) and trail following (e.g., a shark following a prey trail). Gradient climbing relies on a chemical gradient set up by molecular diffusion of a solute from a source. The regularity of such gradients would be scale independent if it were not for turbulence. We can place an upper

REVIEWS IN ADVANCE

Changes may still occur before final publication online and in print

Annu. Rev. Marine. Sci. 2016.8. Downloaded from www.annualreviews.org
Access provided by Technical Information Center & Library of Denmark on 07/31/15. For personal use only.

Stresslet: a Stokes flow produced by two colinear antiparallel point forces acting on a fluid

boundary for gradient climbing between the Batchelor scale and the Kolmogorov scale, in the range of 10–1,000 μm. Another limitation of the ability to follow gradients created by molecular diffusion is whether the trail is diffusing faster than the movement of the prey. This criterion sets an upper limit for predator size of 50 μm (Kiørboe 2011). For trail following, additional criteria come into effect: the movement of the target organism, the rate at which it releases solute, and how well the searching organism can detect this solute above background levels. In any case, organisms smaller than the energy-containing turbulent eddies will experience the trail as patchy and therefore need to search large areas relative to their own size to follow the trail. This scenario is relevant for organisms of a size between the Kolmogorov and integral length scales, i.e., organisms smaller than 1 m. Organisms larger than the integral scale are able to integrate over the subscale trail details and follow a trail without detours. Trail following is therefore most advantageous for large organisms and/or in quiescent environments, e.g., the deep oceans (Martens et al. 2015).

Mechanosensing

Ambush feeders may sense their prey via the fluid mechanical disturbance created by a moving prey (reviewed in Kiørboe 2011). To enhance the sensory range, they employ special sensory arrangements protruding from the body, like the long seta-studded antennules on copepods or the sensory hairs arranged along the slender bodies of chaetognaths (arrow worms). The fluid mechanical disturbance of a self-propelling prey can be modeled as a stresslet, which implies that the signal attenuates as the cube of the distance away from the prey (Visser 2001). The range at which this signal can be sensed is $R \approx (3l_{\text{prey}}^2 l_{\text{sensor}} u_{\text{prey}}/u^*)^{1/3}$, where u^* is the detection limit of the velocity disturbance and l_{sensor} is the length of the sensor (approximately the size of the predator). For $u_{\text{prey}} = b l_{\text{prey}}^{0.74}$ and a predator:prey length ratio $B \approx 10$, the sensing distance is $R \approx c l^{1.24}$, with $c \approx 1.4\,\text{cm}^{-0.24}$ for $u^* = 33$ μm/s (Kiørboe 2011) (**Figure 6**). An upper range comes into effect when the turbulent shear γ across the body of the predator organism approaches the sensitivity, i.e., when $u^* = \gamma l$. For moderate turbulent shears found in the upper ocean (0.03 s^{-1}, which is in the middle of the typical range of 10^{-4}–10^{-1} s^{-1}; Visser & Jackson 2004), this happens for l in the range 500–1,000 μm. Mechanosensing is therefore most advantageous for small organisms (<1 cm) or on short ranges for large organisms.

Vision

Eyes contain photoreceptors that detect light and convert it into neuronal signals. The simple eyes of some microorganisms are only able to detect changes in the ambient light sufficient to detect diurnal rhythms, orientation toward the surface, and nearby movement. Active visual predation requires an eye with sufficient resolution to form an image and preferably also active optical machinery to focus a targeted object. With regard to feeding, the most important property of the eye is the distance at which it can discern a suitable prey.

Dunbrack & Ware (1987) modeled the optical and sensing abilities of a camera eye to estimate the visual range of a predator of length l searching for prey with a fixed fraction of the predator size (see sidebar The Dunbrack & Ware Model of Visual Range). Two important conclusions emerge from their arguments. First, the sensing range scales as $l^{1.75}$ in clear water under high light conditions. Second, the maximum range of large organisms is limited by the optical properties of the water. Under perfect conditions, the range is 40–70 m (Davies-Colley & Smith 1995). The range decreases with the ambient light such that at depth, where the inherent contrast is low, visual range is limited mainly by the optical properties of the water.

REVIEWS IN ADVANCE

Changes may still occur before final publication online and in print

Annu. Rev. Marine. Sci. 2016.8. Downloaded from www.annualreviews.org
Access provided by Technical Information Center & Library of Denmark on 07/31/15. For personal use only.

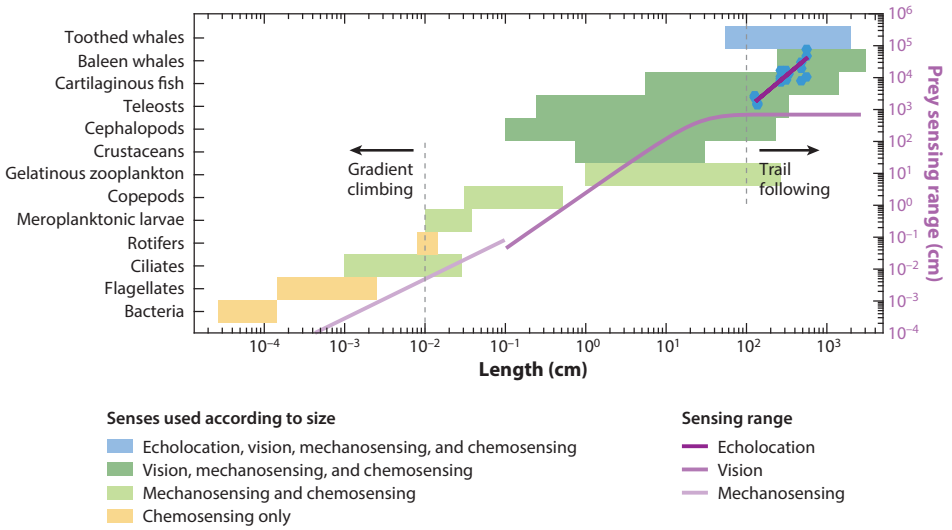

Figure 6

Senses versus size. The left axis and bars show senses used for detecting prey grouped according to size and organismal group (see **Supplemental Table 4**). The right axis and purple lines show the estimated ranges for sensing a prey a factor of 10 shorter than a predator (for details, see sidebar The Dunbrack & Ware Model of Visual Range). For toothed whales (including dolphins), the echolocation ranges were determined from tank and field measurements of individuals of different sizes (*blue hexagons*) (see **Supplemental Table 5**); the line is fitted with exponent 17/8 (see **Table 1**). The vertical dashed gray lines are estimates of the limits of chemotaxis strategies.

A lower size limit of a functioning eye is determined by the finite size of the photoreceptor. Photoreceptors' functioning relies on opsin molecules (rhodopsin) stacked in rod cells with a width $d_{\mathrm{rod}} \approx 1$ μm (Curcio et al. 1990). Taking account of the universality of the opsin design for photoreception, we may consider this length a limiting factor for building eyes. Considering a minimal resolution for sufficient image formation of (for example) 100^2 results in a retina size of $d_{\mathrm{r}} \approx 0.1$ mm. This is approximately one-tenth the size of the smallest aquatic organisms with camera eyes: larval fish and cephalopods. Therefore, vision is only viable as a mode of sensing prey for predators in the size range of a few millimeters and larger.

Echolocation

Echolocation is an active sensing mode in which the animal emits ultrasonic calls and interprets the environment based on the echoes of these calls. It is common for toothed whales (odontocetes), and although it is also used for orientation, here we focus on echolocation and its role in prey detection.

We can estimate how the range R of echolocation scales with the size of the animal based on three assumptions: (*a*) The sensitivity of the ear, P_0, is independent of the size of the animal; (*b*) the emitted power scales with an exponent p as $P_{\mathrm{e}} \propto w^p \propto l^{3p}$; and (*c*) the frequency-dependent attenuation of sound in seawater can be ignored because this attenuation is small compared with the conical spread of the sound wave. In free space, the emitted signal spreads as a conic beam, resulting in the attenuation of the signal power as R^{-2}. The power of the reflected signal is $P_{\mathrm{r}} \propto P_{\mathrm{e}} l_{\mathrm{prey}}^2 (2R)^{-2}$,

REVIEWS IN ADVANCE

Changes may still occur before final publication online and in print

Annu. Rev. Marine. Sci. 2016.8. Downloaded from www.annualreviews.org
Access provided by Technical Information Center & Library of Denmark on 07/31/15. For personal use only.

THE DUNBRACK & WARE MODEL OF VISUAL RANGE

The maximum visual range in clear water can be estimated by considering the properties of a pinhole camera eye, as was done in a largely unrecognized work by Dunbrack & Ware (1987). Here, we provide a simplified derivation of their argument that also corrects several minor errors.

The projection of a visual image of a prey on the retina of a predator activates a number of visual elements n proportional to the area of the projected image multiplied by the density of visual elements. Because we are interested in the maximum distance R at which an object can be discerned, we can assume that the distance is large relative to the diameter of the eye such that the curvature of the eye can be ignored. The number of activated visual elements is $n \propto \rho l_{\text{eye}}^2 l_{\text{prey}}^2 R^{-2}$, where ρ is the density of visual elements and l_{eye} is the diameter of the eye. The density of visual elements is a decreasing function of the size of the eye: $\rho \propto l_{\text{eye}}^{-d}$, with $d \approx 0.5$ (Dunbrack & Ware 1987). Assuming that the size of the eye and the preferred size of the prey scale with the length of the predator gives the number of visual elements as $n \propto l^{4-d} R^{-2}$.

The largest distance R at which a predator can discern a prey of size (length) l_{prey} is the distance at which the apparent contrast (the difference between the visual imprint of the prey and the background) of the prey (C_{a}) equals the contrast threshold that the predator can distinguish (C_{t}). The apparent contrast of the prey declines away from the inherent contrast $C_0 = 0.3$ as $C_{\text{a}} = C_0 e^{-\alpha R}$, where $\alpha = 0.001$ cm^{-1} is the attenuation of light by the water. The contrast threshold is a declining function of the number of visual elements n involved in discerning the object: $C_{\text{t}} = C_{\text{t.min}} + 1/n$, where $C_{\text{t.min}} = 0.15$ is the minimum contrast threshold for vision, which depends on the ambient light. This semiheuristic relationship is known as Ricco's law (Northmore et al. 1978). The maximum distance at which the prey can be perceived is the point at which the apparent contrast reaches the contrast threshold (i.e., where $C_{\text{a}} = C_{\text{t}}$): $C_0 e^{-\alpha R} = C_{\text{t.min}} + K R^2 l^{d-4}$, where $K = 0.025$ cm$^{1.5}$ is a constant that characterizes the sensitivity of the eye.

It is not possible to isolate R from the expression above. However, two limiting cases can be derived. The clear-water limit is where the visual range is limited by the resolution of the eye, i.e., where $e^{-\alpha R} \approx 1$ and $C_0 \gg C_{\text{t.min}}$: $R \approx \sqrt{C_0/K} l^{2-d/2}$. In this case, the maximum visual range increases with $l^{2-2/d} \approx l^{1.75}$ for $d = 0.5$. The turbid-water limit is when the visual range is limited by the sensitivity (the minimum contrast threshold) of a visual element, when $C_{\text{t.min}} \gg K R^2 l^{4-d}$: $R \approx (\ln C_0 - \ln C_{\text{t.min}})/\alpha$. In this limit, the size of the predator does not play a role, and the minimum contrast threshold essentially limits the visual range. The visual range decreases if the light in the water is limited (higher minimum contrast threshold $C_{\text{t.min}}$) or the turbidity α increases. The prediction of this limit has been the subject of more elaborate models (Aksnes & Utne 1997).

where l_{prey}^2 is the area of the reflecting target and the factor 2 is used because the signal attenuates both as it travels toward the target and when it returns. Inserting the power of the emitted signal and absorbing the factor 2 in the proportionality constant gives $P_{\text{r}} \propto l^{3p} l_{\text{prey}}^2 R^{-2}$. The distance where the strength of the returned signal is just at the sensitivity of the ear, i.e., $P_0 = P_{\text{r}}$, scales as $R \propto P_0^{-1/2} l_{\text{prey}} l^{3p/2}$. If the preferred prey size scales with the size of the predator, i.e., $l_{\text{prey}} \propto l$, then

$$R \propto P_0^{-1/2} l^{1+3p/2}.$$

If the power of the emitted sound follows metabolic scaling, $p = 3/4$, then the exponent becomes 17/8. This argument provides only the scaling of the sensing range; the factor can be found by fitting to data (**Figure 6**).

REVIEWS IN ADVANCE

Changes may still occur before final publication online and in print

Annu. Rev. Marine. Sci. 2016.8. Downloaded from www.annualreviews.org
Access provided by Technical Information Center & Library of Denmark on 07/31/15. For personal use only.

Size and Sense

The theoretical arguments outlined above identified three characteristic predator sizes where one sense becomes more efficient than another: (*a*) 100 μm, which is the upper size limit for gradient climbing; (*b*) between 1 mm and 1 cm, where there is a transition from hydromechanical sensing to vision; and (*c*) approximately 1 m, which is the point at which predators are able to realize the upper visible range of up to 80 m in clear water. An extension of the sensory range beyond this length can be achieved only by trail-following chemical tracers or by echolocation.

Analysis of body size and senses used by marine organisms reveals that the number of possible senses available to a predator increases with size (**Figure 6**). Large organisms typically combine several senses for foraging. The lower size limit of vision of approximately 1 cm is clearly borne out; this size indeed corresponds to the smallest size of fish and cephalopod larvae. Some large life forms do not use vision to detect prey, most notably the gelatinous zooplankton, even though they are much larger than 1 cm. From this perspective, the strategy of gelatinous zooplankton is to avoid building a vertebrate body (with its associated high metabolic requirements to utilize the increased sensing range that vision provides) and to instead depend on an inflated body to increase the prey encounter cross section (Kiørboe 2013). Because the superiority of vision declines with ambient light, the relative disadvantage of gelatinous zooplankton compared with fish diminishes in turbid waters and in deep waters (Sørnes & Aksnes 2004).

Physiological mortality: the ratio between mortality and weight-specific consumption; with metabolic scaling of uptake $Aw^{3/4}$ and mortality $cw^{-1/4}$, the physiological mortality becomes $\alpha = c/A$

LIFE HISTORY AND PROGENY SIZE

Though obvious on the individual level, the concept of size becomes ambiguous when applied at the species level because all organisms differ in the sizes of their adults and progeny; even unicellular organisms need to double their size before they can divide. The difference between adult and progeny size is most extreme among the teleosts, where the weight ratio between adults and larvae can be up to 10^8 (for bluefin tuna).

Optimal Life History Theory

The evolution of life history with a pronounced difference between adult and offspring size can be understood from optimal life history theory (Andersen et al. 2008, Christiansen & Fenchel 1979). If we assume (*a*) a standard metabolic scaling of consumption Aw^n with $n \approx 3/4$ (West et al. 1997), (*b*) a metabolic scaling of mortality αAw^{n-1} (Andersen & Beyer 2006, Hirst & Kiørboe 2002, Peterson & Wroblewski 1984), and (*c*) determinate growth, then the lifetime reproductive output R_0 becomes

$$R_0 = \frac{\epsilon}{2\alpha}\left(\frac{W}{w_0}\right)^{1-\alpha}, \tag{7}$$

where W/w_0 is the ratio between the weight at maturation and weight of offspring, ϵ is the efficiency of reproduction, and α is the physiological mortality, which is less than 1 (Andersen et al. 2008) (see sidebar Life History Optimization of Offspring Size). Because the exponent $1-\alpha$ is positive, R_0 is an increasing function of W/w_0. The metabolic assumptions thus predict an evolutionary pressure toward a life history with as large a ratio as possible between adult size and offspring size. Because no organism has an infinite ratio between adult size and offspring size, a full understanding of what limits actual offspring size cannot be achieved from optimal life history theory based on metabolic scaling laws alone; the actual offspring size will be limited by other processes.

REVIEWS IN ADVANCE

Changes may still occur before final publication online and in print

Annu. Rev. Marine. Sci. 2016.8. Downloaded from www.annualreviews.org
Access provided by Technical Information Center & Library of Denmark on 07/31/15. For personal use only.

LIFE HISTORY OPTIMIZATION OF OFFSPRING SIZE

The optimal life history strategy in terms of offspring size and adult size is the strategy that maximizes lifetime reproductive output (Charnov 1993). In optimal life history theory, lifetime reproductive output is determined by the mortality and the available energy as functions of size or age. Here, we determine the offspring size that maximizes lifetime reproductive output using arguments from Christiansen & Fenchel (1979) and Andersen et al. (2008).

The available energy can be assumed from metabolic scaling arguments to be $H(w) = Aw^n$, where the usual metabolic assumption is $n = 3/4$ (West et al. 1997). Consumption results in a prey mortality of $\mu(w) = \alpha w^{n-1}$, where α is a dimensionless constant relating consumption and mortality (Andersen & Beyer 2006). For simplicity, we assume determinate growth where a juvenile uses all acquired energy for growth and a mature individual of size W uses all energy for reproduction; however, the central results are valid for indeterminate growth as well (Andersen et al. 2008). The lifetime reproductive output (expected number of offspring during life) is

$$R_0 = \frac{\epsilon}{2} P_{w_0 \to W} \frac{H(W)}{w_0 \mu(W)},$$

where ϵ is the reproductive efficiency, the division by 2 assumes an even sex ratio, $H(W)$ is the adult rate of reproduction (mass per unit time), $1/\mu(W)$ is the expected adult life span, $1/w_0$ is to convert from units of mass to number of offspring, and the probability of surviving from offspring size w_0 to adult size W is

$$P_{w_0 \to W} = \exp\left[-\int_{w_0}^{W} \frac{\mu(w)}{H(w)} \mathrm{d}w\right].$$

Inserting the metabolic assumptions $H(w) = Aw^n$ and $\mu(w) = \alpha A w^{n-1}$ yields a lifetime reproductive output of

$$R_0 = \frac{\epsilon}{2\alpha} \left(\frac{W}{w_0}\right)^{1-\alpha}.$$

Three conclusions can be drawn from this result:

1. If $R_0 < 1$, then each female produces less than a single offspring throughout life, yielding an unsustainable population.
2. Lifetime reproductive output depends only on the ratio between adult size and offspring size. The absolute values of the two sizes do not matter.
3. The larger the ratio between adult and offspring size, the higher the fitness. Organisms will therefore strive to maximize this ratio under the constraints of other external factors (Neuheimer et al. 2015).

Note that the arguments above ignore the maintenance metabolism and indeterminate growth to simplify the mathematical derivation, but both of these effects can be accounted for (Andersen et al. 2008).

Offspring Size Strategies

Observed offspring size strategies employed by marine life can be roughly partitioned into two groups: a fixed-ratio strategy in which offspring size is a constant fraction of adult size, and a small-eggs strategy in which offspring size is invariant, i.e., independent of adult size (Neuheimer et al. 2015) (**Figure 7**). Crustaceans, cartilaginous fish, and cetaceans employ the fixed-ratio strategy, with an adult:offspring weight ratio of approximately 100:1. The metabolic optimal life history theory (Equation 7) is unable to predict the fixed-ratio strategy. For marine mammals, the fixed-ratio strategy can be explained by the need to perform parental care; it simply becomes increasingly difficult for a parent to provide care when the offspring is much smaller than the parent (Shine

REVIEWS IN ADVANCE

Changes may still occur before final publication online and in print

Annu. Rev. Marine. Sci. 2016.8. Downloaded from www.annualreviews.org
Access provided by Technical Information Center & Library of Denmark on 07/31/15. For personal use only.

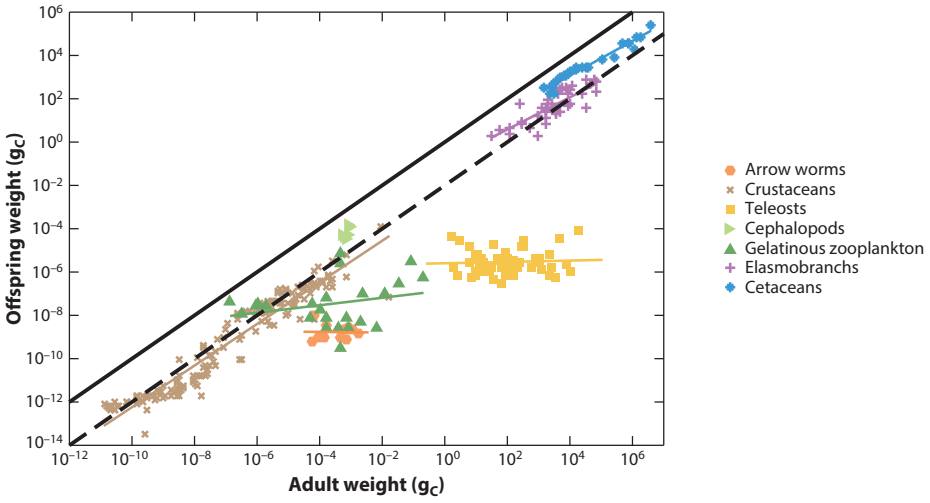

Figure 7

Weights of adults and offspring for metazoans grouped by species of similar taxonomy. Estimates of mean adult and offspring sizes were compiled from the literature, with adults defined as individuals that had reached maturity and offspring defined as the smallest size at which offspring are independent of the parent (see **Supplemental Tables 6 and 7**). The original data included measures of volume, length, wet weight, dry weight, and carbon dry weight, all of which were converted to carbon dry weight; this conversion used species-specific conversion factors when available, and group-specific conversion factors otherwise. The solid line is a 1:1 adult:offspring size ratio, and the dashed line is a 100:1 adult:offspring size ratio. Life forms along this line [cetaceans (*blue*), elasmobranchs (*purple*), and crustaceans (*brown*)] follow the fixed-ratio strategy, whereas life forms with invariant offspring size [most notably teleosts (*yellow*)] follow the small-eggs strategy.

1978). For the other groups, the fixed-ratio strategy can be explained by an elaboration of the evolutionary argument in the second sidebar (Life History Optimization of Offspring Size) to account for density-dependent effects (K. Olsson, H. Gislason & K.H. Andersen, manuscript submitted). Such elaboration shows that the strategy that maximizes W/w_0 is optimal only if the offspring do not experience density-dependent effects at the time of hatching. If they do experience density-dependent survival early in life, an evolutionary stable strategy with $W/w_0 \approx 100$ emerges.

TRANSITIONS BETWEEN LIFE FORMS

We have reviewed how size influences resource acquisition, mobility, ability to sense prey, and life history strategy based on theoretical arguments and cross-species empirical analyses. We now use these relations to understand the mechanisms behind the transitions between the seven realms of marine life: molecular life (viruses), osmo-heterotrophic bacteria, unicellular phototrophs, unicellular mixotrophs and heterotrophs, planktonic multicellular heterotrophs with ontogenetic growth, visually foraging poikilotherms, and homeotherms (**Figure 1**, **Table 1**). These seven realms correspond to the traditional taxonomic division of life into viruses, bacteria, phytoplankton, uni- and multicellular zooplankton, fish, and marine mammals. Our alternative naming reflects the function of the groups and highlights the factors that determine the characteristic sizes where there is a transition between the groups.

REVIEWS IN ADVANCE

Changes may still occur before final publication online and in print

Annu. Rev. Marine. Sci. 2016.8. Downloaded from www.annualreviews.org
Access provided by Technical Information Center & Library of Denmark on 07/31/15. For personal use only.

A central theme is that the development of larger size opens up new possibilities for resource acquisition and sensing. Examples include how the battery of available senses increases with size (**Figure 6**), how the emergence of multicellularity makes it possible to increase the adult:offspring size ratio and thereby increase fitness (see sidebar Life History Optimization of Offspring Size), and how mortality decreases with size. Larger size therefore increases the competitive edge, provides access to new resources, and increases survival. This, of course, only works until the niche related to the larger size is filled, but it explains the evolutionary drive toward larger body size. The sizes where new possibilities appear often mark a transition between the major life forms because the utilization of new senses and other changes require fundamental alterations in body plan and life strategy.

From Viruses to Cells

The smallest size of a cell is approximately 10^{-15} g_C, with a diameter of approximately 0.1–1 μm. Organisms this small are believed to be functionally limited by metabolic constraints (Kempes et al. 2012) and the size of nonscalable components: genome size (DeLong et al. 2010) and in particular the cell wall (Raven 1994). The cell wall size alone can be used to calculate a lower limit for cell size: The wall has a mass $c_{wall}d^2$ and the cell itself has a mass cd^3, where c_{wall} and c are constants. If we ignore the genome, a theoretical lower limit to cell size is where all cell mass is used by the wall:

$$d_{limit} = \frac{c_{wall}}{c}. \quad (8)$$

For a 0.5-μm cell, the wall comprises approximately 30% of the total mass (Raven 1994), so $c_{wall}/c \approx 0.3 \times 0.5$ μm. This gives a lower limit on cell size of $d_{limit} \approx 0.15$ μm.

From Osmo-Heterotrophs to Phototrophs

The smallest unicellular organisms are heterotrophic bacteria feeding on dissolved organic matter encountered through diffusion. At a diameter $(C_{DOM}b_D)/(C_Lb_L)$ (Equation 4), it becomes favorable to fix inorganic carbon through photosynthesis instead of relying on dissolved organic matter. This size depends on the relative concentrations of dissolved organic matter (C_{DOM}) and light (C_L), but it can be as small as 10^{-14} g_C in the upper photic zone with very low concentrations of dissolved organic matter ($C_{DOM} \approx 5$ μg$_C$/L) and abundant light [$C_L \approx 7$ J/(day·m^2)] and increases as light decreases (**Figure 4**).

From Phototrophs to Heterotrophs

The smallest phototrophs are expected to be carbon limited (which in practice means that they are limited by the amount of light, because dissolved inorganic carbon is assumed to be plentiful), whereas the largest phototrophs are expected to be nutrient limited. This difference emerges from the different scaling of nutrient encounter (which scales as l^1) and light encounter (which scales as l^2) (Equations 2 and 3, **Figure 3**). As before, the exact sizes where the transitions between light-limited phototrophs, nutrient-limited phototrophs, and heterotrophs occur depend on the specific conditions of dissolved nutrients, light, and suitable prey (**Figure 4*b***). An order-of-magnitude estimate of the characteristic transition between phototrophs and pure heterotrophs is 10^{-7} g_C ($l \approx 6 \times 10^{-2}$ cm), but it can vary from 10^{-8} g_C in conditions with low light and high nutrients to 10^{-5} g_C in conditions with high light.

REVIEWS IN ADVANCE

Changes may still occur before final publication online and in print

The size that marks the transition between phototrophs and heterotrophs is blurred by a large group of mixotrophic organisms that acquire nutrients and carbon for biomass synthesis through phagotrophy, while photosynthesis provides carbon primarily for metabolism. The mixotrophic strategy is most favorable for organisms with sizes in the transition between phototrophy and heterotrophy. The size range where the mixotrophic strategy is favorable varies with environmental conditions: It is vanishingly small in eutrophic conditions and increases to more than a factor of 10 in diameter in oligotrophic conditions, in agreement with observations (Barton et al. 2013).

Phagotrophy: taking up carbon and nutrients by absorbing other living organisms

Unicellular to Multicellular Life

The drive to develop larger size eventually leads to multicellular organisms. Multicellularity opens the possibility of specialized tissue for, e.g., sensory organs. Among microscopic metazoans, the dominant group of copepods has developed sensory apparatus to detect prey via hydromechanical cues and appendages to generate feeding currents and make jumps to escape predators. We have not developed a specific argument for the size where the transition to multicellularity occurs, but because life history theory predicts that increasing the adult:offspring size ratio increases lifetime reproductive output (Equation 7), it is likely to occur at the smallest possible size. DeLong et al. (2010) argued that this point is approximately 10^{-6} g_C ($\approx$1 μm), the size at which it becomes possible to develop a fractal delivery network.

The life history argument in Equation 7 shows how metabolic constraints create an evolutionary drive to minimize offspring size and maximize adult size. This means that organisms within each metazoan group strive to extend their size range, but they are able to do so only within the limits defined by the sizes where there is a breakdown in a scaling relationship describing a vital function.

From Copepods to Fish

Fishes (including, from a functional perspective, cephalopods) are the dominant organisms in the size range from 1 mg_{WW} to approximately 100 kg_{WW} (1 cm to 2 m). Fish are characterized by being streamlined, visual predators. At sizes smaller than 1 mg_{WW}, the dominating organisms are blind copepods, which have a very nonstreamlined body plan. The transition size between these two very different life forms is characterized by transitions between superior sensing modes (from mechanosensing to vision) and between hydromechanical regimes (from viscous to inertial). The change in hydromechanical regime explains the slender fish shape, but it also entails a change in feeding mode. Fish larvae employ suction feeding, which becomes increasingly difficult the smaller they are (China & Holzman 2014). Probably the most important transition is in sensing, with the lower size limit of fish coinciding with the lower size of a functioning eye. Were fish to make smaller eggs, their larvae would be unable to compete with the tactile-sensing copepods, which have a morphology designed for optimal movement and prey capture in a viscous fluid environment; were copepods to become larger, they would be outcompeted by visually sensing fish with streamlined bodies.

From Fish to Cetaceans

Cetaceans are the largest organisms in the oceans, occupying the size range from approximately 100 kg_{WW} and up. It is tempting to attribute the transition from fish to cetaceans to the appearance of echolocation as a possible sensing mode. However, only toothed cetaceans employ echolocation for sensing; baleen whales rely on the same senses as fish. If there are no change in the power-law relationships determining sensing and food encounter, then why have teleosts not evolved even

Annu. Rev. Marine. Sci. 2016.8. Downloaded from www.annualreviews.org
Access provided by Technical Information Center & Library of Denmark on 07/31/15. For personal use only.

REVIEWS IN ADVANCE

Changes may still occur before final publication online and in print

Annu. Rev. Marine. Sci. 2016.8. Downloaded from www.annualreviews.org
Access provided by Technical Information Center & Library of Denmark on 07/31/15. For personal use only.

larger sizes than the few hundred kilograms of the largest fish (bluefin tuna and sunfish, which have maximum weights of 450 and 1,000 kg_{WW}, respectively)? We propose two arguments for the transition between fish and cetaceans: a metabolically based upper limit of a water-breathing organism (Freedman & Noakes 2002, supplement to Makarieva et al. 2004) and a lower size limit of a homeothermic (warm-blooded) organism.

We have focused on resource acquisition in terms of carbon and nutrients, but heterotrophs also need oxygen to fuel their metabolism. The absorption of oxygen through gills is limited by the surface area of the gills. Because the surfaces of gills are fractal, they scale with an exponent between 2/3 and 1, probably very close to the metabolic exponent of 3/4. The acquisition of oxygen therefore scales with a similar exponent as metabolism, so the relative ability to acquire food and oxygen is independent of size. However, larger organisms accumulate heat created by activity and use this to elevate their metabolism. Notable examples are scombroids (tuna and marlin) and pelagic sharks (Block 1991). A high body temperature means higher activity and therefore higher predatory success against slower heterothermic (cold-blooded) prey. Such an increase in metabolism will eventually require more oxygen than can be obtained by pumping water over the gills. This problem is solved by ram ventilation, which provides a higher flow of water around the gills and therefore a higher oxygen absorption rate. Evidence for this is provided by the largest fish being either very active ram-ventilating fish (large scombroids and sharks) or relatively sluggish pumping fish (sunfish). We conjecture that it would be impossible for fish to develop homeothermy as a means of competing with cetaceans; the solubility of oxygen in water is simply too low to fuel a homeothermic metabolism. Cetaceans fuel their high homeothermic metabolism by breathing air, which has a much higher solubility of oxygen than water does.

For homeotherms, the loss of body heat should be included in the energy budget, as this defines a lower limit for the size of a homeotherm (Haldane 1928). Heat loss is a surface process that scales as $\propto \kappa w^{2/3}$, where κ is the thermal conductivity of water. Because organisms wish to minimize heat loss, their surface is not fractal and the exponent is not larger than 2/3. The energy for heating comes from the acquisition of resources (oxygen and food), which scales metabolically as $Aw^{3/4}$. The size where there is a balance between heat loss and resource acquisition defines a lower limit of homeothermy as $(A/\kappa)^{12}$ (Andersen et al. 2008). This lower limit is highly sensitive to the values of the parameters A and κ because their ratio is raised to a high exponent. For example, the ratio between the lower limits calculated for a marine and a terrestrial habitat is the ratio between the heat conductivity in air and water ($\approx$20) raised to power 12, which gives 4×10^{15}. This factor is much larger than the ratio between the smallest cetacean, a harbor porpoise calf of approximately 10 kg, and the smallest terrestrial homeotherm, an Etruscan shrew (*Suncus etruscus*) of approximately 0.1 g. Nevertheless, it seems evident that the smallest land animals are limited by loss of heat (e.g., shrews huddle together to conserve heat), so how can cetaceans manage to attain a small size in the face of a larger heat loss? We hypothesize that they do so by having an insulating layer of blubber. To achieve a lower size of 10 kg (a factor of 10^6 smaller than predicted), cetaceans need to decrease heat losses by a factor of $10^{6/12} \approx 3.2$ relative to terrestrial animals, which is not out of scope.

BEYOND SIZE

We posit that individual size is the most important trait characterizing a pelagic organism. Knowing the size of an organism makes it possible to estimate, often within an order of magnitude, its metabolic rate, clearance rate, swimming speed, and sensory range. We have shown how that information facilitates inference of trophic strategy, sensory mode, body shape, and, to some degree, reproductive strategy. Although important, we have largely ignored the subtle interplay

REVIEWS IN ADVANCE

Changes may still occur before final publication online and in print

Annu. Rev. Marine. Sci. 2016.8. Downloaded from www.annualreviews.org
Access provided by Technical Information Center & Library of Denmark on 07/31/15. For personal use only.

between temperature, oxygen concentration, and size (Verberk & Atkinson 2013). Our exploration has concentrated on how an individual's physiology and interactions with the surrounding physical and biotic environment are constrained by body size. Because body size also plays a large role in predator-prey interactions (Barnes et al. 2008), it is central in constraining biomass distributions (Boudreau & Dickie 1992, Sheldon & Prakash 1972), food web topology (Petchey et al. 2008), and species diversity (Fenchel & Finlay 2004, May 1975, Reuman et al. 2014), all of which lie beyond our work here but highlight the central role of body size. Even though size can be characterized as a "master trait" (Litchman & Klausmeier 2008), it is not the only trait that characterizes an organism. The relevant question is then which other traits best characterize the variation around the mean in the reviewed relations with size (**Figures 2**, **5**, and **7**). We propose three candidate traits to consider: predator:prey size ratio, feeding mode for heterotrophic metazoans, and jellyness.

Among heterotrophic metazoans, there appear to be two dominant strategies for predator:prey size ratio: a strategy based on a fixed ratio in the range 10–100, which is followed by most fish and copepods (Barnes et al. 2008), and a strategy aimed at preying on organisms much smaller than the predator. The small-prey strategy is used by the largest zooplankton (pelagic tunicates) and the largest vertebrates (whale sharks and baleen whales). Organisms with a large predator:prey size ratio rely on filtering the water to catch the prey. It is presently unknown what drives the development of the two alternative, but apparently equally competitive, strategies.

The feeding mode determines whether an actively feeding predator encounters its prey through ambushing or cruising. It is often assumed that predation pressure is a function of size only and therefore independent of feeding strategy or sensing mode. This is not quite true. It is becoming increasingly evident that feeding strategy is associated with a trade-off in mortality: An ambush feeder will encounter fewer prey than a cruising predator, but it will also have less exposure to predation and therefore lower mortality. This is a special example of how behavior manipulates this trade-off between feeding gains and mortality (Lima & Dill 1990). A quantitative demonstration of this trade-off has been made for zooplankton based on laboratory experiments (Kiørboe 2013), and its importance for seasonal succession has been modeled (Mariani et al. 2013). These trade-offs likely apply at least qualitatively to other predators, e.g., fish.

A related trade-off is the development of a gelatinous body (jellyfish, box jellies, and pelagic tunicates). We argued above (see the section Size and Sensing) that visual predators would be superior to predators sensing their prey through hydromechanical forces. However, the inflated body size of gelatinous organisms results in a large encounter cross section and hence a higher clearance rate than that of nongelatinous organisms with the same carbon body mass. This is what makes the jelly strategy effective even in the same size range where visual predation is possible (Acuña et al. 2011), particularly under low-light conditions (Sørnes & Aksnes 2004). At the same time, the gelatinous body makes the organism less attractive to predators, thereby lowering its mortality. These two examples show how general rules of encounter, mobility, and sensing inferred from size scaling can be broken by other traits.

DISCLOSURE STATEMENT

The authors are not aware of any affiliations, memberships, funding, or financial holdings that might be perceived as affecting the objectivity of this review.

ACKNOWLEDGMENTS

K.H.A. thanks Mick Follows for hospitality at the Massachusetts Institute of Technology while the draft of this article was written. This work was supported by the Centre for Ocean Life, a

REVIEWS IN ADVANCE

Changes may still occur before final publication online and in print

VKR Centre of Excellence supported by the Villum Foundation. Affiliations for authors of this article are as follows:

[1]VKR Centre for Ocean Life and [2]National Institute of Aquatic Resources, Technical University of Denmark, 2920 Charlottenlund, Denmark; email: kha@aqua.dtu.dk

[3]Marine Biological Section, University of Copenhagen, 3000 Helsingør, Denmark

[4]Consejo Nacional de Investigaciones Científicas y Técnicas, C1033AAJ Buenos Aires, Argentina

[5]Estación de Fotobiología Playa Unión, 9103 Rawson, Argentina

[6]Center for Macroecology, Evolution, and Climate, Natural History Museum of Denmark, University of Copenhagen, 2100 Copenhagen, Denmark

[7]Systemic Conservation Biology, J.F. Blumenbach Institute of Zoology and Anthropology, University of Göttingen, 37073 Göttingen, Germany

[8]Centre for Ecology and Evolution in Microbial Model Systems (EEMiS), Linnaeus University, 391 82 Kalmar, Sweden

[9]Department of Biomedical Sciences, University of Copenhagen, 2200 Copenhagen, Denmark

[10]Department of Oceanography, University of Hawai'i at Mānoa, Honolulu, Hawaii 96822

[11]GEOMAR Helmholtz Centre for Ocean Research Kiel, 24148 Kiel, Germany

[12]Department of Physics, Technical University of Denmark, 2800 Kongens Lyngby, Denmark

Annu. Rev. Marine. Sci. 2016.8. Downloaded from www.annualreviews.org
Access provided by Technical Information Center & Library of Denmark on 07/31/15. For personal use only.

LITERATURE CITED

Acuña JL, López-Urutia Á, Colin S. 2011. Faking giants: the evolution of high prey clearance rates in jellyfishes. *Science* 333:1627–29

Aksnes D, Egge J. 1991. A theoretical model for nutrient uptake in phytoplankton. *Mar. Ecol. Prog. Ser.* 70:65–72

Aksnes D, Utne A. 1997. A revised model of visual range in fish. *Sarsia* 82:137–47

Andersen KH, Beyer JE. 2006. Asymptotic size determines species abundance in the marine size spectrum. *Am. Nat.* 168:54–61

Andersen KH, Beyer JE, Pedersen M, Andersen NG, Gislason H. 2008. Life-history constraints on the success of the many small eggs reproductive strategy. *Theor. Popul. Biol.* 73:490–97

Ara R, Amin SMN, Mazlan AG, Arshad A. 2013. Morphometric variation among six families of larval fishes in the Seagrass-Mangrove ecosystem of Gelang Patah, Johor, Malaysia. *Asian J. Anim. Vet. Adv.* 8:247–56

Bagøien E, Kiørboe T. 2005. Blind dating—mate finding in planktonic copepods. I. Tracking the pheromone trail of *Centropages typicus*. *Mar. Ecol. Prog. Ser.* 300:105–15

Barnes C, Bethea DM, Brodeur RD, Spitz J, Ridoux V, et al. 2008. Predator and prey body sizes in marine food webs. *Ecology* 89:881

Barton AD, Finkel ZV, Ward BA, Johns DG, Follows MJ. 2013. On the roles of cell size and trophic strategy in North Atlantic diatom and dinoflagellate communities. *Limnol. Oceanogr.* 58:254–66

Bejan A, Marden JH. 2006. Unifying constructal theory for scale effects in running, swimming and flying. *J. Exp. Biol.* 209:238–48

Berg HC, Purcell EM. 1977. Physics of chemoreception. *Biophys. J.* 20:193–219

Block BA. 1991. Evolutionary novelties: how fish have built a heater out of muscle. *Am. Zool.* 31:726–42

Boudreau PR, Dickie LM. 1992. Biomass spectra of aquatic ecosystems in relation to fisheries yield. *Can. J. Fish. Aquat. Sci.* 49:1528–38

Charnov EL. 1993. *Life History Invariants*. Oxford, UK: Oxford Univ. Press

China V, Holzman R. 2014. Hydrodynamic starvation in first-feeding larval fishes. *PNAS* 111:8083–88

Christiansen FB, Fenchel TM. 1979. Evolution of marine invertebrate reproductive patterns. *Theor. Popul. Biol.* 16:267–82

Cohen J, Pimm S, Yodzis P, Saldaña J. 1993. Body sizes of animal predators and animal prey in food webs. *J. Anim. Ecol.* 62:67–78

REVIEWS IN ADVANCE

Changes may still occur before final publication online and in print

Annu. Rev. Marine. Sci. 2016.8. Downloaded from www.annualreviews.org
Access provided by Technical Information Center & Library of Denmark on 07/31/15. For personal use only.

Collin SP, Whitehead D. 2004. The functional roles of passive electroreception in non-electric fishes. *Anim. Biol.* 54:1–25

Curcio CA, Sloan KR, Kalina RE, Hendrickson AE. 1990. Human photoreceptor topography. *J. Comp. Neurol.* 292:497–523

Davies-Colley RJ, Smith DG. 1995. Optically pure waters in Waikoropupu ("Pupu") Springs, Nelson, New Zealand. *N.Z. J. Mar. Freshw. Res.* 29:251–56

DeLong JP, Okie JG, Moses ME, Sibly RM, Brown JH. 2010. Shifts in metabolic scaling, production, and efficiency across major evolutionary transitions of life. *PNAS* 107:12941–45

Dunbrack RL, Ware DM. 1987. Energy constraints and reproductive trade-offs determining body size in fishes. In *Evolutionary Physiological Ecology*, ed. P Calow, pp. 191–218. Cambridge, UK: Cambridge Univ. Press

Dusenbery DB. 2009. *Living at Micro Scale: The Unexpected Physics of Being Small*. Cambridge, MA: Harvard Univ. Press

Edwards KF, Thomas MK, Klausmeier CA, Litchman E. 2012. Allometric scaling and taxonomic variation in nutrient utilization traits and maximum growth rate of phytoplankton. *Limnol. Oceanogr.* 57:554–66

Fenchel T. 1974. Intrinsic rate of natural increase: the relationship with body size. *Oecologia* 14:317–26

Fenchel T. 1984. Suspended marine bacteria as a food source. In *Flows of Energy and Materials in Marine Ecosystems: Theory and Practice*, ed. MJR Fasham, pp. 301–15. NATO Conf. Ser. 11. New York: Plenum

Fenchel T, Finlay BJ. 2004. The ubiquity of small species: patterns of local and global diversity. *BioScience* 54:777–84

Fiksen Ø, Follows M, Aksnes D. 2013. Trait-based models of nutrient uptake in microbes extend the Michaelis-Menten framework. *Limnol. Oceanogr.* 58:193–202

Finkel ZV. 2001. Light absorption and size scaling of light-limited metabolism in marine diatoms. *Limnol. Oceanogr.* 46:86–94

Freedman JA, Noakes DLG. 2002. Why are there no really big bony fish? A point-of-view on maximum body size in teleosts and elasmobranchs. *Rev. Fish Biol. Fish.* 12:403–16

Froese R, Pauly D. 2013. *FishBase*. **http://www.fishbase.org**

Gillooly J, Charnov E, West G, Savage V, Brown J. 2002. Effects of size and temperature on developmental time. *Nature* 417:70–73

Haldane JBS. 1928. On being the right size. In *A Treasury of Science*, ed. H Shapely, S Raffort, H Wright, pp. 321–25. New York: Harper

Hansen BW, Bjørnsen PK, Hansen PJ. 1994. The size ratio between planktonic predators and their prey. *Limnol. Oceanogr.* 39:395–403

Hansen PJ, Bjørnsen PK, Hansen BW. 1997. Zooplankton grazing and growth: scaling within the 2–2,000-μm body size range. *Limnol. Oceanogr.* 42:687–704

Hemmingsen AM. 1960. *Energy Metabolism as Related to Body Size and Respiratory Surfaces, and Its Evolution*. Rep. Steno Mem. Hosp. Nord. Insulinlab. Vol. 9, Pt. 2. Copenhagen, Den.: Niels Steensens Hosp.

Hirst AG, Kiørboe T. 2002. Mortality of marine planktonic copepods: global rates and patterns. *Mar. Ecol. Prog. Ser.* 230:195–209

Holling CS. 1959. Some characteristics of simple types of predation and parasitism. *Can. Entomol.* 91:385–98

Hueter RE, Mann DA, Maruska KP, Sisneros JA, Demski LS. 2004. Sensory biology of elasmobranchs. In *Biology of Sharks and Their Relatives*, ed. JC Carrier, JA Musick, MR Heithaus, pp. 325–68. Boca Raton, FL: CRC

Huntley ME, Zhou M. 2004. Influence of animals on turbulence in the sea. *Mar. Ecol. Prog. Ser.* 273:65–79

Kempes CP, Dutkiewicz S, Follows MJ. 2012. Growth, metabolic partitioning, and the size of microorganisms. *PNAS* 109:495–500

Kiørboe T. 1993. Turbulence, phytoplankton cell size, and the structure of pelagic food webs. *Adv. Mar. Biol.* 29:1–72

Kiørboe T. 2001. Formation and fate of marine snow: small-scale processes with large-scale implications. *Sci. Mar.* 65(Suppl. 2):57–71

Kiørboe T. 2011. How zooplankton feed: mechanisms, traits and trade-offs. *Biol. Rev. Camb. Philos. Soc.* 86:311–39

REVIEWS IN ADVANCE

Changes may still occur before final publication online and in print

Annu. Rev. Marine. Sci. 2016.8. Downloaded from www.annualreviews.org
Access provided by Technical Information Center & Library of Denmark on 07/31/15. For personal use only.

Kiørboe T. 2013. Zooplankton body composition. *Limnol. Oceanogr.* 58:1843–50
Kiørboe T, Andersen A, Langlois VJ, Jakobsen HH. 2010. Unsteady motion: escape jumps in planktonic copepods, their kinematics and energetics. *J. R. Soc. Interface* 7:1591–602
Kiørboe T, Hirst AC. 2014. Shifts in mass-scaling of respiration, feeding, and growth rates across life-form transitions in marine pelagic organisms. *Am. Nat.* 183:E118–30
Klausmeier C, Litchman E, Daufresne T, Levin S. 2004. Optimal nitrogen-to-phosphorus stoichiometry of phytoplankton. *Nature* 429:171–74
Kleiber M. 1932. Body size and metabolism. *Hilgardia* 6:315–53
Lima SL, Dill LM. 1990. Behavioral decisions made under the risk of predation: a review and prospectus. *Can. J. Zool.* 68:619–40
Litchman E, Klausmeier CA. 2008. Trait-based community ecology of phytoplankton. *Annu. Rev. Ecol. Evol. Syst.* 39:615–39
Litchman E, Klausmeier CA, Schofield OM, Falkowski PG. 2007. The role of functional traits and trade-offs in structuring phytoplankton communities: scaling from cellular to ecosystem level. *Ecol. Lett.* 10:1170–81
Makarieva AM, Gorshkov VG, Bai-Lian L. 2004. Ontogenetic growth: models and theory. *Ecol. Model.* 176:15–26
Marañón E, Cermeño P, López-Sandoval DC, Rodríguez-Ramos T, Sobrino C, et al. 2013. Unimodal size scaling of phytoplankton growth and the size dependence of nutrient uptake and use. *Ecol. Lett.* 16:371–79
Mariani P, Andersen KH, Visser AW, Barton AD, Kiørboe T. 2013. Control of plankton seasonal succession by adaptive grazing. *Limnol. Oceanogr.* 58:173–84
Martens EA, Wadhwa N, Jacobsen NS, Lindemann C, Andersen KH, Visser AW. 2015. Size structures sensory hierarchy in ocean life. *Proc. R. Soc. B.* In review
May RM. 1975. Patterns of species abundance and diversity. In *Ecology and Evolution of Communities*, ed. ML Cody, JL Diamond, pp. 81–120. Cambridge, MA: Belknap
May RM, Godfrey J. 1994. Biological diversity: differences between land and sea. *Proc. R. Soc. B* 343:105–11
Mei Z-P, Finkel ZV, Irwin AJ. 2009. Light and nutrient availability affect the size-scaling of growth in phytoplankton. *J. Theor. Biol.* 259:582–88
Morel A, Bricaud A. 1981. Theoretical results concerning light absorption in a discrete medium, and application to specific absorption of phytoplankton. *Deep-Sea Res. A* 28:1375–93
Morioka S, Vongvichith B, Phommachan P, Chantasone P. 2013. Growth and morphological development of laboratory-reared larval and juvenile bighead catfish *Clarias macrocephalus* (Siluriformes: Clariidae). *Ichthyol. Res.* 60:16–25
Moser HG, Sumida BY, Ambrose DA, Sandknop EM, Stevens EG. 1986. Development and distribution of larvae and pelagic juveniles of ocean whitefish, *Caulolatilus princeps*, in the CalCOFI survey region. *CalCOFI Rep.* 27:162–69
Munk WH, Riley GA. 1952. Absorption of nutrients by aquatic plants. *J. Mar. Res.* 11:215–40
Neuheimer AB, Hartvig M, Heuschele J, Hylander S, Kiørboe T, et al. 2015. Adult and offspring size in the ocean over 17 orders of magnitude follows two life-history strategies. *Ecology.* In press
Northmore D, Volkmann FC, Yager D. 1978. Vision in fishes: colour and pattern. In *The Behavior of Fish and Other Aquatic Animals*, ed. DI Mostofsky, pp. 79–136. San Diego, CA: Academic
Oka S, Higashiji T. 2012. Early ontogeny of the big roughy *Gephyroberex japonicus* (Beryciformes: Trachichtyidae) in captivity. *Ichthyol. Res.* 59:282–85
Petchey OL, Beckerman AP, Riede JO, Warren PH. 2008. Size, foraging, and food web structure. *PNAS* 105:4191–96
Peters RH. 1983. *The Ecological Implications of Body Size*. Cambridge, UK: Cambridge Univ. Press
Peterson I, Wroblewski J. 1984. Mortality rate of fishes in the pelagic ecosystem. *Can. J. Fish. Aquat. Sci.* 41:1117–20
Rall BC, Brose U, Hartvig M, Kalinkat G, Schwarzmüller F, et al. 2012. Universal temperature and body-mass scaling of feeding rates. *Philos. Trans. R. Soc. B* 367:2923–34
Raven JA. 1994. Why are there no picoplanktonic O_2 evolvers with volumes less than 10^{-19} m^3? *J. Plankton Res.* 16:565–80
Reuman DC, Gislason H, Barnes C, Mélin F, Jennings S. 2014. The marine diversity spectrum. *J. Anim. Ecol.* 83:963–79

REVIEWS IN ADVANCE

Changes may still occur before final publication online and in print

Sambilay VC Jr. 1990. Interrelationships between swimming speed, caudal fin aspect ratio and body length of fishes. *Fishbyte* 8:16–20

Schwaderer AS, Yoshiyama K, de Tezanos Pinto P, Swenson NG, Klausmeier CA, Litchman E. 2011. Eco-evolutionary differences in light utilization traits and distributions of freshwater phytoplankton. *Limnol. Oceanogr.* 56:589–98

Sheldon RW, Prakash A. 1972. The size distribution of particles in the ocean. *Limnol. Oceanogr.* 17:327–40

Sheldon RW, Sutcliffe WH Jr, Paranjape MA. 1977. Structure of pelagic food chain and relationship between plankton and fish production. *J. Fish. Res. Board Can.* 34:2344–53

Shine R. 1978. Propagule size and parental care: the "safe harbor" hypothesis. *J. Theor. Biol.* 75:417–24

Sørnes TA, Aksnes DL. 2004. Predation efficiency in visual and tactile zooplanktivores. *Limnol. Oceanogr.* 49:69–75

Stoecker DK. 1998. Conceptual models of mixotrophy in planktonic protists and some ecological and evolutionary implications. *Eur. J. Protistol.* 34:281–90

Taguchi S. 1976. Relationship between photosynthesis and cell size of marine diatoms. *J. Phycol.* 12:185–89

Tambi H, Flaten G, Egge J, Bødtker G, Jacobsen A, Thingstad TF. 2009. Relationship between phosphate affinities and cell size and shape in various bacteria and phytoplankton. *Aquat. Microb. Ecol.* 57:311–20

Tennekes H, Lumley JL. 1972. *A First Course in Turbulence*. Cambridge, MA: MIT Press

Throndsen J, Hasle G, Tangen K. 2003. *Norsk Kystplanktonflora*. Oslo, Nor.: Almater

Tomas CR. 1997. *Identifying Marine Phytoplankton*. San Diego, CA: Academic

Verberk WCEP, Atkinson D. 2013. Why polar gigantism and Palaeozoic gigantism are not equivalent: effects of oxygen and temperature on the body size of ectotherms. *Funct. Ecol.* 27:1275–85

Visser AW. 2001. Hydromechanical signals in the plankton. *Mar. Ecol. Prog. Ser.* 222:1–24

Visser AW, Jackson GA. 2004. Characteristics of the chemical plume behind a sinking particle in a turbulent water column. *Mar. Ecol. Prog. Ser.* 283:55–71

Ware DM. 1978. Bioenergetics of pelagic fish: theoretical change in swimming speed and ration with body size. *J. Fish. Res. Board Can.* 35:220–28

Watkins JL, Brierley AS. 2002. Verification of the acoustic techniques used to identify Antarctic krill. *ICES J. Mar. Sci.* 59:1326–36

Webb P. 1988. Simple physical principles and vertebrate aquatic locomotion. *Am. Zool.* 28:709–25

West GB, Brown JH, Enquist BJ. 1997. A general model for the origin of allometric scaling laws in biology. *Science* 276:122–26

Winberg GG. 1960. *Rate of Metabolism and Food Requirements of Fishes*. Fish. Res. Board Can. Transl. Ser. 194. Nanaimo, BC: Fish. Res. Board Can. Biol. Stn

Annu. Rev. Marine. Sci. 2016.8. Downloaded from www.annualreviews.org
Access provided by Technical Information Center & Library of Denmark on 07/31/15. For personal use only.

REVIEWS IN ADVANCE

Changes may still occur before final publication online and in print

Chapter 10

Size structures sensory hierarchy in ocean life

Paper to appear in Proceedings of the Royal Society B (2015)

Size structures sensory hierarchy in ocean life

Erik A. Martens[1,2,3,5,‡,*] Navish Wadhwa[1,4,5,‡,†] Nis S. Jacobsen[1,2], Christian Lindemann[2], Ken H. Andersen[1,2], and André Visser[1,2]

[1]*VKR Centre for Ocean Life, Technical University of Denmark, Jægersborg Allé 1, 2920 Charlottenlund, Denmark* [2]*National Institute of Aquatic Resources, Technical University of Denmark, Charlottenlund Slot, Jægersborg Allé 1, DK-2920 Charlottenlund, Denmark* [3]*Department of Biomedical Sciences, Copenhagen University, Blegdamsvej 3, 2200 Copenhagen, Denmark* [4]*Department of Physics, Technical University of Denmark, DK-2800 Kgs. Lyngby, Denmark* [5]*These authors contributed equally to this study.* [‡]*Corresponding authors.*

Survival in aquatic environments requires organisms to have effective means of collecting information from their surroundings through various sensing strategies. In this study, we explore how sensing mode and range depend on body size. We find a hierarchy of sensing modes determined by body size. With increasing body size, a larger battery of modes becomes available (chemosensing, mechanosensing, vision, hearing, and echolocation, in that order) while the sensing range also increases. This size-dependent hierarchy and the transitions between primary sensory modes are explained on the grounds of limiting factors set by physiology and the physical laws governing signal generation, transmission and reception. We theoretically predict the body size limits for various sensory modes, which align well with size ranges found in literature. The treatise of all ocean life, from unicellular organisms to whales, demonstrates how body size determines available sensing modes, and thereby acts as a major structuring factor of aquatic life.

Keywords: ocean life, sensing modes, body size, sensing range, fluid physics, traits

I. INTRODUCTION

The marine pelagic environment is sparsely populated. To survive, organisms must scan volumes of water millions of times their own body volumes per day [1]. While searching is a challenge in itself, there is also the continual risk of predation. The result is a strong evolutionary drive to effectively gather information on the proximity of prey, mates and predators [2]. Here, we examine the means by which this information is gathered by marine pelagic organisms, that is, their sensory ability. In particular, we wish to understand relationships between the size of an organism and the usability of the various types of senses.

Indeed, size is a key parameter to characterize biological processes in marine environments [1, 3–6]. A cursory examination indicates at least some size-dependent organization as to which sensory modes organisms use in the marine pelagic environment. For instance, the smallest organisms (e.g., bacteria) depend heavily on chemical signals, while for larger animals (e.g., copepods), sensing of fluid flows becomes important, too. For even larger organisms, vision (e.g., crustaceans and fish), hearing (e.g., fish) and echolocation (e.g., toothed whales) become increasingly relevant sensory modes (Supplementary Figure 1). How can we understand this pattern on the grounds of physiology and physics using scaling rules, which are the two basic constraints on the workings of any organism [7, 8]? Our aim here is to determine the body size limits of different sensing modes based on physical grounds, and to explain how the sensory hierarchy is structured by size.

II. SENSING AS A PHYSICAL PROCESS

Our goal is to understand how size determines sensory modes available to an organism. We restrict ourselves to those sensory modes that are the primary means of remotely detecting the presence of other organisms: chemosensing of compounds, mechanosensing of flow disturbances provoked by moving animals, image vision in sufficiently lit areas, hearing of sound waves, and their generation for echolocation. We further restrict ourselves to the pelagic zone. All sensing involves an organism and a target; thus, we refer to the *organism* of size L and the *target* of size L_t. The two lengths are related via the dimensionless size preference $p = L_t/L$ (we assume $p = 0.1$ for predation, $p = 1$ for mating, $p = 10$ for predator avoidance). Clearly, other modes such as electroreception [9] or magnetoreception [10] may supplement the above mentioned modes, and organisms may switch between sensing modes depending on proximity to the target; here, however, we restrict ourselves to the aforementioned senses and consider them as the predominant primary sensory modes.

It is possible to decompose sensing into three fundamental sub-processes (Figure 1):

Generation. Animals emit signals by creating fluid dis-

* erik.martens@sund.ku.dk
† nawa@fysik.dtu.dk

turbances, creating sounds or reflecting ambient light. The target's features such as its size, L_t, affect the signal. Chemosensing, hearing and mechanosensing require a signal or an action from the target, whereas vision and echolocation do not. Echolocation in particular is an 'active sense', as the signal is generated by the organism and hence influenced by organism features such as size L.

Propagation. The distance over which a signal propagates before getting subdued by noise is sensitive to many factors. For instance, the oceans are awash with traces of various chemicals. Detection of a specific compound requires concentrations higher than the background, and depends on its diffusivity, release rate, stability, etc. This distance sets a sensing range R.

Detection. Is the organism — given the physical constraints — able to build a sensor? This requires a cost-effective mechanism by which information can be collected at a practical level of resolution. Size and complexity of the organism determine this ability.

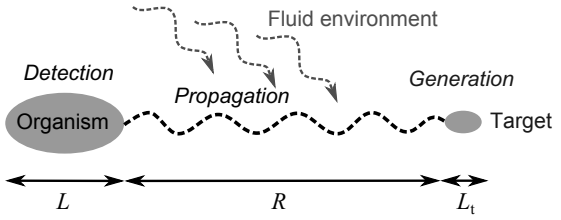

FIG. 1. Schematic of the participants and the processes involved in sensing.

Each of these sub-processes is constrained by size. Thus the length scale imprints itself automatically on the remote detection of other organisms. But limits of the usage of specific sensing modes are not necessarily clear-cut. For instance, in case of vision, the boundary between an image-forming eye (e.g., in fish) and non-image forming 'eye spots' that enable phototaxis (e.g., in copepods, protists) is not sharply defined. Moreover, simultaneous use of multiple senses complicates the situation. We make the simplifying assumption of no integration between senses, and treat them in isolation from each other. Within its limitations, this investigation may not yield exact numbers; it provides *characteristic* body-size limits for the sensory modes and yields valuable understanding of the structure of sensing in marine life, based on first principles.

III. CHEMOSENSING

The ability to detect chemical compounds is ubiquitous. All life forms have this ability and are equipped with chemosensing apparatuses [11]. Chemotaxis and the use of chemosensing in remote detection can be divided into two modes: i) gradient climbing defined as moving along a gradient towards (or away from) a stationary target, and ii) following a trail laid out by a moving target [12, 13].

A. Size limits for chemosensing

Gradient climbing ability would be size independent, were it not for two randomizing physical effects. For very small organisms, gradient climbing ability is impaired due to Brownian rotation [14], caused by molecular motions in the fluid. Due to this, the organism cannot direct itself along a gradient using a biased random walk (Figure 2A). This happens for L less than the length scale characteristic of Brownian motion, L_{Br} $(0.1-1\mu\mathrm{m})$ [15]. Using a similar argument, Dusenbery [16] has argued that below $L = 0.6\,\mu$m, directed motility, and thus chemotaxis, is infeasible due to Brownian rotation.

An upper limit for gradient climbing is imposed when turbulence disrupts the smoothness of the chemical gradient, for L greater than the Batchelor scale $L_{\mathrm{B}} \approx (\nu D^2/\varepsilon)^{1/4}$, where ν is the kinematic viscosity, D the molecular diffusivity, and ε the turbulent energy dissipation rate. L_{B} is the length scale at which the diffusion time scale becomes comparable to the dissipation time for the smallest turbulent eddies (Figure 2B). In the ocean, ε ranges between 10^{-8} and 10^{-3} $\mathrm{m^2 s^{-3}}$ [17, 18]. L_{B} is between 5 and 100 μm in moderate turbulence (for a typical value of $D \sim 10^{-9}$ $\mathrm{m^2 s^{-1}}$), but can become much larger in quiescent environments.

For detecting a moving target that releases a chemical trail, the physical constraints are similar to gradient climbing. For L above the Kolmogorov scale $L_{\mathrm{K}} \approx (\nu^3/\varepsilon)^{1/4}$, directional information in the trail is reduced due to the isotropy in turbulent flows [19], impairing chemotaxis. L_{K} is around 1 cm in moderate turbulence [17], above which trail following becomes progressively worse. When L is larger than the integral length scale L_{I}, trail following may become effective again as the turbulent trail at this scale is anisotropic (Figure 2C). Typical values for L_{I} in a stratified ocean are around 1 m or larger [20, 21]. Thus, between $\sim$ 1 cm and $\sim$ 1 m, trail following is impaired, and requires averaging over space and time [22]. Note that in the absence of environmental turbulence, L_{K} and L_{I} are determined by the size of the trail source.

B. Sensing range for chemosensing

Size limits for the functioning of chemosensing also apply to the sensing range. For example, in gradient climbing, the maximal distance up to which a chemical gradient remains uninterrupted is L_{B}. Another factor affecting the range for gradient climbing is the diffusion time scale. For a typical compound to diffuse

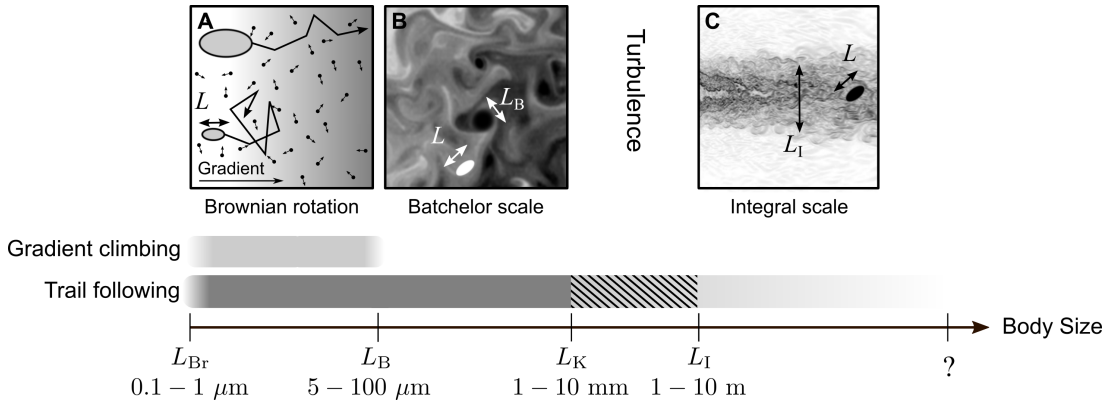

FIG. 2. Body sizes over which chemosensing can be used effectively. A schematic illustration of Brownian rotation (A), Batchelor scale (B), and integral scale (C) is included at the top.

over $d = 1$ cm, it can take up to days ($t = d^2 D^{-1}$ where $D \sim 10^{-9}\mathrm{m}^2\mathrm{s}^{-1}$). This makes the signal irrelevant for many small organisms, because by that time they have moved elsewhere, been preyed upon, or have multiplied several times. Thus, gradient climbing is relevant only up to small distances. Similarly, for trail following, sensing range is limited to L_K.

IV. MECHANOSENSING

Any object moving in fluid generates a hydromechanical disturbance that can potentially be detected with the appropriate sensory apparatus [23]. For many small organisms such as zooplankton [23–25], it is the dominant sensory mechanism. Many fishes, especially in dimly lit environments, also rely heavily on mechanosensing using the lateral line organ [26]. The nature of a fluid disturbance generated by a target of size L_t swimming with a velocity U_t is largely determined by the dimensionless Reynolds number (Re), defined as $\mathrm{Re} = L_t U_t/\nu$, where ν is the kinematic viscosity [27]. For small Re, such as for most plankton, flow is dominated by viscosity and is laminar [28]. For large Re, such as for large fishes or mammals, inertia dominates, and the flow tends to be turbulent [29].

A. Propagation of fluid disturbances

For a target passively sinking at low Re in unbounded fluid (e.g., the pelagic zone), the velocity (u) induced in the fluid decays with distance r as $u \sim r^{-1}$ [23]. For a self-propelled target, the induced velocity decays as $u \sim r^{-2}$ [23]. Recent studies have shown that for breast-stroke swimming plankton and impulsively jumping copepods, u decays more rapidly as $u \sim r^{-3}$ and $u \sim r^{-4}$, respectively [30, 31]. At high Re, the fluid disturbance generated by a target becomes turbulent, if L_t is much larger than L_K, resulting in a turbulent wake.

B. Detection

Setae on the antennae of a copepod are classic examples of mechanosensors (Supplementary Figure 2). Setae sense velocity difference across their length, and activate when it exceeds a certain threshold s [25], defining setae sensitivity [32], typically between 10 and 100 μm/s [23]. In unicellular organisms such as ciliates and dinoflagellates, a response occurs above a critical fluid deformation rate [24, 33], equivalent to a threshold velocity difference across the cell. In the lateral lines of fish, the working sensor is a seta-like kinocilium [34]. In general, mechanosensing requires a velocity differential on the organism's body, as a result of fluid deformation. Given a sensitivity s of a mechanosensor of length b, embedded in fluid with deformation rate Δ (measured in s^{-1}), the criterion for detection can be written as

$$\Delta \cdot b > s. \tag{1}$$

C. Sensing range for mechanosensing

We estimate the sensing range R for the most relevant case of a self-propelled target. For $R \gg b$, Visser [23] has shown that $R \approx (3U_t L_t^2 b/s)^{\frac{1}{3}}$. The swimming velocity of the target is related to its size by the empirical relation $U_t \sim c_1 L_t^{0.79}$ with $c_1 = 6.5\ \mathrm{m}^{0.21}/s$ [1]. For prey detection ($p = 0.1$), assuming that the sensor is about a tenth of the body size ($b = L/10$), we get

$$R \approx c_2 L^{1.26} \tag{2}$$

where $c_2 = 3.98\ \mathrm{m}^{-0.26}$.

From this estimate, a copepod of $L \sim 2$ mm has a prey sensing range of about 1.5 mm. The exact scaling coefficient is determined by the organism's morphology and the swimming characteristics of the target, but equation (2) provides a rough estimate. Like in chemical trail following, an upper limit of mechanosensing range R is set by the Kolmogorov scale, L_K, above which turbulence disrupts the signal.

D. Size limits for mechanosensing

The lower size limit for mechanosensing in the pelagic zone is dictated by inequality (1). We consider the case of a small prey individual detecting a larger predator ($p = 10$). For a target (predator) swimming with a velocity U_t, fluid deformation scales as $\Delta \sim U_t/L_t$. Using again the empirical scaling of $U_t \sim c_1 L_t^{0.79}$ [1], and further using $L = L_t/10$, we can deduce that

$$\Delta \sim c_3 \cdot L^{-0.21}, \tag{3}$$

where $c_3 = 3.98\ \mathrm{m}^{0.21}\mathrm{s}^{-1}$.

To close the problem, we again use $b = L/10$. Combining (1) and (3), substituting b and using an intermediate value for $s = 50\ \mu$m/s, we get a lower size limit of $L > 11\ \mu$m. Thus we expect the lower size limit for an organism to use mechanosensing in the pelagic zone to be of the order of a few micrometers. Given the sensitivity of mechanosensing apparatuses, smaller organisms are unable to detect the hydromechanical disturbances relevant to their size.

The upper size limit of mechanosensing is prescribed by the same constraints as those for chemical trail following. The generated flows are disintegrated by turbulence at $L > L_K$, rendering mechanosensing progressively less effective above organism sizes of around 1 cm. We also conjecture that like trail following, mechanosensing abilities may improve for organisms larger than the integral length scale L_I.

V. VISION

Simple functions of vision include differentiating light from dark, entrainment to a circadian rhythm [35], and orientation [36], while more complex functions involve navigation, pattern recognition, and food acquisition. Prey and predator detection from some distance requires sufficient image resolution. In general only two fundamental principles are used to build an eye: i) compound eyes, which comprise of a number of individual lenses and photo-receptors laid out on a convex hemispherical surface, ii) camera eyes with one concave photoreceptive surface where an image is projected through an optical unit (pinhole or lens).

A. Light propagation in the marine environment

Given that a target is lit and visible, the reflected light must travel through seawater to reach the receiving organism. The intensity of light attenuates geometrically with distance r as r^{-2}, and more steeply due to the added effects of scattering and absorption by solutes and seston [37]. In general, light intensity along a given path decreases as $e^{-\alpha r}$ where α (measured in m^{-1}) is called the absorption coefficient [38].

B. Physiological limits to eye size

The resolution of the compound eye is limited by the size of ommatidia (photoreceptor units in compound eyes). They cannot be reduced in size to achieve a resolution better than 1° [39]. Thus, camera eyes, which we consider in the following, outperform compound eyes in compactness [39, 40]. The functioning of a small eye is limited by two constraints. First, a smaller eye captures less light. Second, a smaller eye has lower resolution: the photoreceptive units constitute the smallest components in an eye and are based on opsin molecules, the universally represented light-capturing design in the animal world [41]. Thus, the width of a photoreceptor $d_p \approx 1\ \mu$m [42] is an absolute limiting factor for any eye design. Therefore, n pixels amount to a retina diameter of $d \approx n^{1/2} d_p$. Considering a minimal required resolution for a usable image-forming eye to be 100^2 pixels, the corresponding retina would have a diameter $d \approx 0.1$ mm. Depending on the eye-to-body size ratio, this corresponds to an organism of around $L \approx 1$ to 3 mm.

Arguments for an upper size limit for eyes are not evident on physical grounds. The largest known marine animals carry eyes (see Discussion). However, the higher resolution and sensitivity resulting from larger eyes do not necessarily yield a larger sensing range as it may be limited by turbidity, as we discuss next.

C. Visual range

The visual range of an organism can be estimated by considering the properties of a (pin-hole) camera eye, following an argument by Dunbrack and Ware [43]. We use Weber contrast $C = (I - I_b)/I_b$, where I and I_b are the intensities of the target and the background, respectively. The maximal distance R at which a predator can discern a prey individual of size L_t requires that the apparent contrast C_a of the target matches the contrast threshold of the eye, C_{th}. The inherent contrast of the target, C_0 declines with distance r, yielding [38]

$$C_a = C_0 \cdot e^{-\alpha r}. \tag{4}$$

$C_{\rm th}$ is a declining function of the number of visual elements n involved in perceiving the target:

$$C_{\rm th} = C_{\rm th,min}(z) + K_{\rm ph}/n. \quad (5)$$

This formula is partly based on Ricco's law [44] that expresses the inverse proportionality between $C_{\rm th}$ and n, and is supplemented by adding the minimum contrast threshold $C_{\rm th,min}$ to represent saturation of the contrast at a minimal value [45]. $C_{\rm th,min}$ varies in different environments and, in particular, depends on the available backlight at a given depth z.

The number of visual elements n involved in image detection is equal to their density, σ (measured in m^{-2}), times the projected image area. Assuming R is large relative to the eye ball diameter $L_{\rm eye}$, we can deduce $n = \sigma\pi/4\,L_{\rm img}^2 \approx \sigma L_{\rm eye}^2 L_{\rm t}^2 R^{-2}$ (Supplementary Figure 3). Noting the universal size of the opsin molecule across species, we may assume that σ is independent of eye size. Introducing the ratio $a = L_{\rm eye}/L$ [46] and using $p = L_{\rm t}/L$, we get $n = \sigma a^2 p^2 L^4 R^{-2}$. The range R is determined by the condition $C_a \geq C_{\rm th}$:

$$C_0 e^{-\alpha R} \geq C_{\rm th,min}(z) + K R^2 L^{-4}, \quad (6)$$

where $K = K_{\rm ph}\sigma^{-1}a^{-2}p^{-2}$ is a constant characterizing the photoreceptor sensitivity, $K_{\rm ph}/\sigma$, eye-to-body-size ratio, a, and size preference, p. Sample solutions for the condition $C_a = C_{\rm th}$ yield the range R at a given body size L (Figure 3A). Isolating R from Eq. (6) is impossible; however, asymptotic solutions can be derived for two limits:

(i) "Clear-water limit": when $\alpha \to 0$, R is limited by the eye's resolution; thus, $R \sim [(C_0 - C_{\rm th,min})/K]^{1/2} L^2$.

(ii) "Turbid-water limit": when $C_0 - C_{\rm th,min} \gg K R^2 L^{-4}$; thus, $R \sim (\ln C_0 - \ln C_{\rm th,min})/\alpha$. R is independent of L and only limited by the sensitivity of a visual element, $C_{\rm th,min}$.

Generally, the visual range decreases if light is reduced, e.g., at large depth z, leading to a higher $C_{\rm th,min}$ [cases (i),(ii)]; or if the turbidity is strong (larger α) [case (ii)]. The cross-over between the two limits occurs when $L \sim L_x \sim \alpha^{-1/2}$ (Supplementary text). The visibility range in pure water for light of 550 nm is theoretically estimated at 74 m [47], and measurements in the open sea range from 44-80 m [48]. The visual range has also been predicted in more elaborate models [49].

VI. HEARING

Sound propagates through the ocean as pressure waves, resulting in alternating compression and rarefaction of water in regions of high and low pressure, respectively. Any form of hearing must detect sound waves by converting them into vibrations of an organ that stimulates nerve cells. In fishes, sound waves displace sensory hairs against the calcareous *otolith*, and this relative motion is detected. By contrast, in mammalian ears, sound waves excite the tympanic membrane (ear-drum), the motion of which is sensed by ciliary hairs in the cochlea.

Most sounds relevant to ocean life, except echolocation, fall into the range of a few hertz up to a few kilohertz. Sounds generated by marine animals due to rapid movements or for communication, have frequencies rarely exceeding 1 kHz [50]. Communication by marine mammals usually consists of a burst of clicks or of whistles (4-12 kHz), while the echolocating signals of odontoceti range between 20 and 200 kHz [51].

A. Underwater sound propagation

As sound waves travel through a medium, sound intensity attenuates with distance from the target r, due to two processes: (i) geometric spreading (r^{-2} in open space), and (ii) absorption in water. The latter is frequency dependent: 1 dB/km at 10 kHz, but only 10^{-4} dB/km at 100 Hz in seawater[1] [38]. Sound is therefore only weakly attenuated in seawater, and it can potentially carry information over large distances.

B. Lower limit for sound detection

Detection of sound requires either an organ of significantly different density than that of water (e.g., the otolith), or a large detector array (e.g., auricle and drum), to allow detection by responding to spatial gradients of particle displacement [38]. A density contrast organ such as the otolith has to move relative to the surrounding fluid, as explained above. Motions in small sound-sensing organs (operating at low Re) are inherently more damped by viscosity than larger ones, impairing the practicality of sound detection by small organisms. Without high density contrast in the hearing organ, the detector array and thus the organism would have to be at least as long as the wavelength of sound (15 cm at 10 kHz). Thus hearing – with or without a density contrast organ – is impractical for pelagic organisms smaller than a few centimetres.

Many fishes have swim bladders (sometimes connected to the otolith-containing cavity through bony connections called the *Weberian ossicles*) that transduce

[1] The decibel level is defined via $I_{\rm dB} = 10\log_{10}(I/I_0)$, where I is the sound intensity and I_0 is a reference frequency.

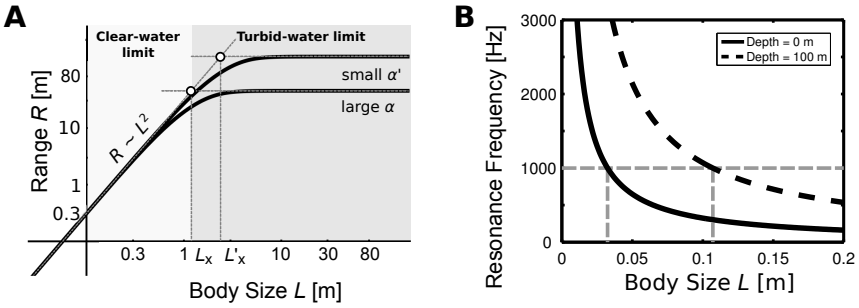

FIG. 3. **A**: Visual sensing range scales with body size, L, as $R \sim L^2$ in the clear-water limit ($L \ll L_x$) and as $R \sim$ constant in the turbid-water limit ($L \gg L_x$). Parameters are $C_0 = 0.3, C_{\mathrm{th,min}} = 0.05$ (adopted from [43]), $K = 2.5 \times 10^{-4}$ m^2, $\alpha = 0.04$ m^{-1} [69] (and α' = 0.01 m^{-1} for comparison). **B**: Relationship of body size and resonance frequency based on Equation (7) and using a swim bladder size $r_\mathrm{b} = L/10$ for an individual at the surface (solid curve) and at 100 m depth (dashed curve). The dashed (grey) horizontal line indicates 1 kHz, below which most sounds generated by marine life are found.

pressure waves to mechanical motion and act as displacement amplifiers for sound via resonance [38, 52]. Similarly, odontocetes use the fat-filled bones of their lower jaw as an amplifying cavity [51]. Swim bladders are air-filled structures that amplify sound maximally when in natural resonance with the sound waves [38]. Frequencies very different from the resonance frequency of the swim bladder do not amplify well, and may even be damped if too different [38]. Based on an assumption of a spherical, air-filled swim bladder, the resonance frequency, f, can be approximated [38] as

$$f = \frac{1}{2\pi r_\mathrm{b}} \sqrt{\frac{3\Gamma P}{\rho}}, \tag{7}$$

where P is the depth-dependent hydrostatic pressure, r_b the radius of the swim bladder, ρ the density of sea water, and Γ the adiabatic exponent (~ 1.4 for air); r_b is typically around 5-10 % [53] of the body size L of the fish. Using $r_\mathrm{b} = L/10$ for a conservative estimate, L would need to be at least 3 cm at the sea surface, in order to amplify the high-frequency end (1 kHz) of the ambient underwater sound spectrum, and $L = 11$ cm at a depth of 100 m (Figure 3B). To hear the more typical lower frequencies, L would have to be larger still. Thus, we approximate that the lower body size limit for detection of sound using swim bladders is around a few centimetres.

VII. ECHOLOCATION

Echolocation is an active sensing mode, in which the organism emits clicks in the ultrasonic range and interprets the environment based on the echoes of these clicks. Echolocation is common in odontocetes (toothed whales) and is generally used for orientation and prey detection. The generation of echolocating signals in toothed whales is associated with the nasal passage leading up to the blowhole and takes place in the phonic lips. Taking into account the anatomical structures, the dominant frequency can be estimated as the resonance frequency of a Helmholtz oscillator [54]. The diffraction limit sets a resolution limit to $\lambda/2\pi$, where λ is the characteristic wavelength of the click [38]. Odontocetes produce clicks with peak energies at frequencies in the range of 20 to 200 kHz [51], the resulting resolution lies between 1 to 8 mm. Using an intermediate value (5 mm), and assuming that the target is at least one order of magnitude larger than the smallest resolvable feature, we get a minimal target size of 50 mm. Echolocation is typically used for prey detection, so $p = 0.1$. Thus we get a lower body size limit for an echolocating organism to be $L \approx 500$ mm. It also implies that objects smaller than about 1 mm do not scatter sound signals in the frequency range we are considering, allowing echolocation to be useful in turbid waters where vision is severely restricted.

A. Sensing range

The generated acoustic signal first travels through water, is then partially reflected by the target, and the remainder of the signal (minus attenuation) travels back to the organism. Emitted sound intensity, I_e, is thus reduced by the processes of reflection and geometric divergence, causing signal intensity to attenuate as $(2r)^{-2}e^{-2\mu r}$. The strength of the returned signal must exceed the threshold intensity for detection in the ear, $I_r = I_0$. Assuming that ear threshold sensitivity is independent of L, but that emitted sound intensity I_e and carrier frequency scale with L, the sensing range can be estimated as (Supplementary Text for details)

$$R \sim p I_0^{-1/2} L^\gamma, \tag{8}$$

where $p = L_\mathrm{t}/L$ is the size preference ratio and the exponent γ lies between 2.125 to 2.5 that compares reasonably

well with data. The scaling factor can be estimated from data describing the echolocation range of small marine mammals (Supplementary Text).

VIII. DISCUSSION

We have attempted to synthesize an understanding of how physiology and the physical environment enable and constrain an aquatic organism's ability to gather information from its surroundings. By reducing the relevant physical mechanisms to their simplest forms, we have identified the most pressing constraints on the functioning of various senses. Our goal has been to explain the transition from one dominant sense to another with changing body size, as observed in nature. A comparison of the predicted size limits with those observed in nature supports our analysis (Table I, Figure 4). The predicted size ranges correspond well with known minimal and maximal sizes of animals using a specific sense. Size limits of a sense do not imply that an organism cannot detect the signal outside the limits at all, but rather that beyond these limits, the usefulness of the sense is compromised in comparison with other senses.

We could not conceive any upper size limits on physical grounds for chemosensing, mechanosensing, hearing, and vision. Indeed, the largest known organism in the ocean, the blue whale ($L = 30$ m), is known to use all of these senses. Chemosensing is the only sense available to the smallest organisms, and its theoretical lower size limit ($L_{\mathrm{Br}} \sim 10^{-7} - 10^{-6}$ m) is consistent with the smallest known motile organisms (bacteria, $L = 0.8$ μm [16]). Chemosensing is presumably slightly impaired due to turbulence in intermediate size ranges, in which integration of multiple senses such as mechanosensing and vision might be very useful. Chemosensing for trail following is an important sensory mode for large bony fishes [61] and sharks [62], which have sizes larger than L_{I}.

The theoretical lower limit for mechanosensing in the pelagic environment is a few micrometers, in the realm of protists; to our knowledge, marine protists sized 7-10 μm are the smallest pelagic organisms known to use mechanosensing [56]. However, it is only the lower limit for pelagic zones; smaller bacteria are known to be able to sense mechanical stresses when getting in contact with a solid body [63]. Large copepods and small fish occupy the size range where mechanosensing starts becoming less effective. Its use by fish is demonstrated in many species using lateral lines to find prey and sense flows [26]. Larger fish receive a poorer signal quality due to turbulence, and for this reason some larger sharks are known not to use lateral lines for prey detection [64]. Some marine mammals (seals and sea lions) have the ability to follow turbulent trails using their mystacial vibrissae [65], likely due to being larger than the integral length scale set by the target.

The camera eye takes records for both the smallest and the largest eye: the smallest image forming eyes (and body sizes) are found in the fish *Schindleria brevipinguis* ($L \approx 7$ mm [66]), and the pygmy squids ($L \approx 1.5$ mm [57]), which compares well with our predicted size limit[2]. The largest known eye belongs to the giant squid, featuring eye-balls up to 30 cm in diameter [67]. Eyes are also found in the largest known species (whales), implying that there is no upper body size limit for image-forming vision in marine animals.

For hearing, the theoretical lower body size limit is found to be a few centimetres. Some fishes are able to manipulate the resonance frequency of swim bladders by changing their membrane elasticities [68]. By hearing outside the resonance frequency, fish larvae of a few millimetres ($L \approx 9$ mm) have been shown to react to sounds [58]. Note that these fishes inhabit shallower waters, where hearing is feasible at smaller sizes (Figure 3B). For echolocation, the predicted lower limit (~ 0.5 m) is close to the observed smallest size among echolocating marine mammals (Commerson's dolphin, [59]).

Upper limits of sensing ranges are dictated by degradation of signal-to-noise ratios via absorption, geometric spreading (divergence), or environmental disturbances. For chemical gradient climbing and mechanosensing, the signals are randomized beyond a characteristic distance given by L_{B} and L_{K}, respectively. For mechanosensing the range scales as $R \sim L^{1.26}$ (Figure 4). When mechanosensing can no longer extend its range, vision becomes a viable solution. Visual sensing range in clear water scales as $R \sim L^2$, but cannot exceed the limit set by turbidity. Even in clear waters, vision cannot exceed the range of roughly 80 m. Here, vision may be complemented by hearing and echolocation mainly because sound is capable of travelling large distances in sea-water without significant attenuation. Although we could not develop a scaling for hearing range, we could determine the sensing range of echolocation, which scales approximately as $R \sim L^{2.3}$ and is as large as kilometres for larger organisms, comparing well with the known range of marine mammals.

The question arises whether there is a general pattern underlying the size structure of primary sensory modes. For instance, can the transitions between senses be related to metabolic demand? Kleiber's law requires that an organism consumes energy at a rate proportional to $L^{9/4}$[3]. This demand must be fulfilled by maintaining a sufficient clearance rate [4], a function of the swimming velocity $V \sim L^x$ and sensing range $R \sim L^y$ with

[2] The smallest compound eyes are found in the genus *Daphnia*, but their image quality is questionable, see Supplementary Text.

TABLE I. Lower and upper size (body length) limits for various senses. Predicted theoretical limits denote orders of magnitude.

	Observed limit				Theoretical limit	
	Lower [m]		Upper [m]		Lower [m]	Upper [m]
Chemosensing	$8 \cdot 10^{-7}$	[16]	30	[55]	$\sim 10^{-7}$	—
Mechanosensing	$7 \cdot 10^{-6}$	[56]	30	[55]	$\sim 10^{-5}$	—
Vision	$1.5 \cdot 10^{-3}$	[57]	30	[55]	$\sim 10^{-3}$	—
Hearing	$9 \cdot 10^{-3}$	[58]	30	[55]	$\sim 3 \cdot 10^{-2}$	—
Echolocation	0.55	[59]	18.6	[60]	~ 0.5	—

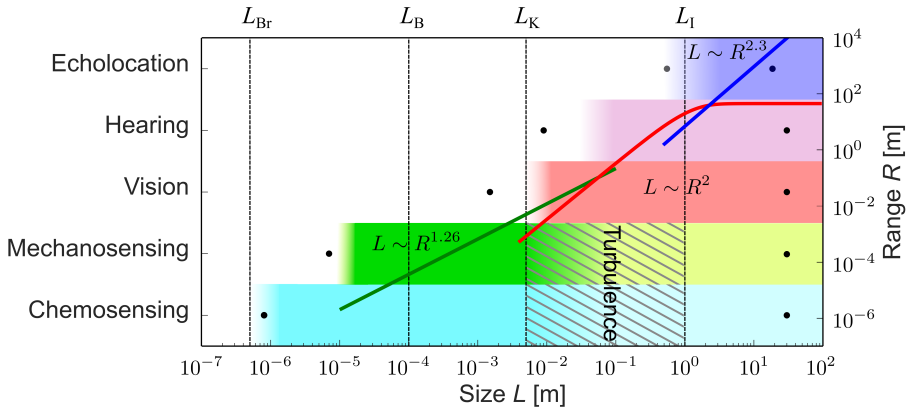

FIG. 4. Upper and lower body size limits and ranges for different senses. Dots denote the largest and smallest sizes known to employ a given sense, and shaded rectangles show the theoretical estimates of the size range in which a sense is expected to work. Green, red, and blue curves show the theoretical scaling of sensing range with size for mechanosensing, vision, and echolocation, respectively.

positive exponents x, y. Thus, the clearance rate also increases with L. The exponent y appears to increase going up the senses axis (Figure 4). With increasing size and metabolic expenditure, an evolutionary pressure arises to extend the sensing range by investing into a more effective sensory strategy, causing the transition from one to the other primary sensing mode. However, rather than being governed by cost efficiency, it seems more plausible that the transitions between senses are set by the physical limitations of signal generation, transmission and reception. To exemplify, carrying larger eyes can improve resolution and thus extend the sensing range, but beyond a critical (eye) size, increased performance is rendered ineffective due to the clear water limit of the visual range. So a transition is necessitated by the required increase in sensing range, achieved by echolocation.

We have combined biological knowledge, physiology and physics to describe the abilities of the sensory modes in ocean life, from bacteria to whales. Our treatise demonstrates how body size determines available sensing modes, and thereby acts as a major structuring factor of aquatic life. When interpreting the scalings and limits we propose, note that our purpose is to provide first-order approximations based on first principles. Further research is needed to evaluate each of the senses in more detail and to gather more data to examine the arguments presented here. We hope that this work may serve as a starting point for future explorations on sensory modalities and their hierarchical structures.

AUTHOR CONTRIBUTIONS

EAM and NW contributed equally to the study, collected data, developed models, and wrote the manuscript. NSJ, CL, KHA and AV collected data and helped drafting the manuscript. All authors participated in the design of the study and gave final approval for publication.

ACKNOWLEDGMENTS

We thank Hanna Rademaker, Julia Dölger and Anders Andersen for helpful discussions, and Thomas Kiørboe for comments on the manuscript. We thank anonymous reviewers for helpful comments that improved the manuscript. The Centre for Ocean Life is a VKR center of excellence supported by the Villum foundation (EAM, NW, CL, NSJ, KHA, AV). The work is part of the Dynamical Systems Interdisciplinary Network, University of Copenhagen (EAM). Partial financial support for CL was provided by EURO-BASIN (FP7, Ref. 264933).

[1] Thomas Kiørboe. How zooplankton feed: Mechanisms, traits and trade-offs. *Biological Reviews*, 86:311–339, 2011.

[2] David B Dusenbery. *Sensory ecology: how organisms acquire and respond to information*. WH Freeman, New York, 1992.

[3] Max Kleiber. Body size and metabolism. *Hilgardia*, 6:315–351, 1932.

[4] KH Andersen and JE Beyer. Asymptotic size determines species abundance in the marine size spectrum. *Am. Naturalist*, 168(1), May 2006.

[5] KH Andersen, Goncalves RJ Berge, T, M Hartvig, J Heuschele, S Hylander, NS Jacobsen, C Lindemann, EA Martens, AB Neuheimer, K Olsson, A Palacz, F Prowe, J Sainmont, SJ Traving, AW Visser, N Wadhwa, and T Kiørboe. Characteristic sizes of life in the oceans, from bacteria to whales. *Annual Review of Marine Sciences*, 8:125, 2016.

[6] David B Dusenbery and Terry W Snell. A critical body size for use of pheromones in mate location. *Journal of Chemical Ecology*, 21(4):427–438, 1995.

[7] David B Dusenbery. Physical constraints in sensory ecology. In FriedrichG. Barth and Axel Schmid, editors, *Ecology of Sensing*, pages 1–17. Springer Berlin Heidelberg, 2001.

[8] David B Dusenbery. *Living at micro scale: the unexpected physics of being small*. Harvard University Press, 2009.

[9] Shaun P Collin and Darryl Whitehead. The functional roles of passive electroreception in non-electric shes. *Animal Biology*, 54(1):1–25, 2004.

[10] Sönke Johnsen and Kenneth J Lohmann. The physics and neurobiology of magnetoreception. *Nature Reviews Neuroscience*, 6(9):703–712, 2005.

[11] Julius Adler. Chemotaxis in bacteria. *Science*, 153(3737):708–716, 1966.

[12] Paul A. Moore, David M. Fields, and Jeannette Yen. Physical constraints of chemoreception in foraging copepods. *Limnology and Oceanography*, 44:166–177, 1999.

[13] John C. Andrews. Deformation of the active space in the low reynolds number feeding current of calanoid copepods. *Canadian Journal of Fisheries and Aquatic Sciences*, 40(8):1293–1302, 1983.

[14] HC Berg. A physicist looks at bacterial chemotaxis. In *Cold Spring Harbor Symposia on Quantitative Biology*, volume 53, pages 1–9, 1988.

[15] James G Mitchell. The influence of cell size on marine bacterial motility and energetics. *Microbial ecology*, 22(1):227–238, 1991.

[16] David B Dusenbery. Minimum size limit for useful locomotion by free-swimming microbes. *Proceedings of the National Academy of Sciences*, 94(20):10949–10954, 1997.

[17] Javier Jiménez. Oceanic turbulence at millimeter scales. *Scientia Marina*, 61:47–56, 1997.

[18] AW Visser, H Saito, E Saiz, and T Kiørboe. Observations of copepod feeding and vertical distribution under natural turbulent conditions in the north sea. *Marine Biology*, 138(5):1011–1019, 2001.

[19] Hendrik Tennekes and John Leask Lumley. *A first course in turbulence*. MIT press, Cambridge, MA, 1972.

[20] H Yamazaki, DL Mackas, and KL Denman. Coupling small-scale physical processes with biology. *The sea: Biological-Physical Interactions in the Ocean*, 12:51–112, 2002.

[21] AW Visser. Small, wet & rational: Individual based zooplankton ecology. Kongens Lyngby, Denmark: Technical University of Denmark, 2010.

[22] Massimo Vergassola, Emmanuel Villermaux, and Boris I Shraiman. 'Infotaxis' as a strategy for searching without gradients. *Nature*, 445(7126):406–409, January 2007.

[23] AW Visser. Hydromechanical signals in the plankton. *Marine Ecology Progress Series*, 222:1–24, 2001.

[24] HH Jakobsen. Escape response of planktonic protists to fluid mechanical signals. *Marine Ecology Progress Series*, 214:67–78, 2001.

[25] J Yen, PH Lenz, DV Gassie, and DK Hartline. Mechanoreception in marine copepods: Electrophysiological studies on the first antennae. *Journal of Plankton Research*, 14:495–512, 1992.

[26] JC Montgomery. Lateral line detection of planktonic prey. In Sheryl Coombs, Peter Görner, and Heinrich Münz, editors, *The Mechanosensory Lateral Line*, pages 561–574. Springer New York, 1989.

[27] Constantine Pozrikidis. *Introduction to Theoretical and Computational Fluid Dynamics*. Oxford University Press, Oxford, UK, 2nd edition, 2011.

[28] Eric Lauga and Thomas R Powers. The hydrodynamics of swimming microorganisms. *Reports on Progress in Physics*, 72(9):096601, September 2009.

[29] George Keith Batchelor. *An introduction to fluid dynamics*. Cambridge University Press, Cambridge, UK, 1967.

[30] Houshuo Jiang and Thomas Kiørboe. The fluid dynamics of swimming by jumping in copepods. *Journal of the Royal Society Interface*, 8:1090–1103, 2011.

[31] Thomas Kiørboe, Houshuo Jiang, Rodrigo Javier Gonçalves, Lasse Tor Nielsen, and Navish Wadhwa. Flow disturbances generated by feeding and swimming zooplankton. *Proceedings of the National Academy of Sciences*, 111(32):11738–11743, 2014.

[32] Thomas Kiørboe and Andre Visser. Predator and prey perception in copepods due to hydromechanical signals. *Marine Ecology-Progress Series*, 179:81–95, 1999.

[33] Elisa M. Maldonado and Michael I. Latz. Shear-stress dependence of dinoflagellate bioluminescence. *The Biological Bulletin*, 212(3):242–249, 2007.

[34] Horst Bleckmann. Role of the lateral line in fish behaviour. In Tony J. Pitcher, editor, *The Behaviour of Teleost Fishes*, pages 177–202. Springer US, 1986.

[35] Georg Kreimer. The green algal eyespot apparatus: a primordial visual system and more? *Current genetics*, 55(1):19–43, February 2009.

[36] Gáspár Jékely, Julien Colombelli, Harald Hausen, Keren Guy, Ernst Stelzer, François Nédélec, and Detlev Arendt. Mechanism of phototaxis in marine zooplankton. *Nature*, 456(7220):395–9, November 2008.

[37] Bogdan Wozniak and Jerzy Dera. *Light Absorption in Sea Water*. Springer New York, New York, NY, USA, 2007.

[38] Mark W Denny. *Air and water: the biology and physics of life's media*. Princeton University Press, 1993.

[39] MF Land. Visual acuity in insects. *Annual Review of Entomology*, 42(46):147–177, 1997.

[40] HB Barlow. The size of ommatidia in apposition eyes. *Journal of Experimental Biology*, (May):667–674, 1952.

[41] MF Land and RD Fernald. The evolution of eyes. *Annual review of neuroscience*, 15(1990):1–29, January 1992.

[42] Helga Kolb, Ralph Nelson, Eduardo Fernandez, and Bryan Jones. Part ii: Anatomy and physiology of the retina: Photoreceptors. In *WEBVISION: The organization of the Retina and Visual System*. 2014.

[43] RL Dunbrack and DM Ware. Energy constraints and reproductive trade-offs determining body size in fishes. In P. Calow, editor, *Evolutionary Physiological Ecology*, pages 191–218. Cambridge University Press, 1987.

[44] Steven Schwartz. *Visual perception: A Clinical Orientation*. McGraw-Hill Professional, 3rd edition, 2004.

[45] D Northmore, FC Volkmann, and D Yager. Vision in fishes: colour and pattern. In *The Behavior of Fish and Other Aquatic Animals*, ed. D. I. Mostofsky, New York: Academic Press, pp 79-136, 1978.

[46] Howard C Howland, Stacey Merola, and Jennifer R Basarab. The allometry and scaling of the size of vertebrate eyes. *Vision research*, 44(17):2043–65, January 2004.

[47] Raymond C Smith and Karen S Baker. Optical properties of the clearest natural waters (200-800nm). *Applied Optics*, 20(2):177–184, 1981.

[48] RJ DaviesColley and DG Smith. Optically pure waters in Waikoropupu ('Pupu') Springs, Nelson, New Zealand. *New Zealand Journal of Marine and Freshwater Research*, 29(2):251–256, 1995.

[49] DL Aksnes and J Giske. A theoretical model of aquatic visual feeding. *Ecological Modelling*, 67(2-4):233–250, June 1993.

[50] AO Kasumyan. Sounds and sound production in fishes. *Journal of Ichthyology*, 48(11):981–1030, December 2008.

[51] DR Ketten. The marine mammal ear: specializations for aquatic audition and echolocation. *The evolutionary biology of hearing*, pages 717–750, 1992.

[52] AD Hawkins. The Behaviour of Teleost Fishes. In *The behaviour of teleost fishes*, ed. Tony J. Pitcher, page 11451, New York, NY: Springer, 1986.

[53] JHS Blaxter. The swimbladder and hearing. In *Hearing and sound communication in fishes*, pp. 6171., eds. WN Tavolga, AN Popper, RR Fay, New York NY: Springer, 1981.

[54] JL Aroyan, MA McDonald, SC Webb, JA Hildebrand, D Clark, JT Laitman, and JS Reidenberg. Acoustic models of sound production and propagation. In Hearing by whales and dolphins (eds. WWL Au, AN Popper, RR Fay), New York NY: Springer, 2000

[55] C Lockyer. Body weights of some species of large whales. *Journal du Conseil*, 36(3):259–273, 1976.

[56] HH Jakobsen, LM Everett, and SL Strom. Hydromechanical signaling between the ciliate mesodinium pulex and motile protist prey. *Aquatic microbial ecology*, 44(2):197–206, 2006.

[57] A Reid. Family idiosepiidae. In *Cephalopods of the world: an annotated and illustrated catalogue of cephalopod species known to date, Vol. I*, pp. 208210, Number 4, Vol 1, eds. P. Jereb and C. F. E. Roper, Rome: FAO, 2005.

[58] KJ Wright, DM Higgs, and JM Leis. Ontogenetic and interspecific variation in hearing ability in marine fish larvae. *Marine Ecology Progress Series*, 424:1–13, March 2011.

[59] BE Joseph, JE Antrim, and LH Cornell. Commerson's dolphin (cephalorhynchus commersonii): a discussion of the first live birth within a marine zoological park. *Zoo biology*, 77:69–77, 1987.

[60] Stephanie L Watwood, Patrick J O Miller, Mark Johnson, Peter T Madsen, and Peter L Tyack. Deep-diving foraging behaviour of sperm whales (physeter macrocephalus). *The Journal of animal ecology*, 75(3):814–25, 2006.

[61] Svein Løkkeborg. Feeding behaviour of cod, *gadus morhua*: activity rhythm and chemically mediated food search. *Animal behaviour*, 56(2):371–378, 1998.

[62] Robert E Hueter, David A Mann, Karen P Maruska, Joseph A Sisneros, and Leo S Demski. Sensory biology of elasmobranchs. In *Biology of sharks and their relatives*, (eds. JC Carrier, JA Musick, MR Heithaus), Boca Raton FL: CRC Press, pages 325–368, 2004.

[63] Pavel Aprikian, Gianluca Interlandi, Brian A. Kidd, Isolde Le Trong, Veronika Tchesnokova, Olga Yakovenko, Matt J. Whitfield, Esther Bullitt, Ronald E. Stenkamp, Wendy E. Thomas, and Evgeni V. Sokurenko. The bacterial fimbrial tip acts as a mechanical force sensor. *PLoS Biol*, 9(5):e1000617, 05 2011.

[64] JM Gardiner and J Atema. Flow sensing in sharks: Lateral line contributions to navigation and prey capture. In Horst Bleckmann, Joachim Mogdans, and Sheryl L. Coombs, editors, *Flow Sensing in Air and Water*, pages 127–146. Springer Berlin Heidelberg, 2014.

[65] Wolf Hanke, Sven Wieskotten, Benedikt Niesterok, Lars Miersch, Matthias Witte, Martin Brede, Alfred Leder, and Guido Dehnhardt. Hydrodynamic perception in pinnipeds. In Cameron Tropea and Horst Bleckmann, editors, *Nature-Inspired Fluid Mechanics*, volume 119 of *Notes on Numerical Fluid Mechanics and Multidisciplinary Design*, pages 255–270. Springer Berlin Heidelberg, 2012.

[66] W Watson and HJ Walker jr. The world's smallest vertebrate, schindleria brevipinguis, a new paedomorphic species in the family schindleriidae (perciformes: Gobioidei). *Records of the Astralian Museum*, 56:139–142, 2004.

[67] MF Land and DE Nilsson. *Animal eyes*. Oxford University Press, 2002.

[68] C Feuillade and RW Nero. A viscous-elastic swimbladder model for describing enhanced-frequency resonance scattering from fish. *The Journal of the Acoustical Society of America*, 103(6):3245–3255, 1998.

[69] Aike Beckmann and Inga Hense. Beneath the surface: Characteristics of oceanic ecosystems under weak mixing conditions – a theoretical investigation. *Progress in Oceanography*, 75(4):771–796, December 2007.

Supplementary Information:
Size Structures Sensory Hierarchy in Ocean Life

Erik A. Martens[1,2,3,5,♯,*] Navish Wadhwa[1,4,5,♯,†] Nis S. Jacobsen[1,2], Christian Lindemann[2], Ken H. Andersen[1,2], and André Visser[1,2]

[1]*VKR Centre for Ocean Life, Technical University of Denmark, Jægersborg Allé 1, 2920 Charlottenlund, Denmark* [2]*National Institute of Aquatic Resources, Technical University of Denmark, Charlottenlund Slot, Jægersborg Allé 1, DK-2920 Charlottenlund, Denmark* [3]*Department of Biomedical Sciences, Copenhagen University, Blegdamsvej 3, 2200 Copenhagen, Denmark* [4]*Department of Physics, Technical University of Denmark, DK-2800 Kgs. Lyngby, Denmark* [5]*These authors contributed equally to this study.* [♯]*Corresponding authors.*

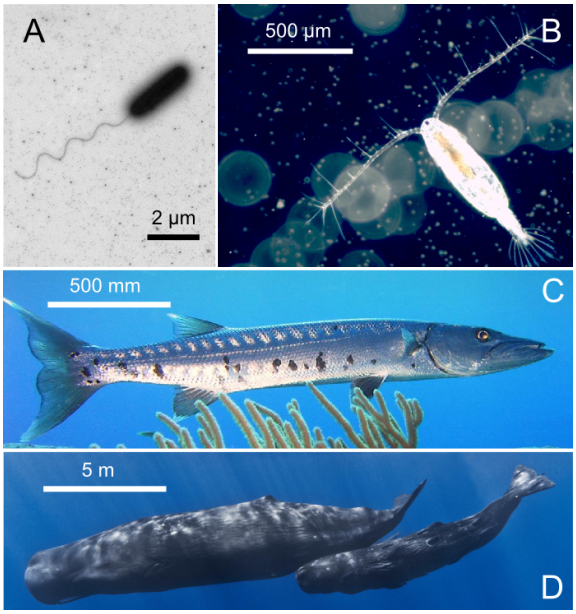

FIG. 1. **Dominant sensing modes** change with increasing size of the organism: (**A**) Small organisms like bacteria (e.g., *Vibrio alginolyticus*) use chemosensing, and move up or down the gradients of chemicals (image courtesy Kwangmin Son and Roman Stocker, MIT). (**B**) Millimetre sized organisms like copepods (e.g. *Acartia tonsa*) use hydromechanical signals to detect predators and prey in the vicinity (image courtesy of Thomas Kiørboe, DTU). (**C**) Larger organisms like fish (e.g. great barracuda *Sphyraena barracuda*) are often visual predators. (**D**) Toothed whales (e.g. *Physeter macrocephalus*) use echolocation. Images in panels C,D are in public domain.

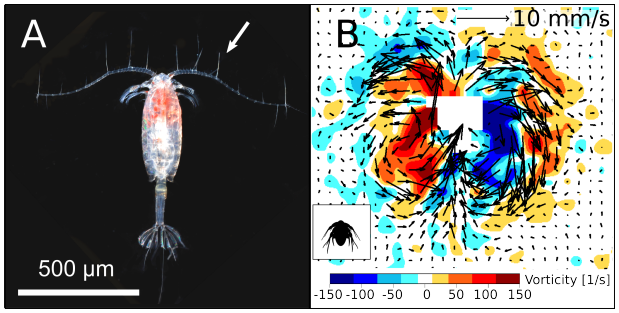

FIG. 2. **Mechanosensing. A:** Dorsal view of an adult *Acartia tonsa*, showing the antennules covered with mechanosensory setae, one of which is marked with an arrow (image courtesy of Erik Selander). **B:** Flow disturbance created by a swimming *Acartia tonsa* nauplius, visualized in the form of velocity vectors and vorticity contours.

I. CHEMOSENSING

A. A note on chemical contrast

An absolute upper limit on sensing range is dictated by the requirement of sufficient chemical contrast. Chemosensing requires spatial variations in signal strength that can be detected and gradients therein tracked. However, chemical gradients tend to become eroded with time to background level. The upper limit chemosensing range is not only related to the size and sensory ability of the organism, but also to the nature of the chemical substrate and its degradation in the environment due to microbial action or chemical reactions. Thus, while it is clear that an upper limit to chemosensing range exists, it is not possible to quantify it.

II. VISION

A. Size limit for compound eyes

The compound eye is hemi-spherical in shape and subdivided into light-detecting units called *ommatidia*. Ommatidia are conical in shape and cover the surface with an opening of width δ. Given that the eye has a radius r, the visual acuity of an ommatidium is given by

$$\Delta\phi = \delta/r. \tag{1}$$

The number of ommatidia covering the hemispherical eye surface may be estimated as the ratio of the eye surface, around $2\pi r^2$, and the surface element covered by an ommatidium,

* erik.martens@sund.ku.dk
† nawa@fysik.dtu.dk

around $r^2\Delta\phi^2$,

$$N = \frac{2\pi r}{\Delta\phi^2}. \tag{2}$$

Increasing the number of ommatidia, N, enlarges the image-resolution of the eye; however, as δ is decreases, diffraction effects becomes increasingly important. Thus, minimization of ommatidia in compound eyes is limited due to diffraction limits, see [1, 2]. Considering this trade-off, the optimal width of the ommatidia can be estimated [1], yielding

$$\delta = \sqrt{\lambda r}, \tag{3}$$

where $\lambda = 400$nm is the wave length of blue light.

Substituting Eqs. (1) and (3) into Eq. (2), we obtain the resolution of an eye with optimal ommatidia, we have

$$N = \frac{2\pi r}{\lambda}. \tag{4}$$

The size of an optimal compound eye is then

$$L_{\rm eye} = 2r = \frac{\lambda N}{\pi}. \tag{5}$$

The size of the optimal compound eye with a reasonably useful resolution of $N = 100^2$ pixels should be $L_{\rm eye} = 1.2$ mm, corresponding to roughly $L \sim 1$ to 3 cm (depending on the size ratio of eye to body). By comparison, some of the smallest organisms carrying compound eyes are *Daphnia*, with adults ranging from 1 to 5 mm [3]. Optimality of the eye, Eq. (5), then implies a resolution of $N \sim 10^2$ pixels – however, this is a resolution which barely produces a usable image.

B. Sensing range

The sensing range condition in the main text is given by

$$C_0 e^{-\alpha R} \geq C_{\rm th,min} + K R^2 L^{-4}. \tag{6}$$

Rescaling the sensing range, $\tilde{R} = \alpha R$ and the size, $\tilde{L} = (C_0\alpha^2/K)^{1/4}$ where $C := C_{\rm th,min}/C_0$, this becomes

$$e^{-\tilde{R}} \geq C + \tilde{R}^2\tilde{L}^{-4}. \tag{7}$$

The clear-water limit corresponds to small $\tilde{R} \ll 1$, yielding

$$\tilde{R} \sim \tilde{L}^2(1-C)^{1/2}, \tag{8}$$

and the turbid-water corresponds to large $\tilde{L}$, yielding

$$\tilde{R} \sim -\ln(C)/\alpha. \tag{9}$$

These expressions match the ones presented in the main text.

Letting the two expressions for the rescaled sensing ranges (8) and (9) be similar, we arrive at the condition for the cross-over between the two regimes:

$$\tilde{L}_x^2 \sim -\ln(C)/(1-C)^{1/2}, \tag{10}$$

which in the original unscaled variables becomes $L_{\rm x}^2 \sim \alpha^{-1}K^{\frac{1}{2}}(C_0 - C_{\rm th,min})^{-\frac{1}{2}}\ln(C_0/C_{\rm th,min})$ or, to leading order,

$$L_{\rm x}^2 \sim \alpha^{-1}K^{\frac{1}{2}}(C_0 - C_{\rm th,min})^{-\frac{1}{2}}. \tag{11}$$

The clear-water limit occurs for $L \ll L_x$ and the turbid water limit for $L \gg L_x$. Thus, the turbid limit is reached in the limit of large α, large $(C_0 - C_{\rm th,min})$, or small sensitivity K, respectively.

Another (rough) estimate of the minimal body size, for which vision is still marginally meaningful, might be feasible from the condition that $L \sim R$. This condition has at most two solutions, whereas the minimal solution is $L \approx [K/(C_0 - C_{\rm th,min})]^{1/2}$. A precise determination of this estimate of the smallest animal carrying an eye is, however, difficult due to the unknown scaling coefficient in this estimate and uncertainties concerning parameter values.

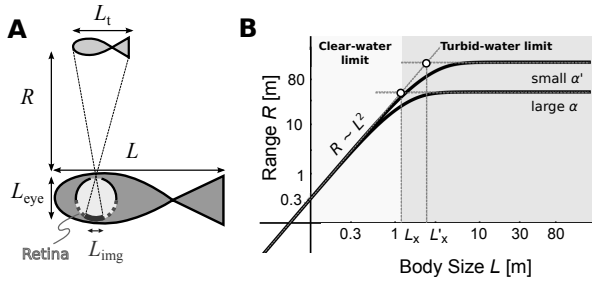

FIG. 3. **Vision. A**: An organism of body size L, with an eye of size $L_{\rm eye}$, detects a target of size L_t at a distance R if the apparent contrast of the target is equal or larger than the threshold contrast of the organism's eye. **B**: Maximal visual sensing range scales with body size L: like $R \sim L^2$ in the clear-water limit ($L \ll L_x$) and like $R \sim$ constant in the turbid-water limit ($L \gg L_x$). Parameters are $C_0 = 0.3, C_{\rm th,min} = 0.05$ (adopted from [4]), $K = 2.5 \times 10^{-4}$ m^2, $\alpha = 0.04$ m^{-1} [5] (and α' = 0.01 m^{-1} for comparison).

III. ECHOLOCATION

A. Scaling argument for sensing range

We estimate how the range of echolocation scales with body size L based on three assumptions: i) the threshold sensitivity of the ear I_0 is independent of organism size L [6], ii) the emitted sound intensity I_e scales with size: $I_e \propto L^{3\phi}$ where $3/4 < \phi < 1$, and iii) the carrier frequency of the signal depends on L (see [7]).

The generated acoustic signal first travels through water, is then partially reflected by the target, and the remainder of the signal travels back to the organism. I_e, is thus reduced by two processes:

i) ***Reflection.*** The signal is reduced upon reflection from the target and the reflected intensity is proportional to the target area which scales as $L_{\rm t}^2$.

ii) ***Attenuation.*** Sound intensity decreases with distance as r^{-2} due to geometric divergence. It is further attenuated exponentially due to absorption in the seawater.

Together, the signal intensity attenuates as $(2r)^{-2}e^{-2\mu r}$, where the factor 2 is due to the doubled travel distance. Geometric attenuation strongly dominates over the absorption processes, thus, $I_r \sim I_e L_t^2 r^{-2} \sim L^{3\phi} L_t^2 r^{-2}$. The strength of the returned signal must exceed the threshold intensity for detection in the ear, $I_r = I_0$, yielding a sensing range $R \sim I_0^{-1/2} L^{3\phi/2} L_\mathrm{t}$. Introducing the size ratio $p = L_\mathrm{t}/L$, we arrive at

$$R \sim p I_0^{-1/2} L^{\gamma}, \tag{12}$$

where the exponent $\gamma = 1 + 3\phi/2$ lies between 2.125 to 2.5. The scaling factor depends on unknown parameters, but can be estimated from data describing the echolocation range of small marine mammals. The resulting scaling coefficient (including p/I_0) is $6.47\ \mathrm{m}^{-1.5}$ for $\gamma = 2.5$, and $9.79\ \mathrm{m}^{-1.125}$ for $\gamma = 2.125$.

Figure 5 compares the scaling for Eq. 12 with data available for dolphins [8–12]. There is considerable scatter in the data, yet we recognize that the prediction compares with the data reasonably well.

1. Signal attenuation

We detail our estimates for the effects of attenuation due to geometric divergence and absorption processes in sea water. First, we discuss the effect of absorption processes on the transmission of pulses. To begin, we note that the absorption coefficient μ is frequency dependent. Each pulse is transmitted and characterized by its center (or carrier) frequency f_c, which is also the dominant frequency of the pulse spectrum. We may disregard all other frequencies and thus the dispersion of the transmitted pulse, leaving us with the task to find the absorption coefficient for f_c. The attenuation of sound in seawater is a complex molecular process which occurs both due to viscous absorption generated by particle motion, but also due to molecular relaxation processes by Boric acid and Magnesium sulphate. A formula for the frequency dependent absorption has been devised [13]. However, this relation is too complicated for our purposes as we desire to establish a simple asymptotic scaling relation between f_c and μ; indeed, the data is well *parameterized* by $\mu \sim f_c^{4/3}$ (see Section 3 below and Figure 5). Further, it is known that f_c depends on body size; experimental data [7] for dolphins (excluding river dolphins), allows us to heuristically deduce a scaling dependence for the absorption, $f_c \approx 370\ \mathrm{m}^{3/4}\ \mathrm{s}^{-1} \times L^{-3/4}$ (see Section 2 below). Combining these two scalings, we obtain for the absorption coefficient (decibel / meter) $\mu \approx 10^{-2} L^{-1}$. Finally, since the fitted data is measured in the logarithmic decibel scale, the attenuation factor due to absorption converts to $10^{-0.1\mu(L)\times 2R}$. Summed up, the intensity is reduced by a factor $I_r/I_e \sim R^{-2} 10^{-0.001\times 2R/L}$. However, further analysis shows that the effect of damping is negligible when compared to the geometric divergence. Thus, the reflected sound intensity simplifies to $I_r \sim L^{3\phi} L_o^2 R^{-2}$.

2. Center frequency

Center frequencies of echolocation signals have been measured for dolphins [7], shown in Figure 4A. The two river dolphins discussed in [7] are excluded from our analysis, since dolphins in such environments operate at different frequencies to adapt for sound transmission in non-free environments. We fitted the relation between the body mass w and the center frequency by $f_c \approx (368.7\ \mathrm{m}^{0.26}\ \mathrm{s}^{-1}) \times m^{-0.26}$. Since the mass scales as $w \sim L^3$, we obtain $f_c \sim L^{-3/4}$.

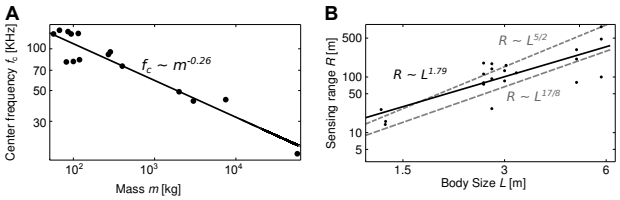

FIG. 4. **Echolocation.** **A:** Power law fit for echolocation center frequencies of dolphins. Data from [7]: f_c = (17.5, 42, 43, 75, 49, 95, 83.4, 80.4, 91, 81, 128, 136, 129, 133, 128) kHz; m = (57000, 3000, 7500, 400, 2000, 285, 119, 82, 270, 100, 94, 67.5, 115, 86, 57) kg. **B:** Comparison of the predicted echolocation sensing range (dashed grey) with data (black dots), which scales like $R \approx 14.2\ \mathrm{m}^{-0.79} \cdot L^{1.79}$ (black line, least squares fit).

For comparison, note that the frequency with maximal intensity produced in the nasal sac is approximated by the Helmholtz frequency [14]:

$$f_p = \frac{c}{2\pi}\left(\frac{A}{V\ L_\mathrm{t}}\right)^{1/2} \propto L^{-1}. \tag{13}$$

where A, V, L_t are the area, volume and length of the nasal sac. Given that m is proportional to L^3, the scaling observed in Fig. 4 appears to deviate somewhat from this theoretical estimate. The deviation may be explained by shortcomings of the simple Helmholtz oscillator model.

3. Sound absorption in marine environments

The authors in [13] derive a simplified equation of the form

$$\mu = A_1 P_1 f_1 f_c^2/(f_1^2 + f_c^2) + A_2 P_2 f_2 f_c^2/(f_2^2 + f_c^2) + A_3 P_3 f_c^2 \tag{14}$$

where the center frequency f_c is measured in Hz at the depth z in km. Further, they determine the following coefficients characteristic to the properties of seawater for boron and for magnesium,

$$\begin{aligned} f_1 &= 0.78 * (S/35)^{1/2} e^{T/26} \\ f_2 &= 42 e^{T/17} \\ A_1 &= 0.106 \\ A_2 &= 0.52 * (1 + T/43)(S/35) \\ A_3 &= 0.00049 \\ P_1 &= e^{(pH-8)/0.56} \end{aligned}$$

$$P_2 = e^{-z/6}$$
$$P_3 = e^{-(T/27+z/17)}.$$

Location	pH	S [ppt]	T [C]	z [km]
Pacific	7.7	34	4	1
Red Sea	8.2	40	22	0.2
Arctic Ocean	8.2	30	-1.5	0
Baltic Sea	7.9	8	4	0

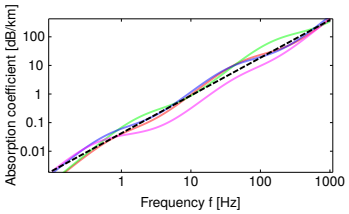

FIG. 5. Power law fit for relation between frequency and sound absorption coefficient in the ocean. **Top:** Parameter values for pH, S, T, z for Eq. 14 valid for different ocean regions. **Bottom:** Absorption rates resulting from parameters for the various regions listed in the top table. Fitting the logarithmic data linearly (dashed line) over the frequency range of interest results in the asymptotic scaling relation μ [db/km] $\approx 0.0434\ \mathrm{s}^{-4/3}\mathrm{km}^{-1} \times f^{4/3}[\mathrm{s}^{-1}]$.

The scaling for the absorption coefficient μ is thus (decibel per meter)

$$\mu \approx 4.2 \times 10^{-5}\mathrm{s}^{4/3}\mathrm{m}^{-1} \times f_c^{4/3}. \tag{15}$$

where the center frequency (s^{-1}) is

$$f_c \approx 65.8\,\mathrm{s}^{-1}\mathrm{m}^{3/4} \times L^{-3/4} \tag{16}$$

where we have used the relation mass w = ρL^3 with $\rho = 10^3$ kg m^{-3}. Thus, we obtain (decibel per meter)

$$\mu \approx 10^{-2} \times L^{-1}. \tag{17}$$

B. Assumptions underlying the scaling argument

The scaling argument for the range rests on assumptions supported by data only in part, which we review here for clarity:

(A1) the threshold sensitivity of the ear I_0 is independent of target size L. This approximation is supported by audiograms (behavioral and auditory brain stem responses) of odontocetes [12, 15–18],

(A2) the emitted sound intensity that an animal produces scales with size: $I_e \propto L^{3\phi}$ where $3/4 < \phi < 1$,

(A3) the carrier frequency of the sonar signal depends on size L.

Assumption (A3) seems fairly well corroborated, as already discussed in section A and B. Assumption (A2) states that the scaling exponent ϕ is allowed to vary in a small range corresponding to a sublinear volume dependence of the generating organ size which is a fairly reasonable assumption. Taking into account the considerable scatter of the data, we recognize that the prediction compares with the data reasonably well, as is evidenced in Figure 7 in the main text. However, better data is required to further underpin assumption (A1). Indeed, within the group of whales and dolphins we find no clear *size*-dependence for the sensitivity threshold I_0 [18]; but it would be desirable to obtain more data to solidify this assumption, as well as to identify a satisfactory physical or biological explanation for why the sensitivity is independent of body size, in contrast to other mammal groups [15–19].

[1] R. P. Feynman. Color vision. In Michael A. (Caltech) Gottlieb and Rudolf (Caltech) Pfeiffer, editors, *The Feynman Lectures on Physics*, chapter 36.4. California Institute of Technology, 2013.

[2] MF Land. Visual acuity in insects. *Annual Review of Entomology*, 42(46):147–177, 1997.

[3] Dieter Ebert. *Ecology, Epidemiology, and Evolution of Parasitism in Daphnia*. Bethesda (MD): National Center for Biotechnology Information (US), 2005.

[4] RL Dunbrack and DM Ware. Energy constraints and reproductive trade-offs determining body size in fishes. In P. Calow, editor, *Evolutionary Physiological Ecology*, pages 191–218. Cambridge University Press, 1987.

[5] Aike Beckmann and Inga Hense. Beneath the surface: Characteristics of oceanic ecosystems under weak mixing conditions – a theoretical investigation. *Progress in Oceanography*, 75(4):771–796, December 2007.

[6] D. R. Ketten. Marine mammal auditory systems: A summary of audiometric and anatomical data and implications for underwater acoustic impacts. *Polarforschung*, 72(2/3):79–92, 2004.

[7] Frants H Jensen, Alice Rocco, Rubaiyat M Mansur, Brian D Smith, Vincent M Janik, and Peter T Madsen. Clicking in shallow rivers: Short-range echolocation of irrawaddy and ganges river dolphins in a shallow, acoustically complex habitat. *PloS one*, 8(4):e59284, January 2013.

[8] WWL Au and KJ Snyder. Long-range target detection in open waters by an echolocating atlantic bottlenose dolphin (tursiopstruncatus). *The Journal of the Acoustical Society of* . . . , pages 1077–1084, 1980.

[9] Lance G Barrett-Lennard, John K Ford, and Kathy A Heise. The mixed blessing of echolocation: Differences in sonar use by fish-eating and mammal-eating killer whales. *Animal Behaviour*, 51:553–565, 1996.

[10] R A Kastelein, W W Au, H T Rippe, and N M Schooneman. Target detection by an echolocating harbor porpoise (phocoena phocoena). *The Journal of the Acoustical Society of America*, 105:2493–2498, 1999.

[11] A. Earl Murchison. *Animal Sonar Systems*. Springer US, Boston, MA, January 1980.

[12] J. Teilmann, L. A. Miller, T. Kirketerp, R. A. Kastelein, P. T. Madsen, B. K. Nielsen, and W. L. Au. Characteristics of echolocation signals used by a harbour porpoise (*Phocoena phocoena*) in a target detection experiment. *Aquatic Mammals*,

28:275–284, 2002.

[13] MA Ainslie and JG McColm. A simplified formula for viscous and chemical absorption in sea water. *The Journal of the Acoustical Society of America*, 103(June 1997):1997–1998, 1998.

[14] JL Aroyan, MA McDonald, SC Webb, JA Hildebrand, D Clark, JT Laitman, and JS Reidenberg. Acoustic models of sound production and propagation. In *Hearing by Whales and Dolphins*, number 2000. 2000.

[15] Paul E. Nachtigall, T. Aran Mooney, Kristen a. Taylor, and Michelle M. L. Yuen. Hearing and auditory evoked potential methods applied to odontocete cetaceans. *Aquatic Mammals*, 33(1):6–13, January 2007.

[16] A F Pacini, P E Nachtigall, L N Kloepper, M Linnenschmidt, A Sogorb, and S Matias. Audiogram of a formerly stranded long-finned pilot whale (globicephala melas) measured using auditory evoked potentials. *The Journal of Experimental Biology*, 213:3138–3143, 2010.

[17] Aude F Pacini, Paul E Nachtigall, Christopher T Quintos, T David Schofield, Dera a Look, Gregg a Levine, and Jason P Turner. Audiogram of a stranded blainville's beaked whale (mesoplodon densirostris) measured using auditory evoked potentials. *The Journal of Experimental Biology*, 214(Pt 14):2409–15, July 2011.

[18] DOSITS.org. What sounds can animals hear? *Discovery of Sound in the Sea (dosits.org)*, 2014.

[19] R. A. Kastelein, P. Bunskoek, M. Hagedoorn, W. L. Au, and D. de Haan. Audiogram of a harbor porpoise (phocoena phocoena) measured with narrow-band frequency-modulated signals. *The Journal of the Acoustical Society of America*, 112(1):334, 2002.

Bibliography

[1] R. J. Adrian, *Particle-image techniques for experimental fluid mechanics*, Annual Review of Fluid Mechanics **23** (1991), 261–304.

[2] N. V. Aladin, *The conservation ecology of the Podonidae from the Caspian and Aral seas*, Cladocera as Model Organisms in Biology (P. Larsson and L. J. Weider, eds.), Developments in Hydrobiology, vol. 107, Springer Netherlands, 1995, pp. 85–97.

[3] A. Andersen, N. Wadhwa, and T. Kiørboe, *Quiet swimming at low Reynolds number*, Physical Review E **91** (2015), 042712.

[4] K. H. Andersen, T. Berge, R. J. Gon çalves, M. Hartvig, J. Heuschele, S. Hylander, N. S. Jacobsen, C. Lindemann, E. A. Martens, A. B. Neuheimer, K. Olsson, A. Palacz, F. Prowe, J. Sainmont, S. J. Traving, A. W. Visser, N. Wadhwa, and T. Kiørboe, *Characteristic sizes of life in the oceans, from bacteria to whales*, Annual Review of Marine Science **8** (2016).

[5] C. M. Andersen Borg, E. Bruno, and T. Kiørboe, *The Kinematics of Swimming and Relocation Jumps in Copepod Nauplii*, PLoS ONE **7** (2012), e47486.

[6] G. K. Batchelor, *An introduction to fluid dynamics*, Cambridge University Press, Cambridge, UK, 1967.

[7] R. N. Bearon and V. Magar, *Simple models of the chemical field around swimming plankton*, Journal of Plankton Research **32** (2010), 1599–1608.

[8] A. Bejan and J. H. Marden, *Unifying constructal theory for scale effects in running, swimming and flying*, Journal of Experimental Biology **209** (2006), 238–248.

[9] J. R. Blake, *A spherical envelope approach to ciliary propulsion*, Journal of Fluid Mechanics **46** (1971), 199.

[10] H. F Bosch and W. R. Taylor, *Distribution of the cladoceran Podon polyphemoides in the Chesapeake Bay*, Marine Biology **19** (1973), 161–171.

[11] C. Brönmark and L.-A. Hansson, *The biology of lakes and ponds*, Oxford University Press, 2005.

[12] H. I. Browman, J. Yen, D. M. Fields, J. F. St-Pierre, and A. B. Skiftesvik, *Fine-scale observations of the predatory behaviour of the carnivorous copepod Paraeuchaeta norvegica and the escape responses of their ichthyoplankton prey, Atlantic cod (Gadus morhua)*, Marine Biology **158** (2011), 2653–2660.

[13] M. H. Bundy and G. A. Paffenhöfer, *Analysis of flow fields associated with freely swimming calanoid copepods*, Marine Ecology Progress Series **133** (1996), 99–113.

[14] E. J. Buskey, P. H. Lenz, and D. K. Hartline, *Escape behavior of planktonic copepods in response to hydrodynamic disturbances: High speed video analysis*, Marine Ecology Progress Series **235** (2002), 135–146.

[15] K. B. Catton, *Aspects of sensory cues and propulsion in marine zooplankton hydrodynamic disturbances*, Ph.D. thesis, Georgia Institute of Technology, 2009.

[16] K. B. Catton, D. R. Webster, J. Brown, and J. Yen, *Quantitative analysis of tethered and free-swimming copepodid flow fields*, Journal of Experimental Biology **210** (2007), 299–310.

[17] K. B. Catton, D. R. Webster, and J. Yen, *The effect of fluid viscosity, habitat temperature, and body size on the flow disturbance of Euchaeta*, Limnology & Oceanography: Fluids & Environments **2** (2012), 80–92.

[18] J. Cosson, M. Cachon, J. Cachon, and M.-P. Cosson, *Swimming behaviour of the unicellular biflagellate oxyrrhis marina: in vivo and in vitro movement of the two flagella*, Biology of the Cell **63** (1988), 117–126.

[19] J. H. Costello, J. R. Strickler, C. Marrasé, G. Trager, R. Zeller, and A. J. Freise, *Grazing in a turbulent environment: behavioral response of a calanoid copepod, Centropages hamatus.*, Proceedings of the National Academy of Sciences of the United States of America **87** (1990), 1648–1652.

[20] A. B. Craig, P. L. Skehan, J. A. Pawelczyk, and W. L. Boomer, *Velocity,stroke rate,and distance per stroke during elite swimmwng competition.*, Medicine & Science in Sports & Exercise **17** (1985).

[21] B. Delmotte, E. E. Keaveny, and F. Plourabou, *Large-scale simulation of steady and time-dependent active suspensions with the force-coupling method*, Arxiv.

[22] M. H. Dickinson, F.-O. Lehmann, and S. P. Sane, *Wing rotation and the aerodynamic basis of insect flight*, Science **284** (1999), 1954–1960.

[23] K. Drescher, J. Dunkel, L. H. Cisneros, S. Ganguly, and R. E. Goldstein, *Fluid dynamics and noise in bacterial cell-cell and cell-surface scattering*, Proceedings of the National Academy of the United States of America **108** (2011), 10940–10945.

[24] K. Drescher, R. E. Goldstein, N. Michel, M. Polin, and I. Tuval, *Direct Measurement of the Flow Field around Swimming Microorganisms*, Physical Review Letters **105** (2010), 168101.

[25] K. Drescher, K. C. Leptos, I. Tuval, T. Ishikawa, T. J. Pedley, and R. E. Goldstein, *Dancing volvox: Hydrodynamic bound states of swimming algae*, Physical Review Letters **102** (2009), 1–4.

[26] D. Feigenbaum and M. R. Reeve, *Prey detection in the Chaetognatha: Responseto a vibrating probe and experimental determination of attack distance in large aquaria*, Limnology and Oceanography **22** (1977), 1052–1058.

[27] T. Fenchel and P. J. Hansen, *Motile behaviour of the bloom-forming ciliate Mesodinium rubrum*, Marine Biology Research **2** (2006), 169–177.

[28] D. M. Fields, *Orientation affects the sensitivity of Acartia tonsa to fluid mechanical signals*, Marine Biology **157** (2010), 505–514.

[29] D. M. Fields, D. S. Shaeffer, and M. J. Weissburg, *Mechanical and neural responses from the mechanosensory hairs on the antennule of Gaussia princeps*, Marine Ecology Progress Series **227** (2002), 173–186.

[30] D. M. Fields, S. D. Shema, H. I. Browman, T. Q. Browne, and A. B. Skiftesvik, *Light primes the escape response of the Calanoid Copepod, Calanus finmarchicus*, PLoS ONE **7** (2012), 1–7.

[31] D. M. Fields and M. J. Weissburg, *Rapid firing rates from mechanosensory neurons in copepod antennules*, Journal of Comparative Physiology A: Neuroethology, Sensory, Neural, and Behavioral Physiology **190** (2004), 877–882.

[32] D. M. Fields and J. Yen, *Outer limits and inner structure: The 3-dimensional flow field of pleuromamma xiphias (calanoida: Metridinidae)*, Bulletin of Marine Science **53** (1993), 84–95.

[33] ———, *The escape behavior of marine copepods in response to a quantifiable fluid mechanical disturbance*, Journal of Plankton Research **19** (1997), 1289–1304.

[34] ———, *Fluid mechanosensory stimulation of behaviour from a planktonic marine copepod, Euchaeta rimana Bradford*, Journal of Plankton Research **24** (2002), 747–755.

[35] R. W. Fox, A. T. McDonald, and P. J. Pritchard, *Introduction to fluid mechanics*, John Wiley & Sons, 2006.

[36] J. A. Freund, S. Mieruch, B. Scholze, K. Wiltshire, and U. Feudel, *Bloom dynamics in a seasonally forced phytoplankton-zooplankton model: Trigger mechanisms and timing effects*, Ecological Complexity **3** (2006), 129–139.

[37] B. J. Gemmell, H. Jiang, and E. J. Buskey, *A new approach to micro-scale particle image velocimetry (μ-PIV) for quantifying flows around free-swimming zooplankton*, Journal of Plankton Research **36** (2014), 1396–1401.

[38] O. M. Gilbert and E. J. Buskey, *Turbulence decreases the hydrodynamic predator sensing ability of the calanoid copepod Acartia tonsa*, Journal of Plankton Research **27** (2005), 1067–1071.

[39] C. W. Gill, *The response of a restrained copepod to tactile stimulation*, Marine Ecology Progress Series **21** (1985), 121–125.

[40] C. W. Gill and D. J. Crips, *Sensitivity of intact and antennule amputated copepods to water disturbance* , Marine Ecology Progress Series **21** (1985), 221–227.

[41] R. E. Goldstein, *Green Algae as Model Organisms for Biological Fluid Dynamics*, Annual Review of Fluid Mechanics **47** (2015), 343–375.

[42] R. J. Gonçalves and T. Kiørboe, *Perceiving the algae: How feeding-current feeding copepods detect their nonmotile prey*, Limnology and Oceanography (2015), n/a–n/a.

[43] B. I. Grosser, E. R. Baylor, and F. E. Smith, *Analysis of geostatical responses in Daphnia magna*, Ecology **34** (1953), 804–805.

[44] J. S. Guasto, K. A. Johnson, and J. P. Gollub, *Oscillatory flows induced by microorganisms swimming in two dimensions*, Physical Review Letters **105** (2010), 18–21.

[45] J. S. Guasto, R. Rusconi, and R. Stocker, *Fluid Mechanics of Planktonic Microorganisms*, Annual Review of Fluid Mechanics **44** (2012), 373–400.

[46] J. H. W. Hain, G. R. Carter, S. D. Kraus, C. A. Mayo, and H. E. Winn, *Feeding behavior of the humpback whale, Megaptera novaeangliae, in the western North Atlantic*, Fishery Bulletin **80** (1982), 259–268.

[47] R. Harris, *Copepods*, Marine biology : a derivative of Encyclopedia of ocean science (John H. Steele, Thorpe Steve A., and Turekian Karl K., eds.), Academic Press, 2009, pp. 40–50.

[48] D. K. Hartline, E. J. Buskey, and P. H. Lenz, *Rapid jumps and bioluminescence elicited by controlled hydrodynamic stimuli in a mesopelagic copepod, Pleuromamma xiphias*, Biological Bulletin **197** (1999), 132–143.

[49] L. R. Haury, D. E. Kenyon, and J. R. Brooks, *Experimental evaluation of the avoidance reaction of Calanus finmarchicus*, Journal of Plankton Research **2** (1980), 187–202.

[50] P. A. Heuch, M. H. Doall, and J. Yen, *Water flow around a fish mimic attracts a parasitic and deters a planktonic copepod*, Journal of Plankton Research **29** (2007).

[51] G. A. Horridge and P. S. Boulton, *Prey Detection by Chaetognatha via a Vibration Sense*, Proceedings of the Royal Society B: Biological Sciences **168** (1967), 413–419.

[52] A. G. Humes, *Copepoda from deep-sea hydrothermal vents and cold seeps*, Hydrobiologia **167-168** (1988), 549–554.

[53] ———, *How many copepods?*, Hydrobiologia **292-293** (1994), no. 1, 1–7.

[54] R. Huys and G. A. Boxshall, *Copepod evolution*, Ray Society, 1991.

[55] T. Ishikawa, M. P. Simmonds, and T. J. Pedley, *Hydrodynamic interaction of two swimming model micro-organisms*, Journal of Fluid Mechanics **568** (2006), 119.

[56] J. D. Jackson, *Classical electrodynamics*, 3 ed., Wiley, New York, 1999.

[57] H. H. Jakobsen, *Escape response of planktonic protists to fluid mechanical signals*, Marine Ecology Progress Series **214** (2001), 67–78.

[58] ———, *Escape of protists in predator-generated feeding currents*, Aquatic Microbial Ecology **26** (2002), 271–281.

[59] C. D. Jersabek, A. Brancelj, F. Stoch, and R. Schabetsberger, *Distribution and ecology of copepods in mountainous regions of the eastern alps*, Copepoda: Developments in Ecology, Biology and Systematics (R. M. Lopes, J. W. Reid, and C. E. F. Rocha, eds.), Developments in Hydrobiology, vol. 156, Springer Netherlands, 2001, pp. 309–324.

[60] K. Katija and J. O. Dabiri, *In situ field measurements of aquatic animal fluid interactions using a Self-Contained Underwater Velocimetry Apparatus (SCUVA)*, Limnology and Oceanography: Methods **6** (2008), 162–171.

[61] J. Katz and J. Sheng, *Applications of Holography in Fluid Mechanics and Particle Dynamics*, Annual Review of Fluid Mechanics **42** (2010), 531–555.

[62] W. C. Kerfoot, *Combat between predatory copepods and their prey: Cyclops, Epischura, and Bosmina*, Limnology and Oceanography **23** (1978), 1089–1102.

[63] T. Kiørboe, *How zooplankton feed: Mechanisms, traits and trade-offs*, Biological Reviews **86** (2011), 311–339.

[64] ———, *What makes pelagic copepods so successful?*, Journal of Plankton Research **33** (2011), 677–685.

[65] T. Kiørboe, A. Andersen, V. J. Langlois, and H. H. Jakobsen, *Unsteady motion: escape jumps in planktonic copepods, their kinematics and energetics.*, Journal of the Royal Society, Interface **7** (2010), 1591–1602.

[66] T. Kiørboe, H. Jiang, and S. P. Colin, *Danger of zooplankton feeding: the fluid signal generated by ambush-feeding copepods*, Philosophical transactions of the Royal Society of London. Series B, Biological sciences **277** (2010), 3229–3237.

[67] T. Kiorboe, H. Jiang, R. J. Goncalves, L. T. Nielsen, and N. Wadhwa, *Flow disturbances generated by feeding and swimming zooplankton*, Proceedings of the National Academy of Sciences of the United States of America **111** (2014), 6–11.

[68] T. Kiørboe, E. Saiz, and A. Visser, *Hydrodynamic signal perception in the copepod Acartia tonsa*, Marine Ecology Progress Series **179** (1999), 97–111.

[69] T. Kiørboe and A. Visser, *Predator and prey perception in copepods due to hydromechanical signals*, Marine Ecology Progress Series **179** (1999), 81–95.

[70] K. L. Kirk, *Water flows produced by Daphnia and Diaptomus: Implications for prey selection by mechanosensory predators*, Limnology and Oceanography **30** (1985), 679–686.

[71] G. S. Klindt and B. M. Friedrich, *Flagellar swimmers oscillate between pusher- and puller-type swimming*, Arxiv (2015), 1–12.

[72] L. D. Landau and E. M. Lifshitz, *Fluid mechanics*, 2 ed., Course of Theoretical Physics, vol. 6, Butterworth-Heinemann.

[73] M. R. Landry, *Detection of prey by Calanus pacificus: Implications of the first antennae*, Limnology and Oceanography **25** (1980), 545–549.

[74] G. V. Lauder, *Fish Locomotion: Recent Advances and New Directions*, Annual Review of Marine Science **7** (2015), 521–545.

[75] L. G. Leal, *Advanced transport phenomena: fluid mechanics and convective transport processes*, Cambridge University Press, 2007.

[76] L. Legendre and F. Rassoulzadegan, *Food-web mediated export of biogenic carbon in oceans: Hydrodynamic control*, Marine Ecology Progress Series **145** (1996), 179–193.

[77] M. F. Legier-Visser, J. G. Mitchell, A. Okubo, and J. a. Fuhrman, *Mechanoreception in calanoid copepods*, Marine Biology **90** (1986), 529–535.

[78] M. J. Lighthill, *On the Squirming Motion of Nearly Spherical Defomable Bodies through Liquids at Very Small Reynolds Numbers*, Communications on Pure and Applied Mathematics **5** (1952), 109–118.

[79] K. Lillelund and R. Lasker, *Laboratory studies of predation by marine copepods on fish larvae*, Fishery Bulletin **69** (1971), 655–667.

[80] A. R. Longhurst, *The structure and evolution of plankton communities*, Progress in Oceanography **15** (1985), 1–35.

[81] V. Magar, T. Goto, and T. J. Pedley, *Nutrient uptake by a self-propelled steady squirmer*, Quarterly Journal of Mechanics and Applied Mathematics **56** (2003), 65–91.

[82] E. Malkiel, J. Sheng, J. Katz, and J. R. Strickler, *The three-dimensional flow field generated by a feeding calanoid copepod measured using digital holography*, Journal of Experimental Biology **206** (2003), 3657–3666.

[83] E. A. Martens, N. Wadhwa, N. S. Jacobsen, C. Lindemann, K. H. Andersen, and A. Visser, *Size structures sensory hierarchy in ocean life*, bioRxiv (2015).

[84] J. Mauchline, *Advances in marine biology: The biology of calanoid copepods*, vol. 33, Academic Press, 1998.

[85] A. Mazumdar, *Principles and Techniques of Schlieren Imaging*, Tech. report, Department of Computer Science, Columbia University, New York, NY, USA, 2011.

[86] W. Merzkirch, *Flow Visualization*, Elsevier, 1987.

[87] Sébastien Michelin and Eric Lauga, *Optimal feeding is optimal swimming for all Péclet numbers*, Physics of Fluids **23** (2011).

[88] J. J. Molina, Y. Nakayama, and R. Yamamoto, *Hydrodynamic interactions of self-propelled swimmers*, Soft Matter **9** (2013), 4923.

[89] D. W. Murphy, *Planktonic propulsion: the hydrodynamics, kinematics, and design of metachrony*, Ph.D. thesis, Georgia Institute of Technology, 2012.

[90] D. W. Murphy, D. R. Webster, and J. Yen, *A high-speed tomographic PIV system for measuring zooplanktonic flow*, Limnology and Oceanography: Methods **10** (2012), 1096–1112.

[91] T. K. Newbury, *Vibration Perception by Chaetognaths*, Nature **236** (1972), 459–460.

[92] L. T. Nielsen and T. Kiørboe, *Feeding currents facilitate a mixotrophic way of life*, ISME Journal (2015).

[93] J. W. Nybakken and M. D. Bertness, *Marine biology: an ecological approach*, 6th ed., Benjamin Cummings, San Francisco, 2005.

[94] O. S. Pak and E. Lauga, *Generalized squirming motion of a sphere*, Journal of Engineering Mathematics (2014), 1–28.

[95] E. K. Pikitch, C. Santora, E. A. Babcock, A. Bakun, R. Bonfil, D. O. Conover, P. Dayton, P. Doukakis, D. Fluharty, B. Heneman, E. D. Houde, J. Link, P. A. Livingston, M. Mangel, M. K. McAllister, J. Pope, and K. J. Sainsbury, *Ecosystem-based fishery management*, Science **305** (2004), 346–347.

[96] C. W. Pitt Ford and H. Babinsky, *Lift and the leading-edge vortex*, Journal of Fluid Mechanics **720** (2013), 280–313.

[97] L. R. Pomeroy, *The Ocean's Food Web, A Changing Paradigm*, BioScience **24** (1971), 499–504.

[98] F. H. Post and T. van Walsum, *Fluid flow visualization*, Focus on Scientific Visualization (Hans Hagen, Heinrich MÃ¼ller, and Gregory M. Nielson, eds.), Computer Graphics: Systems and Applications, Springer Berlin Heidelberg, 1993, pp. 1–40.

[99] S. Pournazeri, P. S. Segre, M. Princevac, and D. L. Altshuler, *Hummingbirds generate bilateral vortex loops during hovering: evidence from flow visualization*, Experiments in Fluids **54** (2012), no. 1.

[100] C. Pozrikidis, *Introduction to Theoretical and Computational Fluid Dynamics*, Oxford University Press, USA, 2011.

[101] R. Preston, *Climbing the redwoods*, The New Yorker (2005), 212–225.

[102] E. M. Purcell, *Life at low reynolds number*, American Journal of Physics **45** (1977), no. 1, 3–11.

[103] M. Raffel, C. E. Willert, S. T. Wereley, and J. Kompenhans, *Particle image velocimetry: a practical guide*, Springer-Verlag Berlin Heidelberg, 2007.

[104] O. Reynolds, *An Experimental Investigation of the Circumstances Which Determine Whether the Motion of Water Shall Be Direct or Sinuous, and of the Law of Resistance in Parallel Channels*, Philosophical Transactions of the Royal Society of London **174** (1883), 935–982.

[105] E. Saiz, A. Calbet, and E. Broglio, *Effects of small-scale turbulence on copepods: The case of Oithona davisae*, Limnology and Oceanography **48** (2003), 1304–1311.

[106] J. G. Santiago, S. T. Wereley, C. D. Meinhart, D. J. Beebe, and R. J. Adrian, *A particle image velocimetry system for microfluidics*, Experiments in Fluids **25** (1998), no. 4, 316–319.

[107] R. Schröder, *Echoorientierung bei Mixodiaptomus laciniatus*, Die Naturwissenschaften **47** (1960), 548–549.

[108] K. V. Singarajah, *Escape reactions of zooplankton: The avoidance of a pursuing siphon tube*, Journal of Experimental Marine Biology and Ecology **3** (1969), 171–178.

[109] E. Stamhuis and J. Videler, *Quantitative flow analysis around aquatic animals using laser sheet particle image velocimetry*, Journal of Experimental Biology **198** (1995), 283–94.

[110] J. R. Strickler, *Intra-and interspecific information flow among planktonic copepods: Receptors*, Verhandlungen des Internationalen Verein Limnologie **19** (1975), 2951–2958.

[111] ———, *Swimming of Planktonic Cyclops Species (Copepoda, Crustacea): Pattern, Movements and Their Control*, Swimming and Flying in Nature (TheodoreY.-T. Wu, CharlesJ. Brokaw, and Christopher Brennen, eds.), Springer US, 1975, pp. 599–613.

[112] J. R Strickler, *Observation of swimming performances of planktonic copepods*, Limnology and Oceanography **22** (1977), 165–170.

[113] J. R. Strickler, *Calanoid copepods, feeding currents, and the role of gravity*, Science **218** (1982), 158–160.

[114] J. R. Strickler and A. K. Bal, *Setae of the First Antennae of the Copepod Cyclops scutifer (Sars): Their Structure and Importance.*, Proceedings of the National Academy of Sciences of the United States of America **70** (1973), 2656–2659.

[115] J. R. Strickler and G. Balázsi, *Planktonic copepods reacting selectively to hydrodynamic disturbances.*, Philosophical transactions of the Royal Society of London. Series B, Biological sciences **362** (2007), 1947–1958.

[116] C. Svensen and T. Kiørboe, *Remote prey detection in Oithona similis: hydromechanical versus chemical cues*, Journal of Plankton Research **22** (2000), 1155–1166.

[117] K. M. Swadling, A. Slotwinski, C. Davies, J. Beard, A. D. McKinnon, F. Coman, N. Murphy, M. Tonks, W. Rochester, D. V. P. Conway, G. W. Hosie, and A. J. Richardson, *Australian marine zooplankton: a taxonomic guide and atlas*, February 2013.

[118] L. Szlauer, *Reaction of Daphnia pulex de Geer to the approach of different objects*, Polskie Archiwum Hydrobiologii **12** (1964), 7–16.

[119] A. Thu, Y. Byun, and J. Lee, *Dye Visualization of the Vortical Flow Structure over a Double-Delta Wing*, Journal of Aerospace Engineering **25** (2011), 541–546.

[120] B. W. Tobalske, *Biomechanics of bird flight.*, Journal of Experimental Biology **210** (2007), 3135–3146.

[121] J. T. Turner, *Zooplankton fecal pellets, mrine snow and sinking phytoplankton blooms.*, Aquatic Microbial Ecology **27** (2002), 57–102.

[122] J. T. Turner and P. A. Tester, *Toxic marine phytoplankton, zooplankton grazers, and pelagic food webs*, Limnology and Oceanography **42** (1997), 1203–1214.

[123] E. D. Tytell and G. V. Lauder, *The hydrodynamics of eel swimming: I. Wake structure.*, Journal of Experimental Biology **207** (2004), 1825–1841.

[124] UN-Oceans, *UN Atlas of the Oceans*, 2015.

[125] L. A. van Duren, *Copepod feeding currents: flow patterns, filtration rates and energetics*, Journal of Experimental Biology **206** (2003), 255–267.

[126] ———, *Escape from viscosity: the kinematics and hydrodynamics of copepod foraging and escape swimming*, Journal of Experimental Biology **206** (2003), 269–279.

[127] L. A. van Duren, E. J. Stamhuis, and J. J. Videler, *Reading the copepod personal ads: increasing encounter probability with hydromechanical signals*, Philosophical Transactions of the Royal Society of London B: Biological Sciences **353** (1998), 691–700.

[128] M. Van Dyke, *An album of fluid motion*, Parabolic Press, Stanford, Ca., 1982.

[129] M. Viitasalo, T. Kiørboe, J. Flinkman, L. W. Pedersen, and A. Visser, *Predation vulnerability of planktonic copepods: Consequences of predator foraging strategies and prey sensory abilities*, Marine Ecology Progress Series **175** (1998), 129–142.

[130] A. Visser, *Hydromechanical signals in the plankton*, Marine Ecology Progress Series **222** (2001), 1–24.

[131] N. Wadhwa, A. Andersen, and T. Kiørboe, *Hydrodynamics and energetics of jumping copepod nauplii and copepodids*, Journal of Experimental Biology **217** (2014), no. 17, 3085–3094.

[132] S. Wang and A. Ardekani, *Inertial squirmer*, Physics of Fluids **24** (2012).

[133] D. M. Ware, *Bioenergetics of pelagic fish: Theoretical change in swimming speed and ration with body size*, Journal of the Fisheries Research Board of Canada **35** (1978), 220–228.

[134] P. W. Webb, *Simple physical principles and vertebrate aquatic locomotion*, American Zoologist **28** (1988), 709–725.

[135] J. Yen and D. Fields, *Escape responses of Acartia hudsonica (Copepoda) nauplii from the flow field of Temora longicornis (Copepoda)*, Archiv fur Hydrobiologie Beih. Ergebn. Limnol. **36** (1992), 123–134.

[136] J. Yen, D. W. Murphy, L. Fan, and D. R. Webster, *Sensory-Motor Systems of Copepods involved in their Escape from Suction Feeding*, Integrative and Comparative Biology (2015), 1–13.

[137] J. Yen and A. Okubo, *Particle and prey detection by mechanoreceptive copepods: A mathematical analysis*, Hydrobiologia **480** (2002), 165–173.

[138] J. Yen, B. Sanderson, J. R. Strickler, and A. Okubo, *Feeding currents and energy dissipation by Euchaeta rimana, a subtropical pelagic copepod*, Limnology and Oceanography **36** (1991), 362–369.

[139] J. Yen and J. R. Strickler, *Advertisement and concealment in the plankton: What makes a copepod hydrodynamically conspicuous*, Invertebrate Biology **115** (1996), 191–205.